

**The role of endothelial glutamine synthetase in  
vascular tone and atherogenesis**

Katie Elizabeth Musialowski

Submitted in accordance with the requirements for the degree of Doctor of  
Philosophy

The University of Leeds

Faculty of Medicine and Health

Leeds Institute of Cardiovascular and Metabolic Medicine

April 2020

The candidate confirms that the work submitted is her own and that appropriate credit has been given where reference has been made to the work of others.

This copy has been supplied on the understanding that it is copyright material and that no quotation from the thesis may be published without proper acknowledgement

The right of Katie Elizabeth Musialowski to be identified as Author of this work has been asserted by her in accordance with the Copyright, Designs and Patents Act 1988.

© The University of Leeds and Katie Elizabeth Musialowski

## Acknowledgements

Firstly, I must say a big thank you to my supervisor, Dr. Richard Cubbon. Thank you for your support and guidance over the last 4 years, for always being understanding, for letting me ask the same questions over and over again and for encouraging me to be positive about data, even when it doesn't show you what you wanted!

I could not have completed this project without Dr. Nadira Yuldasheva. Thank you, not only for the time you have spent teaching me, but for all of our chats too. I have learnt much more from you than just science. You have been a wonderful teacher and have shown me endless kindness, for which I am eternally grateful.

I also extend my thanks to Professor Mark Kearney for letting me become part of such a welcoming and supportive research group. In addition, I thank Professor Peter Carmeliet for providing the VEGS Hom line. My gratitude also goes to the University of Leeds for funding this project; I hope that one day my work will make a difference.

I must acknowledge Professor David Beech, my supervisor during my undergraduate research project and Masters in Research. Thank you for all the opportunities you have given to me; I would not have been able to take this PhD if it wasn't for you. Thank you also for always commending my large appetite.

It is also important that I mention the advice and help given to me by Dr. Karen Porter – thank you, it helped me more than you know.

Next, I need to thank all the members of the Kearney Group, particularly the following:

Anna – I think over the last year I became the bane of your life! Thank you so much for all the time that you spent harvesting with me, for teaching me how to use the microtome and for all the aortae you helped me stain. I hope one day I can repay you with a pot of bigos!

Natasha – You have always been there to help me, from teaching me how to genotype to bandaging my finger in the histology room! Thank you for putting up with my endless questions and for appreciating my love of His Dark Materials and Harry Potter audiobooks.

Katie S – Thank you for being my number one HUVEC supplier, but more importantly, for the great chats. I'll miss our laughs about your time in Newcastle, the antics of Erin and Freya and my failed attempts of holding onto luggage.

Tom – I really appreciate all those hours you spent helping me with the organ bath when you were snowed down with your own work. Also, thank you for not judging my questionable scientific knowledge, or my inability to do anything to time!

Alex – For letting me steal your reagents and use that amazing bag sealer, but especially for advising me and helping me with experiments when you didn't have to.

Hema – For encouraging me to take this PhD, supporting me through it and teaching me how not to poison myself with radioactive carbon.

Jess – For always helping me, answering all my questions and, of course, sharing your baking secrets.

Lauren – For listening to my PhD woes, always giggling with me and for being an all-round top friend. Oh, and for saving me with toothpaste...

Natalie – For putting up with my incessant ordering requests, lending me reagents and always helping me with injections.

Katy P – For all the funny chats and always taking the time to teach me.

Chloé – For being a great lab bench buddy, letting me steal your stuff and for offering to help me with my western blots when you had enough of your own work to do.

Nicole – For showing me how to get a beautiful endothelial cell pellet and encouraging me to find a way to combine my love for art with science.

Claire – For solving my PCR problems and teaching me to stain in the frantic last few weeks.

Mike D – For providing hilarious gossip and saving my bacon when I really needed superfrost slides.

Stacey, Peysh & Asjad – For all your patience and helping me with the initial organ bath experiments.

I also need to acknowledge the Beech Group. I have loved sitting amongst you, I feel like I'm still a Beech lab member. It has been such good fun and I will miss you all.

From here, I have to extend thanks to the very special Dr. Melanie Ludlow/Bettale. Isn't it funny to look back to the first week of my undergraduate project when I couldn't understand how to get 0.1% DMSO! I am so grateful for everything you have done for me, all of the ridiculous questions you've answered (I still don't know what Gibson Assembly is – I'm sorry!) and for the countless times you've helped me when it was no

longer your job. We've made a lot of good memories and I know we will keep in touch to make some more.

To another Melanie – or 'Mel' – thank you for all your help in CEU, you really got me out of some tricky spots! Thank you also for all the laughter and for appreciating both my cone-head and my passion for Love Island. I know I'll convert you eventually.

There are also a few more LICAMM members, past and present, that I need to thank for brightening my days in the lab.

Thank you to Lucia, Pete, Nick and Adam for all the fun times. Also, thank you to the members of biscuit club for trying to maintain normality during lockdown.

Marj & Fiona – Merci beaucoup neighbour friends for letting me teach you real French, oui oui le pantalon! I know that you will miss my graceful eating style and elegant, non-sweaty entrances into the office. On a serious note, thank you for being great friends. There are many more laughs to come out of the lab I'm sure. Although on second thoughts, sounds good but not with you...

Hannah – Who would have thought from my first week in the Beech lab that I'd come to find out that you're not 'edgy' or 'coool'. In fact, you're just as weird as me. Thank you for all our giggles, we've had some great times and I can't wait to continue galloping with you,

Beth – Thank you for being my fellow food fetcher and for putting up with my bad language and inappropriate jokes. More importantly, thank you for all your kindness and for cheering me on, even though you're now thousands of miles away.

Kat – From your first week in the lab when we agreed to use 'aubergine' as a code word, I knew we would be great friends. We've made some lovely memories, from K&K dinners to 'pregante!'. You have always encouraged me and have helped me through some really tough times. I will forever be grateful that you're my chum

Nikki – I couldn't have asked for a better lab partner in crime, but also for a better friend. From Adelaide, all the way to this PhD, you have been an amazing support and have always been able to put a smile on my face. You were there for me in my hardest moments and I will never be able to say how much that means.

Finally, I must say thank you to 4 very special people.

Michael – you have filled the last 18 months of my life with happiness and so much laughter that it hurts. I cannot thank you enough for everything you've done: listening

to me rant, driving out late to the lab to bring me my tea and providing me with a hipflask! You have given me so much encouragement and somehow know exactly how to pick me up when I think things look bleak. You are truly fantastic and I hope I can support you just as much on your own journey to becoming a doctor.

Crike, Cath and Matthew – There is no way I could have done this without you. These past 4 years have been the hardest of my life. You have loved and supported me through every step and made me believe I can accomplish anything. I am very proud of what I've achieved through this PhD, but nothing will ever give me as much pride as being able to call you my family. Thank you for everything.

## Abstract

Endothelial dysfunction characterises both atherosclerosis and diabetes. These diseases have complex aetiologies which are not adequately addressed by current treatments. One approach to addressing this unmet need is developing therapies targeting genetic predisposition.

Recent genome wide association studies have implicated the enzyme glutamine synthetase (GS) in diabetic vascular disease. GS catalyses the conversion of glutamate and ammonia to glutamine. It is enriched in arterial endothelial cells and upregulated in unstable atherosclerotic plaques. Besides the promotion of angiogenic sprouting through palmitoylation of the GTPase, RhoJ, the role of GS in the endothelium is unclear. This thesis aims to explore the role of endothelial GS in regulating arterial function in health and disease.

Mice with endothelial-specific GS deletion (VEGS Hom) or haploinsufficiency (VEGS Het) were used to examine the influence of endothelial GS on vascular function. VEGS Hom exhibited reduced aortic vasoconstriction to phenylephrine, which was lost upon inhibition of endothelial nitric oxide synthase (eNOS), suggesting increased basal nitric oxide (NO) bioavailability. This was not seen in VEGS Het. Vasorelaxation to acetylcholine and sodium nitroprusside was unchanged in VEGS Hom, implying stimulated NO formation and responsiveness are unaltered. Neither model displayed differences in endothelial repair following denuding wire-injury. Induction of diabetes in VEGS Hom with streptozocin prevented the reduction of aortic vasoconstriction to phenylephrine, indicating a loss of increased basal NO bioavailability. GS inhibition in HUVECs elevated basal eNOS activity, the mechanism of which requires further investigation. ApoE<sup>-/-</sup> mice with endothelial-specific GS deletion (VEGA Hom) or haploinsufficiency (VEGA Het) demonstrated significantly reduced atheroma burden after western diet. A similar trend was noted in VEGA Hom receiving both streptozocin and western diet.

Endothelial GS deficiency enhances basal eNOS activity, alongside suppressing atherosclerosis formation. Greater understanding of GS in the endothelium may aid development of more efficacious and personalised treatments for diabetic vascular disease.

## Table of contents

<b>Acknowledgements</b> .....	<b>iii</b>
<b>Abstract</b> .....	<b>vii</b>
<b>Table of contents</b> .....	<b>viii</b>
<b>List of Figures</b> .....	<b>xiii</b>
<b>List of Tables</b> .....	<b>xvi</b>
<b>Abbreviations</b> .....	<b>xvii</b>
<b>Chapter 1 Introduction</b> .....	<b>1</b>
1.1 Physiology of the vascular endothelium.....	1
1.1.1 Endothelial transport .....	1
1.1.2 Immune response .....	1
1.1.3 Haemostasis and coagulation .....	2
1.1.4 Angiogenesis .....	2
1.1.5 Vascular tone.....	3
1.1.5.1 Endothelin-1 .....	3
1.1.5.2 Prostacyclin and Thromboxane A <sub>2</sub> .....	4
1.1.5.3 Endothelial-derived hyperpolarising factors .....	4
1.2 Nitric oxide .....	5
1.2.1 Nitric oxide synthase enzymes in vascular physiology .....	5
1.2.2 eNOS.....	6
1.2.3 eNOS signalling .....	8
1.2.3.1 Vasodilation.....	8
1.2.3.2 S-nitrosylation of proteins .....	10
1.2.3.3 Interactions with O <sub>2</sub> and reactive oxygen species .....	10
1.2.4 Regulation of eNOS activity .....	12
1.2.4.1 Post-translational modifications of eNOS.....	12
1.2.4.1.1 Phosphorylation .....	12
1.2.4.1.2 Acylation .....	13
1.2.4.1.3 S-nitrosylation .....	14
1.2.4.2 Protein interactions .....	15
1.2.4.2.1 Caveolin-1 and calmodulin .....	15
1.2.4.2.2 Heat shock protein 90 .....	15
1.2.4.2.3 Actin.....	16
1.2.5 eNOS uncoupling.....	17
1.3 Endothelial dysfunction.....	18

1.4 Atherosclerosis.....	18
1.4.1 Plaque vulnerability and rupture.....	23
1.5 Insulin resistance.....	24
1.6 Diabetes.....	25
1.6.1 Type 1 diabetes mellitus.....	25
1.6.2 Type 2 diabetes mellitus.....	26
1.6.3 Glucose homeostasis and insulin secretion.....	26
1.6.3.1 Insulin release and amino acids.....	27
1.6.3.2 Insulin release and fatty acids.....	28
1.6.3.3 Physiological effects of insulin.....	28
1.6.3.4 Insulin and the vasculature.....	29
1.7 Macrovascular complications and diabetes.....	30
1.7.1 Genetic associations between vascular disease and diabetes.....	33
1.8 Glutamine synthetase.....	34
1.8.1 Glutamine metabolism in physiology and disease.....	35
1.8.1.1 Glutamine metabolism and the liver.....	35
1.8.1.2 Glutamine metabolism and the kidney.....	36
1.8.1.3 Glutamine metabolism and the CNS.....	36
1.8.1.4 Glutamine metabolism and diabetes.....	38
1.8.1.5 Glutamine metabolism and the vasculature.....	38
1.9 Summary.....	42
1.10 Aims and objectives.....	43
1.10.1 Overall aim.....	43
1.10.2 Hypothesis.....	43
1.10.3 Objectives.....	43
<b>Chapter 2 Materials and methods.....</b>	<b>44</b>
2.1 Materials.....	44
2.2 Methods.....	50
2.2.1 Animal husbandry.....	50
2.2.1.1 General housing.....	50
2.2.2 Generation of mouse models.....	50
2.2.2.1 CreLoxP technology.....	50
2.2.2.2 VEGS Hom.....	53
2.2.2.3 VEGS Het.....	55
2.2.2.4 VEGA.....	58
2.2.2.4.1 VEGS Het/ApoE <sup>-/-</sup> (VEGA Het).....	58

2.2.2.4.2 VEGS Hom/ApoE <sup>-/-</sup> (VEGA Hom) .....	60
2.2.3 Tamoxifen preparation and induction .....	64
2.2.4 STZ preparation and administration .....	64
2.2.5 Mouse liver endothelial cell isolation .....	65
2.2.5.1 Tissue preparation and single cell suspension.....	65
2.2.5.2 Magnetic bead coating.....	65
2.2.5.3 Cell isolation .....	68
2.2.5.4 Culturing of mouse liver endothelial cells .....	68
2.2.6 RNA extraction.....	69
2.2.7 DNase digestion.....	69
2.2.8 Reverse transcription .....	69
2.2.9 Real-time quantitative polymerase chain reaction (RT-qPCR).....	70
2.2.10 Protein analysis.....	72
2.2.10.1 Aorta homogenisation.....	72
2.2.10.2 Protein quantification .....	72
2.2.10.3 Western blotting.....	72
2.2.10.4 Protein visualisation and analysis .....	74
2.2.11 Organ bath.....	74
2.2.11.1 Principle.....	74
2.2.11.2 Tissue collection .....	78
2.2.11.3 Preparation of aortic rings.....	78
2.2.11.4 Endothelial-dependent vasodilation .....	78
2.2.11.5 Endothelial-regulated vasoconstriction.....	78
2.2.11.6 Endothelial-independent vasorelaxation .....	79
2.2.12 Metabolic testing .....	79
2.2.13 Blood pressure measurements .....	79
2.2.14 Histology .....	80
2.2.15 Aortic sinus .....	80
2.2.15.1 Processing and paraffin embedding.....	80
2.2.15.2 Microtome sectioning.....	81
2.2.15.3 Miller van Gieson staining.....	81
2.2.15.4 Imaging and analysis .....	82
2.2.16 <i>En face</i> analysis of whole aorta.....	84
2.2.16.1 Oil Red O staining .....	84
2.2.16.2 Imaging and quantification of atherosclerosis .....	84
2.2.17 Vascular injury .....	86

2.2.17.1 Procedure conditions .....	86
2.2.17.2 Arterial injury.....	86
2.2.17.3 Assessment of endothelial regeneration .....	87
2.2.17.3.1 Evans Blue dye and tissue collection .....	87
2.2.17.3.2 Imaging and analysis.....	87
2.2.18 Nitrite/nitrate (NO <sub>x</sub> ) measurement .....	90
2.2.19 Human umbilical vein endothelial cell culture .....	90
2.2.20 Immunofluorescence.....	92
2.2.20.1 eNOS-β-actin staining.....	92
2.2.20.2 Confocal imaging and analysis .....	92
2.2.21 eNOS activity assay .....	95
2.2.21.1 Principle.....	95
2.2.21.2 Quantification of eNOS activity .....	95
2.2.22 Data analysis and presentation .....	96
<b>Chapter 3 Results .....</b>	<b>98</b>
3.1 The impact of endothelial GS holoinsufficiency on the vasculature <i>in vivo</i> ..	98
3.2 Exploring endothelial GS holoinsufficiency on vascular function in a STZ model of diabetes.....	116
3.3 The effect of endothelial GS haploinsufficiency on vascular function <i>in vivo</i> 122	
3.4 Pharmacological inhibition of endothelial GS <i>in vitro</i> .....	133
3.5 The consequences of endothelial GS deficiency on the development of atherosclerosis .....	138
3.6 Examining the influence of endothelial GS holoinsufficiency on diabetic vascular disease <i>in vivo</i> .....	152
<b>Chapter 4 Discussion .....</b>	<b>157</b>
4.1 Key findings.....	157
4.2 The effect of endothelial-specific GS holoinsufficiency on vascular function .. 159	
4.2.1 Vasomotor function .....	159
4.2.2 Endothelial regeneration .....	160
4.2.3 Expression of eNOS and phosphorylated eNOS S1177 .....	161
4.2.4 NO metabolism .....	161
4.2.5 eNOS activity .....	162
4.2.6 Vascular reactivity following STZ treatment.....	163
4.3 Endothelial GS haploinsufficiency and vascular phenotype .....	164
4.4 The impact of pharmacological inhibition of GS in endothelial cells .....	166

4.4.1 eNOS activity .....	166
4.4.2 Colocalisation of eNOS and $\beta$ -actin .....	166
4.5 The influence of endothelial GS deficiency on diabetic vascular disease..	168
4.5.1 Atherosclerotic plaque development .....	168
4.5.2 Plaque stability and rupture.....	171
4.6 Endothelial GS insufficiency and increased NO bioavailability .....	174
4.6.1 Arginine.....	174
4.6.2 iNOS.....	175
4.7 Measurement of NO .....	177
4.8 The interaction between endothelial GS deficiency and diabetes in atherosclerosis .....	179
4.9 Project limitations .....	180
4.9.1 Murine models .....	180
4.9.2 STZ as a model of diabetes .....	181
4.9.3 ApoE <sup>-/-</sup> mice for studying atherosclerosis .....	181
4.9.4 Origin of endothelial cells .....	183
4.10 Future work .....	184
4.11 Conclusion .....	186
<b>References .....</b>	<b>189</b>

## List of Figures

Figure 1.1 eNOS protein structure and NO formation .....	7
Figure 1.2 NO-mediated relaxation of vascular smooth muscle .....	9
Figure 1.3 Stages of atherosclerosis.....	22
Figure 1.4 Schematic summary of the role of glutamine synthetase in various physiological systems .....	41
Figure 2.1 Tamoxifen-inducible gene excision by the CreLoxP system.....	52
Figure 2.2 VEGS Hom breeding strategy.....	54
Figure 2.3 VEGS Het breeding strategy.....	56
Figure 2.4 VEGS Hom and VEGS Het experimental schedule.....	57
Figure 2.5 VEGA Het breeding strategy.....	59
Figure 2.6 VEGA Hom breeding strategy (Stage 1) .....	61
Figure 2.7 VEGA Hom breeding strategy (Stage 2) .....	62
Figure 2.8 VEGA Het and VEGA Hom experimental schedules.....	63
Figure 2.9 Magnetic bead cell separation .....	67
Figure 2.10 Organ bath apparatus.....	76
Figure 2.11 Representative traces of murine aortic vasomotor responses measured using organ bath equipment .....	77
Figure 2.12 Imaging of aortic sinus sections and assessment of atherosclerotic lesion coverage following Miller van Gieson staining .....	83
Figure 2.13 Quantification of atherosclerotic plaques.....	85
Figure 2.14 Visualisation and analysis of femoral arteries following wire-injury surgery .....	89
Figure 2.15 Immunofluorescent staining of HUVECs .....	94
Figure 3.1 Metabolic profile of VEGS Hom mice and control littermates .....	99
Figure 3.2 Validation of GS knockdown in VEGS Hom endothelial cells .....	101
Figure 3.3 Vasoconstriction of aortic rings from VEGS Hom and control mice following PE treatment with and without L-NMMA.....	103
Figure 3.4 Relaxation responses of aortic rings from VEGS Hom and control mice to Ach and SNP .....	104
Figure 3.5 Blood pressure measurements of VEGS Hom mice and control littermates.....	105
Figure 3.6 Contractile responses of aortic rings from VEGS Hom and control mice following PE treatment with and without catalase.....	107
Figure 3.7 Vasorelaxation of aortic rings from VEGS Hom and control mice in response to vasodilators Ach and SNP.....	108
Figure 3.8 Assessment of endothelial denudation induced by wire-injury surgery using Evans Blue dye .....	110

Figure 3.9 Degree of endothelial regeneration 4 days following wire-injury surgery .....	111
Figure 3.10 Protein expression of eNOS, p-eNOS S1177 and GS in whole aorta lysates from VEGS Hom and control mice .....	113
Figure 3.11 Evaluation of eNOS activity and NO <sub>x</sub> concentration in control and VEGS Hom mice.....	115
Figure 3.12 Metabolic profiles of VEGS Hom mice and control littermates in response to STZ treatment .....	117
Figure 3.13 Vasomotor function of aortic rings from STZ-treated VEGS Hom and control mice following exposure to PE with and without L-NMMA .....	119
Figure 3.14 Ach and SNP-induced vasorelaxation of aortic rings from STZ-treated VEGS Hom and control mice .....	120
Figure 3.15 Summary of key findings from VEGS Hom experiments .....	121
Figure 3.16 Metabolic profile of VEGS Het mice and control mice .....	123
Figure 3.17 Validation of GS knockdown in VEGS Het endothelial cells .....	125
Figure 3.18 Vasoconstriction of aortic rings from VEGS Het and control mice following PE treatment with and without L-NMMA.....	126
Figure 3.19 Vasorelaxation of aortic rings from VEGS Het and control mice in response to vasodilators Ach and SNP .....	127
Figure 3.20 Blood pressure of VEGS Het mice and control littermates .....	128
Figure 3.21 Endothelial repair in VEGS Het and control femoral arteries 4 days following wire-injury .....	130
Figure 3.22 Protein expression of eNOS, p-eNOS S1177 and GS in control and VEGS Het aortic lysates .....	131
Figure 3.23 Summary of key findings from VEGS Het experiments .....	132
Figure 3.24 eNOS activity in HUVECs following pharmacological inhibition of GS with MSO .....	134
Figure 3.25 Co-immunofluorescence of eNOS and F-actin in HUVECs with and without GS inhibition .....	136
Figure 3.26 Summary of key findings from <i>in vitro</i> experiments .....	137
Figure 3.27 Weight profile of VEGA Hom and control mice.....	140
Figure 3.28 Validation of GS knockdown in VEGA Hom endothelial cells .....	141
Figure 3.29 Glucose and insulin tolerance of control and VEGA Hom mice at the start of western diet feeding.....	142
Figure 3.30 Aortic atherosclerotic plaque burden in control and VEGA Hom mice following 12 weeks of western diet.....	144
Figure 3.31 Atherosclerotic lesion development within the aortic sinus of VEGA Hom and control mice .....	145
Figure 3.32 Weight profile of VEGA Het and control mice.....	147

Figure 3.33 Glucose and insulin tolerance of control and VEGA Het mice at the start of western diet feeding..... 148

Figure 3.34 Aortic atherosclerosis development in control and VEGA Het mice following 12 weeks of western diet feeding ..... 150

Figure 3.35 Atherosclerotic lesion development at the level of the aortic sinus in VEGA Het and control littermates ..... 151

Figure 3.36 Metabolic profile of VEGA Hom and control mice treated with STZ and receiving western diet ..... 153

Figure 3.37 Whole aortic atherosclerosis development in VEGA Hom and control mice treated with STZ and receiving 12 weeks of western diet ..... 154

Figure 3.38 Summary of key findings from VEGA Hom experiments ..... 155

Figure 3.39 Summary of key findings from VEGA Het experiments ..... 156

Figure 4.1 Key project findings..... 188

## List of Tables

Table 2.1 Summary of solutions, the components at final working concentrations and final solution pH .....	49
Table 2.2 Thermocycler conditions for reverse transcription of RNA samples using the LunaScript RT Supermix Kit.....	70
Table 2.3 RT-qPCR primer sequences, respective melting temperature and product lengths.....	71
Table 2.4 RT-qPCR cycling conditions.....	71
Table 2.5 Summary of primary antibodies used for protein analysis .....	73
Table 2.6 Summary of secondary antibodies used for protein analysis .....	74
Table 2.7 Preparation of M199 media for HUVEC culture .....	91
Table 2.8 Summary of antibodies and dyes used for immunofluorescent staining..	93

## Abbreviations

•OH	Hydroxyl radical
17-ODYA	17-octadecynoic acid
2-EOH	2-hydroethidium
4-OHT	4-hydroxytamoxifen
AAS	Antibiotic antimycotic solution
ABS	Actin-binding sequence
Ach	Acetylcholine
ADP	Adenosine diphosphate
AGE	Advanced glycation end-product
AMP	Adenosine monophosphate
AMPK	AMP-activated protein kinase
ApoB100	Apolipoprotein B100
ApoE	Apolipoprotein E
Arg	Arginine
ASL	Argininosuccinate lyase
ASS	Argininosuccinate synthetase
ATP	Adenosine triphosphate
AUC	Area under the curve
BCA	Bicinchoninic acid
BH <sub>4</sub>	Tetrahydrobiopterin
BSA	Bovine serum albumin
Ca <sup>2+</sup>	Calcium ion
CaCl <sub>2</sub> ·2H <sub>2</sub> O	Calcium chloride dihydrate
CaM	Calmodulin
CAT-1	Cationic amino acid transporter-1
CD146	Cluster of differentiation 146
CD36	Cluster of differentiation 36
cDNA	Complementary DNA

CETP	Cholesteryl ester transfer protein
cGMP	Cyclic guanosine monophosphate
CHD	Coronary heart disease
CHIP	C-terminal hsp70-interacting protein
Cit	Citrulline
CNS	Central nervous system
CO <sub>2</sub>	Carbon dioxide
CO <sub>3</sub> <sup>-</sup>	Carbonate radical
COX	Cyclooxygenase
Cu <sup>+</sup>	Cuprous ion
Cu <sup>2+</sup>	Cupric ion
DAF-2	Diaminofluorescein diacetate
DAG	Diacylglycerol
DAPI	4',6-diamidino-2-phenylindole
DBP	Diastolic blood pressure
DHE	Dihydroethidium
DNA	Deoxyribonucleic acid
DPMI	Disintegrations per minute
e <sup>-</sup>	Electron
ECGS	Endothelial cell growth serum
ECM	Extracellular matrix
EDHF	Endothelial-derived hyperpolarising factors
EDTA	Ethylenediaminetetraacetic acid
EET	Epoxyeicosatrienoic acid
eNOS	Endothelial nitric oxide synthase
EPR	Electron paramagnetic resonance
ER	Endoplasmic reticulum
ER (in reference to CreLoxP technology)	Oestrogen receptor

ET	Endothelin-1 receptor
ET-1	Endothelin-1
FA	Fatty acid
FAD	Flavin adenine dinucleotide
FBS	Foetal bovine serum
Fe <sup>2+</sup>	Ferrous iron
FMN	Flavin mononucleotide
FRET	Förster resonance energy transfer
GABA	Gamma aminobutyric acid
GCN2	General control nonderepressible 2
geNOp	Genetically encoded NO probe
GIP	Gastric inhibitory peptide
GLP1	Glucagon-like peptide-1
GLUT	Glucose transporter
GPCR	G-protein coupled receptor
GS	Glutamine synthetase
GSIS	Glucose-stimulated insulin secretion
GTP	Guanosine-5'-triphosphate
GTT	Glucose tolerance test
GWAS	Genome wide association studies
H <sup>+</sup>	Hydrogen ion
H <sub>2</sub> CO <sub>3</sub>	Carbonic acid
H <sub>2</sub> O <sub>2</sub>	Hydrogen peroxide
H <sub>2</sub> S	Hydrogen sulphide
HBSS	Hank's balanced salt solution
HCO <sub>3</sub> <sup>-</sup>	Bicarbonate
HEPES	4-(2-hydroxyethyl)-1-piperazineethanesulfonic acid
HRP	Horseradish peroxidase

Hsp90	Heat shock protein 90
HUVECs	Human umbilical vein endothelial cells
ICAM-1	Intercellular adhesion molecule-1
IL	Interleukin
ILK	Integrin-linked kinase
iNOS	Inducible nitric oxide synthase
IP	Prostacyclin receptors
IP <sub>3</sub>	Inositol 1,4,5-trisphosphate
IP <sub>3</sub> R	Inositol 1,4,5-trisphosphate receptor
IRS	Insulin receptor substrate
ITT	Insulin tolerance test
JNK3	c-Jun N-terminal kinase 3
K <sup>+</sup>	Potassium ion
KCl	Potassium chloride
KH <sub>2</sub> PO <sub>4</sub>	Potassium dihydrogen phosphate
KMnO <sub>4</sub>	Potassium permanganate
LDL	Low density lipoprotein
LDLr	Low density lipoprotein receptor
LEC	Liver endothelial cell
L-NAME	N <sup>ω</sup> -nitro-L-arginine methyl ester
L-NMMA	L-N <sup>G</sup> -monomethyl arginine
LOX-1	Lectin-type oxidized low density lipoprotein receptor 1
LPL	Lipoprotein lipase
LSEC	Liver sinusoidal endothelial cells
MAPK	Mitogen activated protein kinase
MBP	Mean blood pressure
MgSO <sub>4</sub> .7H <sub>2</sub> O	Magnesium sulphate
MKP7	Mitogen-activated protein kinase phosphatase

MLCK	Myosin light-chain kinase
MLCP	Myosin light-chain phosphatase
MMP	Matrix metalloprotease
mRNA	Messenger ribonucleic acid
MSO	Methionine sulfoximine
mTOR	Mammalian target of rapamycin
NaCl	Sodium chloride
NAD <sup>+</sup>	Nicotinamide adenine dinucleotide
NADPH	Nicotinamide adenine dinucleotide phosphate
NaHCO <sub>3</sub>	Sodium bicarbonate
NaN <sub>3</sub>	Sodium azide
NFBG	Non-fasting blood glucose
NF- $\kappa$ B	Nuclear factor- $\kappa$ B
NH <sub>3</sub>	Ammonia
NH <sub>4</sub> <sup>+</sup>	Ammonium ion
nNOS	Neuronal nitric oxide synthase
NO	Nitric oxide
NO <sup>+</sup>	Nitrosonium
NO <sub>2</sub>	Nitrite
NO <sub>2</sub> -FA	Nitro-fatty acids
NOS	Nitric oxide synthase
NO <sub>x</sub>	Nitrite and nitrate
O <sub>2</sub>	Oxygen
O <sub>2</sub> <sup>-</sup>	Superoxide
O-GlcNAc	O-linked acetylglucosamine
oxLDL	Oxidised low density lipoprotein
PAI-1	Plasminogen activator inhibitor-1
PBS	Phosphate-buffered saline
PDGF	Platelet derived growth factor

PE	Phenylephrine
p-eNOS	Phosphorylated endothelial nitric oxide synthase
PFA	Paraformaldehyde
PGH <sub>2</sub>	Prostaglandin H <sub>2</sub>
PGI <sub>2</sub>	Prostacyclin
PI3K	Phosphoinositide 3-kinase
PKA	Protein kinase A
PKC	Protein kinase C
PKG	Protein kinase G
PLC	Phospholipase C
PP	Protein phosphatase
RNA	Ribonucleic acid
RNS	Reactive nitrogen species
ROCK	Rho-associated protein kinase
ROS	Reactive oxygen species
RT-qPCR	Real-time quantitative polymerase chain reaction
SBP	Systolic blood pressure
SDS	Sodium dodecyl sulphate
SEM	Standard error of the mean
Ser	Serine
SERCA	Sarcoplasmic reticulum Ca <sup>2+</sup> -ATPase
sGC	Soluble guanylyl cyclase
shRNA	Short hairpin ribonucleic acid
SNO	S-nitrosothiol
SNP (in reference to genetic associations)	Single nucleotide polymorphism
SNP (in reference to organ bath experiments)	Sodium nitroprusside

Sp1	Specificity protein 1
SR	Sarcoplasmic reticulum
STAT	Signal transducer and activator of transcription
STZ	Streptozocin
T1DM	Type 1 diabetes mellitus
T2DM	Type 2 diabetes mellitus
TAMRA	5-carboxytetramethylrhodamine
TBS	Tris buffered saline
TBS-T	Tris buffered saline with Tween-20 (0.05%)
TCA	Tricarboxylic Acid
TGF- $\beta$	Transforming growth factor- $\beta$
Thr	Threonine
TLR-4	Toll-like receptor-4
TNF- $\alpha$	Tumor necrosis factor- $\alpha$
TP	Thromboxane-prostanoid
TXA <sub>2</sub>	Thromboxane A <sub>2</sub>
UPR	Unfolded protein response
VCAM-1	Vascular cell adhesion protein
VE-CAD	VE-Cadherin promoter region
VEGF	Vascular endothelial growth factor
VLDL	Very low density lipoprotein
VSMC	Vascular smooth muscle cell
Zn	Zinc

## **Chapter 1 Introduction**

### **1.1 Physiology of the vascular endothelium**

A monolayer of specialised epithelia, or endothelial cells, lines the lumen of the vasculature. The endothelium separates luminal contents and adjacent tissue. It was originally thought to exist as a non-reactive barrier, but it is now clear that endothelial cells are highly dynamic and play a vital role in maintaining vascular homeostasis. Alongside controlling movement of molecules between the blood and surrounding tissue, they interact with multiple cell types to regulate vascular tone, immune response and new vessel formation (Galley & Webster, 2004).

#### **1.1.1 Endothelial transport**

Endothelial cells exhibit several different mechanisms for transferring macromolecules from the vessel lumen to neighbouring tissue. They express the glucose transporters GLUT1 and GLUT4, as well as various transport systems required for movement of amino acids (Galley & Webster, 2004). The endothelium is a continuous layer, with cells connected by intercellular junctions. 3 types can exist between endothelial cells: tight junctions, adherens junctions and gap junctions. These are distinguished based on differences in their protein composition and function. They facilitate movement of various cellular signals needed for cell growth and apoptosis, as well as modulating leukocyte infiltration and cell polarity (Bazzoni & Dejana, 2004; Hirase & Node, 2012). Additionally, intercellular junctions influence permeability of the endothelial layer and this is heterogeneous across vascular beds. A continuous, non-fenestrated endothelium exists in the coronary, splanchnic and pulmonary vasculature, creating a tight barrier between the circulation and adjacent tissue. By contrast, lymphatic and renal vessels exhibit discontinuous junctions, allowing for high permeability (Sukriti et al., 2014).

#### **1.1.2 Immune response**

Cytokines are classed as soluble, low-molecular weight proteins and interact with various cell types to regulate inflammatory and immune reactions (Michiels

2003). The endothelium reacts to cytokines made by leukocytes, bacterial products and other inflammatory stimuli. Endothelial cells can also synthesise cytokines, which signal in both an autocrine and paracrine manner. In times of injury, this characteristic enables endothelial cells to mediate their own proliferation and migration. Similarly, it allows changes to vascular permeability and adhesion molecule expression, directing leukocytes to areas of tissue damage. Display of adhesion proteins, such as ICAM-1 and VCAM-1, attracts white blood cells to the luminal surface of the endothelium, where they then attach, before passing between endothelial cells (Pearson 2000; Galley & Webster, 2004).

### **1.1.3 Haemostasis and coagulation**

Healthy endothelial cells produce a multitude of substances which prevent coagulation and thrombosis, thereby maintaining normal blood flow. They express ectonucleotidases, which break down ATP and ADP into AMP and adenosine, making them unable to activate platelets (Michiels 2003). Endothelial cells also regulate the action of thrombin, a protease critical in the formation of fibrin through its conversion of circulating fibrinogen to the fibrin monomer. The endothelium exhibits the membrane protein thrombomodulin, which inhibits thrombin activity by binding to the same site as fibrinogen. Interaction with this region also stops thrombin from activating platelets (Galley & Webster, 2004). Additionally, thrombin activity is suppressed by antithrombin displayed on the endothelial cell surface by glycosaminoglycans (Pearson 2000). Tissue factor is another important activator of coagulation, communicating with numerous coagulation factors to create fibrin. Tissue factor pathway inhibitor is generated by endothelial cells and attenuates tissue factor activity (Wang et al., 2018).

### **1.1.4 Angiogenesis**

The formation of new blood vessels from existing ones, or 'angiogenesis', is vital in many physiological states. Endothelial cells adopt different phenotypes depending upon their location during the creation of a new vessel. At the forefront, tip cells lead migration and guide the vessel sprout. Behind tip cells,

proliferative stalk cells mediate vessel extension. Stability is provided by quiescent phalanx cells, which line the pre-existing vasculature underlying the stalk cells (Vandekeere et al., 2015).

A number of processes must be carefully co-ordinated for angiogenesis to be achieved, and many are controlled by the endothelium. It displays receptors for vascular endothelial growth factor (VEGF), which enhances endothelial cell migration, proliferation and inhibits apoptotic mechanisms. Endothelial cells also communicate with other substances like platelet derived growth factor (PDGF) and fibroblast growth factors. These can promote pericyte recruitment and evoke formation of endothelial tubes, respectively (Papetti & Herman, 2002; Góth et al., 2003).

### **1.1.5 Vascular tone**

A large number of vasoactive substances are endothelial-derived and act upon underlying smooth muscle cells to regulate blood pressure through vessel constriction and/or relaxation.

#### **1.1.5.1 Endothelin-1**

Endothelin-1 (ET-1) is a potent vasoconstrictor, released continuously by endothelial cells. In healthy conditions, it is generated at low levels and exerts its tonic effect on vascular tone through ET<sub>A</sub> and ET<sub>B</sub> receptors found on vascular smooth muscle cells (VSMCs) via activation of phospholipase C (PLC). In addition to causing vasoconstriction directly, it can amplify the effects of other vasoconstrictors, such as serotonin and noradrenaline (Michiels 2003; Thorin & Webb, 2010). Interestingly, interaction between ET-1 and endothelial ET<sub>B</sub> receptors induces vasodilation via release of the vasodilators nitric oxide (NO) and prostacyclin (PGI<sub>2</sub>) (Sandoo et al., 2010). While it is necessary for vascular tone maintenance, excessive ET-1 release stimulates proliferation of VSMCs and inflammatory processes. Increased ET-1 production has been documented in several cardiovascular pathologies, such as atherosclerosis and hypertension (Cahill & Redmond, 2016).

### 1.1.5.2 Prostacyclin and Thromboxane A<sub>2</sub>

PGI<sub>2</sub> and thromboxane A<sub>2</sub> (TXA<sub>2</sub>) are lipid mediators derived from arachidonic acid, otherwise known as eicosanoids (Smyth et al., 2009). They are secreted by endothelial cells and have opposing actions on vascular tone. Cyclooxygenase (COX) enzymes are responsible for the creation of both PGI<sub>2</sub> and TXA<sub>2</sub>. COX-1 and COX-2 isoforms are found in the endothelium, with the former constitutively expressed. COX-2, by contrast, is induced upon endothelial damage and inflammation (Sandoo et al., 2010).

PGI<sub>2</sub> is formed through COX-mediated conversion of arachidonic acid to prostaglandin H<sub>2</sub> (PGH<sub>2</sub>), which is then transformed by the action of prostacyclin synthase. PGI<sub>2</sub> interacts with prostacyclin (IP) receptors on VSMCs, evoking vessel relaxation through reducing intracellular Ca<sup>2+</sup> levels. This occurs via activation of the adenylate cyclase signalling pathway and protein kinase A (PKA) phosphorylation (Mitchell et al., 2008).

By contrast, TXA<sub>2</sub> is a vasoconstrictor. TXA<sub>2</sub> synthesis involves the same first step as that of prostacyclin, but PGH<sub>2</sub> is converted to TXA<sub>2</sub> by thromboxane synthase (Sandoo et al., 2010). Binding of TXA<sub>2</sub> to thromboxane-prostanoid or 'TP' receptors on VSMCs leads to smooth muscle contraction. This vasoconstriction is mediated by stimulating PLC, generation of inositol 1,4,5-trisphosphate (IP<sub>3</sub>) and ultimately an increase in intracellular Ca<sup>2+</sup> (Ellinsworth et al., 2014).

### 1.1.5.3 Endothelial-derived hyperpolarising factors

Although not their main mechanism of action, the vasodilators NO and PGI<sub>2</sub> can elicit vasorelaxation through hyperpolarisation of VMSCs. Upon blockade of NO and PGI<sub>2</sub>, however, hyperpolarisation can still take place, indicating the contribution of other endothelial-derived hyperpolarising and dilatory substances. These are referred to as endothelial-derived hyperpolarising factors or 'EDHFs' (Ozkor & Quyyumi, 2011).

At present, it is believed that EDHFs elicit a rise in intracellular Ca<sup>2+</sup>. This increases conductance of Ca<sup>2+</sup>-sensitive K<sup>+</sup> channels, causing K<sup>+</sup> efflux. Gap junctions allow movement of current from the endothelium to VSMCs, where

K<sub>ir</sub>2.1 inward-rectifier K<sup>+</sup> channels and/or Na<sup>+</sup>/K<sup>+</sup>-ATPase pumps are stimulated. Subsequent closure of voltage-dependent Ca<sup>2+</sup> channels results in relaxation of VSMCs (Jia et al., 2016). Substances that are often regarded as EDHFs include hydrogen peroxide (H<sub>2</sub>O<sub>2</sub>), C-type natriuretic peptide, hydrogen sulphide (H<sub>2</sub>S) and epoxyeicosatrienoic acids (EETs) (Cahill & Redmond, 2016; Jia et al., 2016).

## 1.2 Nitric oxide

NO is a signalling molecule and a powerful vasodilator. Its particular importance to the vasculature was first shown by the work of Furchgott and Zawadzki (1980), which demonstrated that the vasodilatory effect of acetylcholine (ACh) is abolished *in vitro* following removal of the endothelium (Vanhoutte et al., 2016). Since then, numerous studies have demonstrated the potent anti-atherogenic capacity of NO, through modulation of platelet aggregation, VSMC proliferation and leukocyte chemotaxis (Napoli et al., 2006). NO can also affect non-vascular cell-types, influencing metabolic processes within brown and perivascular fat, as well as the homeostasis of the immune and central nervous systems (Farah et al., 2018).

### 1.2.1 Nitric oxide synthase enzymes in vascular physiology

Nitric oxide synthase (NOS) enzymes synthesise NO. Neuronal NOS (nNOS), inducible NOS (iNOS) and endothelial NOS (eNOS) are the 3 NOS isoforms and are encoded by 3 different genes, which are *NOS1*, *NOS2* and *NOS3*, respectively (Vanhoutte et al., 2016). In neuronal cells, nNOS is constitutively expressed and continuously generates NO. This is also true of eNOS in the endothelium (Lundberg et al., 2015). For these 2 isoforms, an increase in intracellular Ca<sup>2+</sup> leads to enzyme activation, but stimulation can also occur in a Ca<sup>2+</sup>-independent manner. By contrast, iNOS expression and action is induced upon exposure to inflammatory agents, such as cytokines and bacterial lipopolysaccharides. Intracellular Ca<sup>2+</sup> elevations are also not necessary for iNOS activity (Förstermann & Sessa, 2012).

### 1.2.2 eNOS

In vascular endothelial cells, eNOS is the main generator of NO (Dudzinski & Michel, 2007). It exists as a homodimer protein and manufactures NO and citrulline from molecular O<sub>2</sub> and arginine. Several cofactors are also required for eNOS to carry out NO production (Gielis et al., 2011).

An eNOS monomer is formed of an amino-terminal oxygenase domain and a reductase domain located at the carboxyl-terminus. The oxygenase region exhibits binding sites for arginine, the cofactor tetrahydrobiopterin (BH<sub>4</sub>) and O<sub>2</sub>, in addition to a haem cluster, which is needed for dimerisation of the monomers. The reductase domain has sites for interaction with nicotinamide adenine dinucleotide phosphate (NADPH), flavin mononucleotide (FMN) and flavin adenine dinucleotide (FAD) (Gielis et al., 2011; Förstermann & Sessa, 2012; Farah et al., 2018).

Formation of NO begins with a transfer of electrons from NADPH via FMN and FAD to the oxygenase haem site, which allows NOS enzymes to carry out 2 oxidation stages. Arginine is first converted to N<sup>ω</sup>-hydroxy-L-arginine, followed by oxidation to citrulline and NO. The domains of each monomer contain a sequence for interaction with the Ca<sup>2+</sup>-complexed protein, calmodulin, the involvement of which is critical for the aforementioned electron transfer (Förstermann & Sessa, 2012; Farah et al., 2018). eNOS protein structure and eNOS-mediated NO synthesis is depicted in Figure 1.1.

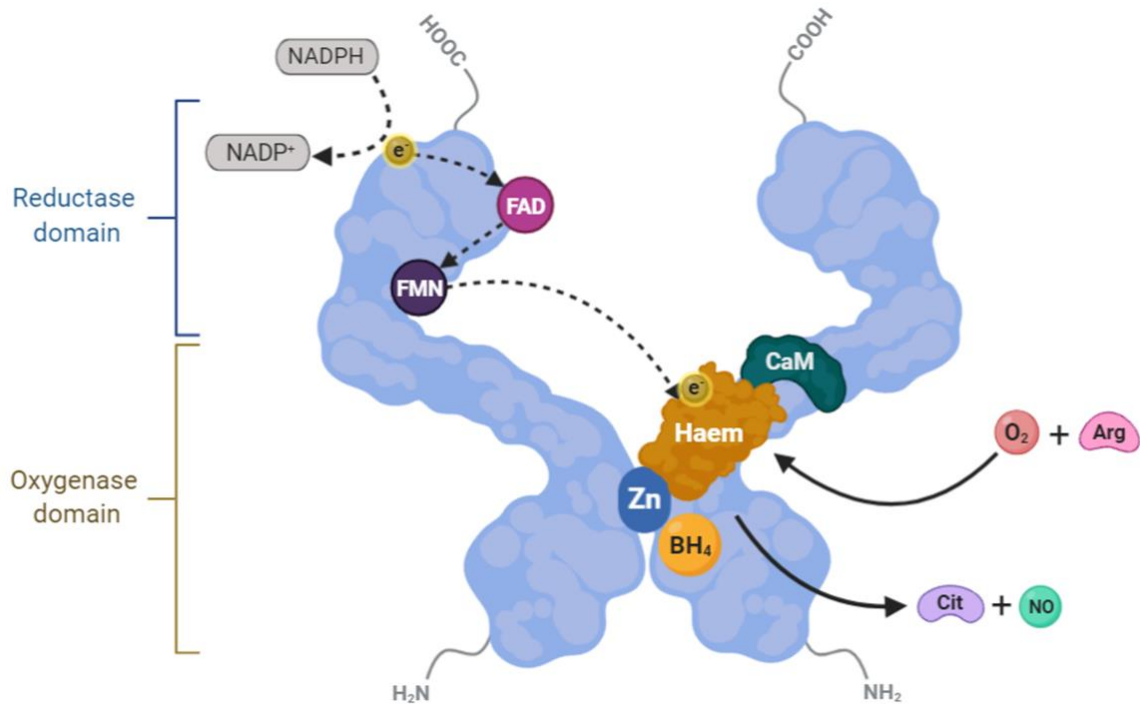


### Figure 1.1 eNOS protein structure and NO formation

The eNOS protein is synthesised as a monomer, with a reductase domain at the carboxyl terminus and an oxygenase region at the amino terminus. Sites for NADPH, FMN and FAD are present on the reductase domain. Arginine (Arg), BH<sub>4</sub>, O<sub>2</sub> and haem interact with the protein at the oxygenase domain. Each monomer also possesses an interaction site for calmodulin (CaM). Dimerisation, facilitated by haem and a zinc ion (Zn), is essential for eNOS enzymatic function. Electrons (e<sup>-</sup>) are initially supplied by NADPH to the flavin groups. Movement of electrons (shown by dashed lines) from the flavins to the haem of the opposite monomer allows haem to bind O<sub>2</sub>. Arginine can then undergo hydroxylation by eNOS, resulting in the production of NO and citrulline (Cit). Only electron transfer from the reductase region of one eNOS monomer to the oxygenase region of the second monomer is shown for simplicity (Förstermann & Munzel, 2006; Förstermann & Sessa, 2012).

### 1.2.3 eNOS signalling

#### 1.2.3.1 Vasodilation

NO possesses an unpaired electron, making it a free radical. Its high reactivity with transition metals and other radicals stabilise the lone electron and these mechanisms direct its physiological actions (Lundberg et al., 2015).

NO mediates its vasodilatory effects by interaction with the enzyme soluble guanylyl cyclase (sGC), which is composed of an  $\alpha_1$  or  $\alpha_2$  subunit connected to a  $\text{Fe}^{2+}$ -containing  $\beta$ -subunit. NO displays high affinity for  $\text{Fe}^{2+}$ -containing moieties and so can form a complex with sGC. sGC activity is triggered upon interaction with NO, resulting in the generation of the second messenger cGMP from GTP (Hill et al., 2010; Farah et al., 2018).

cGMP activates protein kinase G-I (PKG-I). PKG-I $\alpha$  is the principal isoform in VSMCs and stimulated PKG causes vasorelaxation by lowering VSMC intracellular  $\text{Ca}^{2+}$  (Farah et al., 2018). This happens through several pathways. PKG-I $\alpha$  phosphorylation of the  $\text{IP}_3$  receptor-associated PKG substrate attenuates  $\text{Ca}^{2+}$  extrusion from the sarcoplasmic reticulum (SR). PKG-I $\alpha$  also phosphorylates phospholamban, a SR membrane protein. This induces SR  $\text{Ca}^{2+}$ -ATPase (SERCA) activity and encourages SR  $\text{Ca}^{2+}$  uptake from the cytoplasm (Vanhoutte et al., 2016). Additionally, large conductance  $\text{Ca}^{2+}$ -activated  $\text{K}^+$  channels are activated by PKG-I $\alpha$ , leading to hyperpolarisation and inhibition of voltage-dependent L-type  $\text{Ca}^{2+}$ -channels. All of these processes decrease VSMC intracellular  $\text{Ca}^{2+}$  below the threshold necessary for  $\text{Ca}^{2+}$ -dependent myosin light-chain kinase (MLCK) to phosphorylate myosin. Lower  $\text{Ca}^{2+}$  conditions also stimulate myosin light-chain phosphatase (MLCP) and inhibit Rho-associated protein kinase (ROCK). Together, these prevent myosin-actin binding. Contraction can no longer occur and VSMC relaxation results (Vanhoutte et al., 2016; Farah et al., 2018) (Figure 1.2).

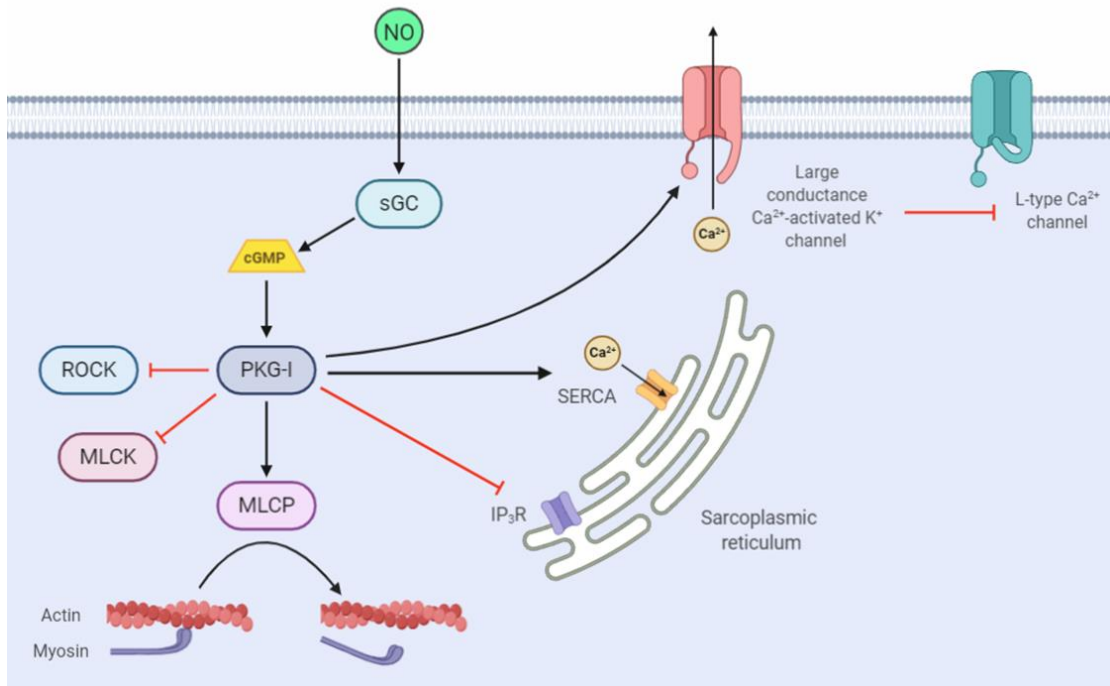


### Figure 1.2 NO-mediated relaxation of vascular smooth muscle

NO initiates vessel relaxation through reducing the intracellular  $\text{Ca}^{2+}$  concentration in VSMCs. NO activation of sGC evokes formation of the second messenger cGMP, which triggers the activity of PKG-I. This kinase phosphorylates  $\text{IP}_3\text{R}$  on the sarcoplasmic reticulum, suppressing  $\text{IP}_3\text{R}$   $\text{Ca}^{2+}$  release. PKG-I stimulation also leads to activation of SERCA, causing an increase in  $\text{Ca}^{2+}$  uptake from the cytoplasm. Large conductance  $\text{Ca}^{2+}$ -activated  $\text{K}^+$  channels are stimulated by PKG-I and the resulting hyperpolarisation inhibits L-type  $\text{Ca}^{2+}$  channels. Cumulatively, these processes lower the intracellular  $\text{Ca}^{2+}$  level. This  $\text{Ca}^{2+}$  decrease inactivates MLCK and ROCK, whilst activating MLCP, leading to disruption of actin-myosin cross-bridges which induces VSMC relaxation (Vanhoutte et al., 2016; Farah et al., 2018).

### **1.2.3.2 S-nitrosylation of proteins**

Recently, S-nitrosylation of proteins by NO has emerged as another important component of NO signalling. The process involves formation of a covalent bond between NO and the thiol group present on cysteine residues, creating S-nitrosothiols (SNOs). When compared to other post-translational alterations of proteins, S-nitrosylation is distinct in that there is no sole, defined reaction for SNO formation. Various electron acceptors, transition metals or dioxygen are needed and this is often dictated by the target protein or peptide (Foster et al., 2003; Anand & Stamler, 2012).

S-nitrosylation is a specific, tightly regulated event and can occur with NO concentrations much lower than those necessary for cGMP production (Treuer & Gonzalez, 2015). Since an extensive range of proteins can undergo this process, compared with the cGMP route of NO signalling which utilises PKG alone as its effector molecule, S-nitrosylation may underlie the breadth of cardiovascular actions of NO (Lima et al., 2010). Pi et al. (2009) revealed that eNOS-dependent nitrosylation of mitogen-activated protein kinase phosphatase 7 (MKP7) was crucial to endothelial cell migration by preventing MKP7 induced inhibition of JNK3. S-nitrosylation also encourages the function of the GTPase dynamin-2, in turn promoting endocytosis and signalling pathways important for angiogenesis and endothelial cell survival (Kang-Decker et al., 2007).

There is a fine balance between S-nitrosylation serving a protective role in the endothelium and having deleterious effects. For example, increased S-nitrosylation of arginase is linked with the development of the vascular stiffness associated with ageing vessels (Kim et al., 2009). Endothelial clock proteins are also a target for S-nitrosylation and suppression of this has been linked with hypertension (Kunieda et al., 2008).

### **1.2.3.3 Interactions with O<sub>2</sub> and reactive oxygen species**

Oxidative reactions between NO and O<sub>2</sub>, or reactive oxygen species (ROS), constitute redox reactions that create reactive nitrogen species (RNS). Such products exhibit the chemical characteristics of nitrogen dioxide (NO<sub>2</sub>) or nitrosonium (NO<sup>+</sup>) and are considered to be another mode of NO signalling with the vasculature (Lundberg et al., 2015).

Nitro-fatty acids or 'NO<sub>2</sub>-FAs' have received increasing research attention, with it postulated that they may act as a source of NO. While NO release from NO<sub>2</sub>-FAs has been shown to cause endothelial-independent vasodilation, their main effects within the cardiovascular system appear to be modulated via post-translational modifications (Villacorta et al., 2016). A growing body of data suggests that these protein alterations can have significant cardio-protective results. Vascular inflammation is reduced by NO<sub>2</sub>-FAs, as reported by Villacorta et al. (2013). Mice treated with nitro-oleic acid displayed both attenuated expression of adhesion proteins in the aorta and leukocyte recruitment at the vascular wall. This was induced by inhibition of Toll-like receptor 4 (TLR-4) expression and nuclear factor-κB (NF-κB) signalling. Nitro-oleic acid has also been shown to improve atherosclerotic plaque stability in mice deficient in apolipoprotein E (ApoE). This is in addition to suppressing foam cell generation by blocking phosphorylation of STAT-1 transcription factor by oxidised low density lipoproteins (oxLDLs) (Rudolph et al., 2010).

Another product of NO interaction with ROS is peroxynitrite, created via reaction between NO and superoxide (O<sub>2</sub><sup>-</sup>). Like NO, peroxynitrite is highly diffusible and plays an important role in modification of proteins. Protonated peroxynitrite is generated in an aqueous setting, which can give rise to NO<sub>2</sub> and a hydroxyl radical (•OH). The latter is particularly reactive and capable of taking electrons from almost any biological molecule. Another notable example is the production of nitrotyrosine, following reaction of peroxynitrite with protein tyrosine residues (Adams et al., 2015). Peroxynitrite actions are also mediated through reaction with CO<sub>2</sub>, producing NO<sub>2</sub> and a carbonate radical (CO<sub>3</sub><sup>-</sup>), and oxidation of thiols or metal centres in proteins (Liaudet et al., 2009).

Peroxynitrite is imperative for correct function of certain cellular processes. Allen and colleagues (2012) demonstrated that the microbicidal capacity of activated macrophages was reliant upon macrophage peroxynitrite generation. Impairment of NO or O<sub>2</sub><sup>-</sup> manufacture attenuated both macrophage peroxynitrite levels and their ability to destroy *E.coli*. Excessive peroxynitrite concentrations, however, are often detrimental. In human fibronectin, a glycoprotein found in extracellular matrices and plasma, tyrosine and tryptophan residues are particularly susceptible to modification by peroxynitrite, which results in protein fragmentation. Human coronary artery endothelial cells exhibit impaired

adherence when cultured on peroxynitrite-modified fibronectin. Co-localisation of nitrated tyrosine residues and fibronectin have also been observed in human atheroma. This suggests that peroxynitrite promotes both dysfunction of endothelial cells and a weakening of atherosclerotic fibrous caps (Degendorfer et al., 2016).

#### **1.2.4 Regulation of eNOS activity**

eNOS is modulated by a complicated array of transcriptional and post-translational modifications. It is also heavily influenced by interactions with other proteins in the endothelium.

##### **1.2.4.1 Post-translational modifications of eNOS**

###### **1.2.4.1.1 Phosphorylation**

One of the most important post-translational changes to eNOS is phosphorylation, where a phosphate group is added to various serine, tyrosine or threonine residues. This addition is catalysed by kinase enzymes, with phosphorylation of different residues having different functional effects (Zhao et al., 2015). The most well-studied eNOS phosphorylation sites are human serine 1177 (or serine 1179 in bovine tissue) and human threonine 495 (bovine threonine 497), which are found in the region of eNOS which binds to calmodulin (Fleming 2010).

Serine 1177 (Ser1177) phosphorylation causes eNOS activation by impairing the displacement of eNOS from calmodulin, enabling eNOS activity at basal concentrations of  $\text{Ca}^{2+}$ . It also causes increased eNOS activity by enhancing electron flux through the enzyme (Dudzinski & Michel, 2007). Ser1177 is located on the C-terminus of eNOS. This area is thought to be positioned between 2 eNOS monomers, an arrangement which may prevent the movement of electrons between domains. The conformational change arising from Ser1177 phosphorylation removes this blockade of electron transfer, so increasing eNOS activity (Heiss & Dirsch, 2014).

Ser1177 can be phosphorylated through multiple kinases. These include PKG, Akt, AMP-activated protein kinase (AMPK) and Ca<sup>2+</sup>/calmodulin-dependent protein kinase II (Dudzinski & Michel, 2007). The action of these kinases is mediated by a varied group of stimuli. For example, adiponectin and metformin treatment have been documented to induce AMPK activity, while the Akt pathway is activated by insulin, ROS and shear stress. Such a range of stimuli show that Ser1177 is a particularly integrative and important phosphorylation site (Heiss & Dirsch, 2014).

By contrast, eNOS activity is negatively regulated by phosphorylation of threonine 495 (Thr495), and can occur through PKC and AMPK signalling (Dudzinski & Michel, 2007). Aoyagi and colleagues (2003) demonstrated using crystallography that phosphorylated Thr495 causes a conformational change in eNOS, reducing its ability to bind calmodulin. It was also shown that certain glutamate residues within calmodulin are subject to electrostatic repulsion by phosphorylated Thr495, further hindering potential binding. Studies from cultured endothelial cells suggest that Thr495 is under constitutive phosphorylation and undergoes dephosphorylation when intracellular Ca<sup>2+</sup> increases by the phosphatases PP1, PP2A or PP2B (Heiss & Dirsch, 2014). It was thought that Thr495 dephosphorylation needed to be accompanied by Ser1177 phosphorylation for eNOS activation (Michell et al., 2001). However, more recent evidence from Schmitt et al. (2009) indicates that eNOS can be stimulated by dephosphorylation of Thr495 alone.

#### **1.2.4.1.2 Acylation**

The covalent attachment of fatty acids to proteins, or 'acylation', is an important form of protein modification (Resh 1999). eNOS undergoes dual acylation through the addition of the fatty acids myristate and palmitate (Feron et al., 1998). The myristoylation of eNOS is vital for its presence at the plasma membrane, through the hydrophobic interaction between membrane lipids and the myristoyl group. This relationship alone is weak, and it is believed that palmitoylation strengthens the association with extra hydrophobic interactions (Heiss & Dirsch, 2014).

It has been proposed that eNOS undergoes an acylation cycle, with transfer between the Golgi and the cell membrane (Oess et al., 2006). eNOS exists mainly, although not exclusively, in small invaginations displayed on the endothelial plasma membrane known as caveolae. This location is particularly important for communication between eNOS and receptors and signalling pathways. eNOS myristoylation appears to direct general membrane localisation and happens co-translationally at ribosomes in the cytoplasm. Palmitoylation guides the targeting of eNOS to caveolae specifically (Oess et al., 2006). 5 members of the DHHC-palmitoyltransferase enzyme family palmitoylate eNOS at the Golgi, as shown by Fernández-Hernando et al. (2006), who demonstrated colocalisation with Golgi matrix protein GM-130. eNOS depalmitoylation occurs following prolonged stimulation and is thought to induce retrograde movement of eNOS to the Golgi (Heiss & Dirsch, 2014).

#### **1.2.4.1.3 S-nitrosylation**

eNOS can undergo S-nitrosylation by its own production of NO, with S-nitrosylated eNOS displaying reduced activity. Enzyme function is amplified upon de-nitrosylation; this has been seen both in culture and *ex vivo* when endothelial cells are exposed to eNOS agonists (Dudzinski & Michel, 2007).

For S-nitrosylation to occur, eNOS needs to be localised at the membrane. In cells expressing an acylation-deficient eNOS mutant (Myr-), S-nitrosylation was almost abolished. Excessive S-nitrosylation occurred when cells were co-transfected with the Myr- mutant and a membrane tethered fusion protein called CD8 (Erwin et al., 2006). Subcellular localisation is equally important for denitrosylation, with CD8-Myr- eNOS retained at the membrane in its hypernitrosylated state, even when exposed to eNOS agonists (Erwin et al., 2006).

S-nitrosylation of eNOS takes place at a cysteine residue in a zinc cluster, which is required for enzyme dimerisation (Ravi et al., 2004). It is possible that S-nitrosylation attenuates eNOS activity by promoting dissociation of the enzyme to its monomers, stopping electron flux between the reductase and oxygenase regions, thereby halting NO synthesis (Ravi et al., 2004). However, some studies have not seen a correlation between disruption of the zinc cluster and reduced

enzymatic action (Erwin et al., 2005). Other evidence suggests S-nitrosylation negatively regulates eNOS through altering binding of substrates or cofactors, or preventing electron movement in the dimerised form of the enzyme (Dudzinski & Michel, 2007).

#### **1.2.4.2 Protein interactions**

##### **1.2.4.2.1 Caveolin-1 and calmodulin**

The caveolae of the endothelial cell membrane contain caveolin-1 scaffolding protein. Caveolin-1 associates with eNOS, anchoring it within caveolae, where it negatively regulates eNOS activity. Drab and colleagues (2001) demonstrated this with generation of mice deficient in caveolin-1, which displayed markedly increased basal NO release and amplified endothelial-dependent relaxation responses. Caveolin-1 blocks signal transduction to eNOS from caveolae located receptors and prevents eNOS-calmodulin binding when intracellular  $\text{Ca}^{2+}$  levels are low (Dudzinski & Michel, 2007; Zhao & Malik, 2009).

Elevation of intracellular  $\text{Ca}^{2+}$  exposes hydrophobic regions of calmodulin allowing interaction with eNOS, resulting in separation of eNOS from caveolin-1 (Greif et al., 2004; Vanhoutte et al., 2016). This dissociation can also happen in a  $\text{Ca}^{2+}$ -independent manner. The subsequent conformational change in eNOS structure permits its movement into the cytoplasm and electron transfer to occur through the heme moiety, producing NO (Siragusa & Fleming, 2016). It is also within the cytoplasm that eNOS can undergo post-translational modifications (Vanhoutte et al., 2016).

##### **1.2.4.2.2 Heat shock protein 90**

Heat shock protein 90 (Hsp90) is a molecular chaperone protein, involved in protein folding and trafficking. With regard to eNOS, hsp90 can act as a scaffold molecule, allowing interaction between eNOS and numerous other proteins which influence eNOS activity. Its formation of a regulatory complex with eNOS and co-chaperone protein, cell division cycle 37, inhibits eNOS. Hsp90 can also mediate the inhibitory action of C-terminal hsp70-interacting protein (CHIP). CHIP downregulates eNOS activity by impairing its movement through the Golgi

(Siragusa & Fleming, 2016). Conversely, proteins stimulating eNOS can bind to hsp90. Integrin-linked kinase or 'ILK', a serine/threonine kinase, associates with hsp90 and eNOS, eliciting both eNOS activation and preventing eNOS-dependent  $O_2^-$  production (Siragusa & Fleming, 2016).

#### **1.2.4.2.3 Actin**

Actin represents the major cytoskeletal protein within eukaryotic cells, making up around between 5–10% of total cell protein content. It has 3 isoforms in vertebrates:  $\alpha$ -,  $\beta$ - and  $\gamma$ - (Dominguez & Holmes, 2011).  $\beta$ -actin is found in the endothelium and can exist in its monomeric form, known as globular or G-actin. G-actin monomers can also arrange into tight double helices through head-to-tail interactions with two other monomers. This polymerisation creates actin filaments with a molecular polarity, often referred to as F-actin (Cooper 2000; Kondrikov et al., 2010). F-actin can be classified as cortical actin, where filaments are organised in a mesh running underneath the plasma membrane. Additionally, it can form stress fibres, which stretch across the cell to form an attachment between two adhesion proteins (Chalut & Paluch, 2016).

$\beta$ -actin has been widely documented to interact with and regulate the activity of eNOS. Colocalisation between eNOS and F-actin occurs at the plasma membrane. By contrast, eNOS found in peri-nuclear regions, such as the Golgi, associates with monomeric G-actin. Communication with either form of  $\beta$ -actin promotes eNOS activity, with G-actin inducing a larger activity increase (Su et al., 2003).

It is thought that  $\beta$ -actin and eNOS can interact indirectly via several eNOS associated proteins (Su et al., 2007), but there is also a strong body of evidence for a direct physical interaction. Co-precipitation of the 2 proteins has been observed (Su et al., 2003), and is supported by the work of Kondrikov and colleagues (2010), who demonstrated direct communication between  $\beta$ -actin filaments and eNOS at the oxygenase region of the enzyme. The exact mechanism by which  $\beta$ -actin induces eNOS activity was not clarified in its entirety, although their data highlighted residues 326–333 on human eNOS as an area of importance. Treatment of purified eNOS and  $\beta$ -actin with a synthetic actin-binding sequence (ABS) peptide, possessing the amino acid sequence of

these residues on human eNOS, prevented  $\beta$ -actin and eNOS association. Impairment of an interaction was mirrored in experiments with COS-7 cells where site-directed mutagenesis targeted these same eNOS residues. In both systems, disrupting communication between the enzyme and  $\beta$ -actin through eNOS residues 326–333 caused decreased NO formation and amplified production of  $O_2^{\cdot-}$  (Kondrikov et al., 2010).

It has been proposed that this interaction elicits a conformational change in eNOS structure, altering electron flux or eNOS dimerisation. However, the means by which the association is regulated remains uncertain. It is also unclear what causes the difference in eNOS activity depending upon whether it is communicating with F- or G-actin (Su et al., 2007).

In spite of these questions, it is evident that  $\beta$ -actin modulation of eNOS activity is important to vascular function. Mechanical stimulation of endothelial cells by shear stress causes an acute increase in eNOS activity, followed by upregulation of eNOS mRNA and protein expression. Disruption of F-actin integrity has been shown to attenuate this NO release in response to blood flow (Hutcheson & Griffith, 1996; Davis et al., 2004). Trafficking of the enzyme may be mediated by caveolae and caveolin through actin filaments. Zharikov et al. (2001) demonstrated that the physical state of actin filaments impacts eNOS usage of arginine. The group observed that the cationic amino acid transporter, CAT-1, which facilitates arginine influx, interacts with eNOS via the actin-binding protein, fodrin. Stabilisation of the actin cytoskeleton resulted in stimulation of arginine uptake by eNOS and increased production of NO, without a change in eNOS expression or activity (Zharikov et al., 2001).

### **1.2.5 eNOS uncoupling**

eNOS production of NO is highly regulated, influenced by substrate and cofactor availability, post-translational alterations and a multitude of interactions between the enzyme and other proteins. In conditions where these factors are perturbed, like oxidative stress, eNOS becomes dysfunctional or 'uncoupled' (Siragusa & Fleming, 2016).

eNOS uncoupling leads to the generation of  $O_2^{\cdot-}$  rather than NO. It is widely accepted that the main cause is deficiency of the cofactor  $BH_4$ . High levels of

oxidative stress results in oxidation of BH<sub>4</sub> to BH<sub>2</sub>, and this reduction in BH<sub>4</sub> induces the eNOS dimer to separate into two monomers, impairing enzyme function. O<sub>2</sub><sup>-</sup> can react with NO to form peroxynitrite, which is also capable of oxidising BH<sub>4</sub>, serving to amplify existing high oxidative conditions (Li et al., 2014; Gielis et al., 2011).

### **1.3 Endothelial dysfunction**

Disruption of the normal homeostatic processes of the endothelium causes a phenotypic switch in endothelial cells to a pathophysiological, 'activated' state. This is referred to as 'endothelial dysfunction', of which eNOS uncoupling and the resulting reduction in NO bioavailability is a primary feature (Sena et al., 2013). It is also marked by impaired endothelium-mediated vasorelaxation, elevated production of pro-thrombotic and pro-inflammatory substances, increased vascular permeability, a rise in ROS and levels of oxidative stress, as well as increased expression of leukocyte adhesion molecules (Sitia et al., 2010; Sena et al., 2013).

There are multiple risk factors associated with the initiation of endothelial dysfunction. These include hypertension, smoking, elevated triglycerides, increased low density lipoprotein (LDL) cholesterol and hyperglycaemia (Sena et al., 2013). It is widely accepted that endothelial dysfunction underlies numerous pathophysiological conditions. It appears to contribute significantly to the initiation and progression of atherosclerosis (Sitia et al., 2010).

### **1.4 Atherosclerosis**

Atherosclerosis is the development of cholesterol-rich lipid lesions or 'plaques' within the wall of major arteries. Progression is slow, with the disease often only observed clinically upon plaque rupture. This produces a thrombus, which causes local vessel occlusion and tissue ischaemia. Plaque debris following rupture can also be transported through the bloodstream, blocking vessels at distal sites (Gisterå & Hansson, 2017). These processes underlie stroke and ischaemic heart disease, making atherosclerosis the leading cause of death worldwide (World Health Organisation 2018).

The classic risk factors associated with atherogenesis: hypertension, smoking, hypercholesterolaemia and diabetes, are all linked by promotion of endothelial injury or dysfunction (Ross et al., 1977). Under normal conditions, leukocytes are carried past the endothelium. Endothelial injury causes expression of adhesion molecules, allowing for leukocyte attachment. Additionally, alterations to endothelial cell permeability and the collagen and elastic scaffold enables accumulation of LDL in the arterial wall (Libby et al., 2011) (Figure 1.3).

In regions of turbulent blood flow, proteoglycans of the arterial wall are more exposed to the luminal contents. LDL containing apolipoprotein B100 (ApoB100) preferentially bind to these negatively charged proteoglycans, which facilitates their sub-endothelial penetration of the artery (Kwon et al., 2008; Weber & Noels, 2011). LDL particle build-up within the arterial intima renders them susceptible to oxidative alterations by lipoxygenases or myeloperoxidase, or by other sources of ROS. Such modifications to the lipid, protein and lipoprotein molecules within LDLs encourages endothelial cells to adopt an activated phenotype, in turn stimulating endothelial and macrophage expression of chemokines and adhesion molecules (Hansson & Hermansson, 2011).

Chemokines orchestrate the rolling and adhesion of leukocytes to the endothelium, followed by their lateral migration and movement between endothelial cells. Soluble chemokines can elicit direct recruitment. Other chemokines fixed on the membrane of activated endothelial cells stimulate leukocyte integrin expression via leukocyte GPCRs. The subsequent reaction with integrin ligands on the endothelial surface, such as ICAM-1, causes leukocyte capture (Weber & Noels, 2011). Production of substances like macrophage colony-stimulating factor by endothelial cells trigger infiltrating monocytes to differentiate into macrophages (Gisterå & Hansson, 2017). During differentiation, macrophage scavenger receptors are upregulated. They facilitate uptake of oxLDL, which pushes activated macrophages to become foam cells (Simionescu & Sima, 2012). The appearance of fatty streaks, of which foam cells are a main constituent, is the first stage in plaque development (Esper et al., 2006).

Engulfing of oxLDL by macrophages may appear beneficial in its initial stages. This uptake, however, alters important macrophage functions which prevents their clearance of such lipids from the vessel wall (Moore et al., 2013). For

example, interaction between oxLDL and scavenger receptor CD36 changes the cytoskeletal properties of foam cells, causing impaired migration and their accumulation in the intima. The foam cells soon start to degenerate, creating a necrotic centre within the plaque, containing cholesterol crystals and cells in various stages of necrosis and apoptosis. The cholesterol stimulates various inflammatory signalling pathways, like that of interleukin-1 $\beta$  (IL-1 $\beta$ ), which has implications on the behaviour of nearby VSMCs (Gisterå & Hansson, 2017).

VSMCs play a key part in atheroma development. Following exposure to atherogenic stimuli, they can adopt qualities normally associated with other cells, such as lipid uptake and production of cytokines and adhesion molecules (Doran et al., 2008). They can be found in the intimal layer of the vasculature as well as the media. Where VSMCs are observed intinally, they are classed as either 'diffuse' or 'eccentric'. The former appear in vessels regardless of anatomical location and are thought to arise during normal ageing. 'Eccentric' intimal thickenings are consistently seen in regions where blood flow is at higher pressure and more turbulent, such as branching points. Their cellular behaviour also contrasts from those VSMCs of the media. This coupled with their presence in areas of turbulent blood flow suggests they make specific contributions to plaque formation in humans (Doran et al., 2008).

Like endothelial cells, VSMCs can undergo phenotype switching, existing in either a synthetic or contractile state (Basatemur et al., 2019). The latter is needed during generation of new vasculature and allows for increased intracellular myofilament formation and attenuation of extracellular matrix (ECM) production. Vascular damage induces a synthetic phenotype, where VSMCs are proliferative, can migrate into the intima and secrete increased ECM constituents, growth factors and cytokines (Rudijanto 2007). This switching is reversible, and cells return to a contractile phenotype when injury is resolved (Basatemur et al., 2019).

In early atherosclerosis, the generation of inflammatory substances such as PDGF and IL-1 $\beta$  by macrophages and the build-up of cholesterol encourages VSMCs to become synthetic (Gisterå & Hansson, 2017; Basatemur et al., 2019). Subsequent VSMC production of ECM, which contains large amounts of proteoglycans and glycosaminoglycans, causes further retention of LDLs (Basatemur et al., 2019). Continued accumulation of oxLDL and macrophages

triggers apoptosis of the various cell types within plaques. As a repair response, VSMCs secrete modified ECM with a higher collagen content, resulting in the appearance of a fibrous cap (Basatemur et al., 2019). Initially this stabilises lesions, but fibrous caps can weaken over time, leading to plaque rupture and thrombosis.

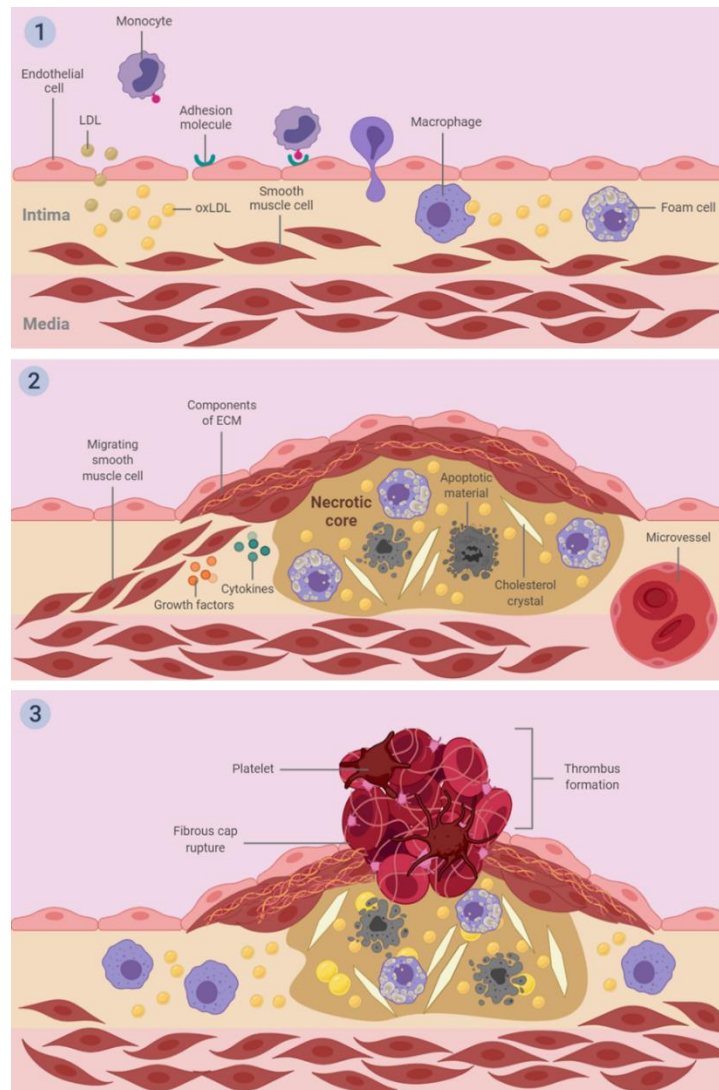


**Figure 1.3 Stages of atherosclerosis**

Endothelial dysfunction promotes expression of adhesion molecules. Leukocytes attach to the endothelium via these adhesion proteins and move into the vessel intima. Increased endothelial permeability and changes to the composition of the elastic and collagen scaffold also allows sub-endothelial LDL build-up to occur. LDL particles undergo oxidative modifications, becoming oxLDL. Monocytes differentiate into macrophages and their uptake of oxLDL triggers their transformation into foam cells (1). VSMCs adopt a synthetic phenotype and travel into the intima, where they secrete growth factors, cytokines and ECM components. Secretion of ECM forms a fibrous cap over the lesion. As plaques advance, foam cells and VSMCs degenerate. Accumulation of these apoptotic and necrotic cells, alongside the lipid released during their degradation, creates a necrotic core. Lesions at this stage also contain microvessels and cholesterol crystals (2). Weakening of the fibrous cap leads to plaque rupture. Exposure of the necrotic contents to circulating coagulation proteins initiates the coagulation cascade, resulting in thrombosis (3) (Libby et al., 2011).

### 1.4.1 Plaque vulnerability and rupture

Large clinical studies, histo-pathological and intravascular imaging analyses have demonstrated that it is most often this rupture of thin, fibrous caps and the resulting blood clot which is responsible for acute cardiac events (Halvorsen et al., 2008). The main features of an unstable or 'vulnerable' plaque are a necrotic core, a cap less than 65  $\mu\text{M}$  in thickness and a large concentration of inflammatory cells. The fibrous covering is also comprised of a reduced level of VSMCs and ECM (Sakakura et al., 2013; Silvestre-Roig et al., 2014). Upon plaque rupture, the contact between the necrotic contents and the blood activates circulating platelets. The subsequent triggering of the coagulation cascade creates a thrombus. It is also possible for thrombosis to result from plaque erosion or from plaques that have become heavily calcified, although these mechanisms are less common (Sakakura et al., 2013).

Multiple pathways are responsible for the weakening of fibrous caps. High levels of cell death within a lesion are often linked with plaque destabilisation. VSMC apoptosis is provoked by inflammatory factors secreted by both lymphocytes and macrophages within an atheroma. The breakdown of contact between VSMCs by matrix metalloproteases (MMPs), and the build-up of other degraded ECM components can induce further apoptotic death of VSMCs (Silvestre-Roig et al., 2014).

Similarly, the presence of oxidised cholesterol within foam cells activates their apoptosis through the unfolded protein response (UPR). Normally, UPR protects the endoplasmic reticulum (ER) from ER stressors (Silvestre-Roig et al., 2014). Long-term stimulation of UPR by accumulation of oxidised cholesterol, however, triggers apoptosis. This occurs via several mechanisms. UPR activates  $\text{Ca}^{2+}$  release from the ER and consequently increases the activity of calcium/calmodulin-dependent protein kinase II, in turn initiating various downstream pro-apoptotic pathways (Silvestre-Roig et al., 2014). Chronic oxidative and ER stress within macrophages can also provoke apoptotic death independent of UPR. Defective macrophages are commonly eliminated by autophagy, which prevents the production of ROS. In atherosclerosis,

macrophage apoptosis is favoured instead. This results in a larger necrotic core and so plaques with a higher chance of rupture (Silvestre-Roig et al., 2014).

Efferocytosis is used to describe phagocytic elimination of apoptotic cells. The signals which usually allow phagocytes to detect and clear apoptotic macrophages are reduced or modified in plaques, causing accumulation of dying cells and unresolved inflammation. For example, phagocyte migration can be stimulated by substances like lysophosphatidylcholine, produced upon a caspase-dependent activation of phospholipase A<sub>2</sub> (Silvestre-Roig et al., 2014). In plaques, oxLDLs compete with lysophosphatidylcholine for the same receptor on phagocytes. Similarly, thrombospondin-1 is found on apoptotic membranes and interacts with macrophages to induce engulfment, but its expression is reduced in vulnerable plaques (Moura et al., 2008). Plaque stability is further influenced by the expression of ECM degrading proteases, such as MMPs. Leukocytes are a rich source of MMPs and there is an inverse correlation between MMP expression and plaque stability (Silvestre-Roig et al., 2014).

Neoangiogenesis can also contribute to plaque vulnerability. It arises as macrophages at the centre of lesions become hypoxic. Consequently, they generate hypoxia-inducible factors which promote the creation of new vessels. These neovessels deliver the substances needed for further plaque growth and are themselves weak and highly permeable, and so aid in plaque destabilisation (Stefanadis et al., 2017).

## **1.5 Insulin resistance**

Insulin is a peptide hormone, critical for regulating systemic glucose and lipid metabolism. It promotes cellular glucose uptake from the bloodstream and initiates various anabolic processes (Wilcox 2005). Insulin resistance is the state where the signalling and physiological effects of insulin are reduced in normally insulin-sensitive cells, at both normal and increased levels of the protein. The presence of insulin resistance precedes the emergence of type 2 diabetes, but is also common across other metabolic disorders such as obesity, hypertension and atherosclerosis (Wilcox 2005; Yaribeygi et al., 2019;). The complexity of the insulin signalling pathway, which involves numerous regulatory proteins and enzymes, makes it difficult to determine the exact mechanism underlying insulin

resistance. There is most likely interplay from several factors, with receptor mutations, inflammatory factors, ROS and mitochondrial dysfunction all believed to play a role (Yaribeygi et al., 2019).

## **1.6 Diabetes**

Diabetes mellitus encompasses the disorders characterised by dysfunctional glucose metabolism, causing high levels of blood glucose or 'hyperglycaemia'. This metabolic abnormality results from either an absolute deficiency of insulin or impaired ability to respond to it, and leads to a variety of dangerous complications (Harcourt et al., 2013; World Health Organisation 2016). Diabetes now represents an important global health problem. 700 million sufferers are predicted by 2045, with world leaders citing the disease as one of four non-communicable diseases to be tackled as a matter of priority (World Health Organisation 2016; IDF Diabetes Atlas 2019).

Diabetes usually falls within one of three categories: Type 1 diabetes (T1DM), type 2 diabetes (T2DM) and gestational diabetes. Additionally, there are other lesser known types such as monogenic diabetes, which arises from genetic mutations, and those which develop secondary to other disorders. These can include diabetes induced by diseases like pancreatitis, or by drugs which impair insulin release or action (Ahlqvist et al., 2018; IDF Diabetes Atlas 2019).

### **1.6.1 Type 1 diabetes mellitus**

T1DM results from autoimmune destruction of  $\beta$ -cells of the pancreas, which are responsible for insulin production. This immune reaction induces absolute insulin deficiency. Those with T1DM are reliant upon insulin replacement therapy. While this is effective, patients are still susceptible to the long-term problems associated with diabetes and experience a reduced life expectancy (Needell & Zipris, 2017).

T1DM is often diagnosed in childhood and occurs more amongst men (Atkinson et al., 2014). It is believed that genetic predisposition and epigenetic factors contribute to T1DM initiation. Recently, a rapid rise in T1DM incidence has led researchers to place more emphasis on environmental influences, since the

increase cannot be explained by genetic alterations or a change in birth rates (Atkinson et al., 2014). Areas which have attracted research interest include the gut microbiome, viral infections and vitamin D deficiency (Kondrashova & Hyöty, 2014; Mitri & Pittas, 2014; Tai et al., 2015).

### **1.6.2 Type 2 diabetes mellitus**

T2DM is the most common form of diabetes, accounting for around 90% cases (Tao et al., 2015). In those with genetic or epigenetic susceptibility, long-term over-nourishment is the primary trigger for T2DM development. However, many individuals classed as overweight do not develop T2DM due to several adaptive mechanisms. The pancreatic  $\beta$ -cells of such people can counteract over-nourishment, keeping blood glucose levels within normal limits. Excess calories are distributed to subcutaneous adipose tissue, rather than visceral adipose tissue, minimising nutrient-induced damage to other organs (Nolan et al., 2011). In those vulnerable to developing T2DM,  $\beta$ -cells fail to produce enough insulin to compensate for the calorie excess. This is often associated with expansion of visceral adipose tissue and 'ectopic' lipid storage at key organs, such as the heart and liver, as well as an increase in levels of inflammatory cytokines. These events lead to the emergence of T2DM (Nolan et al., 2011).

### **1.6.3 Glucose homeostasis and insulin secretion**

Arranged in islets with a rich blood supply, pancreatic  $\beta$ -cells are well positioned to detect the nutritional state. By comparison to cells of neighbouring exocrine organs,  $\beta$ -cells islets receive 10 times more blood. Islet capillaries are adapted with a large number of pores, also known as 'fenestrae', which enable increased contact between  $\beta$ -cells and the circulation. This greater level of permeability allows for both prompt detection of nutrient levels in the bloodstream and fast release of insulin (Fu et al., 2013).

In humans, glucose enters pancreatic  $\beta$ -cells by facilitated diffusion through GLUT1 glucose transporters. Its metabolism through glycolysis and the Krebs/Tricarboxylic Acid (TCA) cycle ultimately causes membrane depolarisation,

inducing exocytosis of insulin-containing secretory granules (De la Vega-Monroy & Fernandez-Mejia, 2011; Fu et al., 2013).

Glucose is a main nutritional constituent of food of the human diet. This coupled with its rapid accumulation following food consumption means that it has developed evolutionarily as the principal stimulus for insulin secretion. However, release of insulin is also evoked by other monosaccharides, fatty acids and amino acids (Fu et al., 2013).

### **1.6.3.1 Insulin release and amino acids**

Diet-derived amino acids cause insulin release from  $\beta$ -cells. Insulin secretion also occurs as an indirect result of breakdown of skeletal muscle proteins, since protein catabolism generates free amino acids. Increase in blood amino acid concentrations evokes secretion of glucagon, thereby causing a rise in blood glucose, with insulin released as a consequence.

There are a limited number of amino acids that can elicit or potentiate insulin secretion, and they do so by different mechanisms. Glutamine does not induce insulin release alone, nor does it enhance glucose-stimulated insulin secretion (GSIS), but instead amplifies the secretion caused by leucine. In the  $\beta$ -cell cytoplasm, glutaminase converts glutamine to glutamate. From here, glutamate is metabolised to  $\alpha$ -ketoglutarate by glutamine dehydrogenase; an action which is stimulated by leucine. Consequently, more carbon acquired from glutamine is pushed into the TCA cycle. This leads to ATP production,  $\beta$ -cell depolarisation and insulin is secreted (Newsholme et al., 2007; Fu et al., 2013). The relevance of glutamine to insulin homeostasis is also highlighted by the association between insulin resistance and reduced plasma glutamine concentration (Cheng et al., 2012).

There is confusing data regarding glutamate and insulin release. GSIS has been seen to be increased by intracellular glutamate by some research groups, with others observing no effect (Newsholme et al., 2007). Recent data suggests that glutamate transport is important for insulin vesicle exocytosis, with disruption to glutamate flux across these granules significantly reducing insulin secretion (Gammelsaeter et al., 2011). Arginine is also involved in insulin regulation. Its influx via the mCAT2A transporter causes  $\beta$ -cell depolarisation, intracellular  $\text{Ca}^{2+}$

increase and ultimately secretion of insulin. Similarly, the co-transport of alanine with  $\text{Na}^+$  into  $\beta$ -cells provokes a rise in intracellular  $\text{Ca}^{2+}$  and insulin release (Newsholme & Krause, 2012). For both alanine and arginine, however, no associations have been made between altered plasma levels and an insulin resistant phenotype (Cheng et al., 2012).

In addition, amino acids can influence secretion of insulin through glucagon-like peptide-1 (GLP-1) and gastric inhibitory peptide (GIP). L- and K-cells of the intestines produce GLP-1 and GIP respectively in response to dietary amino acids.  $\beta$ -cells possess receptors specific to both hormones and their interaction with GLP-1 and GIP magnifies GSIS (Fu et al., 2013). Insulin secretion may also be influenced by long-term exposure to particular amino acids through their effect on  $\beta$ -cell gene expression (Newsholme & Krause, 2012).

#### **1.6.3.2 Insulin release and fatty acids**

GSIS is amplified by fatty acids (FAs) and attenuated in their absence, a state which can be reversed by addition of exogenous FAs (Stein et al., 1996; Roduit et al., 2004). Long term exposure to excess saturated FAs, especially in combination with hyperglycaemia, causes blunted manufacture and release of insulin, alongside  $\beta$ -cell apoptosis (El-Assaad et al., 2003; Poitout et al., 2006).

FAs are acquired by  $\beta$ -cells endogenously from phospholipid stores or intracellular triglycerides. Exogenous FAs are obtained from the plasma via diffusion, or from breakdown of lipoproteins via the action of the enzyme lipoprotein lipase (LPL), which can be found in islet tissue (Nolan et al., 2006). Once in the cytoplasm, FAs are metabolised to long-chain acyl-coA and membrane depolarisation results, leading to exocytosis of insulin granules (Newsholme & Krause, 2012). FAs can further enhance insulin secretion via direct stimulation of  $\beta$ -cell free fatty acid receptors (Nolan et al., 2006).

#### **1.6.3.3 Physiological effects of insulin**

Insulin binds to the insulin receptor at cell membranes. This interaction leads to activation of its tyrosine kinase domain, resulting in autophosphorylation and tyrosine phosphorylation of various intracellular proteins. These are categorised

as insulin receptor substrates or 'IRS', and their downstream activity allows insulin to exert its effects (Wilcox 2005; Ormazabal et al., 2018). The outcome of insulin signalling is tissue-dependent, with muscle and adipose tissue particularly sensitive to the hormone. Up to 70% of insulin-directed glucose uptake occurs at muscle, where it stimulates generation of glycogen and protein synthesis. In adipose tissue, insulin causes lipogenesis, inhibits fat breakdown and promotes triglyceride storage by encouraging pre-adipocyte differentiation to mature adipocytes. It also activates lipoprotein lipase, allowing for increased FA uptake from lipoproteins in the bloodstream (Wilcox 2005; Yaribeygi et al., 2019).

The liver is another important site of insulin metabolism, contributing to around 30% of whole-body insulin-facilitated glucose uptake. Insulin directs key hepatic metabolic reactions, inhibiting gluconeogenesis and the formation of ketone bodies, whilst driving glycogen and protein synthesis (Wilcox 2005).

#### **1.6.3.4 Insulin and the vasculature**

Insulin can evoke both vasodilation and vasoconstriction, with these effects mediated by two separate branches of the insulin signalling pathway.

Insulin is a well-known eNOS activator. The predominant IRS in endothelial cells is IRS-2 and this is phosphorylated upon interaction between insulin and the insulin receptor. PI3K is then activated, leading to stimulation of Akt/PKB. Akt/PKB directly phosphorylates eNOS at Ser1177, causing increased NO production and ultimately vasodilation (Muniyappa et al., 2007; Tokarz et al., 2018). Unlike other classic vasodilators, such as Ach, insulin induces NO-mediated dilation in a Ca<sup>2+</sup>-independent manner. In embryonic fibroblasts transiently transfected with eNOS, the presence of the Ca<sup>2+</sup> chelator BAPTA does not impair phosphorylation of Ser1177 by insulin (Montagnani et al., 2001). Hartell et al. (2005) also observed that insulin treatment of cultured endothelial cells elevated NO production without changing the concentration of intracellular Ca<sup>2+</sup>. In addition, insulin can exert vasodilatory effects through promoting PGI<sub>2</sub> generation, although the exact mechanism by which this occurs has not been clarified (Sobrevia et al., 1996).

Phosphorylation of IRS-1 can activate the other arm of the insulin signalling cascade, involving stimulation of the GTP binding protein, Ras. This elicits

mitogen activated protein kinase (MAPK) activity, which controls various pathways linked with cell differentiation and growth (Muniyappa et al., 2007). Further to affecting mitogenic processes, insulin-mediated MAPK activation can evoke ET-1 secretion, leading to vasoconstriction, as seen by Cardillo and colleagues (1999). This work is supported by the observation that endothelial-specific insulin receptor knockout mice display markedly reduced ET-1 expression (Vicent et al., 2003).

## **1.7 Macrovascular complications and diabetes**

Vascular complications, particularly atherosclerosis, are common amongst those with diabetes. In these individuals, macrovascular disease appears earlier, with lesions being more advanced and widespread. Hyperglycaemia and the subsequent glucose toxicity play a key part in the emergence of diabetic vascular disease. Constant exposure to high glucose concentrations results in excessive ROS production within endothelial cells, which initiates several atherogenic processes (Madonna & De Caterina, 2011a).

Activation of PKC results from high intracellular glucose levels through increased synthesis of DAG. This elicits VEGF expression, which augments vascular permeability. PKC also induces production of ECM proteins and various inflammatory factors, as well as adding to the existing oxidative stress by stimulating NADPH oxidase  $O_2^{\cdot-}$  generation. Attenuated eNOS activity, alongside a rise in endothelin-1, occurs following PKC activation, which promotes an atherogenic environment (Paneni et al., 2013).

The increase in intracellular ROS caused by hyperglycaemia also alters metabolic pathways. It stimulates aldose reductase, part of the polyol pathway, which is responsible for forming sugar alcohols from excess glucose. Amplified aldose reductase activity leads to elevated conversion of glucose to sorbitol. This requires NADPH and increased flux through this pathway results in less available NADPH for production of reduced glutathione, exacerbating the high oxidative conditions in the endothelial cell. Diabetic mice overexpressing human aldose reductase exhibit both decreased expression of genes involved in glutathione regeneration and elevated atherosclerosis (Vikramadithyan et al., 2005). Increased activity also occurs through the hexosamine biosynthetic pathway,

which creates O-linked acetylglucosamine (O-GlcNAc). O-GlcNAc is involved in various transcription factor and protein modification. Very little glucose normally enters the hexosamine pathway. Abnormal activation of the pathway leads to increased O-GlcNAc alteration of Specificity Protein 1 (Sp1) transcription factor. This amplifies the expression and activity of plasminogen activator inhibitor-1 (PAI-1) and transforming growth factor-beta (TGF- $\beta$ ), both of which favour plaque development (Du et al., 2000).

Hyperglycaemia and the presence of ROS results in the reaction of glucose and intracellular sugars with the amino groups presents on proteins, nucleic acids and lipids. The resulting substances are known as advanced glycation end-products (AGEs) and can drastically alter endothelial cell function (Singh et al., 2001). Within the context of atherosclerosis, they activate NF- $\kappa$ B, causing an upregulation in expression of leukocyte adhesion molecules on the endothelial luminal surface. NF- $\kappa$ B can also increase ET-1 expression and has been associated with reduced NO bioavailability, thus promoting vasoconstriction (Singh et al., 2001).

Mechanisms independent of glucose have been implicated in diabetic vascular disease development. In a state of insulin resistance and diabetes, the IRS-1/PI3K/Akt pathway, by which insulin produces its metabolic effects, is downregulated. This manifests as impaired glucose uptake and reduced Akt-mediated phosphorylation of eNOS S1177, and so reduced NO availability (Kashiwagi et al., 2013). By contrast, the mitogenic and pro-inflammatory arm of insulin signalling, mediated by Ras and MAPK, is not affected. The compensatory hyperinsulinaemia seen in insulin resistance and diabetes continues to activate this pathway, and a subsequent increase in pro-inflammatory factors, ET-1 and adhesion proteins create conditions ideal for atherosclerotic lesion formation (Madonna & De Caterina, 2011a). Indeed, mice possessing a dominant negative mutant human insulin receptor exclusively in endothelial cells, in the absence of hyperglycaemia, experience accelerated atherosclerosis development with western diet feeding (Gage et al., 2013). Despite a clear relationship between attenuated insulin receptor signalling and exacerbation of atherosclerosis, hyperactivity of the signalling cascade can also be pro-atherogenic. Overexpression of the human insulin receptor in the murine

endothelium results in hampered eNOS activity and increased  $O_2^{\cdot-}$  production (Viswambharan et al., 2017).

Lipotoxicity also appears to link insulin resistance and dysfunction of endothelial cells. Excessive FAs elevate ROS concentrations and so stimulate production of peroxynitrite, which is well-known for inducing endothelial cell damage. With regard to insulin signalling, this augmented ROS generation disrupts the cascade by activating PKC- $\theta$ , leading to decreased Akt activity (Kim et al., 2006). Inflammation is another commonality coupling insulin resistance and endothelial dysfunction. The pro-inflammatory cytokine, tumour necrosis factor- $\alpha$  (TNF- $\alpha$ ), promotes proteasomal breakdown of IRS-1. Additionally, it activates several serine kinases, which subsequently suppress PI3K and Akt (Emanuelli et al., 2001; Gao et al., 2003). Certain features typical of endothelial dysfunction are also encouraged by TNF- $\alpha$  and similar inflammatory mediators, usually through their upregulation of various inflammatory proteins. C-reactive protein is one such example and has been documented to inhibit eNOS expression, alongside stimulating ET-1 release from the endothelium (Venugopal et al., 2002).

Vascular progenitor cells perform a vital role in repair of the endothelium following injury. The emergence of atherosclerosis in those with diabetes may be promoted by defects in the function of these cells, as well as a reduction in their number. This is partly facilitated by diminished NO levels; NO can act as a stem cell growth factor at normal concentrations. Additionally, certain factors regulating senescence and apoptosis of vascular progenitors, are suppressed in diabetes (Madonna & De Caterina, 2011b).

It is evident that glucose toxicity, insulin resistance and hyperinsulinaemia contribute significantly to atherosclerosis development in diabetes. However, a proportion of individuals presenting with diabetes do not ever develop vascular disease (Harcourt et al., 2013). Furthermore, strict control of blood glucose in patients with diabetes has been shown to lessen the likelihood of atherosclerosis, but the degree of this effect is small (Madonna & De Caterina, 2011a). This indicates that diabetic vascular complications are not wholly influenced by abnormal glucose metabolism or insulin signalling. Consequently, there have been increased research efforts directed at other factors, such as genetic susceptibility and epigenetics.

### 1.7.1 Genetic associations between vascular disease and diabetes

Genetic variants underlying various diseases are increasingly being discovered by means of genome wide association studies or 'GWAS'. This approach is used to uncover associations between genetic variants and particular traits of interest in a population sample (Visscher et al., 2017). While GWAS data does not explain the mechanism responsible for a phenotype-genotype association, it can provide an important first step in highlighting a potential disease pathway and in determining risk prediction (Visscher et al., 2017).

While GWAS have proved useful in demonstrating that cardiovascular disease and diabetes often share a genetic background, few studies have been able to identify genetic variants jointly responsible for the 2 diseases (Dahlström & Sandholm, 2017; Strawbridge & van Zuydam, 2018). However, one investigation of 1517 coronary heart disease (CHD) with T2DM patients and 2671 CHD free controls with T2DM across 5 cohorts highlighted a novel single nucleotide polymorphism (SNP) (rs10911021) which attained genome-wide significance (Qi et al., 2013). No association was found between rs10911021 and CHD in further analysis of 2374 non-diabetic cases, implying the SNP is only relevant in people with diabetes. The variant is located on chromosome 1, in a noncoding region upstream of the gene *GLUL*. Risk allele homozygotes (C/C) exhibited a decrease of 32% in the expression of *GLUL* in their endothelial cells compared with those who were homozygotes for the protective allele (T/T). Heterozygotes displayed a reduction in endothelial *GLUL* expression to intermediate levels. Further examination revealed that rs10911021 was not associated with the expression of 7 other genes in the locus. Importantly, every copy of the risk allele was associated with a 36% increase in the odds of CHD, yet was not associated with altered measures of glucose homeostasis or insulin resistance (Qi et al., 2013).

*GLUL* encodes the enzyme glutamine synthetase (GS), which is responsible for the production of glutamine from glutamate and ammonia. Individuals carrying the rs10911021 risk allele did not show differences in circulating concentrations of glutamine or glutamate, but did present with significantly lower plasma pyroglutamic to glutamic acid ratios. Pyroglutamic acid is a downstream metabolite of glutamate, created following conversion of glutamate to glutathione

and then glutathione degradation (Kumar & Bachhawat, 2012). A rise in glutamate concentrations could be expected with decreased GS expression. This may not have been seen in this study due to increased metabolism of glutamate into glutathione and subsequently pyroglutamic acid. Overall, these observations suggest that rs10911021 may be involved in exacerbating CHD risk in patients with T2DM by altering glutamine metabolism in the endothelium (Qi et al., 2013; Alkayyali & Lyssenko, 2014).

Notably, the findings of Qi et al. (2013) have been independently reproduced in a different cohort examined by the Look AHEAD Research Group (2016). Alongside reaffirming that rs10911021 is significantly associated with increased cardiovascular risk in patients with T2DM, the team discovered that the association is unaltered by introducing intensive lifestyle changes, such as increased physical activity and weight loss. Analysis of another 2 independent studies by Prudente et al (2015) revealed that all-cause mortality was significantly increased in T2DM subjects carrying rs10911021, and that the risk of death increased by 32% with each risk allele.

## 1.8 Glutamine synthetase

In mammals, glutamine is the most abundant amino acid in the bloodstream and is critical for normal cell function. Ehrensvard et al. (1949) was the first to establish its importance to cell survival in culture. This was supported later by Eagle et al. (1966), who demonstrated that glutamine was required *in vitro* at concentrations 10–100 times higher than any other amino acid. It also could not be substituted with glucose or glutamate.

Glutamine is crucial for nucleic acid, peptide and protein synthesis. Its amide nitrogen is used for the manufacture of the amino groups in guanine and cytidine, as well as the 3<sup>rd</sup> and 9<sup>th</sup> nitrogens in purine rings and the amide group of NAD<sup>+</sup>. Additionally, it contributes to important detoxification processes, such as removal of phenylacetic acid. This potentially harmful metabolite originates from phenylalanine and its coupling with glutamine allows it to be excreted in the urine (Cooper 1988; Newsholme et al., 2003). Glutamine also provides the glutamate needed for manufacture of glutathione, which acts as a powerful antioxidant (Sappington et al., 2016).

While there are many reactions that consume glutamine, most body fluids exhibit it at high levels. In human plasma and cerebrospinal fluid, it comprises roughly 20% and 70% of the amino acid content, respectively (Cooper 1988). Glutamine can be obtained from the diet and is transferred across the cell membrane by amino acid transporter proteins (Xiao et al., 2016). It is also created *de novo* by the action of the aforementioned enzyme, GS.

GS directs glutamine production from ammonia and glutamate through a reversible and ATP-dependent reaction (Cooper 1988). It is composed of 373 amino acids and has 3 domains: the N-terminus, a  $\beta$ -grasp domain and a C-terminal catalytic region. 5 of these monomers assemble as a ring structure and mammalian GS is formed following the stacking of 2 of these pentamers (Jeitner et al., 2015).

GS-mediated glutamine production begins with the binding of ATP and 3 manganese ions to the catalytic region of the enzyme. This repositions the terminal phosphate group, allowing interaction with glutamate. The presence of ammonia closes the active site and aligns the bound ATP terminal phosphate with the  $\gamma$ -carboxyl of glutamate, enabling transfer of a phosphate group between them. An acylphosphate intermediate is created, which gains an electron pair from ammonia to become glutamine (Jeitner et al., 2015).

### **1.8.1 Glutamine metabolism in physiology and disease**

The action of GS is tightly regulated and it is often compartmentalised to distinct areas of tissues, which dictates its activity and expression level (Cooper 1988). The role of GS in various physiological systems are highlighted in Figure 1.4.

#### **1.8.1.1 Glutamine metabolism and the liver**

Hepatic GS activity plays an important part in the urea cycle, a series of reactions used for the metabolism and removal of excess nitrogen. Catabolism of dietary and endogenous proteins releases toxic ammonium nitrogen. The urea cycle transforms ammonia into non-toxic urea which can then be excreted in the urine (Deignan et al., 2008). Nitrogen is taken to the liver from peripheral tissues in the form of glutamine. In periportal cells, it is metabolised by glutaminase, releasing

nitrogen as ammonia. Ammonia is then converted to carbamoyl phosphate. Its combination with ornithine leads to citrulline formation and ultimately synthesis of urea (Newsholme et al., 2003). Excess ammonia which cannot be taken up by the urea cycle is directed to perivenous cells of the liver, where GS acts to utilise it in production of glutamine (Qvartskhava et al., 2015).

The significance of GS in ammonia detoxification has been highlighted by *in vivo* liver-specific GS knockout models. Hepatic GS deficiency was observed to cause systemic hyperammonaemia, accompanied by elevated oxidative stress markers and abnormalities in cognitive and motor function (Qvartskhava et al., 2015; Chepkova et al., 2017).

#### **1.8.1.2 Glutamine metabolism and the kidney**

GS also contributes to acid-base homeostasis in the kidney. Here, ammonia, in both the form of  $\text{NH}_3$  and  $\text{NH}_4^+$ , undergoes transfer into the urine. Carbonic acid ( $\text{H}_2\text{CO}_3$ ) dissociates to give  $\text{HCO}_3^-$  and  $\text{H}^+$ , with  $\text{NH}_3$  able to react with  $\text{H}^+$  to become  $\text{NH}_4^+$ .  $\text{HCO}_3^-$  is transported into the bloodstream where it buffers excess  $\text{H}^+$ , reforming  $\text{H}_2\text{CO}_3$ , which quickly breaks down to  $\text{CO}_2$  and  $\text{H}_2\text{O}$  (Weiner & Verlander, 2017). However, renal ammonia can be directed to GS and glutamine manufacture. GS-mediated production of glutamine produces  $\text{H}^+$ . This can mop up the  $\text{HCO}_3^-$  that results from the generation of  $\text{NH}_4^+$ . Thus, GS exhibits opposing action to those enzymes responsible for ammoniogenesis (Lee et al., 2016). Genetic deletion of GS within the proximal tubule of the kidney results in a marked impairment in ammonia excretion upon metabolic acidosis. This change cannot be compensated for by upregulation of other proteins involved in ammonia metabolism, demonstrating the importance of GS in acid-base regulation (Lee et al., 2016).

#### **1.8.1.3 Glutamine metabolism and the CNS**

The brain is another organ which utilises GS for detoxifying ammonia. Ammonia can pass the blood brain barrier, but the urea cycle does not occur in cerebral tissue. Consequently, astrocytes express high levels of GS for ammonia metabolism (Castegna & Menga, 2018). They also employ GS as a means of

balancing concentrations of glutamate, which has a role in neurotransmission. Following completion of its action at a neuronal synapse, glutamate is removed from the synaptic cleft by astrocytes. It either enters the TCA cycle, or is metabolised by astrocytic GS to glutamine. Glutamine can then be shuttled to neighbouring glutamatergic or GABAergic neurons, where it is used in the replenishment of glutamate and GABA, respectively (Schousboe et al., 2014).

Perhaps unsurprisingly then, abnormalities in GS expression and activity have been associated with several neurological disorders. Kulijewicz-Nawrot et al. (2013) observed a decrease in GS expression in the astrocytes of a murine model of Alzheimer's disease. Alterations are also exhibited in human subjects. Reductions in GS activity has been reported in patients with schizophrenia (Steffek et al., 2008), and similar changes were noted in the amygdala and hippocampal formation of individuals with mesial temporal lobe epilepsy (Eid et al., 2012). The importance of cerebral GS is probably most clearly highlighted, however, by the embryonic lethality that results *in vivo* upon astrocytic GS deficiency (He et al., 2010).

Many neurological disorders are speculated to arise from, or have, neuroinflammation as a contributing factor to disease progression. Action of GS can control immune response, with leukocytes widely documented to require high levels of glutamine (Newsholme et al., 2003). Palmieri et al. (2017a) saw that inhibiting GS pharmacologically in cultured microglia resulted in an elevated inflammatory response to lipopolysaccharide insult. This was supported *in vivo*, where inflammatory markers were raised in a microglia-specific GS knockout mouse compared with wild-type controls. The same group reported that GS activity and glutamine generation promotes the adoption and maintenance of the M2 phenotype in macrophages. This state is associated with tissue repair and remodelling mechanisms. Pharmacological inhibition of GS pushed macrophages to the pro-inflammatory M1 phenotype (Palmieri et al., 2017b).

Interestingly, it was noted that alongside an increased inflammatory response when microglial GS activity was blocked, there was reduced insulin-stimulated glucose uptake. Many of the physiological abnormalities seen in insulin-resistance and diabetes, such as impaired glucose metabolism, ER stress and amplified inflammation, have also been reported in neurological conditions (Castegna & Menga, 2018). In Alzheimer's disease, various cytokines in

microglia stimulate phosphorylation of IRS-1, which attenuates its action (Talbot et al., 2012; Castegna & Menga, 2018). Within the CNS, insulin can limit the effects of oxidative stress by increasing ATP concentrations and intracellular adenosine (Duarte et al., 2006). In addition, it prevents a build-up of extracellular glutamate, thus excitotoxicity (Duarte et al., 2003). Together, these observations highlight GS as a link between inflammation, insulin resistance and metabolism (Castegna & Menga, 2018).

#### **1.8.1.4 Glutamine metabolism and diabetes**

Human metabolomics studies have detected elevated plasma glutamine in patient groups with diabetic retinopathy (Rhee et al., 2018). However, other investigations using metabolomics have revealed opposing results. Analysis of subjects from the Framingham Heart Study and the Malmö Diet and Cancer Study by Cheng et al. (2012) found that those with insulin resistance presented with lower plasma glutamine concentrations. Higher glutamine to glutamate was associated with a reduced diabetes incidence rate. *In vivo* data from the group corroborated that elevated glutamine may exert protective effects in diabetes, with improved glucose tolerance noted following glutamine supplementation, with similar findings made by Zhou et al. (2013). In contrast, Lee and colleagues (2018) reported no change in plasma glutamine in individuals with diabetes or impaired fasting glucose.

Decreased GS expression has been recorded in both rat Müller cells cultured in high glucose conditions, and in Müller cells isolated from diabetic rats. The downregulation of GS was alleviated upon inhibition of the pro-inflammatory cytokine IL-17A (Qiu et al., 2017). This is in line with the lower glutamine levels found in retinas of streptozocin (STZ) treated rats (do Carmo et al., 1998) and in vitreous samples from patients with diabetic retinopathy (Ishikawa et al., 1995).

#### **1.8.1.5 Glutamine metabolism and the vasculature**

Glutamine metabolism can impact vascular biology through influencing NO production. An increase in plasma glutamine attenuated vasodilation in rat cerebral arterioles in response to CO<sub>2</sub>, and was thought to occur through reduced

arginine manufacture (Okada et al., 2000). It was speculated that glutamine negatively regulates argininosuccinate synthetase (ASS) activity, which would ultimately decrease available arginine, rather than directly impairing the catalytic potential of NOS (Okada et al., 2000). Other studies, however, have not been able to replicate this. In endothelial cell culture, NO synthesis induced by both Ca<sup>2+</sup>-mediated and receptor-directed activation has been reported to be inhibited by glutamine, but was not due to a change in uptake or intracellular concentration of arginine (Arnal et al., 1995; Meininger & Wu, 1997). There have been similar findings in aortic ring preparations, although inconsistencies exist with regard to eNOS stimulation by Ca<sup>2+</sup>. Arnal and colleagues (1995) observed that glutamine suppressed NO generation in rabbit aorta in response to Ach and ADP, but not to the Ca<sup>2+</sup> ionophore A23187.

Endothelial NO levels also appear to be regulated by the metabolism of glutamine to glucosamine. Blocking glucosamine production abrogated glutamine induced reduction of NO synthesis, without affecting arginine, intracellular Ca<sup>2+</sup> or eNOS activity. Instead, glutamine and glucosamine caused a marked decrease in the activity of the pentose cycle, which, in endothelial cells, is a principal supplier of the eNOS substrate, NADPH (Wu et al., 2001).

In addition to influencing NO production, glutamine metabolism may have implications for other processes in the vasculature. Following balloon-induced injury of the carotid artery in rats, GS expression was seen to be highly elevated, suggesting it could affect vessel repair mechanisms (Kang et al., 2015). Other investigations have highlighted potential involvement of GS in atherosclerosis development. Atherosclerotic plaques within the internal carotid artery are amongst the principal risk factors for ischaemic stroke. Those which rupture to cause a cerebral infarction can be often distinguished from asymptomatic carotid lesions by certain histological characteristics, such as thinner fibrous caps and intra-plaque haemorrhage (Saksi et al., 2011). Saksi et al. (2011) found, through comparison of gene expression profiles, a 2.2-fold increase in expression of *GLUL* in stroke-associated plaques versus asymptomatic lesions. Similar results were documented in a more recent, independent study by Perisic and colleagues (2013). This upregulation in *GLUL* correlates with several features of unstable plaques, including plaque ulceration and various markers of cell death and

proliferation. *GLUL* was also strongly expressed in the necrotic lipid core, macrophages and VSMCs of stroke-associated plaques (Saksi et al., 2011).

Palmieri et al. (2017b) assessed the angiogenesis-stimulating capacity of M2-macrophages following pharmacological inhibition of GS and saw a significant reduction in endothelial capillary network formation. Examination of GS within the context of angiogenesis has also been undertaken by Eelen et al. (2018). Mice with genetic deletion of endothelial GS displayed vascular abnormalities, such as hypobranching and reduced radial expansion in the postnatal retina. These sprouting defects were replicated using human umbilical vein endothelial cells (HUVECs) using GS knockdown or pharmacological inhibition of GS. This was not caused by changes in levels of oxidative stress, endothelial cell viability, concentrations of NADPH or glutathione; nor was it due to alterations in glycolysis or oxidation of either glucose or glutamine. It was concluded from these observations that GS depletion caused impaired cell migration through remodelling of the actin cytoskeleton. Indeed, GS knockdown induced an increase in F-actin. Further investigation by the group demonstrated that diminished GS activity inhibits endothelial cell motility and angiogenesis through decreased auto-palmitoylation and subsequent attenuated palmitoylation of the GTPase, RhoJ (Eelen et al., 2018). This suggests an entirely novel role for GS in the vasculature, independent of its generation of glutamine from ammonia and glutamate. It remains unclear, however, whether GS influences aspects of endothelial biology beyond sprouting angiogenesis. Recent single cell RNA-sequencing analysis of endothelial cells indicate that GS is highly enriched in arterial endothelial cells, supporting the need for further characterisation of mice with endothelial GS deletion (Kalucka et al., 2020).

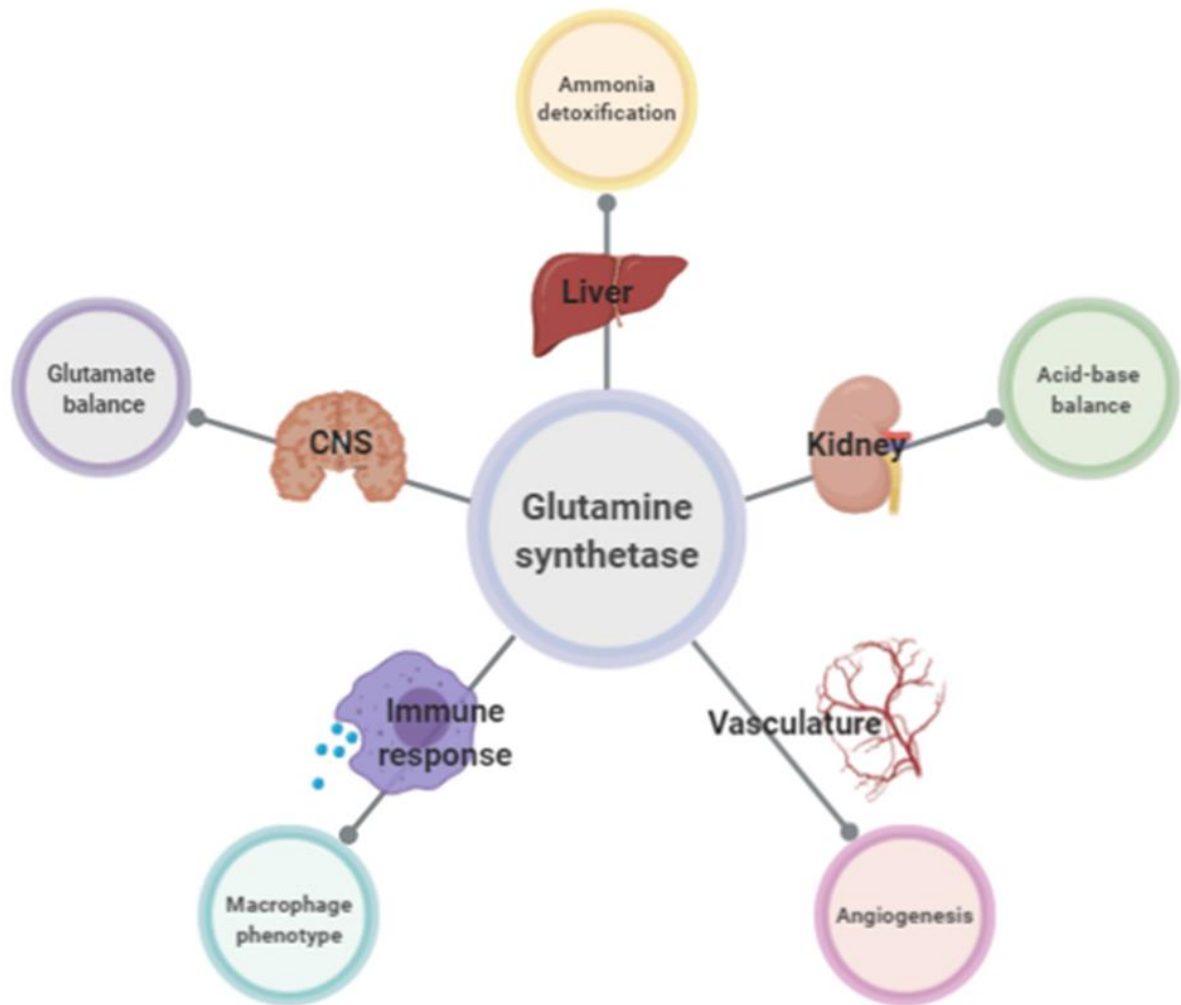


**Figure 1.4 Schematic summary of the role of glutamine synthetase in various physiological systems**

## 1.9 Summary

Endothelial cells are critical for maintaining vascular homeostasis, representing important mediators of vessel permeability and tone, as well as immune response, angiogenesis and coagulation. Dysfunction of the endothelium characterises multiple vascular diseases and appears to be a key contributor to the development of atherosclerosis and the complications of T2DM.

The importance of understanding endothelial dysfunction is highlighted by the rising prevalence of both conditions and the challenges in treatment when they occur simultaneously. Current therapeutic strategies offer only minimal improvements to cardiovascular risk in those with T2DM. These patients are still twice as likely to experience a fatal cardiovascular event, indicating diabetic vascular disease is caused by unique mechanisms which are not affected by existing therapies (Kahn et al., 2012; IDF Diabetes Atlas 2019;).

Consequently, growing emphasis has been placed on finding genetic variants to explain this distinct pathophysiology. The identification in 2013 of rs10911021 as a risk factor for diabetic vascular disease, associated with endothelial GS expression, was an important discovery, although many questions remain. More recent studies by Eelen and colleagues (2018) established that the enzyme has essential roles in the vasculature beyond that of glutamine synthesis, re-emphasising the significance of examining endothelial GS.

Understanding the function of GS in endothelial cells may lead, not only to personalised therapies for atherosclerosis and diabetes, but also to the development of strategies for risk prediction.

## 1.10 Aims and objectives

### 1.10.1 Overall aim

The overall aim of this project was to examine the role of GS in normal endothelial biology, and to investigate how it may influence development of atherosclerosis and diabetes.

### 1.10.2 Hypothesis

Endothelial GS expression is important in normal vascular function and its perturbation may promote vascular dysfunction, especially diabetic macrovascular disease

### 1.10.3 Objectives

- Determine how reduced GS expression in the endothelium affects vascular phenotype, using an endothelial-specific GS knockout mouse model, alongside mice with endothelial-specific GS haploinsufficiency
- Explore the effect of impaired GS activity *in vitro* using HUVECs and pharmacological inhibition of the enzyme
- Investigate how GS deficiency influences atherosclerosis development by studying ApoE<sup>-/-</sup> mice with either endothelial-specific GS haploinsufficiency, or holoinsufficiency
- Define the added impact of STZ-induced diabetes on atherosclerosis in ApoE<sup>-/-</sup> mice with endothelial-specific GS holoinsufficiency

## Chapter 2 Materials and methods

### 2.1 Materials

<b>Material</b>	<b>Supplier</b>
0.5 mL U-100 insulin syringe	BD
1 mL U-100 insulin syringe	Terumo Medical (324892)
10 kDa spin columns	Abcam (93349)
<sup>14</sup> C-arginine	Perkin Elmer (NEC267E050UC)
14G cannula	BD
27G needle	Terumo Medical
70 µm cell strainer	Grenier bio-one (542170)
8.0 suture thread	Ethicon
AAS	Sigma (A5955)
Acetylcholine	Sigma (A6625)
Bromochloropropane	Sigma (B9673)
BSA 7.5% solution	Sigma (A8412)
BSA powder	Sigma (810535)
Buprenorphine	Animalcare; York, UK
BX41 microscope	Olympus
CaCl <sub>2</sub> ·2H <sub>2</sub> O	Fisher Scientific (10786634)
Catalase	Sigma (C30)
CD146 LSEC magnetic beads	Miltenyi Biotec (130-092-007)
Cell extraction buffer	Thermo Fisher Scientific (FNN0011)
Chow diet	B&K Universal Ltd.; Hull, UK (#BK001E)
Citric acid	Sigma (C0759)
Coda Non-invasive Tail BP system	Kent Scientific
Collagenase type II	Worthington Biochemical (LS004179)

Color Prestained Protein Standard, Broad Range (11–245 kDa)	New England Biolabs (P7712S)
Corn oil	Sigma (C8267)
DAPI Fluoromount-G	Southern Biotech (0100-20)
DNA Engine Tetrad 2 Thermal Cycler	Bio-Rad
DNase kit	Thermo Fisher Scientific (AM1906)
Donkey serum	Sigma (D9663)
DOWEX resin (50WX8 hydrogen form; 50-100 mesh)	Sigma (44509)
DPX mountant	Sigma (44581)
DS-11 FX spectrophotometer	Denovix
ECGS	Sigma (E2759)
EDTA	Sigma (E6758)
Elastin Miller stain	Avantor
Ethanol	Fisher Scientific (15622470)
Evans Blue	Fisher Scientific (Acros Organics 10656402)
Falcon tubes	Sarstedt
FBS	Biosera
G:BOX imaging equipment	Syngene
Gelatin powder	Sigma (G7041)
GeneSys software	Syngene
Glucometer	Accu-Chek
Glucometer recording strip	Accu-Chek
Glucose	Sigma (G8270)
Glycine	Fisher Scientific (10061073)
GM500 cages	Techniplast
GraphPad Prism 8.1.0 software	GraphPad Software Inc, San Diego, California USA
HBSS	Thermo Fisher Scientific (24020133)

Heparin	LEO Pharma (00043/0041R)
HEPES 1 M solution	Sigma (H0887)
HEPES powder	Sigma (H3375)
Hitorque Cross-it 200XT angioplasty guide wire	Abbott
Human umbilical vein endothelial cells (pooled)	Promo-Cell
ImageJ software	NIH, Bethesda, Maryland, USA
Image-Pro Plus 7.0 software	Media Cybernetics, MD, USA
Immobilon Western Chemiluminescent HRP Substrate Kit	Merck Millipore (WBKLS0500)
Insulin	Sigma (I9278)
Iris scissors	Fine Science Tools
Irripod (sterile NaCl)	Unither
Isoflurane	Zoetis
Isopropanol	Fisher Scientific (10284250)
KCl	Fisher Scientific (10697623)
KH <sub>2</sub> PO <sub>4</sub>	Fisher Scientific (10573181)
KMnO <sub>4</sub>	Sigma (1.05080)
L-arginine	Sigma (A5131)
LightCycler 480	Roche
Lignocaine	Arnolds; Harlescott, UK
L-NMMA	Merck Millipore (M7033)
LSM880 confocal microscope	Zeiss
Lunascript RT Supermix Kit	New England Biolabs (E3010)
M199 cell culture media	Sigma (M4530)
MACS separator	Miltenyi Biotec
MACSmix rotator	Miltenyi Biotec
Methanol	Fisher Scientific (10675112)

MgSO <sub>4</sub> ·7H <sub>2</sub> O	Sigma (230391)
MiniMACS MS columns	Miltenyi Biotec (130-042-201)
MSO	Sigma (M5379)
MV2 cell culture media	Promo-Cell (C-22221)
MV2 supplement mix	Promo-Cell (C-39226)
NaCl	Fisher Scientific (10428420)
NaHCO <sub>3</sub>	Fisher Scientific (10518640)
NaN <sub>3</sub>	Sigma (S2002)
Nitrite/Nitrate Colorimetric Assay Kit	Cayman Chemical (780001)
Novex™ Tris-Glycine SDS Running Buffer	Thermo Fisher Scientific (LC26754)
NuPAGE™ 4-12% Bis-Tris Protein Gels, 1.5 mm	Thermo Fisher Scientific (NP0335)
Oil red O powder	Sigma (O0625)
OPMI 1-FC dissecting microscope	Zeiss
Organ bath apparatus	PanLabs SD, CA
OriginPro 2019b software	OriginLab, Northampton, MA, USA
Oxalic acid	Fisher Scientific (O/0650/53)
PBS (Modified, without calcium chloride and magnesium chloride, liquid, sterile-filtered)	Sigma
PFA	Sigma (158127)
Phenylephrine	Sigma (P6126)
Phosphatase inhibitor cocktail	Sigma (P5726)
Pierce™ BCA Protein Assay Kit	Thermo Fisher Scientific (23225)
Ponceau S	Sigma (09189)
Povidone-iodine solution	Sigma (Y0000466)
PrecisionPLUS qPCR Master Mix	PrimerDesign
Protease inhibitor cocktail	Sigma (P8340)
PVDF membrane	Bio-Rad (1704157)
QICAM Fast 1394 camera	Teledyne QImaging, Canada

Reducing agent	Thermo Fisher Scientific (NP0009)
RM2235 microtome	Leica
Sample buffer	Thermo Fisher Scientific (NP0007)
Scintillation cocktail	Perkin Elmer
SDS 10% solution	Sigma (71736)
Sodium citrate	Sigma (C0909)
Sodium nitroprusside	Honeywell Fluka (15696840)
Sodium pyruvate 100 mM solution	Sigma (S8636)
SpeedVac SPD111V concentrator	Thermo Fisher Scientific
Stainless steel beads	Qiagen (69990)
STZ	Sigma (S0130)
Sucrose	Sigma (S9378)
SuperFrost Plus™ Adhesion slides	Thermo Fisher Scientific (J1800AMNT)
SZ61 microscope	Olympus
Tamoxifen	Sigma (T5648)
TES 99 Paraffin Embedding Center	Medite
Trans-Blot Turbo System	Bio-Rad
Tri-Carb 2800TR liquid scintillation analyser	Perkin Elmer
TRI-Reagent	Thermo Fisher Scientific (AM9738)
Tris base	Fisher Scientific (10376743)
Triton	Sigma (X100)
Tween-20	Sigma (P1379)
Van Gieson stain	Thermo Scientific (RA Lamb Dry Chemical Stains) (LAMB/400-D)
Vicryl 6.0 suture thread	Ethicon
Vicryl 8.0 suture thread	Ethicon
Western diet	Dietex International Ltd (#829100)
Xylene	Avantor

**Table 2.1 Summary of solutions, the components at final working concentrations and final solution pH**

<b>Solution</b>	<b>Components (final concentration)</b>	<b>Solution pH</b>
HEPES-BSA	HEPES (10 mM) NaCl (145 mM) KCl (5 mM) MgSO <sub>4</sub> ·7H <sub>2</sub> O (1 mM) Glucose (10 mM) CaCl <sub>2</sub> ·2H <sub>2</sub> O (1.5 mM) BSA (0.25%)	7.4
Krebs-Henseleit	NaCl (119 mM) NaHCO <sub>3</sub> (25 mM) Glucose (11 mM) KCl (4.7 mM) CaCl <sub>2</sub> ·2H <sub>2</sub> O (2.5 mM) MgSO <sub>4</sub> ·7H <sub>2</sub> O (1.19 mM) KH <sub>2</sub> PO <sub>4</sub> (1.18 mM)	7.4
Stripping buffer	SDS (0.1%) Glycine (0.2 M) Tween-20 (0.1%)	2.5
TBS-T	Tris (20 mM) NaCl (150 mM) Tween-20 (0.05%)	7.6

## 2.2 Methods

### 2.2.1 Animal husbandry

#### 2.2.1.1 General housing

All murine studies described were conducted in accordance with the UK Animals (Scientific Procedures) Act 1986 under project licences 40/3523 and P144DD0D6 and personal license I9D99DE7D. All work was approved by the University of Leeds Animal Welfare and Ethics Board and the UK Home Office. A designated facility at the University of Leeds was used for housing. Individually ventilated GM500 cages were employed and maintained in an environment of 21°C, 50–70% humidity, with 12 hr light/dark cycle and *ad libitum* access to food and water. Weaning occurred at 3–4 weeks of age. Females were sacrificed pre-weaning, unless required for establishing new breeding colonies. Mice scheduled for experiments were group-housed with no more than 5 animals per cage. Ear notching was carried out for identification and genotyping purposes, with the latter performed by Transnetyx, Inc. (Cordova, TN, USA). Unless stated otherwise, any C57BL/6 mice utilised were of the J strain.

### 2.2.2 Generation of mouse models

#### 2.2.2.1 CreLoxP technology

All mouse models were created using Cre-LoxP technology, which allows for both temporal and spatial control of genetic manipulation.

The Cre enzyme is a DNA recombinase, encoded by the *CRE* gene. Cre recognises loxP sites as areas to target its recombination. LoxP sites are 34 base-pairs in length and their directionality dictates which type of recombination event takes place. When on the same chromosome, loxP sites orientated in the same direction direct Cre to excise all intervening DNA. Genes that are flanked by loxP sequences in this manner are said to be ‘floxed’ (Feil et al., 2009; van der Weyden et al., 2009).

The timing of Cre activity can be regulated by employing CreERT2 (Payne et al., 2018). This system uses fusion of the oestrogen receptor exhibiting a

mutant binding domain to a modified form of Cre. CreERT2 normally exists in the cytoplasm bound to Hsp90, rendering it inactive until exposure to 4-hydroxytamoxifen (4-OHT), a synthetic oestrogen receptor ligand. This induction of CreERT2 is achieved through administration of tamoxifen, which is metabolised to 4-OHT. 4-OHT disturbs the interaction between CreERT2 and Hsp90, allowing CreERT2 to migrate to the nucleus where DNA recombination can occur (Feil et al., 2009; Kim et al., 2018).

Cell lineage-specific CreERT2 expression can also be achieved by positioning the CreERT2 sequence downstream of particular promoter or enhancer element. This project utilised models with CreERT2 expression directed by a VE-Cadherin promoter. Since VE-Cadherin is an adhesion molecule found exclusively in the vascular endothelium, this allows for endothelial-specific CreERT2 activity.

Murine *GLUL* has 7 exons. For all the mouse models outlined in this project, the location of loxP sites enabled excision of exons 2–7. The targeting of these exons by CreERT2 in endothelial cells is depicted in Figure 2.1.

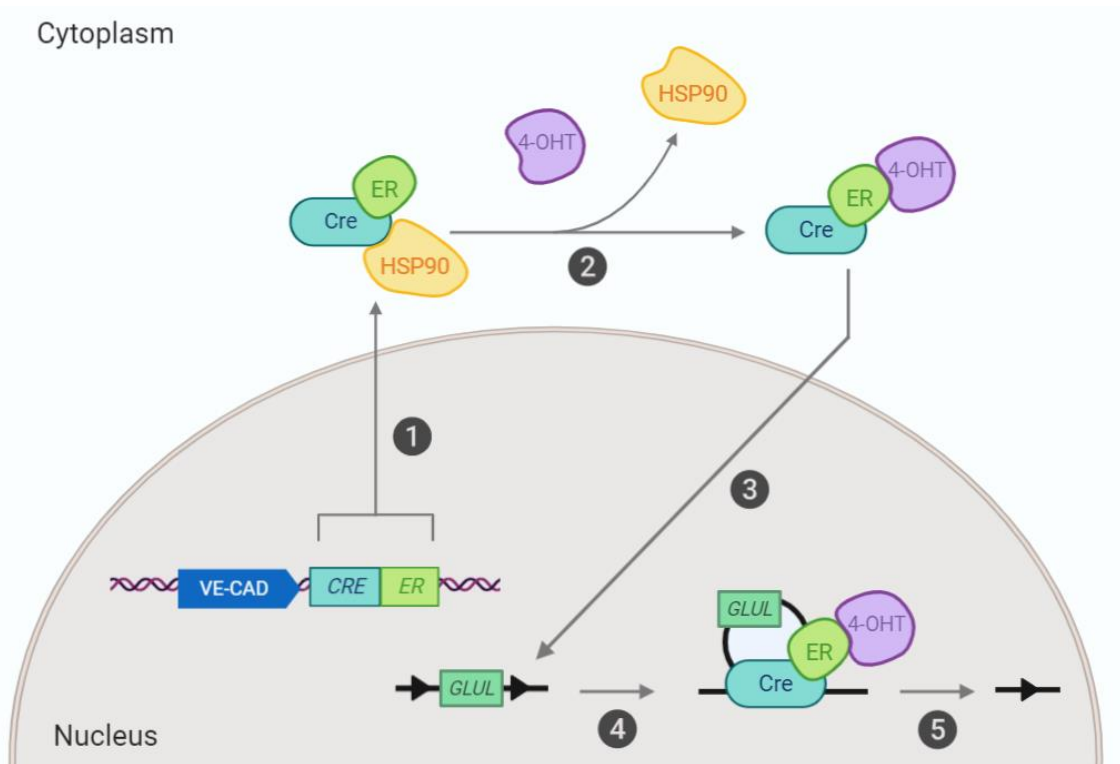


### Figure 2.1 Tamoxifen-inducible gene excision by the CreLoxP system

CreERT2 is a modified form of the Cre enzyme, fused to an oestrogen receptor (ER) with a mutated ligand binding domain. In the models used for this project, CreERT2 expression is under the control of a VE-Cadherin promoter region (VE-CAD). CreERT2 exists in the cytoplasm bound to Hsp90 (1). When exposed to the tamoxifen metabolite, 4-OHT, the relationship between CreERT2 and Hsp90 is disrupted (2) and CreERT2 can move into the nucleus (3). Here, CreERT2 recognises loxP sites flanking exons 2 and 7 in *GLUL* and excises this portion (4), thereby causing inactivating truncation of the gene in endothelial cells (5) (Feil et al., 2009; Kim et al., 2018).

### 2.2.2.2 VEGS Hom

Mice with tamoxifen-inducible endothelial-specific deletion of *GLUL* were obtained from Professor Peter Carmeliet (KU Leuven, Belgium), and for the purposes of this project are referred to as 'VEGS Hom'. Generation of this model was achieved through crossing VE-Cadherin<sup>CreERT2</sup> mice with *GLUL*<sup>flx/flx</sup> mice. These 2 lines were created as previously outlined by Benedito et al. (2009) and He et al. (2010), respectively.

A breeding cage with a *GLUL*<sup>flx/flx</sup> male and 2 VEGS Hom females was maintained, producing either *GLUL*<sup>flx/flx</sup> or VEGS Hom offspring. *GLUL*<sup>flx/flx</sup> progeny were classed as littermate controls.

Mice were fed chow diet and treated with tamoxifen at 6 weeks of age. The tamoxifen schedule consisted of a single injection per mouse, given daily over 5 consecutive days. When the additional impact of diabetes was investigated, STZ injections were administered at 8 weeks of age, with each animal receiving a single daily dose of STZ for 5 consecutive days. Unless otherwise stated, all VEGS Hom experiments were conducted between 10–14 weeks of age. The breeding plan and experimental schedule are outlined in Figure 2.2 and Figure 2.4, respectively.

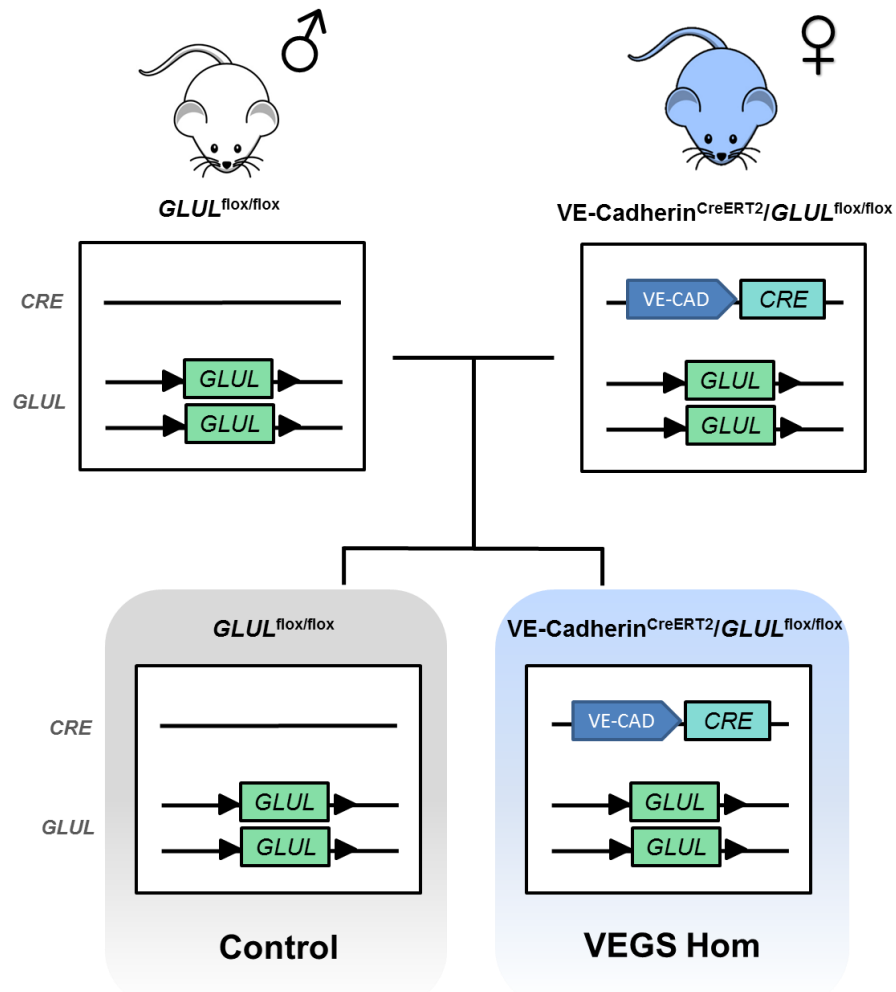


### Figure 2.2 VEGS Hom breeding strategy

VEGS Hom was maintained by a breeding trio of a male with 2 floxed  $GLUL$  alleles, but no Cre recombinase expression ( $GLUL^{flox/flox}$ ), and 2 VEGS Hom females. This produced offspring at a predicted ratio of 50%  $GLUL^{flox/flox}$  to 50% VEGS Hom.  $GLUL^{flox/flox}$  comprised the control group.

Dark blue 'VE-CAD' arrows followed by light blue  $CRE$  boxes indicate the presence of the CreERT2 recombinase DNA sequence downstream of the VE-Cadherin promoter region, thus enabling CreERT2 expression in endothelial cells. Black arrows represent loxP sites, and therefore a 'floxed allele'. The  $GLUL$  gene is shown by green boxes labelled ' $GLUL$ '.

### 2.2.2.3 VEGS Het

Mice with inducible endothelial-specific GS haploinsufficiency, named 'VEGS Het', were created by the crossing of VEGS Hom with C57BL/6J mice. This strategy gave rise to either VEGS Het offspring or to progeny expressing loxP sites on one *GLUL* allele, but no Cre recombinase (*GLUL*<sup>flox/+</sup>). The latter genotype served as control mice for VEGS Het experiments.

Mice were maintained on chow diet and received tamoxifen injections at 6 weeks of age. A single injection was administered daily to each mouse over 5 consecutive days. All experiments were carried out between 10–14 weeks of age. Figure 2.3 outlines the breeding strategy and the experimental schedule is shown in Figure 2.4.

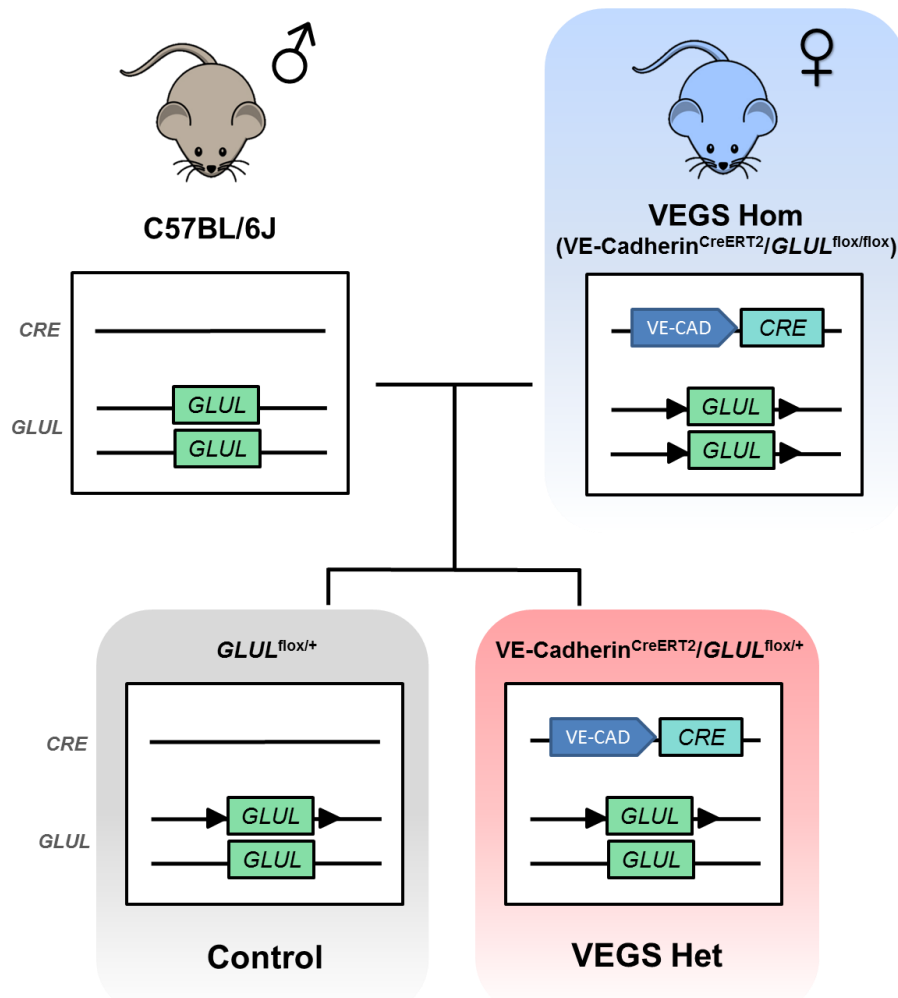


### Figure 2.3 VEGS Het breeding strategy

The strategy for VEGS Het consisted of a C57BL/6J male and 2 VEGS Hom females, producing a predicted 50% of offspring with Cre recombinase under the VE-CAD promoter and 1 floxed *GLUL* allele, therefore giving a model of endothelial *GLUL* haploinsufficiency. The remaining 50% inherited 1 floxed *GLUL* allele, but no Cre recombinase (*GLUL*<sup>flox/+</sup>). These animals were considered control mice for VEGS Het experiments.

Dark blue 'VE-CAD' arrows followed by light blue *CRE* boxes indicate the presence of the CreERT2 recombinase DNA sequence downstream of the VE-Cadherin promoter region, so allowing CreERT2 expression in endothelial cells. Black arrows represent loxP sites, and therefore a 'floxed allele'. The *GLUL* gene is shown by green boxes labelled '*GLUL*'.

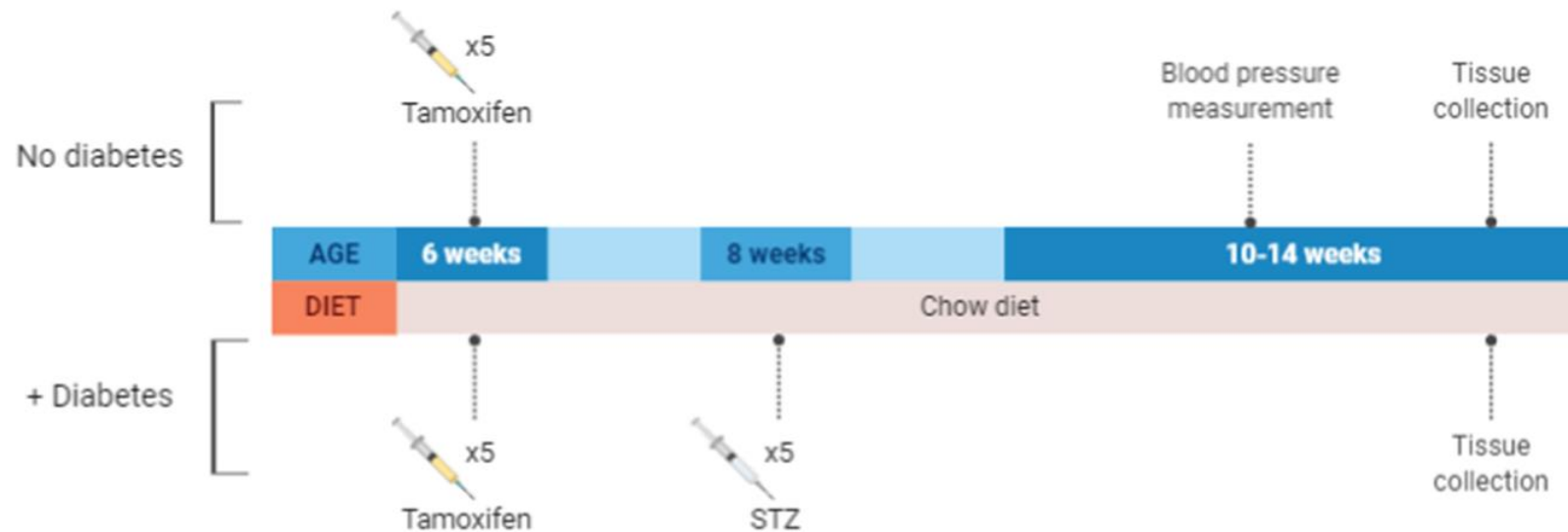


**Figure 2.4 VEGS Hom and VEGS Het experimental schedule**

Mice from both VEGS Hom and VEGS Het colonies followed the same schedule. Tamoxifen injections were given at 6 weeks of age, with a single injection administered per mouse occurring daily over 5 consecutive days. Experimental procedures were undertaken between 10–14 weeks of age. In the subset of mice in which diabetes was induced, STZ injections were administered at 8 weeks of age, with each animal receiving a single daily STZ injection over 5 consecutive days. Mice received chow diet for the entirety of the study.

#### 2.2.2.4 VEGA

To assess the effect of reduced endothelial GS expression on atherosclerosis development, both VEGS Het and VEGS Hom mice were crossed with mice deficient in ApoE (*ApoE*<sup>-/-</sup>). Mice with unaltered *ApoE* expression are highly resistant to atherosclerosis, even after high-fat feeding (Lo Sasso et al., 2016). This led to the creation of the *ApoE*<sup>-/-</sup> model in 1992 by 2 different laboratories. These mice exhibit accelerated atherosclerosis when fed a high-cholesterol 'western diet', allowing a more accurate recapitulation of a human atherosclerotic phenotype (Getz & Reardon, 2016).

##### 2.2.2.4.1 VEGS Het/*ApoE*<sup>-/-</sup> (VEGA Het)

To generate VEGS Het/*ApoE*<sup>-/-</sup> mice, (referred to as 'VEGA Het'), a VE-Cadherin<sup>CreERT2</sup>/*ApoE*<sup>-/-</sup> male was crossed with a *GLUL*<sup>flox/+</sup>/*ApoE*<sup>-/-</sup> female. This approach produced offspring with the following genotypes: VEGA Het; VE-Cadherin<sup>CreERT2</sup>/*ApoE*<sup>-/-</sup>, *GLUL*<sup>flox/+</sup>/*ApoE*<sup>-/-</sup> and *ApoE*<sup>-/-</sup>. VEGA Het and *GLUL*<sup>flox/+</sup>/*ApoE*<sup>-/-</sup> were the experimental and control animals, respectively.

Tamoxifen was administered following the same schedule as that used for VEGS Hom (section 2.2.2.2) and VEGS Het (section 2.2.2.3). Animals received chow diet until 8 weeks old, at which time they were switched to western diet (21% fat from lard supplemented with 0.15% cholesterol). Tissue was collected at 20 weeks of age. The breeding strategy for VEGA Het is shown in Figure 2.5. The experimental timeline is depicted in Figure 2.8.

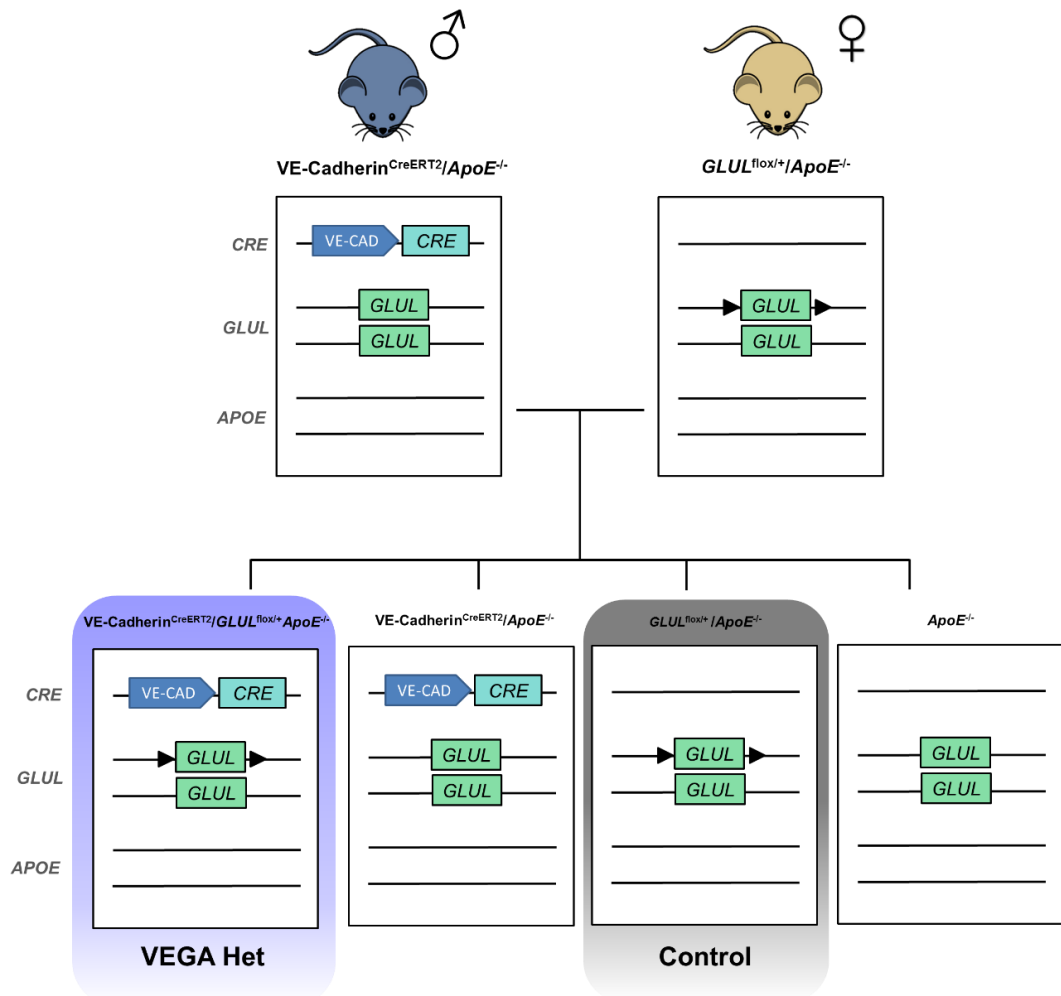


### Figure 2.5 VEGA Het breeding strategy

VEGA Het was established through breeding an *ApoE*<sup>-/-</sup> male expressing endothelial Cre recombinase (VE-Cadherin<sup>CreERT2</sup>/ApoE<sup>-/-</sup>) and *ApoE*<sup>-/-</sup> females with 1 floxed *GLUL* allele (*GLUL*<sup>flox/+</sup>/ApoE<sup>-/-</sup>). Around 25% of the offspring were therefore positive for both VE-CAD-CreERT2 and carried 1 floxed *GLUL* allele; all offspring were fully deficient in *ApoE*.

Dark blue 'VE-CAD' arrows followed by light blue *CRE* boxes indicate the presence of the CreERT2 recombinase DNA sequence downstream of the VE-Cadherin promoter region, so allowing CreERT2 expression in endothelial cells. Black arrows represent loxP sites, and therefore a 'floxed allele'. The *GLUL* gene is shown by green boxes labelled 'GLUL'.

#### 2.2.2.4.2 VEGS Hom/ApoE<sup>-/-</sup> (VEGA Hom)

'VEGA Hom' were created by first crossing a *GLUL*<sup>flox/+</sup>/*ApoE*<sup>-/-</sup> male and VEGA Het female, as depicted in Figure 2.6. To increase the likelihood of generating VEGA Hom progeny, a second colony was then established with a VEGA Hom male and *GLUL*<sup>flox/flox</sup>/*ApoE*<sup>-/-</sup> females. This latter breeding strategy enabled approximately 50% of offspring to be of the VEGA Hom genotype (Figure 2.7).

Tamoxifen was administered following the same schedule as that used for VEGS Hom (section 2.2.2.2) and VEGS Het (section 2.2.2.3). Chow diet was provided until 8 weeks old, at which time mice were switched to western diet. Tissue collection took place at 20 weeks of age.

Where mice were treated with STZ to induce diabetes, injections were administered at 8 weeks of age, following the same protocol employed for VEGS Hom, as outlined in section 2.2.2.2. The experimental schedule for VEGA Hom is shown in Figure 2.8.

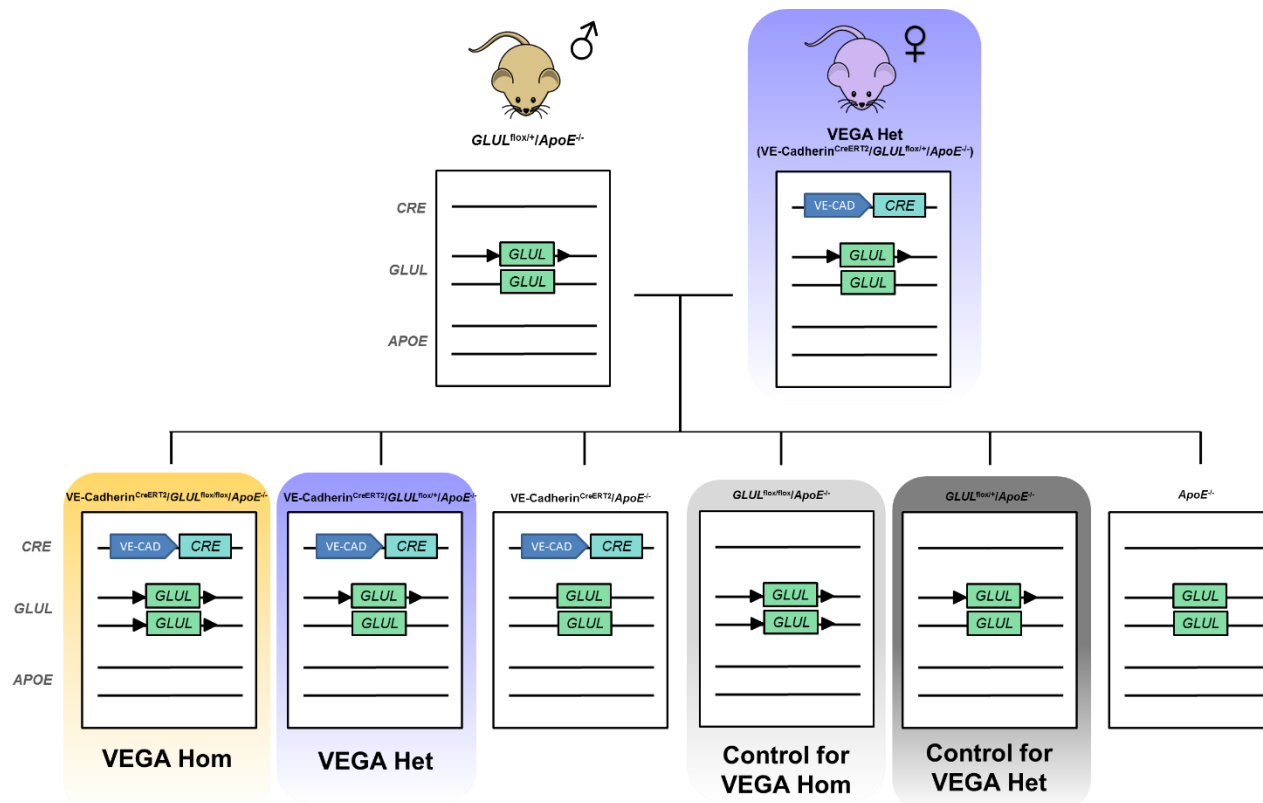


### Figure 2.6 VEGA Hom breeding strategy (Stage 1)

VEGA Hom mice carry VE-CAD-CreERT2 and have loxP sites flanking both  $GLUL$  alleles, in addition to being  $ApoE^{-/-}$ . To produce an adequate number of VEGA Hom mice, initial breeding required 2 steps. The first stage involved crossing a  $GLUL^{fllox/+}/ApoE^{-/-}$  male and VEGA Het female, allowing for 16.6% of offspring to be of the VEGA Hom genotype. Dark blue 'VE-CAD' arrows followed by light blue  $CRE$  boxes indicate the presence of the CreERT2 recombinase DNA sequence downstream of the VE-Cadherin promoter region, therefore allowing CreERT2 expression in endothelial cells. Black arrows represent loxP sites, and therefore a 'floxed allele'. The  $GLUL$  gene is shown by green boxes labelled ' $GLUL$ '.

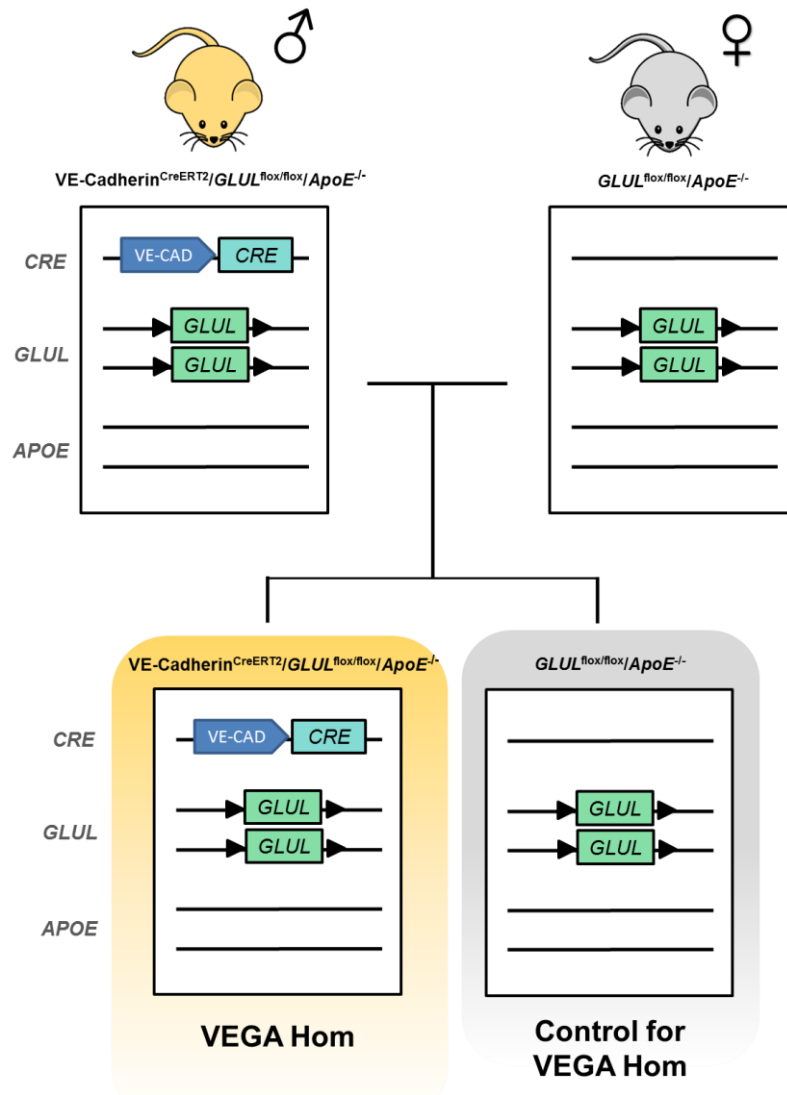


### Figure 2.7 VEGA Hom breeding strategy (Stage 2)

The second stage of establishing VEGA Hom was completed through a breeding trio of a VEGA Hom male and two *ApoE*<sup>-/-</sup> females carrying 2 floxed *GLUL* alleles. Approximately half of their progeny were VEGA Hom, with the remainder being *GLUL*<sup>flox/flox</sup>/*ApoE*<sup>-/-</sup>, which served as littermate controls.

Dark blue 'VE-CAD' arrows followed by light blue *CRE* boxes indicate the presence of the CreERT2 recombinase DNA sequence downstream of the VE-Cadherin promoter region, thereby allowing CreERT2 expression in endothelial cells. Black arrows represent loxP sites, and therefore a 'floxed allele'. The *GLUL* gene is shown by green boxes labelled '*GLUL*'.

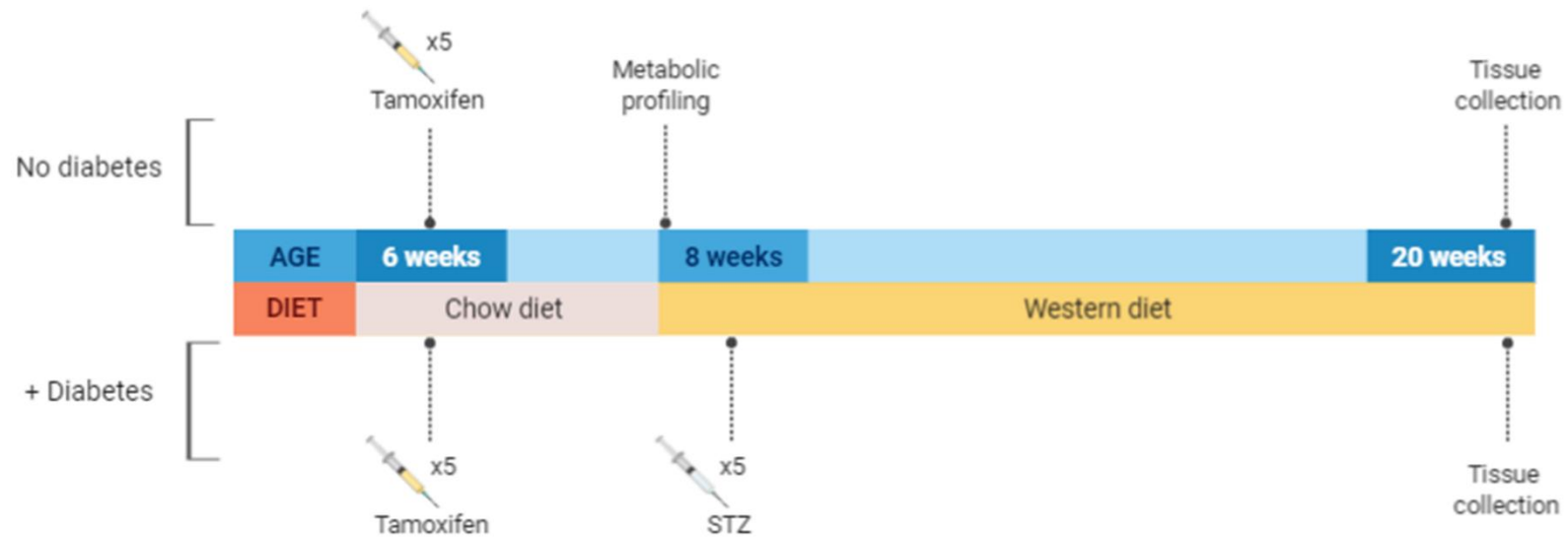


**Figure 2.8 VEGA Het and VEGA Hom experimental schedules**

Tamoxifen injections were administered to all VEGA Het and VEGA Hom mice at 6 weeks of age, with each animal receiving a single daily injection over 5 consecutive days. At 8 weeks old, all mice were switched from chow to western diet, and selected animals were given STZ injections for the study of diabetes. STZ-treated mice were injected daily with a single STZ dose for 5 consecutive days. Metabolic profiling was conducted on those not receiving STZ at 8 weeks of age. Tissue was collected at 20 weeks of age for all mice.

### **2.2.3 Tamoxifen preparation and induction**

Tamoxifen powder was added to corn oil, to achieve a final concentration of 10 mg/mL. Incubation at 60°C for 3–4 hrs was undertaken to aid dissolution, upon which the solution was aliquoted and stored at -20°C for no longer than 2 months.

Due to its potential teratogenic effects, all handling of tamoxifen solutions was conducted in a designated fume hood, using double-gloves. Since tamoxifen is light-sensitive, vials used for preparation and storage were wrapped in foil.

Injections were carried out daily over 5 consecutive days at 40 mg/kg and were administered in a single dose intraperitoneally using 0.5 mL U-100 insulin syringes. This was performed in a designated area at the University of Leeds animal facility, using protective gowns and double gloves.

### **2.2.4 STZ preparation and administration**

50 mL 0.1 M sodium citrate was prepared by dissolution of sodium citrate tribasic dihydrate powder in distilled H<sub>2</sub>O. 50 mL 0.1 M citric acid was also made with citric acid monohydrate dissolved in distilled H<sub>2</sub>O. 33 mL of 0.1 M sodium citrate and 17 mL of 0.1 M citrate were mixed to make 0.1 M citric buffer. The pH was adjusted to 4.0–4.5 before filter sterilisation.

STZ administration was undertaken in the designated animal facility at the University of Leeds. Injections were given daily over 5 consecutive days. On the days of injection, non-fasting blood glucose (NFBG) was measured. A small tail score was made using a sterile scalpel blade and <5 µL blood was applied to a blood glucose meter recording strip and read using a glucometer. Animal weight was also recorded. Mice were then fasted for 6 hrs, with access to water at all times. At the end of the fast, STZ powder was dissolved in the citric buffer to give a final STZ concentration of 12.5 mg/mL. This solution was kept on ice while syringes were prepared. STZ was administered via a single intraperitoneal injection at a dose of 50 mg/kg. 10% sucrose solution was given during the injection period to prevent fatal hypoglycaemia (Tesch & Allen, 2007). The development of diabetes was monitored over the following 4 weeks,

with weekly weight and NFBG readings taken. Mice were considered diabetic if NFBG values exceeded 11.1 mmol/L.

## **2.2.5 Mouse liver endothelial cell isolation**

### **2.2.5.1 Tissue preparation and single cell suspension**

Animals were euthanised by cervical dislocation, followed by a midline sternotomy incision and removal of the heart. Whole liver was carefully dissected and placed in a bijoux tube containing ice-cold Hank's Balanced Salt Solution (HBSS). Specimens underwent thorough mincing in petri dishes to a pulp-like consistency using scalpel blades, before transfer to falcon tubes containing 10 mL collagenase type II solution made to 1 mg/mL in HBSS. Samples were incubated for 45 mins at 37°C with constant agitation using a MACSmix rotator. Repeat pipetting with a 5 mL stripette and a 14G cannula was then used to achieve a single cell suspension. This was passed through a 70 µm cell strainer and washed with 8 mL PBS-BSA solution. This wash buffer consisted of PBS without CaCl<sub>2</sub> or MgCl<sub>2</sub> and 0.5% BSA, which was diluted from a sterile 7.5% BSA stock solution. Samples underwent centrifugation at 100 g for 5 mins. Supernatant was removed by aspiration and the cell pellet was washed with 5 mL PBS-BSA. This centrifugation step and supernatant removal was repeated and the sample pellet was re-suspended in 500 µL PBS-BSA.

### **2.2.5.2 Magnetic bead coating**

The protocol for isolating murine liver endothelial cells (LECs) was modified from Sobczak et al. (2010). Endothelial cells are selected using magnetic beads conjugated to an anti-CD146 antibody. CD146 or 'cluster of differentiation 146', is a protein found on the membrane of endothelial cells and is involved in cell adhesion (Wang & Yan, 2013). Cell suspensions are incubated with CD146 LSEC microbeads, which label endothelial cells, and then passed through a MiniMACS filtering column assembled in a magnetic MACS separator. The magnetic field of the separator equipment allows for labelled endothelial cells to be kept within the column, while unlabelled cells

pass through. Upon removal from the magnetic MACS separator, the retained CD146 positive cells can be eluted (Miltenyi Biotec 2019). The principle is depicted in Figure 2.9.

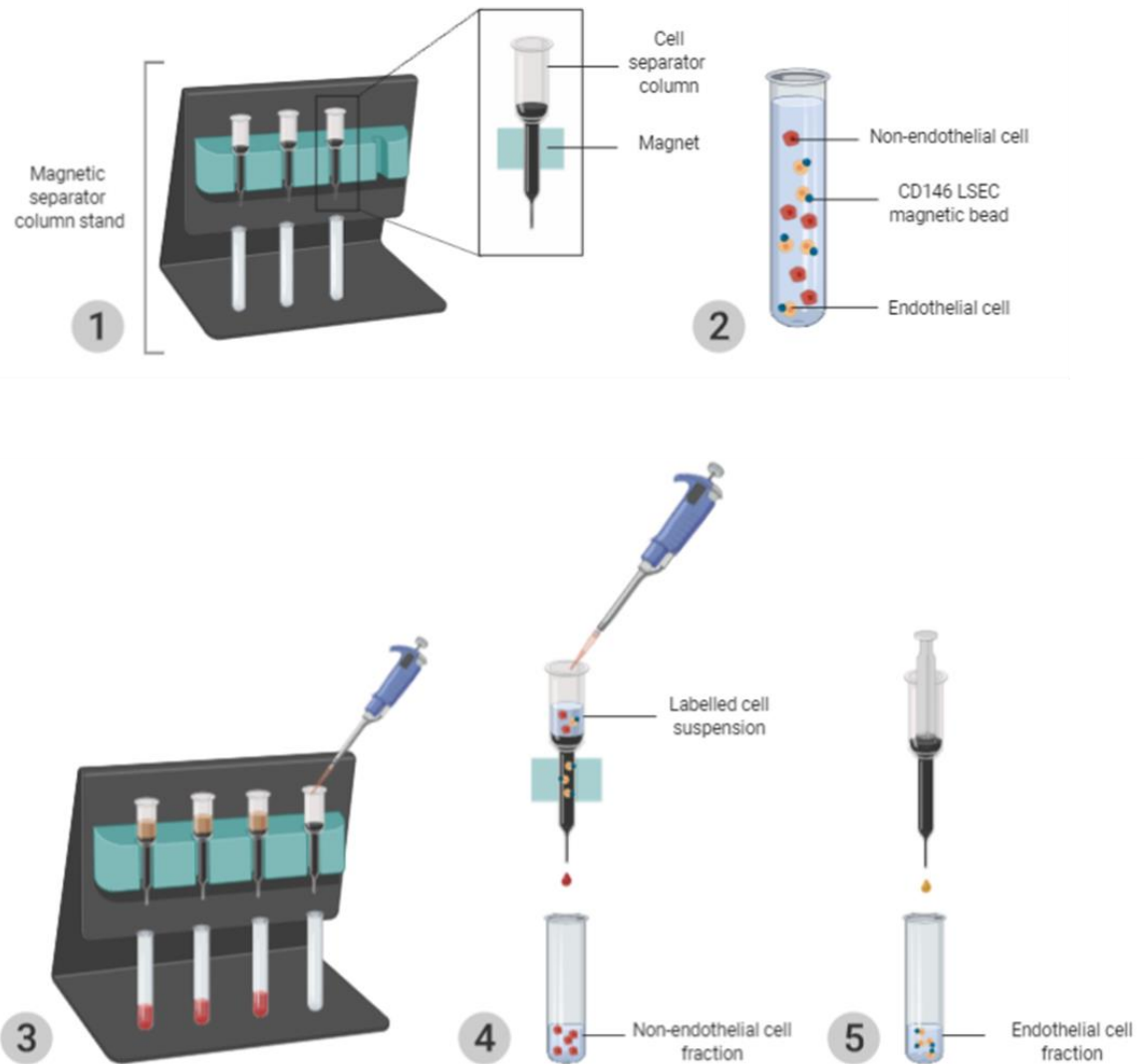


### Figure 2.9 Magnetic bead cell separation

Cell separator columns are held within a magnetic separator stand (1). For labelling of endothelial cells, CD146 LSEC microbeads were added to cell suspensions (2). Treated suspensions were applied to columns (3), where the magnetic field of the stand traps the magnetic beads and therefore labelled cells. Non-magnetic, non-target cells move through the column and are collected as the non-endothelial cell fraction (4). Columns are removed from the magnetic stand and flushed to collect endothelial cells in a new tube (5).

### **2.2.5.3 Cell isolation**

15  $\mu\text{L}$  anti-CD146 antibody-coated magnetic beads was pipetted into the 500  $\mu\text{L}$  cell suspensions, before incubation at  $4^{\circ}\text{C}$  for 20 mins using a MACSmix rotator. A further 500  $\mu\text{L}$  PBS-BSA was then added, followed by centrifugation at 1500 g for 5 mins. The supernatant was aspirated and cell pellets were suspended in 500  $\mu\text{L}$  PBS-BSA. MiniMACS columns were positioned in a magnetic MACS separator and primed with 500  $\mu\text{L}$  PBS-BSA. Each sample was filtered through an individual column. Once each suspension had drained, 500  $\mu\text{L}$  PBS-BSA was applied to the columns. This step was repeated another 4 times to give a total of 5 PBS-BSA washes. Columns were removed from the separator, placed into 15 mL falcons and flushed mechanically using MiniMACS column plungers and 500  $\mu\text{L}$  PBS-BSA. This solution was considered the endothelial cell fraction. To increase sample purity, this eluted solution underwent centrifugation at 1500 g for 5 mins with the resulting supernatant removed and the cell pellet re-suspended in 500  $\mu\text{L}$  PBS-BSA, before being applied to a new MiniMACS column and washed again with 5 PBS-BSA washes. Columns were then taken from the stand and flushed with 500  $\mu\text{L}$  PBS-BSA, before another 5 min centrifugation step of 5 mins and supernatant removal.

When required for RT-qPCR, the resulting cell pellet was mixed with 500  $\mu\text{L}$  of TRI-Reagent. If protein was to be analysed, the pellet was re-suspended in 100  $\mu\text{L}$  cell extraction buffer.

### **2.2.5.4 Culturing of mouse liver endothelial cells**

If the endothelial fraction was to be cultured, pellets were re-suspended and maintained in MV2 media containing MV2 supplement mix and 5 mL antibiotic antimycotic solution (AAS). After being seeded onto culture plates coated with 0.1% gelatin, LECs were kept at  $37^{\circ}\text{C}$  and 5%  $\text{CO}_2$ . Media was changed every 48 hrs. Unless otherwise stated, experiments with LECs were undertaken when cells reached 95% confluence. If LECs were required for experimentation involving serum starvation, culture was carried out using MV2 media containing 5 mL AAS and 0.2% foetal bovine serum (FBS).

### 2.2.6 RNA extraction

Cell or tissue samples were treated with TRI-Reagent, before centrifugation at 13,300 g at 4°C for 10 mins. The resulting supernatant was transferred to a new Eppendorf tube and 50 µL bromochloropropane was added, with thorough mixing achieved using vortex equipment. Samples were left at room temperature for 15 mins and then centrifuged at 13,300 g for 15 mins at 4°C, allowing for the separation of DNA, RNA and protein. Samples were placed on ice and the RNA layer was carefully transferred to a new Eppendorf tube. A volume of isopropanol equal to that of the extracted RNA layer was added and samples were mixed by vortexing, before incubation on ice for 10 mins. Centrifugation at 13,300 g was undertaken at 4°C for 20 mins to pellet RNA. The supernatant was discarded and the RNA pellets were resuspended in 70% ethanol. Samples were then centrifuged at 13,300 g for 2 mins. The ethanol was removed and pellets were dissolved thoroughly in 20 µL DNase/RNase free H<sub>2</sub>O. RNA quantification was performed using a DS-11 FX spectrophotometer.

### 2.2.7 DNase digestion

The DNA-free™ DNA Removal Kit was used to remove any potential contaminating DNA from RNA samples. Each 20 µL RNA sample was treated with 2.4 µL 10x DNase I buffer and 1 µL rDNase I and gently mixed before incubation for 1 hr at 37°C. 4 µL DNase Inactivation Reagent was then added to each sample and incubated at room temperature for 5 mins. Tubes underwent centrifugation at 13,300 g at 4°C for 2 mins before careful transfer of the supernatant into new Eppendorf tubes. Samples were then kept at -80°C.

### 2.2.8 Reverse transcription

Complimentary DNA (cDNA) was created using the LunaScript RT Supermix Kit. 1 µg RNA samples were added to PCR tubes, along with 4 µL LunaScript RT Supermix (5x) and made to a final reaction volume of 20 µL using nuclease-free water. Control reactions containing either no RNA template or

DNase/RNase free H<sub>2</sub>O alone were also carried out. Samples were mixed and quickly centrifuged before incubation in a DNA Engine Tetrad 2 Peltier Thermal Cycler using the conditions outlined in Table 2.2. If not used immediately, the resulting cDNA was stored at -20°C.

**Table 2.2 Thermocycler conditions for reverse transcription of RNA samples using the LunaScript RT Supermix Kit**

Cycle step	Temperature	Time	Cycles
Primer annealing	25°C	2 mins	1
cDNA synthesis	55°C	10 mins	
Heat inactivation	95°C	1 min	

### 2.2.9 Real-time quantitative polymerase chain reaction (RT-qPCR)

SYBR Green I fluorescent probes and LightCycler 480 equipment were used to conduct RT-qPCR reactions. SYBR Green I has excitation and emission wavelengths of 497 and 520 nm, respectively. As double stranded DNA complexes are created during the PCR reaction, SYBR Green I probes bind to them and fluoresce. Intercalation of SYBR Green I with double stranded DNA causes a near 1000-fold increase in fluorescence (Bio-Rad Laboratories 2019). With further PCR cycling, SYBR Green I continues to bind and fluorescence accumulates. The level of this fluorescence is recorded and since it is proportional to the amount of cDNA that has been amplified, it is used to quantify relative DNA concentrations.

For each RT-qPCR reaction, total final volume was 20 µL, consisting of 10 µL PrecisionPLUS qPCR Master Mix containing SYBR green dye, 1µL forward primer, 1 µL reverse primer, 7 µL nuclease free H<sub>2</sub>O and 1 µL cDNA. Primer sequences and RT-qPCR conditions are listed in Table 2.3 and Table 2.4, respectively.

**Table 2.3 RT-qPCR primer sequences, respective melting temperature and product lengths**

Gene	Primer sequence (5'-3')	Melting temperature (°C)	Product size (base pairs)	Supplier
Mouse <i>GLUL</i>	Fwd: CGGAAACCTGCAGAGACCAA	60.25	120	Integrated DNA Technologies
	Rev: GTGGCCGTCTGTTCCATAA	60.04		
Mouse <i>HPRT</i>	Fwd: GTTGGGCTTACCTCACTGCT	59.96	125	
	Rev: TAATCACGACGCTGGGACTG	59.83		

**Table 2.4 RT-qPCR cycling conditions**

Cycle step	Temperature	Time	Cycles
Pre-incubation	95°C	10 mins	1
Amplification	95°C	15 secs	45
	54°C	1 min	
Cooling	37°C	Hold	

## **2.2.10 Protein analysis**

### **2.2.10.1 Aorta homogenisation**

Animals were euthanised by cervical dislocation, followed by a midline sternotomy incision and removal of the heart. The aorta was exposed and carefully dissected from the aortic arch to the renal arteries using fine curved forceps and iris scissors, before being collected in Eppendorf tubes. These were immediately placed into liquid nitrogen, before storage at  $-80^{\circ}\text{C}$ . When specimens were required for homogenisation, thawing was undertaken on ice. Each sample was then dissected into 3–4 mm pieces to aid homogenisation and transferred to a 2mL safe-lock Eppendorf tube containing 200  $\mu\text{L}$  cell extraction buffer with protease and phosphatase inhibitors. A 7 mm stainless steel bead was added to each sample. Tubes were inserted into a tissue homogeniser set at 25.0 Hz for 2 mins. This was repeated twice. The resulting lysates were pipetted into new Eppendorfs, centrifuged at 13,300 g for 10 mins at  $4^{\circ}\text{C}$  and the supernatants collected.

### **2.2.10.2 Protein quantification**

Protein quantification was achieved with the Pierce™ BCA Protein Assay Kit. The assay uses the Biuret reaction and bicinchoninic acid (BCA) as the detection method for protein. The former involves the reduction of  $\text{Cu}^{2+}$  to  $\text{Cu}^{+}$  by protein in an alkaline environment. Two BCA molecules then react with the resulting  $\text{Cu}^{+}$  to produce a purple-coloured complex, which displays a strong absorbance at 562 nm (Thermo Scientific 2019).

Protein samples were treated with kit reagents to generate the purple reaction product. Using plate reader equipment, absorbance values at 562 nm were measured and compared to a BSA standard curve with a range of 0–2000  $\mu\text{g}/\text{mL}$  for determination of protein levels.

### **2.2.10.3 Western blotting**

NuPAGE™ 4–12% Bis-Tris Protein Gels (1.5 mm) were used for all western blot experiments. Protein samples were prepared by mixing protein

supernatant, distilled H<sub>2</sub>O, sample buffer (4x) and dithiothreitol reducing agent (10x), before heating at 95°C for 5 mins. Gels were immersed in Novex™ Tris-Glycine SDS running buffer and samples were loaded into the gel wells, alongside Color Prestained Protein Standard ladder (11–245 kDa). Electrophoresis was carried out for 90 mins at 160V. Protein was transferred to PVDF membranes, pre-treated with methanol, using a Trans-Blot Turbo Machine. Adequate protein transfer was verified by treatment of the membrane with Ponceau S stain for 5 min at room temperature. Ponceau S was removed with washing in distilled H<sub>2</sub>O. Membranes were then blocked with 5% BSA in Tris Buffered Saline with Tween-20 (TBS-T) for 1 hr at room temperature. Exposure to primary antibodies was conducted overnight at 4°C. Primary antibody information and dilutions are described in Table 2.5. After 3 washes with TBS-T, membranes were incubated with appropriate secondary antibodies (Table 2.6) in 5% BSA at room temperature for 1 hr, before a further set of 3 TBS-T washes.

**Table 2.5 Summary of primary antibodies used for protein analysis**

Primary antibody	Dilution	Species raised in	Supplier	Product code
GS	1:1000	Mouse	Sigma	WH0002752M1
eNOS		Mouse	BD Biosciences	610297
Phospho-eNOS (s1177)		Rabbit	Cell Signaling Technology	9571
β-actin		Mouse		4970

All dilutions were made in 3% BSA in TBS-T with 0.02% NaN<sub>3</sub>

**Table 2.6 Summary of secondary antibodies used for protein analysis**

Secondary antibody	Dilution	Species raised in	Supplier	Product code
Anti-mouse HRP	1:5000	Sheep	GE Healthcare Life Sciences	NA931
Anti-rabbit HRP		Donkey		NA934

#### 2.2.10.4 Protein visualisation and analysis

The Immobilon Western Chemiluminescent HRP Substrate Kit was used for chemiluminescence detection and membranes were imaged with G:BOX equipment and GeneSys software. Analysis of protein bands was carried out with ImageJ software. Band intensities were measured and background intensity of the membrane deducted. Sample intensity values were then normalised to that of the  $\beta$ -actin loading control. For re-probing of membranes, stripping buffer was applied for 15 mins at room temperature. This was removed with 3 washes with TBS-T. The western blotting protocol was then repeated from the stage of blocking with 5% BSA.

#### 2.2.11 Organ bath

I performed the majority of organ bath experiments, with training by Stacey Galloway, Peysh Patel and Asjad Visnagri, who also helped to conduct the initial experiments. All tissue mounting was carried out by Thomas Slater.

##### 2.2.11.1 Principle

Organ bath systems are used regularly in cardiovascular research to analyse vasomotor function of contractile tissues in a tightly controlled physiological environment. Tissue samples are mounted onto triangular opposing wires and suspended in chambers containing 10 mL Krebs-Henseleit solution. One wire is connected to a support, while the other is connected to a force transducer

which records tension responses of the attached tissue. To maintain tissue viability, chambers are bubbled with 95% O<sub>2</sub> and 5% CO<sub>2</sub>, and fixed within a water bath heated to 37°C, as depicted in Figure 2.10.

Constriction and dilation of aortic tissue is regulated by multiple signalling pathways, which can be manipulated pharmacologically within the organ bath to study vessel response. The data presented in this thesis was generated using an established organ bath protocol with phenylephrine (PE), Ach, L-N<sup>G</sup>-monomethyl arginine (L-NMMA), sodium nitroprusside (SNP) and catalase (Wheatcroft et al., 2004; Viswambharan et al., 2017). Representative traces are shown in Figure 2.11.

PE is an α<sub>1</sub>-adrenoceptor agonist and was used to induce vasoconstriction. Upon interaction with PE, α<sub>1</sub>-adrenoceptors stimulate PLC, which evokes a rise in intracellular Ca<sup>2+</sup> and contraction of VSMCs (Hrometz et al., 1999). Ach was applied to examine endothelial-dependent vasodilatory response. Its activation of muscarinic cholinergic receptors on the endothelial membrane causes eNOS-mediated NO production by promoting calmodulin activity (Zhao et al., 2015). SNP also induces vasodilation, but acts as a NO donor, rather than an eNOS activator. For this reason, it was employed to assess endothelial-independent relaxation of aortic rings in response to exogenous NO (Hottinger et al., 2014).

For investigation of basal NO production in vasomotor response, the arginine derivative and competitive NOS inhibitor L-NMMA was used (Víteček et al., 2012). Catalase, which breaks down H<sub>2</sub>O<sub>2</sub> to H<sub>2</sub>O and O<sub>2</sub>, was employed in a similar fashion to evaluate the potential impact of H<sub>2</sub>O<sub>2</sub> on vasomotor function (Alfonso-Prieto et al., 2009).

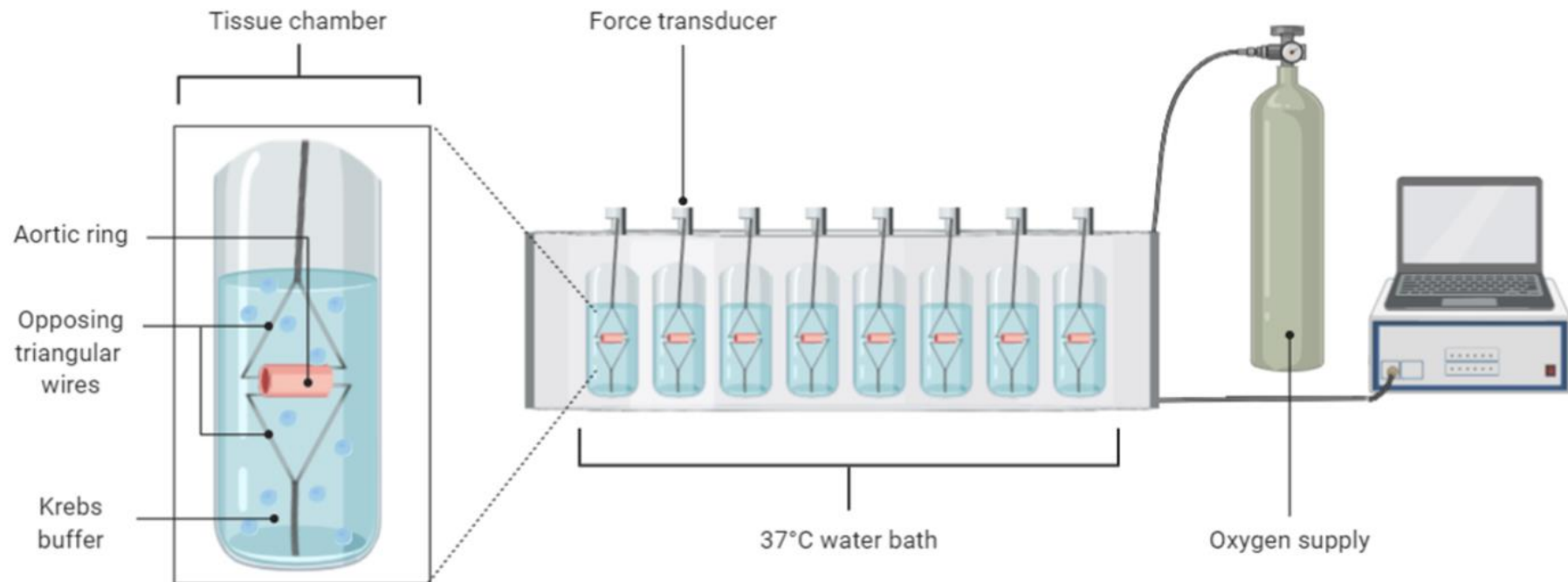


### Figure 2.10 Organ bath apparatus

The equipment is composed of 8 chambers fixed within a large water bath heated to 37°C, each supplied with 95% O<sub>2</sub> and 5% CO<sub>2</sub>. Aortic rings are positioned in the chambers by opposing triangular wires. Chambers contain Krebs-Henseleit buffer, into which pharmacological agents can be injected. Tension responses of the tissue are detected by a force transducer.

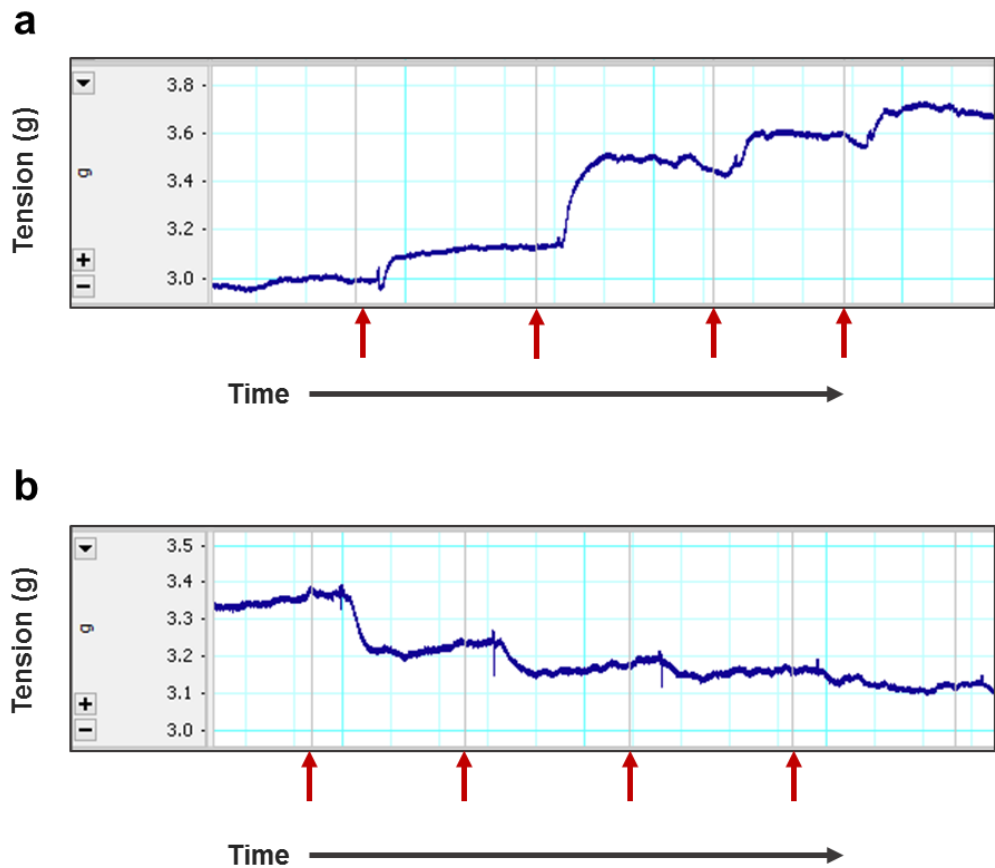


**Figure 2.11 Representative traces of murine aortic vasomotor responses measured using organ bath equipment**

Each trace displays raw data from an individual aortic ring. A step-wise increase in tension induced following incremental doses of a vasoconstrictor would be observed as depicted in a. A typical vasorelaxation response to increasing concentrations of a vasodilator is shown in b. Red, upward arrows indicate when doses of respective compounds were applied.

### **2.2.11.2 Tissue collection**

Aortae were harvested following euthanasia using a chamber with increasing concentrations of CO<sub>2</sub> and then removal of the heart. The vessel was dissected from the aortic arch to the renal arteries and then placed on ice in Krebs-Henseleit solution.

### **2.2.11.3 Preparation of aortic rings**

Using a SZ61 light microscope, connective and perivascular adipose tissue were removed from the aorta. Samples were divided into 3–5 mm rings and mounted onto the triangular opposing wires of the organ bath apparatus. Aortic rings were placed under a tension of 0.5 g, which was increased in increments of 0.5 g every 5 mins, until a final resting tension of 3 g was reached. Tissue was allowed to equilibrate for 20 mins before chambers were emptied of Krebs solution and replaced with 10 mL KCl (40 mM) to verify tissue viability. KCl removal was achieved by 3 washes with fresh Krebs. Rings which did not exhibit  $\geq 10\%$  constriction after 2 KCl treatments were excluded.

### **2.2.11.4 Endothelial-dependent vasodilation**

Rings were re-equilibrated to 3 g resting tension and then pre-constricted with PE at a final bath concentration of 300 nM. Samples were exposed to stepwise incremental concentrations of Ach (1 nM – 10  $\mu$ M). Tension values were recorded and used to generate a dose-response curve. Tissue was washed with fresh Krebs and equilibrated back to 3 g tension.

### **2.2.11.5 Endothelial-regulated vasoconstriction**

Aortic rings were exposed to stepwise incremental concentrations of PE (1 nM – 10  $\mu$ M) and dose-response curves were constructed. Tissue was washed with Krebs to remove PE from the chamber and assessment of either NO or H<sub>2</sub>O<sub>2</sub> availability was conducted. For analysis of NO production, the aforementioned PE treatment was repeated after 1 hr incubation with L-NMMA. If study of H<sub>2</sub>O<sub>2</sub> was required, catalase (1250 U/ml) was added to each

chamber instead of L-NMMA and immediately followed by the PE treatment regimen. Tensions were recorded and dose-response data was generated.

#### **2.2.11.6 Endothelial-independent vasorelaxation**

Following examination of endothelial-regulated vasoconstriction and the effect of L-NMMA or catalase, samples were not washed with Krebs solution, but were instead treated with increasing concentrations of SNP (1 nM – 10  $\mu$ M) and dose-response data was gathered.

#### **2.2.12 Metabolic testing**

Glucose tolerance tests (GTTs) and insulin tolerance tests (ITTs) were conducted following a period of fasting, taking place overnight or for 2 hrs, respectively. Mice had unrestricted access to water at all times during both fasting and experimentation.

Animal weights and fasting blood glucose concentrations were documented. Sterile scalpel blades were used to make a small tail score. <5  $\mu$ L blood was analysed using a blood glucose meter recording strip and a glucometer. For GTTs, 20% glucose solution was injected intraperitoneally at a dose of 1 mg/g. For ITTs, insulin was also administered intraperitoneally, at a concentration of 0.75 IU/kg. Blood glucose measurements were taken at 30, 60, 90 and 120 mins post glucose or insulin injection. Mice were observed throughout the experiment and transferred to clean cages with access to food and water *ad libitum* upon completion of testing. In the case of ITTs, 20% glucose solution and a heat chamber were available in the event that mice became symptomatically hypoglycaemic.

#### **2.2.13 Blood pressure measurements**

Tail cuff plethysmography was employed to record murine blood pressure, using the Coda Non-invasive Tail BP system. Experiments were conducted with conscious mice between 10–14 weeks of age. The system includes occluder and sensor cuffs, which prior to each use, were checked for

satisfactory inflation. If inadequate inflation was detected, the rubber bladders of the cuffs were replaced. Mice were placed in perspex restrainers and tail cuffs were fitted. To promote tail vasodilation, restrainers were positioned in a heat chamber programmed to 37°C. A pre-warming period of 10 mins was conducted before recording commenced. Each measurement session consisted of 10 acclimisation cycles, then 3 sets of measurements, each separated by 5 secs of recovery time. Animals underwent 3 sessions, the first and second allowing for habituation to the restrainer and cuff system, as well as the heated environment. Data was taken from the third experiment. Mice displaying signs of agitation were immediately removed from the equipment and measurements were attempted at a later date.

## **2.2.14 Histology**

### **Tissue collection**

Tissue was acquired under terminal anaesthesia. Animals were placed in an anaesthetic induction chamber supplied with oxygen at 2 L/min and 5% isoflurane. When appropriate anaesthesia was achieved, mice were carefully transferred to the operating table and placed in a supine position. Their heads were gently oriented into a nose cone, to which isoflurane was re-directed at a concentration of 3%. Once anaesthesia was verified by tail-tip stimulation, an incision was made along the linea alba and the vena cava exposed. Blood was obtained from the vessel using a 1 mL U-100 insulin syringe and a 27G needle and transferred to tubes kept on ice. The vena cava was then cut above the liver and 10 mL PBS was slowly injected via cardiac puncture, followed by slow perfusion of 5 mL 4% paraformaldehyde (PFA). Hearts were dissected and stored in plastic cassettes in 4% PFA. The aorta was revealed and carefully removed from the ascending aorta to the bifurcation into the iliac arteries, before being transferred to Eppendorf tubes containing 4% PFA.

## **2.2.15 Aortic sinus**

### **2.2.15.1 Processing and paraffin embedding**

Tissue underwent a process of dehydration with ethanol, followed by treatment with xylene in preparation for embedding in paraffin wax. All such processing was carried out at St James's University Hospital, Leeds. Tissue samples were embedded by Anna Skromna at University of Leeds using a TES 99 Paraffin Embedding Center.

### **2.2.15.2 Microtome sectioning**

The paraffin blocks of embedded tissue were placed on ice, before being inserted into the metal clamp of a Leica RM2235 microtome. A stainless steel blade was carefully inserted into the microtome blade holder. Blocks were trimmed at a cutting thickness of 20  $\mu\text{m}$  until tissue was exposed. This was then adjusted to 10  $\mu\text{m}$  until the inferior portion of the aortic root was reached, at which point the thickness was reduced to 4  $\mu\text{m}$ . Embedded samples were cut to create ribbons of 4–6 slices. These serial sections were gently lifted from the microtome blade using forceps and a fine paintbrush and transferred to a water bath, heated to 45–50°C. Ribbons were allowed to flatten for 15–20 secs before being picked up on SuperFrost Plus™ Adhesion slides. Slide edges were carefully tapped against tissue paper to remove excess water and left to dry at room temperature.

### **2.2.15.3 Miller van Gieson staining**

Miller van Gieson is an established staining technique for detecting elastic fibres. Following the protocol described below, elastin and cell nuclei are stained blue to black, collagen fibres appear pink to red and other cellular components stain yellow (Percival & Radi, 2016).

Slides were assembled in plastic staining racks before incubation at 80°C for 30 mins, followed by deparaffinisation. This was achieved through 3 separate 4 min treatments in 100% xylene solution with occasional agitation. Slides then underwent 3 washes in 100% ethanol, each wash lasting 3 mins, before being moved briefly into distilled H<sub>2</sub>O. Racks were wrapped in tissue and tapped to remove excess water. Samples were placed into 0.5% KMnO<sub>4</sub> for 10 mins. After another rinse in distilled H<sub>2</sub>O, slides were bleached with 2% oxalic acid for

2 mins, followed by a further distilled H<sub>2</sub>O wash. Racks were quickly dipped into 100% ethanol before Miller stain was applied for 2.5 hrs. Upon completion of Miller staining, samples were washed with 100% ethanol and then distilled H<sub>2</sub>O, prior to placement in van Gieson dye for 30 mins. Racks were again wrapped in tissue paper and excess stain was eliminated by tapping. A brief rinse in distilled H<sub>2</sub>O was performed, excess water was removed and racks were kept at 80°C for 45 mins. Following another 3 separate treatments in 100% xylene of 3 mins each, rectangular glass covers were fixed to slides using DPX mountant.

#### **2.2.15.4 Imaging and analysis**

A BX41 bright-field microscope with an eyepiece magnification of 10x was used for visualising aortic sinus sections at a further 40x magnification. Images were captured digitally using a QImaging QICAM Fast 1394 camera and analysed using Image-Pro Plus 7.0 software (Figure 2.12). The outer aortic wall was defined manually as the region of analysis. Atherosclerotic plaques within this area were also outlined manually (Figure 2.12b). Any manually defined regions on images are labelled with the abbreviation 'PG' for polygon. Mean aortic sinus plaque coverage was calculated as a percentage of the total sinus area and was determined by averaging 4 sections from each specimen, with sections separated by 40–60 µm.

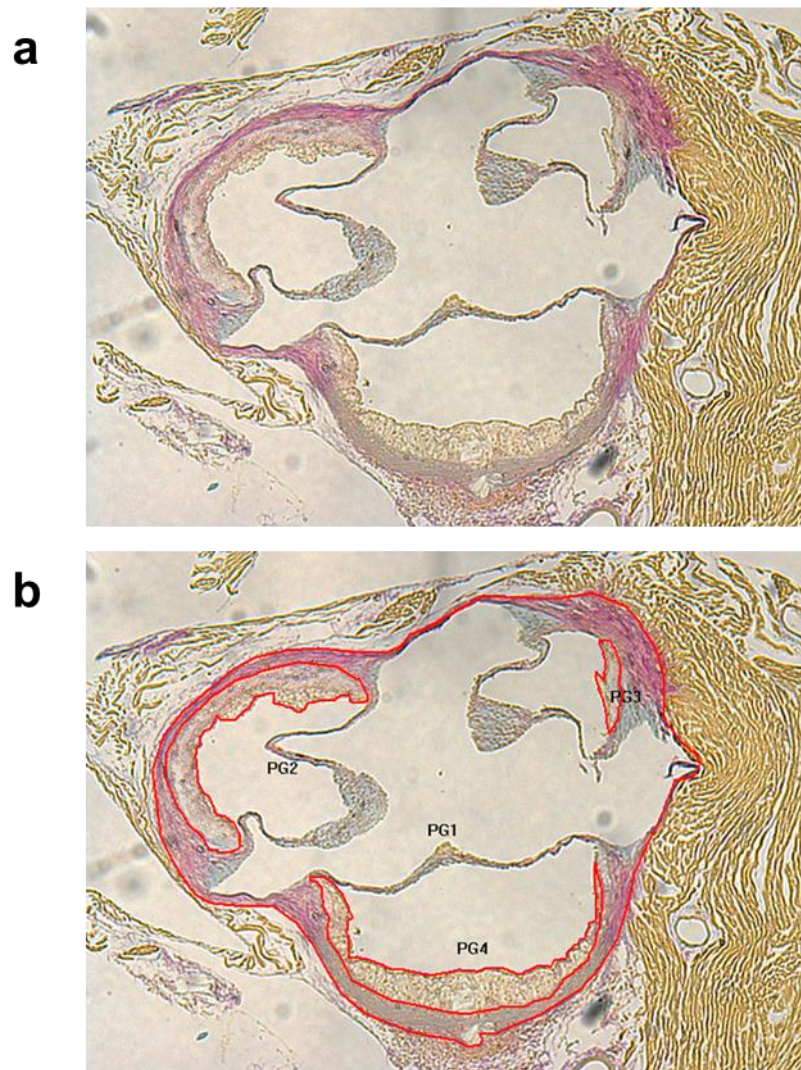


**Figure 2.12 Imaging of aortic sinus sections and assessment of atherosclerotic lesion coverage following Miller van Gieson staining**

A representative section is presented in (a). Elastic fibres and cell nuclei stain blue to black, collagen stains pink to red and other tissues appear yellow. Subsequent image analysis, which was carried out using Image-Pro Plus 7.0, is displayed in (b). The wall of the aorta was defined and lesions within this area were outlined. All these regions of interest are bordered in red. Total area of the sinus was calculated and the percentage covered by atherosclerosis was determined. 'PG' abbreviation stands for 'polygon'.

## **2.2.16 *En face* analysis of whole aorta**

### **2.2.16.1 Oil Red O staining**

Aortae were cleaned of surrounding connective and perivascular adipose tissue. Vessels were then cut longitudinally and the adventitia was removed; this stage was performed by Dr. Nadira Yuldasheva or Anna Skromna. Specimens were placed in distilled H<sub>2</sub>O for 1 min before transfer to tubes containing 60% isopropanol. These were incubated for 1 min with gentle inversion. Samples were removed from isopropanol, briefly placed against tissue paper to eliminate excess solution and then placed into Eppendorf tubes of oil red O dye. These were incubated at room temperature for 1 hr on electric tube roller equipment. Aortae were taken from the tubes, touched against tissue paper to remove excess dye and placed back into 60% isopropanol for 20 secs. Specimens were transferred to distilled H<sub>2</sub>O, before being mounted *en face* on a glass slide with a coverslip.

### **2.2.16.2 Imaging and quantification of atherosclerosis**

Aortae were visualised with a SZ61 dissecting microscope at 12x magnification and images captured using a QImaging QICAM Fast 1394 camera. Image-Pro Plus 7.0 was employed for quantification of plaques. The area of analysis was manually defined, with exclusion of the brachiocephalic artery, left common carotid artery and left subclavian artery. Within this area, regions stained by oil red O were highlighted by the program and were calculated as a percentage of the total aorta analysis area. Aortic length was also measured (Figure 2.13).

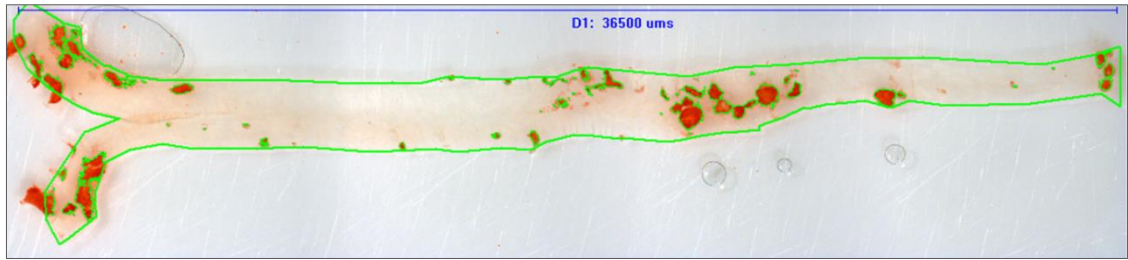


### **Figure 2.13 Quantification of atherosclerotic plaques**

Specimens were analysed using Image-Pro Plus 7.0 software. Vessel length was measured, as shown by the blue line, with the length value in  $\mu\text{m}$  displayed underneath. The area of analysis is outlined in green. Within the defined area of analysis, the software detected oil red O stained regions and these were quantified as a percentage of the analysis area.

## **2.2.17 Vascular injury**

All vascular injury surgery was performed by Dr. Nadira Yuldasheva.

### **2.2.17.1 Procedure conditions**

All operating procedures were conducted using recovery anaesthesia. Isoflurane was added to a vaporiser tank and delivered to mice via an induction chamber or a nose cone positioned on operating tables heated to 38°C. O<sub>2</sub> was supplied with isoflurane at 2 L/min. Mice were weighed and then transferred to the induction chamber. The isoflurane was released from the vaporiser at concentration of 5%. A loss of consciousness and a drop in respiratory rate indicated appropriate anaesthesia. Anaesthetic was re-directed from the chamber to the nose cone and animals moved to the operating table. Here, they were carefully placed in a supine position with their heads gently orientated into the cone and limbs were secured with surgical tape. Buprenorphine was given by intraperitoneal injection for analgesia. Isoflurane dose was then adjusted to 2.5% and an adequate level of anaesthesia was confirmed by tail-tip stimulation.

### **2.2.17.2 Arterial injury**

Surgery was performed using a OPMI 1-FC dissecting microscope. Fur was removed from the lower limbs using an electric shaver and the areas sterilised with 0.75% povidone-iodine solution. To expose the femoral artery, a small mid-thigh incision was made, followed by removal of subcutaneous tissues. Upon isolation from the neurovascular bundle, a Vicryl 8.0 suture thread was loosely tied around the femoral artery. A clamp was then attached to the bundle proximally. To prevent vasospasm, the femoral artery was treated with a drop of 1% lignocaine.

Iris scissors were used to make a small incision in the wall of the saphenous branch of the femoral artery and a 0.014 inch diameter Hitorque Cross-it 200XT angioplasty guide wire was inserted. The clamp was removed and the wire gently advanced along the vessel for 1.5–2 cm. It was then retracted to near the point of insertion, but not removed from the artery. This passage of the wire

was carried out a total of 3 times, before it was removed fully. To ligate the saphenous vessel, the suture was tightened. The incision site was closed using a continuous Vicryl 6.0 suture. A sham procedure (ie. the aforementioned operation without the insertion of the wire) was then undertaken on the contralateral lower limb. On completion of surgery, intraperitoneal injection of 300  $\mu$ L sterile Irripod saline was administered for hydration. Mice were transferred to cages on warming tables in a post-operative recovery area and closely monitored. A soaked diet was given for 24 hrs following the procedure and daily checks were conducted until the end of the experiment.

### **2.2.17.3 Assessment of endothelial regeneration**

#### **2.2.17.3.1 Evans Blue dye and tissue collection**

Femoral arteries were harvested 4 days after wire-injury surgery under terminal anaesthesia. An incision was made along the linea alba to expose the vena cava, into which 50  $\mu$ L 5% Evans Blue dye was injected. Evans Blue dye binds to albumin, which cannot pass an intact endothelium. However, in conditions where the endothelium has been damaged or its permeability has increased, albumin, and so Evans Blue, can move across to underlying tissue. The degree of endothelial denudation can therefore be assessed by the area of the harvested vessel that is stained blue (Radu & Chernoff, 2013).

Perfusion fixation was performed 3 mins after injection of Evans Blue dye using 4% PFA. This was administered into the left ventricle with a 27G needle. Femoral arteries were then removed up to the bifurcation of the aorta and stored in 4% PFA. Vessels were cleaned of any surrounding tissue under light microscopy with a SZ61 dissecting microscope, before being mounted *en face* on glass slides with coverslips

#### **2.2.17.3.2 Imaging and analysis**

A QImaging QICAM Fast 1394 camera was used for imaging at 20x magnification. The region of analysis was always 5 mm in length, beginning 5 mm from the aortic bifurcation. Using Image-Pro Plus 7.0 software, blue-

stained areas (and so areas of endothelial denudation) were demarcated and quantified as a percentage of the 5 mm region of analysis (Figure 2.14).

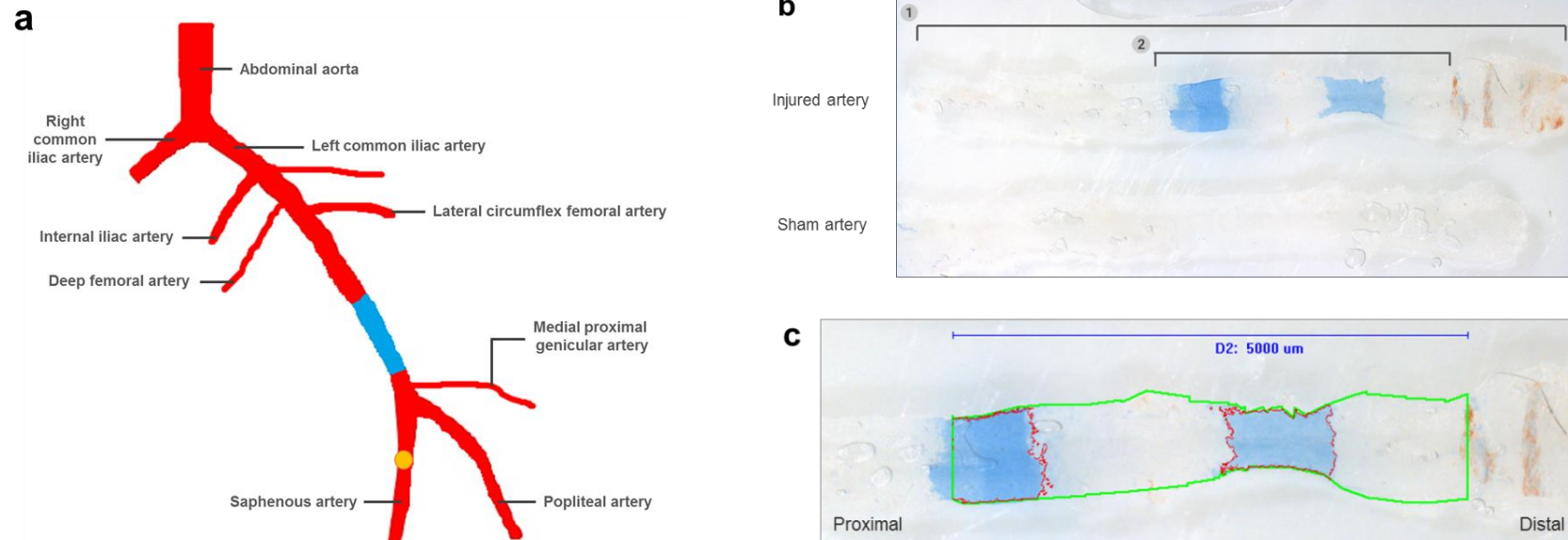


### Figure 2.14 Visualisation and analysis of femoral arteries following wire-injury surgery

Schematic diagram illustrating the vasculature of the murine hindlimb (a) and adapted from Aref et al. (2019). The area of endothelial denudation achieved with wire-injury surgery is highlighted in blue. The guidewire entry point is marked by the yellow circle. In (b), bracket 1 encompasses the harvested injured vessel from the origin of the common femoral artery to the femoral artery bifurcation. Bracket 2 highlights the 5 mm injured area of analysis, which begins 5 mm from the origin of the common femoral artery. Regions stained blue indicate endothelial denudation and areas of endothelial regeneration appear white. The sham vessel is from the contralateral vessel from the same mouse. Since the wire was not inserted into this artery, it exhibits an undamaged, white endothelium. In (c), the area of analysis marked by the green line begins 5 mm from the origin of the common femoral artery and is 5 mm long. Regions stained blue and outlined in red, were detected by Image-Pro Plus 7.0 software and quantified as a percentage of the area of analysis. This data was then used to calculate the percentage of endothelial regeneration present in the vessel.

### **2.2.18 Nitrite/nitrate (NO<sub>x</sub>) measurement**

Total nitrite/nitrate (NO<sub>x</sub>) concentration in murine serum was analysed using a Nitrite/Nitrate Colorimetric Assay Kit. The kit uses the principle of the Griess reaction to determine the levels of NO<sub>x</sub>. Any nitrate in samples is first converted to nitrite via the action of nitrate reductase, before addition of Griess reagents which transform nitrite to a purple azo compound. The absorbance is recorded using a plate reader and NO<sub>x</sub> concentrations can be determined (Cayman Chemical 2019).

To reduce haemoglobin background absorbance, mouse serum was applied to 10 kDa spin columns and centrifuged at 14,000 g for 10 mins at 4°C. Samples were then kept on ice. A nitrate standard curve was prepared on a 96 well flat clear bottom plate using a nitrate standard and assay buffer provided in the kit, to give a final nitrate concentration range of 0–35 µM. Undiluted, filtered serum samples were added to the plate. A cofactor mix and nitrate reductase enzyme, also supplied in the kit, were injected into wells. Plates were then incubated at room temperature for 3 hrs. Griess reagents were applied before a further incubation at room temperature for 10 mins. Absorbance values were measured at 550 nm using a plate reader.

### **2.2.19 Human umbilical vein endothelial cell culture**

Pooled donor samples of HUVECs were stored as 1 mL aliquots in liquid nitrogen. When required for experiments, aliquots were thawed in a water bath at 37°C and added to 9 mL of M199 cell culture media containing 20% serum, which was pre-prepared as described in Table 2.7. HUVECs were grown to 80–90% confluence before passage.

Passaging was performed through removal of media, one PBS wash, followed by 5 min incubation with 0.25% trypsin-EDTA to detach cells. M199 media was then added to neutralise trypsin-EDTA action. Cell counting was performed at this stage using a haemocytometer.

HUVECs were seeded accordingly onto plates coated with 0.1% gelatin. Where HUVECs were maintained for future experiments, cells were passed on into

T75 flasks, with a full media change every 48 hrs and kept at 37°C and 5% CO<sub>2</sub>. HUVECs were utilised at full confluence for experiments, unless stated otherwise. Where experiments required a period of serum starvation, HUVEC culture was carried out with M199 media containing 2% serum, as outlined in Table 2.7.

**Table 2.7 Preparation of M199 media for HUVEC culture**

Component	Volume	
	Standard conditions	Serum starvation
M199 media	370 mL	465 mL
FBS	100 mL	10 mL
1 M HEPES solution	10 mL	10 mL
AAS	5 mL	5 mL
Endothelial cell growth supplement (ECGS)	2.5 mL	-
100 mM sodium pyruvate solution	10 mL	10 mL
1000 U/mL heparin	2.5 mL	-

Reduction of GS activity in HUVECs was achieved through treatment with methionine sulfoximine (MSO). The compound is a known, irreversible inhibitor of GS. This inhibition is thought to occur through phosphorylation of MSO by GS, allowing it to occupy the glutamate and ammonia binding sites (Ronzio & Meister, 1968). An established treatment strategy of 1 mM MSO for 24 hrs was conducted in HUVEC experiments (Eelen et al., 2018).

## **2.2.20 Immunofluorescence**

All antibodies, dyes and working dilutions used for immunofluorescent staining are listed in Table 2.8.

### **2.2.20.1 eNOS- $\beta$ -actin staining**

0.1% gelatin coated glass coverslips were placed into wells of 24 well plates. HUVECs were seeded onto the coverslips at a density of  $0.7 \times 10^5$  cells per well to achieve 100% confluency. MSO or a vehicle of DNase/RNase free H<sub>2</sub>O were added to the media 4 hrs post-seeding. After 24 hrs, 4% PFA was added to the media and incubated for 10 mins at 37°C, followed by 3 washes with PBS and 5 min incubation at room temperature in 0.1% Triton. Coverslips were washed again 3 times in PBS, before blocking with 5% donkey serum for 1 hr at 4°C. eNOS primary antibody was applied and kept overnight at 4°C. The primary antibody was removed with 3 PBS wash steps and anti-mouse DyLight 549 secondary antibody was added. Plates were protected from light and placed at room temperature for 1 hr. Following a further 3 PBS washes, coverslips were incubated at 4°C overnight with phalloidin pre-conjugated to Alexa Fluor 647. Plates were wrapped in foil to avoid exposure to light. 2 PBS wash steps were conducted and coverslips were then mounted onto glass slides using DAPI Fluoromount-G. Slides were kept at 4°C and protected from light until the time of confocal imaging.

### **2.2.20.2 Confocal imaging and analysis**

Imaging and analysis was performed by Dr. Richard Cubbon to allow blinded assessment. Images were captured with a LSM880 confocal microscope using a 40x oil objective. ImageJ software was used for image analysis. At least 15 images were collected per condition, using appropriate excitation and emission parameters for DAPI, Alexa Fluor 549, and Alexa Fluor 647. The pinhole was set to generate a thickness of 0.9  $\mu$ m and z-stack of 4 slices was always collected before generating a maximum intensity projection. Cells were manually counted using the DAPI channel and the ImageJ 'Cell Counter' tool. F-actin and eNOS abundance were assessed using their respective mean

fluorescence intensities across the whole image. To define the co-localisation, the ImageJ 'Image calculator' function was employed to generate a new channel combining eNOS AND F-actin, which was used to define mean fluorescence intensity. Representative images are presented in Figure 2.15.

**Table 2.8 Summary of antibodies and dyes used for immunofluorescent staining**

Reagent	Target	Species raised in	Dilution	Supplier	Product code
eNOS primary antibody	eNOS	Mouse	1:100	BD Biosciences	610297
anti-mouse DyLight 549 secondary antibody	Mouse IgG	Donkey		Novus Biologicals	NBP1-72933
Phalloidin Alexa Fluor 647	F-actin	n/a		Thermo Fisher Scientific	A22287

All dilutions were made in PBS

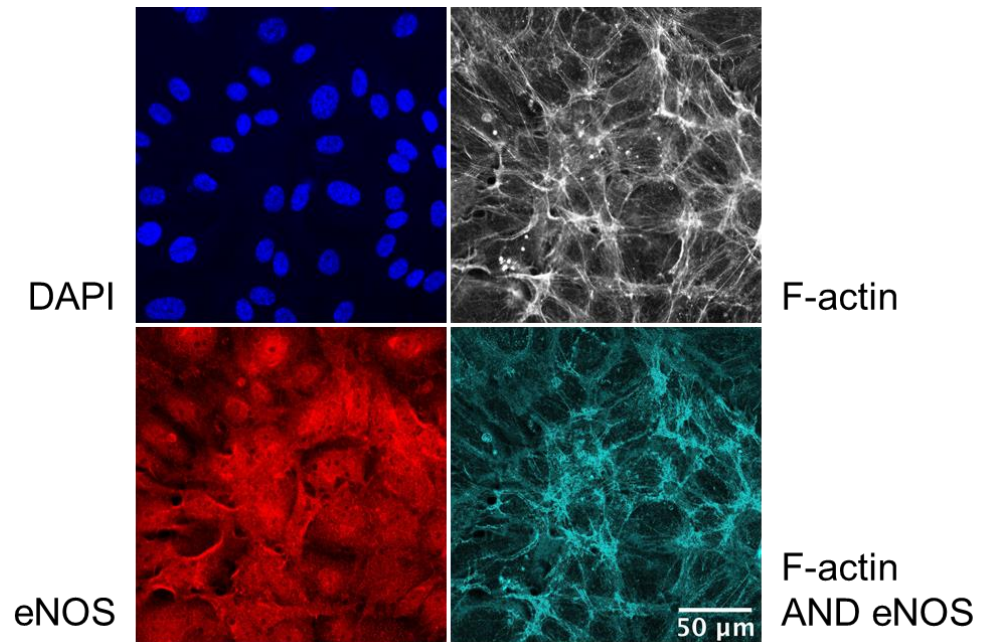


**Figure 2.15 Immunofluorescent staining of HUVECs**

Representative images of HUVEC culture stained positively for DAPI (blue), F-actin (white) and eNOS (red). The combined signal of F-actin and eNOS was also visualised (cyan).

## **2.2.21 eNOS activity assay**

### **2.2.21.1 Principle**

eNOS activity was evaluated with  $^{14}\text{C}$ -radiolabelled arginine. During eNOS-mediated production of NO, it enzymatically converts radioactive  $^{14}\text{C}$ -arginine to  $^{14}\text{C}$ -citrulline. Quantification of generated  $^{14}\text{C}$ -citrulline can therefore be deemed an indicator of eNOS activity.

The assay employs an ion exchange resin, which is composed of porous styrene beads, containing two types of ions. The first type possesses a particular electrical charge and is permanently attached to the beads. The second, or 'counter ion', is oppositely charged and is free to move from the beads when the resin is placed in a solution within which it is insoluble. This allows the counter ion to be exchanged for other similarly charged molecules. The DOWEX resin used for this project utilises  $\text{H}^+$  as the counter ion and is insoluble in water (Sigma-Aldrich 2020).

The principle of ion exchange allows for the removal of arginine from assay samples. Arginine has a strong positive charge at physiological pH and so binds to the DOWEX beads in place of  $\text{H}^+$ . Citrulline, however, is neutral and thus is left unbound in solution (Sigma-Aldrich 2020).

### **2.2.21.2 Quantification of eNOS activity**

Cells were seeded onto 6 well plates. With regard to HUVECs, these were then treated with either 1 mM MSO or vehicle control for 24 hrs. Cells underwent overnight serum starvation, before media was removed and replaced with HEPES-BSA buffer for 30 mins at  $37^\circ\text{C}$ .  $10\ \mu\text{L}$   $^{14}\text{C}$ -arginine ( $0.5\ \mu\text{Ci}/\text{mL}$ ) was then added to each well and incubated for 5 mins at  $37^\circ\text{C}$ .  $100\ \text{nM}$  insulin was applied to one well of each condition as a positive control and plates were returned to  $37^\circ\text{C}$  for a further 45 mins.  $1\ \text{mL}$  cold stopping buffer, which consisted of PBS containing  $4\ \text{mM}$  L-arginine and  $5\ \text{mM}$  EDTA, was gently injected into each well to stop the reaction. All solution was carefully removed and the previous step repeated. The stopping buffer was pipetted from wells again before addition of another  $500\ \mu\text{L}$ , within which cells were collected by

cell scraping. Plates were washed with a further 500  $\mu$ L stopping buffer per well and samples centrifuged at 1200 g for 6 mins. Disposal of the supernatant was followed by resuspension and denaturation of the cell pellet in 95% ethanol. After an overnight incubation at 4°C, ethanol was eliminated from samples using SpeedVac Vacuum Concentrator equipment for 25 mins. Resulting pellets were dissolved in 100  $\mu$ L 20 mM HEPES-Na<sup>+</sup> solution (pH 5.5), before centrifugation at 5000 g for 15 mins. Sample supernatant was then transferred to tubes containing 2.8 mL DOWEX resin, which had been mixed with distilled H<sub>2</sub>O at a 1:1 ratio, and pellets were re-suspended in 70  $\mu$ L cell extraction buffer containing protease and phosphatase inhibitors for protein quantification. The tubes containing resin and the sample supernatant were vortexed thoroughly, before incubation at room temperature for 15 mins. This incubation period allows resin beads to settle at the bottom of the tube. 1 mL of the soluble fraction above these beads was transferred to vials containing 10 mL scintillation cocktail. These were placed into a Tri-Carb 2800TR liquid scintillation analyser, which quantifies <sup>14</sup>C-labelled citrulline in disintegrations per minute or 'DPMI'. DPMI values were normalised to total protein content of respective cell pellets, which were determined using the Pierce™ BCA Protein Assay Kit as described in section 2.2.10.2. Results were then expressed as 'DPMI/total protein content'.

### **2.2.22 Data analysis and presentation**

All data are presented as mean  $\pm$  SEM. GraphPad Prism 8.1.0 software was used to produce all graphs. It was also employed to fit curves to organ bath data with the 'log(agonist) vs. response' or 'log(inhibitor) vs. response' functions, and to conduct statistical testing. Unless otherwise indicated, statistical testing assumed normal distribution.

When assessing if an interaction between 2 or more factors affected response data, a two-way repeated measures ANOVA was performed, followed by the Sidak post-hoc test. For comparison of 2 data sets, analysis was done using paired or unpaired Student's t-tests. If unequal variance was present, an unpaired t-test with Welch's correction was used. Statistical significance is shown by \* ( $p < 0.05$ ), \*\* ( $p < 0.01$ ) or \*\*\* ( $p < 0.001$ ). For data sets which required

calculation of area under the curve (AUC), these values were generated with the 'Integrate' tool in OriginPro 2019b.

With regard to mouse studies, experiments involved male mice only. Unless stated otherwise, investigations were not blinded or randomised.

' $n$ ' denotes the number of independent experiments. In the case of *in vitro* multi-well assays, ' $N$ ' represents the number of wells used for one condition within an independent experiment. All schematics were created using BioRender.

## Chapter 3 Results

### 3.1 The impact of endothelial GS holinsufficiency on the vasculature *in vivo*

The endothelium is a dynamic cellular monolayer comprising the innermost wall of blood vessels. It has a critical role in maintaining vascular homeostasis and its dysfunction is a classic feature of atherosclerosis and diabetes. Recently, it was established that the enzyme, GS, makes important contributions to endothelial cell biology, aside from its canonical function of manufacturing glutamine. Eelen et al. (2018) observed that endothelial GS expression levels heavily influence angiogenic processes. It is unknown, however, how it affects other aspects of vascular function.

The main aims of this chapter were to study a number of these other areas, including vasomotor response and endothelial regeneration. This was achieved by use of VEGS Hom, an endothelial-specific GS knockout murine model.

Tamoxifen-inducible deletion of GS in endothelial cells was conducted as previously described, through the crossing of VE-Cadherin<sup>CreERT2</sup> mice with *GLUL*<sup>flox/flox</sup> mice. The breeding strategy used for this model, or 'VEGS Hom', is depicted in Figure 2.2 and produced offspring of either the VEGS Hom or *GLUL*<sup>flox/flox</sup> genotype. The latter were used as control animals.

Body weights of VEGS Hom mice were recorded to ascertain if systemic metabolic perturbation resulted from endothelial GS knockout. This data was collected at the start and end of the 5-day tamoxifen injection course and then weekly until the time of experimentation. Control mice and VEGS Hom displayed similar weights prior to and post tamoxifen induction (Figure 3.1a). Weekly weights were also comparable from 7 weeks to 14 weeks of age (Figure 3.1b), with no significant differences witnessed between the genotypes (repeated measures ANOVA  $p=0.924$ ; AUC  $p=0.2516$ ).

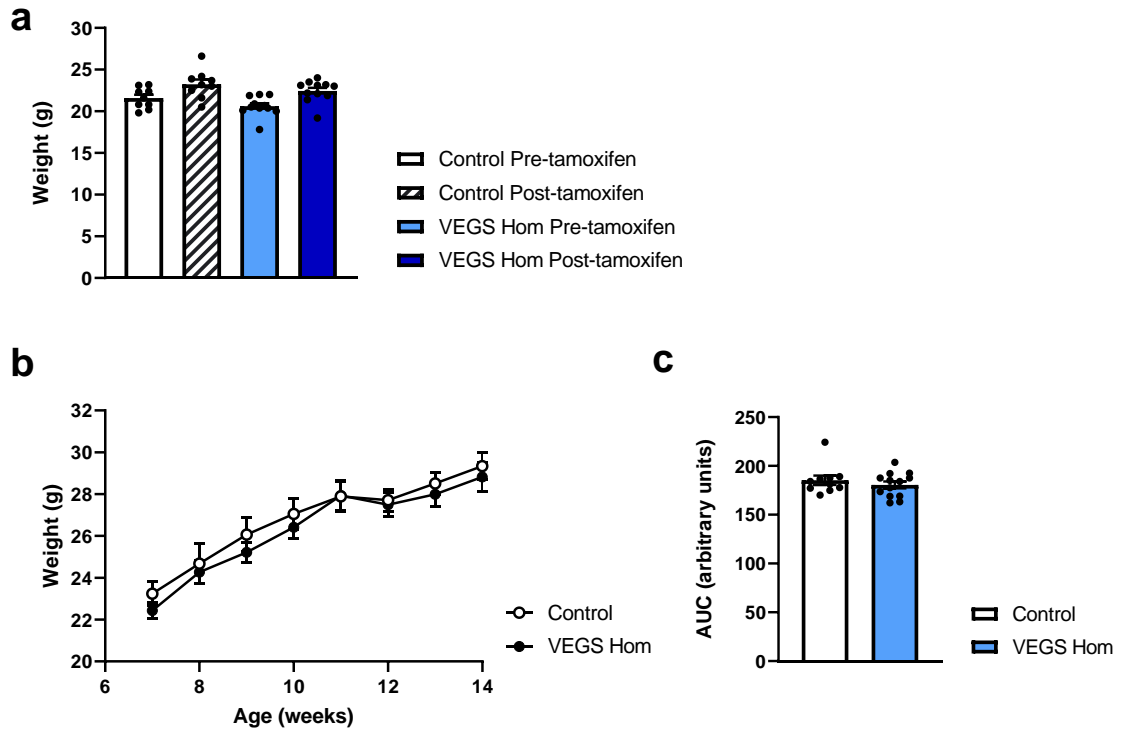


**Figure 3.1 Metabolic profile of VEGS Hom mice and control littermates**

Mean body weight of control and VEGS Hom mice at 6 weeks of age, pre and post 5-day tamoxifen treatment (control  $n=9$ , VEGS Hom  $n=11$ ) (a). Mean weekly weights of control and VEGS Hom mice were recorded from 7 to 14 weeks of age and overall change was evaluated using a repeated measures ANOVA and the Sidak post-hoc test (control  $n=11$ , VEGS Hom  $n=13$ ) (b). AUC was also calculated and tested using an unpaired t-test (c). In a and b, black circles represent individual data points.

A marked reduction in endothelial GS expression in VEGS Hom was documented by Eelen et al. (2018). To confirm an adequate decrease in GS mRNA expression for the work of this project, mouse LECs were isolated as outlined in section 2.2.5 and RT-qPCR analysis of GS mRNA was performed. HPRT was examined as the housekeeper gene, to which GS expression was normalised. A highly significant reduction in GS mRNA of 58.5% was noted in LECs collected from VEGS Hom compared to those from control mice ( $p=0.0001$ ), validating knockdown of endothelial GS in the VEGS Hom model (Figure 3.2). The residual GS expression may reflect GS mRNA from contaminating non-endothelial cells. It could also result from differences in tamoxifen efficiency between littermates, a phenomenon documented by other groups utilising endothelial-specific CreERT2 murine models (Payne et al., 2018).

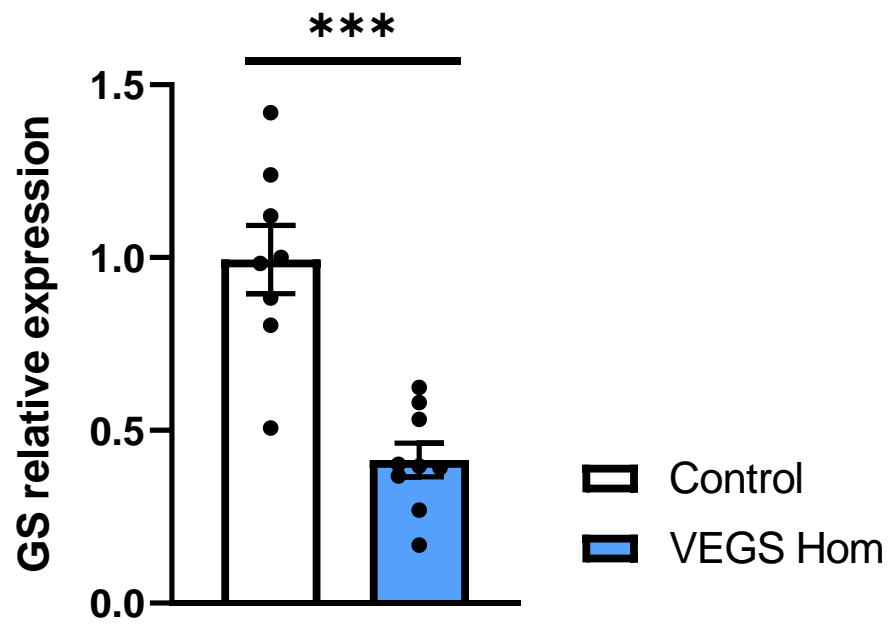


**Figure 3.2 Validation of GS knockdown in VEGS Hom endothelial cells**

Relative GS mRNA expression in LECs isolated from VEGS Hom mice and control littermates, determined with RT-qPCR. HPRT was used as the housekeeping gene. Black circles indicate values from individual LEC samples. Data was assessed using an unpaired t-test (\*\*\*) ( $p < 0.001$ ) (control  $n=8$ ; VEGS Hom  $n=9$ ).

The impact of endothelial GS deletion on vasomotor function has not previously been explored. Investigation was carried out as part of this project using organ bath apparatus as shown in Figure 2.10.

Vasoconstriction was examined using increasing concentrations of PE (Figure 3.3a). The mean maximum tension exerted by VEGS Hom aortic rings was  $0.61 \pm 0.08$  g, whereas that displayed by control mice was  $0.81 \pm 0.07$  g. The overall response to rising PE concentrations was statistically different between genotypes upon both repeated measured ANOVA testing ( $p=0.0002$ ) and analysis of AUC ( $p=0.028$ ). When PE treatment was repeated following incubation with the NOS inhibitor, L-NMMA (Figure 3.3b), vasoconstrictor responses were no longer significantly different (repeated measures ANOVA  $p=0.848$ ; AUC  $p=0.5185$ ), suggesting that NO bioavailability is elevated in aortic rings of VEGS Hom mice.

Aortic rings from VEGS Hom and control counterparts were also exposed to increasing concentrations of Ach to assess endothelial-dependent vasorelaxation (Figure 3.4a). Dose-response data was collected and AUC was analysed. Upon treatment with Ach, there was no significant difference in the relaxation response exhibited by VEGS Hom compared with control mice (repeated measures ANOVA  $p=0.192$ ; AUC  $p=0.2606$ ), suggesting that stimulated NO production is similar between genotypes. Additionally, it was important to evaluate endothelial-independent vasorelaxation, which was done using application of increasing concentrations of SNP; no significant change was recorded between responses of VEGS Hom and controls (Figure 3.4b).

The possibility of increased endothelial NO availability in VEGS Hom was also reflected in blood pressure measurements, with systolic (SBP), diastolic (DBP) and mean (MBP) blood pressure all markedly reduced in VEGS Hom mice versus controls (Figure 3.5). Average VEGS Hom SBP was  $101.3 \pm 2.6$  mm/Hg, compared with  $122.8 \pm 6.4$  mm/Hg in controls ( $p=0.014$ ). For DBP, VEGS Hom exhibited  $71.5 \pm 2.6$  mm/Hg, whereas controls were  $95.5 \pm 6.9$  mm/Hg ( $p=0.0119$ ). MBP was  $81.2 \pm 2.5$  mm/Hg for VEGS Hom and  $104.3 \pm 6.7$  mm/Hg for control littermates ( $p=0.0125$ ).

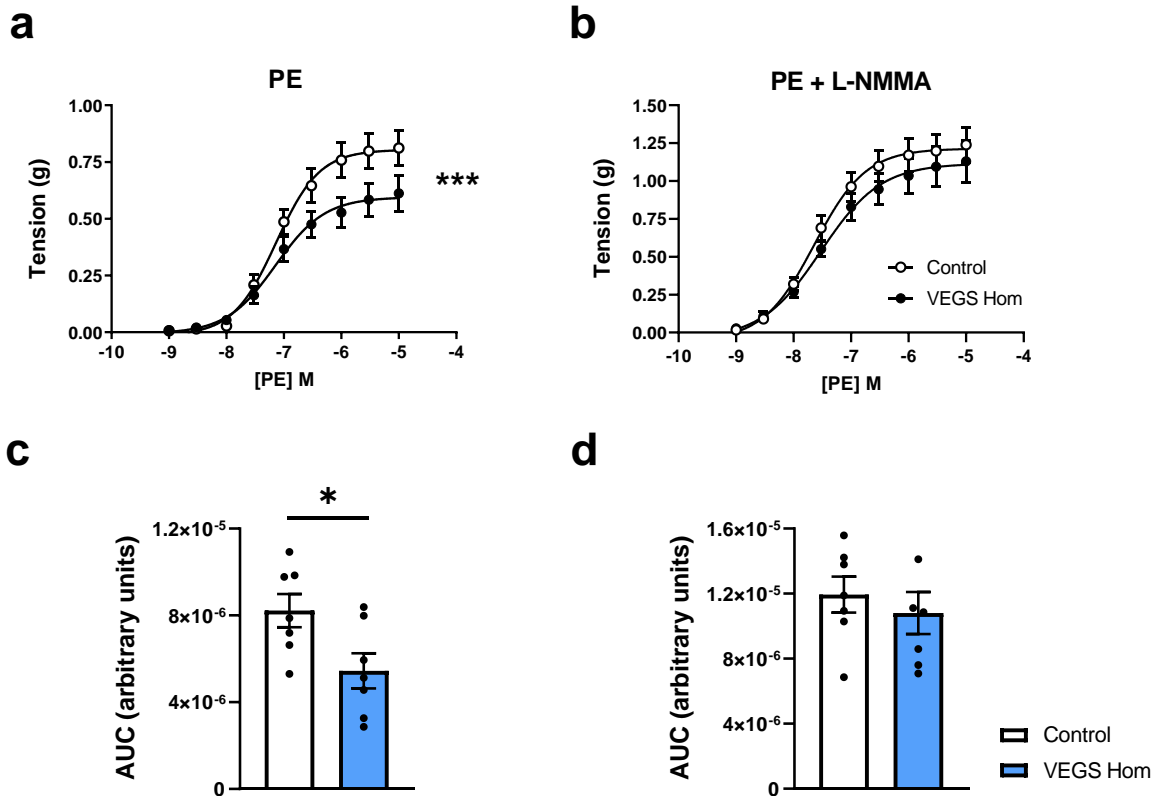


**Figure 3.3 Vasoconstriction of aortic rings from VEGS Hom and control mice following PE treatment with and without L-NMMA**

Aortic rings were treated with incremental doses of PE to induce vasoconstriction (a). This was repeated following incubation with NOS inhibitor L-NMMA (b). Dose-response data was assessed using a repeated measures ANOVA and the Sidak post-hoc test and tested the PE concentration x genotype interaction ( $***p < 0.001$ ). AUC was also calculated for PE (c) and PE with L-NMMA (d) treatments and analysed using an unpaired t-test ( $*p < 0.05$ ). In (c) and (d), black circles indicate data from individual mice. (Control  $n=7$ ; VEGS Hom  $n=7$ ).

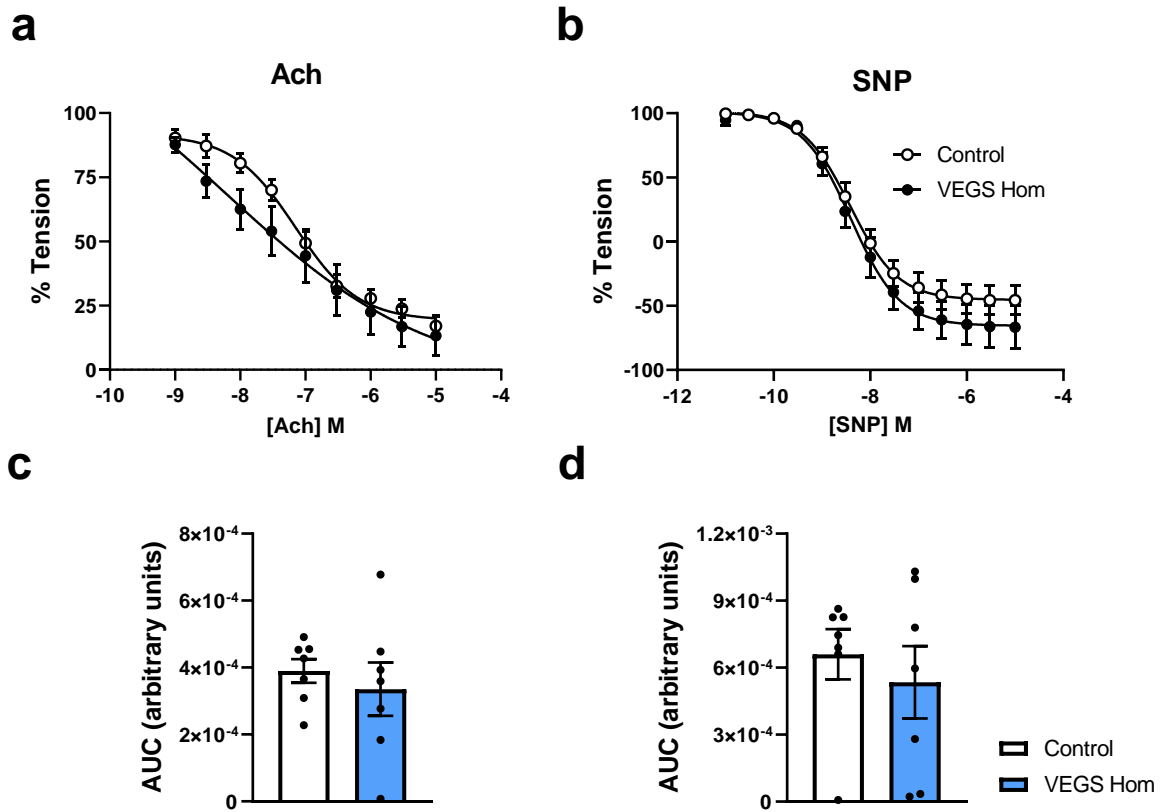


**Figure 3.4 Relaxation responses of aortic rings from VEGS Hom and control mice to Ach and SNP**

Tissue was pre-constricted with PE followed by incremental concentrations of Ach (a) or SNP (b). Dose-response data was assessed using a repeated measures ANOVA and Sidak post-hoc test. AUC of Ach and SNP responses were also calculated and analysed using an unpaired t-test (c and d respectively; black circles indicate individual data points). (Control  $n=7$ ; VEGS Hom  $n=7$ ).

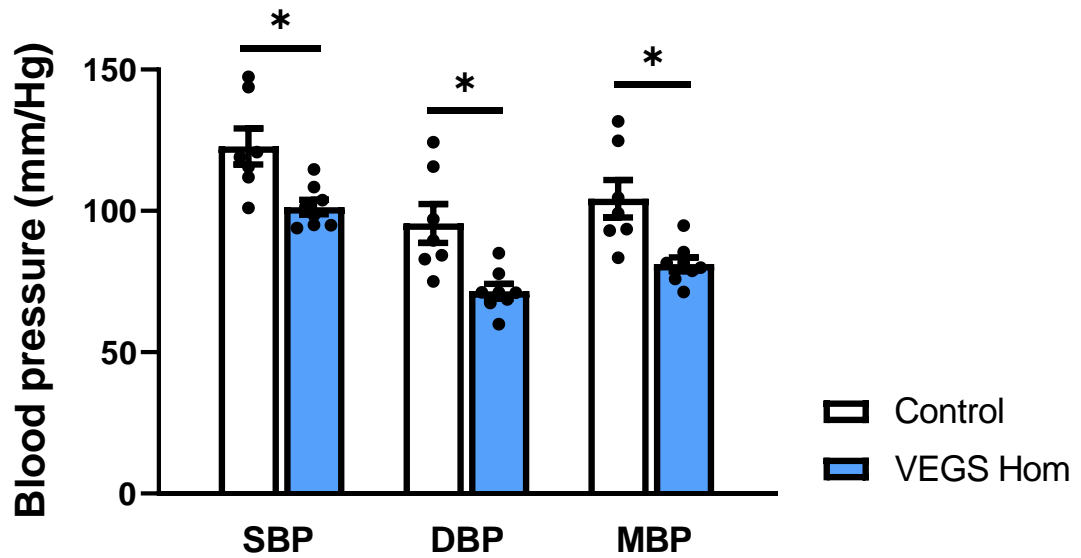


**Figure 3.5 Blood pressure measurements of VEGS Hom mice and control littermates**

Systolic (SBP), diastolic (DBP) and mean (MBP) blood pressure readings were recorded for VEGS Hom and compared with those of controls using an unpaired t-test ( $*p < 0.05$ ). Black circles represent values from individual mice. (Control  $n=7$ ; VEGS Hom  $n=8$ ).

Despite there being no statistically significant difference in vasoconstriction to PE after eNOS inhibition with L-NMMA, VEGS Hom tension response was not completely normalised to that of the control group (Figure 3.3b). This highlighted the potential impact of endothelial GS deficiency on other vasodilators. Since GS plays a role in ROS regulation, a possible effect on H<sub>2</sub>O<sub>2</sub> was investigated using organ bath equipment and application of catalase.

PE evoked a reduced maximal tension response in aortic rings from VEGS Hom ( $0.67 \pm 0.05$  g) versus controls ( $0.93 \pm 0.17$  g) and overall constriction responses were deemed significantly different upon testing with repeated measures ANOVA ( $p=0.0018$ ), as had been seen in earlier organ experiments (Figure 3.6a). VEGS Hom continued to exhibit decreased maximal constriction in response to PE in the presence of catalase compared to control mice ( $0.79 \pm 0.06$  g and  $1.07 \pm 0.07$  g, respectively) (Figure 3.6b), and overall tension response remained significantly lower (repeated measures ANOVA  $p=0.0012$ ). These data suggest that the differences in PE-induced vasoconstriction between genotypes are unlikely to be a result of changes in aortic H<sub>2</sub>O<sub>2</sub> generation. There was no difference in vasorelaxation in response to Ach exposure between VEGS Hom and controls, in line with previous observations (Figure 3.7a). Vasodilation following SNP application was almost identical between VEGS Hom and control mice (Figure 3.7b).

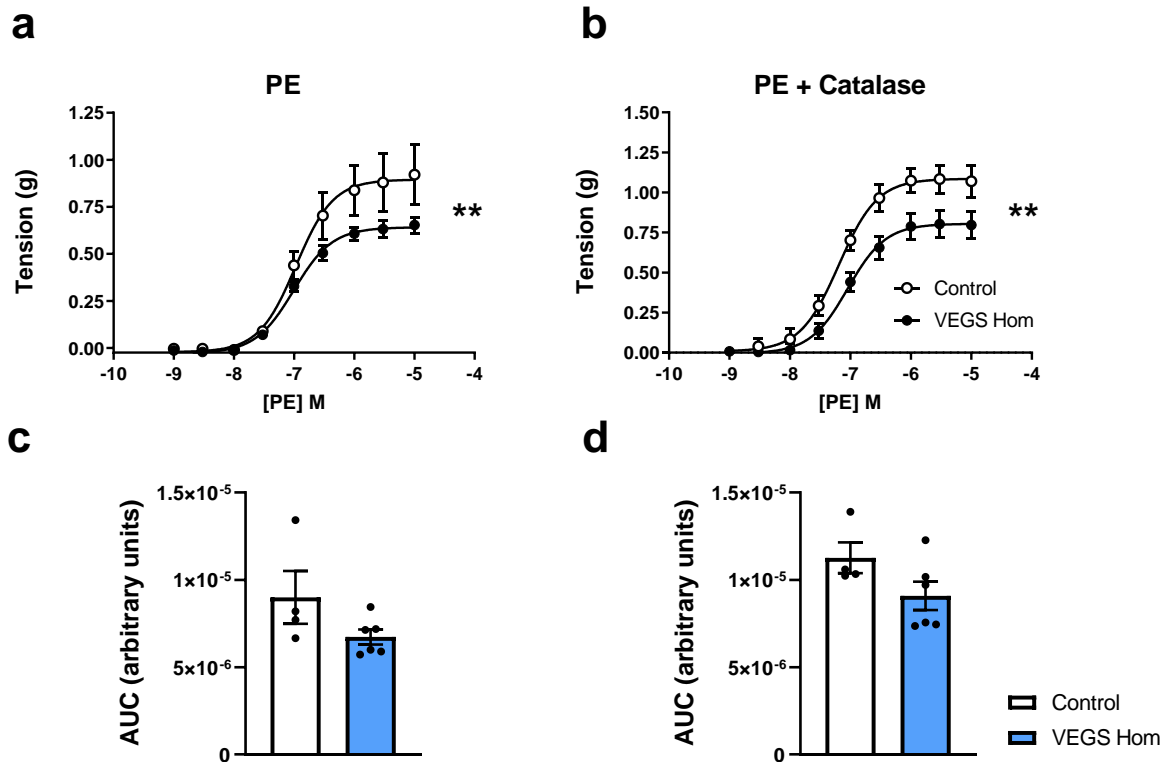


**Figure 3.6 Contractile responses of aortic rings from VEGS Hom and control mice following PE treatment with and without catalase**

Aortic rings were treated with incremental concentrations of PE and vasoconstriction was recorded (a). This was repeated following application of catalase (b). Subsequent tension responses were evaluated with a repeated measures ANOVA and the Sidak post-hoc test and examined the PE concentration x genotype interaction (\*\* $p < 0.01$ ). AUC was also calculated for PE (c) and PE with catalase (d) and analysed using an unpaired t-test. In c and d, black circles represent data from individual mice. (Control  $n=4$ ; VEGS Hom  $n=6$ ).

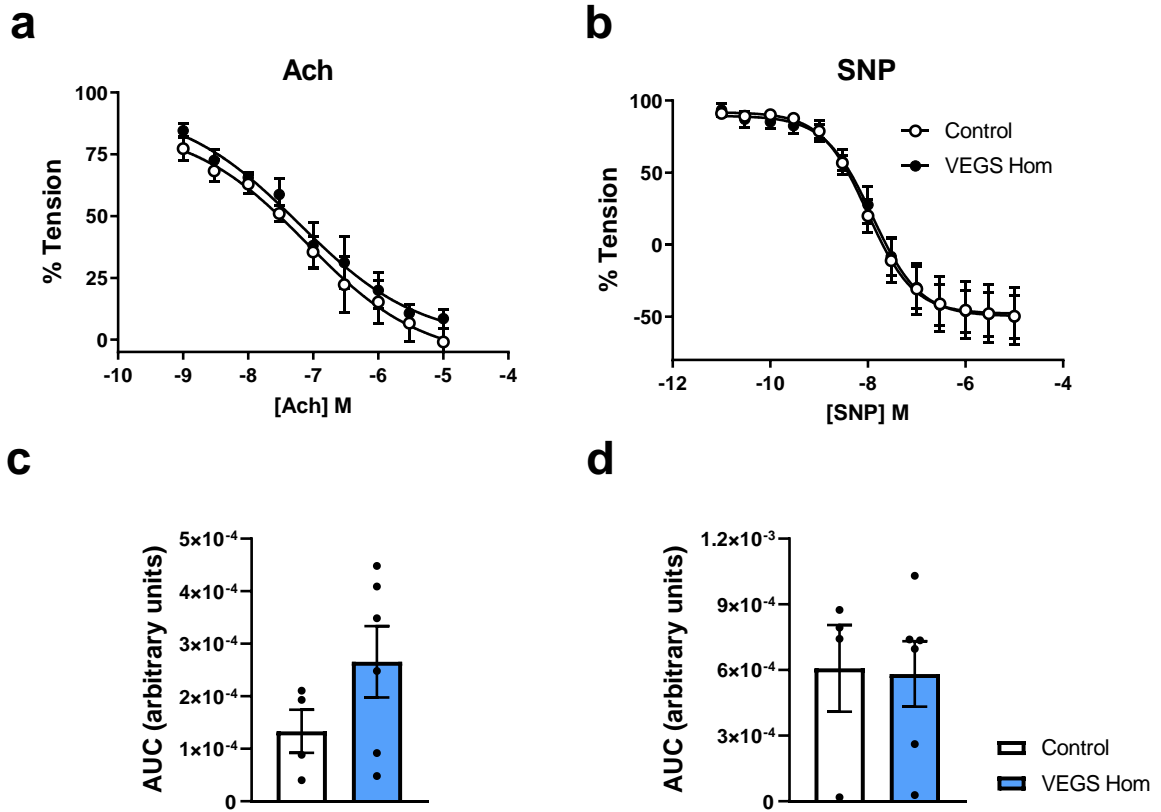


**Figure 3.7 Vasorelaxation of aortic rings from VEGS Hom and control mice in response to vasodilators Ach and SNP**

Tissue was pre-constricted with PE prior to incremental concentrations of Ach and dose-response data was recorded (a). Vasodilation in response to SNP application was also investigated (b). Response data was evaluated with a repeated measures ANOVA and the Sidak post-hoc test. AUC of the dose-response data for Ach (c) and SNP (d) were also analysed using an unpaired t-test. Black circles in c and d indicate individual data points. (Control  $n=4$ ; VEGS Hom  $n=6$ ).

VEGS Hom mice and control counterparts underwent femoral artery wire-injury to determine how GS knockdown in the endothelium influences endothelial repair. In view of the lower vascular tone in VEGS Hom, it was first important to establish that transgenic and control femoral arteries were equally sensitive to wire-induced endothelial denudation. Therefore, wire-injury was performed, followed by immediate vessel harvest after Evans Blue dye perfusion. There was no significant difference in the percentage area of the femoral artery stained with Evans Blue between VEGS Hom and controls, indicating equivalent levels of endothelial denudation, thus similar susceptibility to wire-injury surgery damage (Figure 3.8).

The degree of endothelial repair in VEGS Hom and control mice was then examined 4 days following wire-injury surgery. There was no significant difference in the percentage area unstained by Evans Blue dye (indicative of an intact, repaired endothelium) in VEGS Hom ( $61.3 \pm 4.4\%$ ) by comparison to control mice ( $53.0 \pm 3.4\%$ ) ( $p=0.1524$ ) (Figure 3.9).

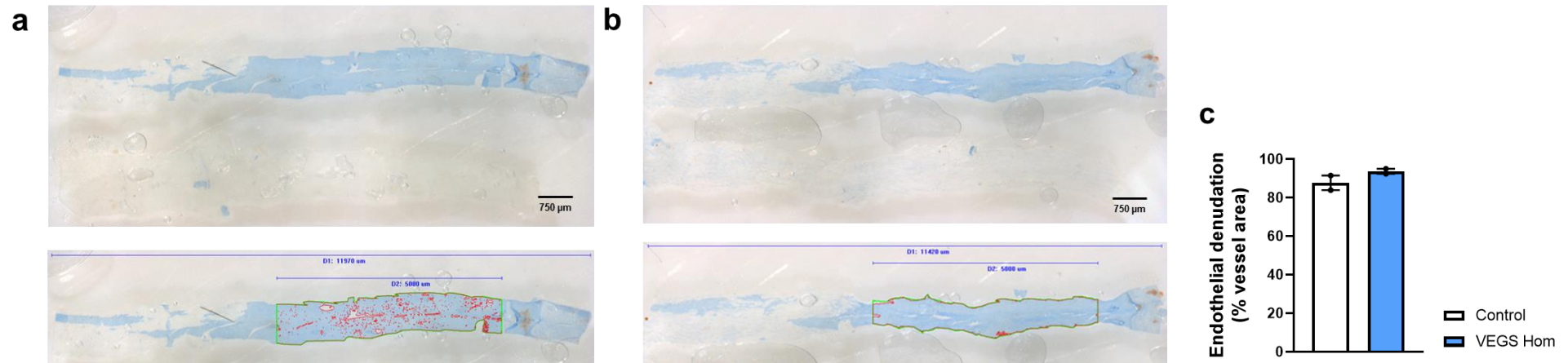


### Figure 3.8 Assessment of endothelial denudation induced by wire-injury surgery using Evans Blue dye

Wire-injury of the femoral artery was performed on control and VEGS Hom. Vessels were harvested immediately after perfusion with Evans Blue dye. Representative images of explanted arteries with scale bars demonstrating 750 µm are shown for controls (a) and VEGS Hom (b), as are images depicting the corresponding areas of analysis (lower panels). The vessel length is shown by the top blue line and the lower blue line defines the 5 mm region of interest, which is then marked around the artery in green. Quantification of Evans Blue staining (i.e. endothelial denudation) is presented in c. (Control  $n=2$  VEGS Hom  $n=2$ ).

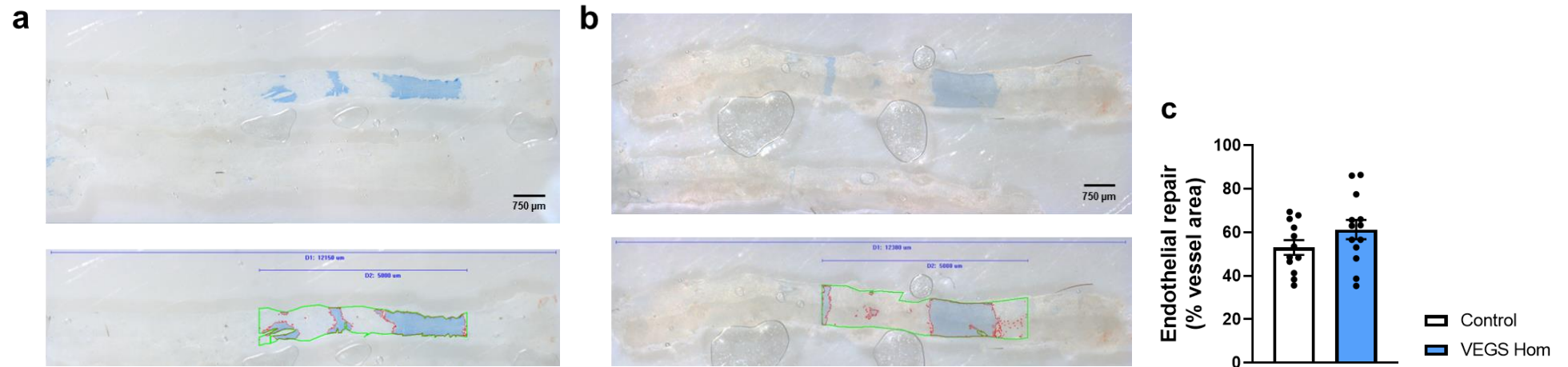


### Figure 3.9 Degree of endothelial regeneration 4 days following wire-injury surgery

Femoral artery wire-injury was performed on control mice and VEGS Hom. Vessels were harvested 4 days later, after perfusion with Evans Blue dye. Representative images of explanted arteries with scale bars demonstrating 750  $\mu\text{m}$  are shown for controls (a) and VEGS Hom (b), as are images demonstrating the corresponding areas of analysis (lower panels). The vessel length is shown by the top blue line and the lower blue line defines the 5 mm field of analysis, which is marked around the vessel in green. Areas of Evans Blue staining are outlined in red. Endothelial repair (i.e. areas free from Evans Blue staining) was calculated (c) and evaluated using an unpaired t-test ( $p=0.152$ ). Black circles represent individual data points. (Control  $n=12$ ; VEGS Hom  $n=13$ ).

The protein expression of eNOS, phosphorylated eNOS (p-eNOS S1177) and GS was analysed in whole aorta lysates from VEGS Hom and control mice.  $\beta$ -actin was also examined as the loading control (Figure 3.10). While the group sizes were too small to effectively test statistical significance, VEGS Hom lysates appeared to have nominally lower expression of eNOS than those from controls (Figure 3.10b). p-eNOS S1177 expression relative to eNOS was also nominally decreased versus control counterparts (Figure 3.10c). Levels of GS protein were mildly reduced in VEGS Hom (Figure 3.10d), but remained easily detectable, most likely due to the presence of non-endothelial aortic cells types expressing GS.

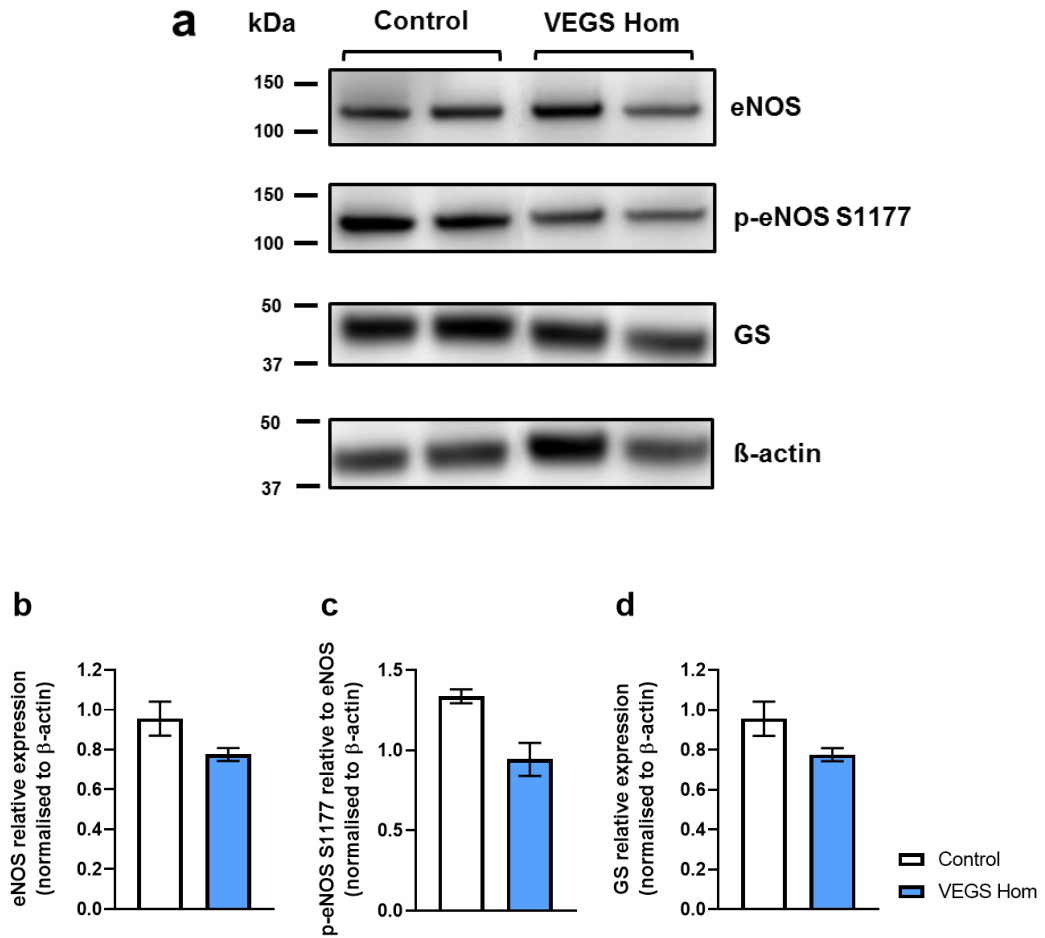


**Figure 3.10 Protein expression of eNOS, p-eNOS S1177 and GS in whole aorta lysates from VEGS Hom and control mice**

Representative western blot of eNOS, p-eNOS S1177, and GS in control and VEGS Hom (a). Mean data showing relative expression of eNOS (b), expression of p-eNOS S1177 relative to eNOS and GS relative expression. Data in b, c and d are all normalised to  $\beta$ -actin. (Control  $n=2$ ; VEGS Hom  $n=2$ ).

Since total eNOS expression and its S1177 phosphorylation did not appear to be increased (Figure 3.10), an alternative explanation for amplified endothelial NO availability may be an increase in basal eNOS activity. This was explored by exposing cultured LECs from VEGS Hom and control mice to arginine radiolabelled with  $^{14}\text{C}$  and measuring its conversion to citrulline. LECs were also treated in parallel with  $^{14}\text{C}$ -arginine and 100 nM insulin as a positive control for the assay. Following incubation with  $^{14}\text{C}$ -arginine, with or without insulin, cells were lysed to quantify  $^{14}\text{C}$ -citrulline. This quantification was expressed as DMPI using a scintillation counter. These values were then normalised to the total protein content of their corresponding cell lysate.

After treatment with  $^{14}\text{C}$ -arginine alone, LECs from VEGS Hom exhibited increased DMPI/total protein ratios ( $8.14 \pm 0.8$ ) in comparison to control mice LECs ( $6.79 \pm 0.54$ ). However, this was not significant ( $p=0.1804$ ), perhaps due to small groups. When  $^{14}\text{C}$ -arginine was applied to LECs along with insulin, an increase in DMPI/total protein ratio was observed in VEGS Hom LECs ( $10.57 \pm 1.59$ ) versus those derived from controls ( $8.06 \pm 0.96$ ), but this also failed to reach significance ( $p=0.1877$ ). eNOS activity did increase significantly in both control and VEGS Hom LECs in response to insulin ( $p=0.046$  and  $p=0.033$ ), confirming that the assay was successful (Figure 3.11a).

The concentration of the NO breakdown products nitrate and nitrite, or 'NO<sub>x</sub>', in VEGS Hom blood serum were also analysed. No significant difference was noted between VEGS Hom and control mice ( $23.1 \pm 3.8 \mu\text{M}$  versus  $27.4 \pm 4.8 \mu\text{M}$  respectively;  $p=0.4839$ ) (Figure 3.11b).

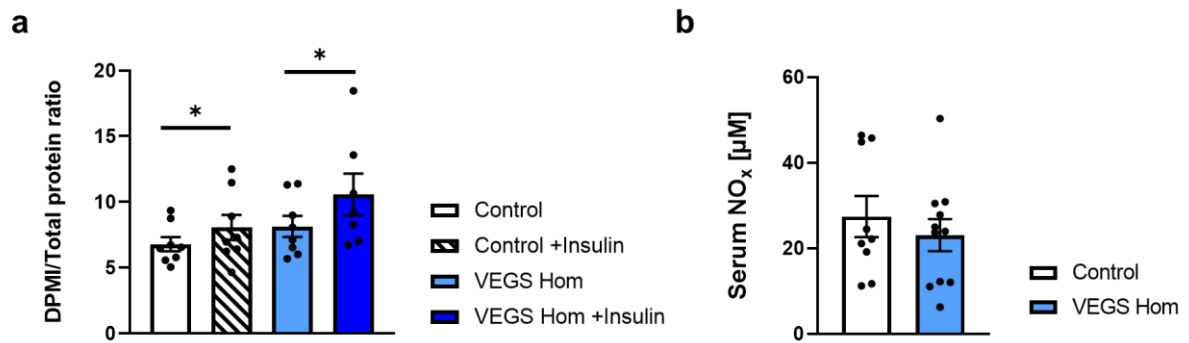


**Figure 3.11 Evaluation of eNOS activity and NO<sub>x</sub> concentration in control and VEGS Hom mice**

LECs were incubated with <sup>14</sup>C-arginine alone or <sup>14</sup>C-arginine with insulin (a). The resulting production of <sup>14</sup>C-citrulline was assessed and quantified as DPMI normalised to the total protein concentration of the sample lysate. For testing of results from LECs of the same genotype (ie. control LECs vs control LECs +insulin), a paired t-test was used. If LECs were of different genotypes (ie. control LECs vs VEGS Hom LECs), an unpaired t-test was employed (\**p*<0.05) (control *n*=8/*N*=1; VEGS Hom *n*=8/*N*=1) (a). Mean concentrations of NO<sub>x</sub> in serum samples from control and VEGS Hom mice were determined and compared with an unpaired t-test (b). Black circles indicate individual data points. (Control *n*=9; VEGS Hom *n*=11).

### 3.2 Exploring endothelial GS holoinsufficiency on vascular function in a STZ model of diabetes

Since the *GLUL* gene locus has been linked to cardiovascular risk in people with T2DM, it was necessary to consider endothelial GS deficiency in the setting of diabetes. This section presents preliminary data from VEGS Hom mice treated with the alkylating agent, STZ, which induces hyperglycaemia through the destruction of pancreatic  $\beta$ -cells (Szkudelski 2001). Diabetic VEGS Hom mice were characterised and vasomotor function was assessed using organ bath apparatus.

VEGS Hom underwent a 5 consecutive day course of single dose, daily STZ injections to investigate the interaction between endothelial GS deficiency and diabetes. Body weight and fasting blood glucose were measured on day 1 and day 5 of this induction period. Weekly weights and NFBG readings were recorded in the 4 weeks succeeding the STZ regimen. Mice were deemed diabetic when NFBG exceeded 11.1 mmol/L. If this level was not reached at the time of experimentation, mice were excluded.

Potential genotype-specific differences in response to STZ treatment were investigated. VEGS Hom and control mice experienced a comparable, negligible change in weight over the 5-day injection course (Figure 3.12a). STZ has been documented to impair weight gain in mice, so this result was expected (Song et al., 2016). Both groups demonstrated similar NFBG on day 1 prior to STZ administration (Figure 3.12b).

In the 4 weeks post-STZ, both VEGS Hom and controls exhibited comparable weight gain (Figure 3.12c) (repeated measures ANOVA  $p=0.77$ ; AUC  $p=0.3869$ ). Increases in NFBG levels were anticipated and were observed over the 4 weeks, with both groups displaying robust increases compared with their respective NFBG readings taken before STZ injections (Figure 3.12d). NFBG increase was analysed and no significant difference between VEGS Hom and controls was detected, indicating similar sensitivity to STZ (repeated measures ANOVA  $p=0.399$ ; AUC  $p=0.3770$ ).

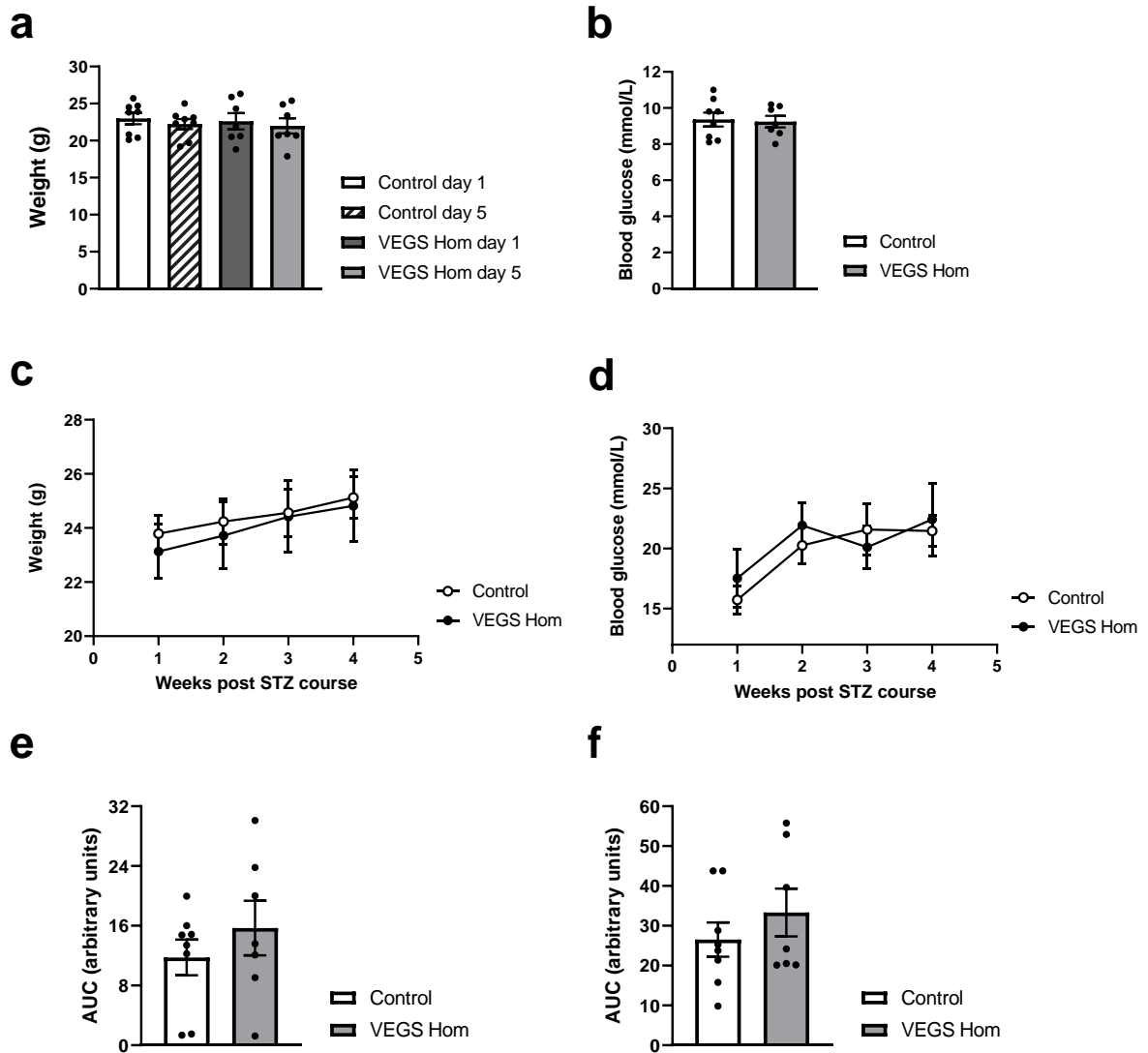


**Figure 3.12 Metabolic profiles of VEGS Hom mice and control littermates in response to STZ treatment**

Mice received single daily injections of STZ over 5 consecutive days. Mean body weight was documented on day 1 and day 5 of the STZ injection course (a). NFBG was measured on day 1 prior to STZ administration (b). VEGS Hom and control mice weights were monitored weekly (c), as was NFBG (d). Data presented in c and d were evaluated with a repeated measures ANOVA and the Sidak post-hoc test. AUC was also determined for weight and NFBG data (e and f, respectively). Statistical testing of AUC was done using an unpaired t-test. Black circles shown in a, b, e and f represent data from individual mice. (Control  $n=8$ ; VEGS Hom  $n=7$ ).

Preliminary investigations into the effect of STZ-induced diabetes on vasomotor function in the VEGS Hom model were carried out. The maximal vasoconstriction of aortic rings to PE was almost identical between VEGS Hom and control littermates ( $0.811 \pm 0.138$  g versus  $0.773 \pm 0.103$  g, respectively) (Figure 3.13a), as was overall response (repeated measures ANOVA  $p=0.978$ ; AUC  $p=0.7963$ ), in contrast with non-diabetic mice (Figure 3.3a). When this was repeated in the presence of NOS inhibitor, L-NMMA, control mice exhibited a nominally greater maximal constriction to PE ( $1.425 \pm 0.061$  g) compared with VEGS Hom mice ( $1.263 \pm 0.059$  g) (Figure 3.13b), but testing of overall response did not achieve significance (repeated measures ANOVA  $p=0.386$ ; AUC  $p=0.1098$ ). Exposure to increasing concentrations of Ach (Figure 3.14a) revealed no difference in vasorelaxation response between VEGS Hom and controls (repeated measures ANOVA  $p=0.998$ ; AUC  $p=0.2294$ ). A similar trend was observed with SNP (Figure 3.14b), which was also not significantly different following analysis (repeated measures ANOVA  $p=0.126$ ; AUC  $p=0.5798$ ).

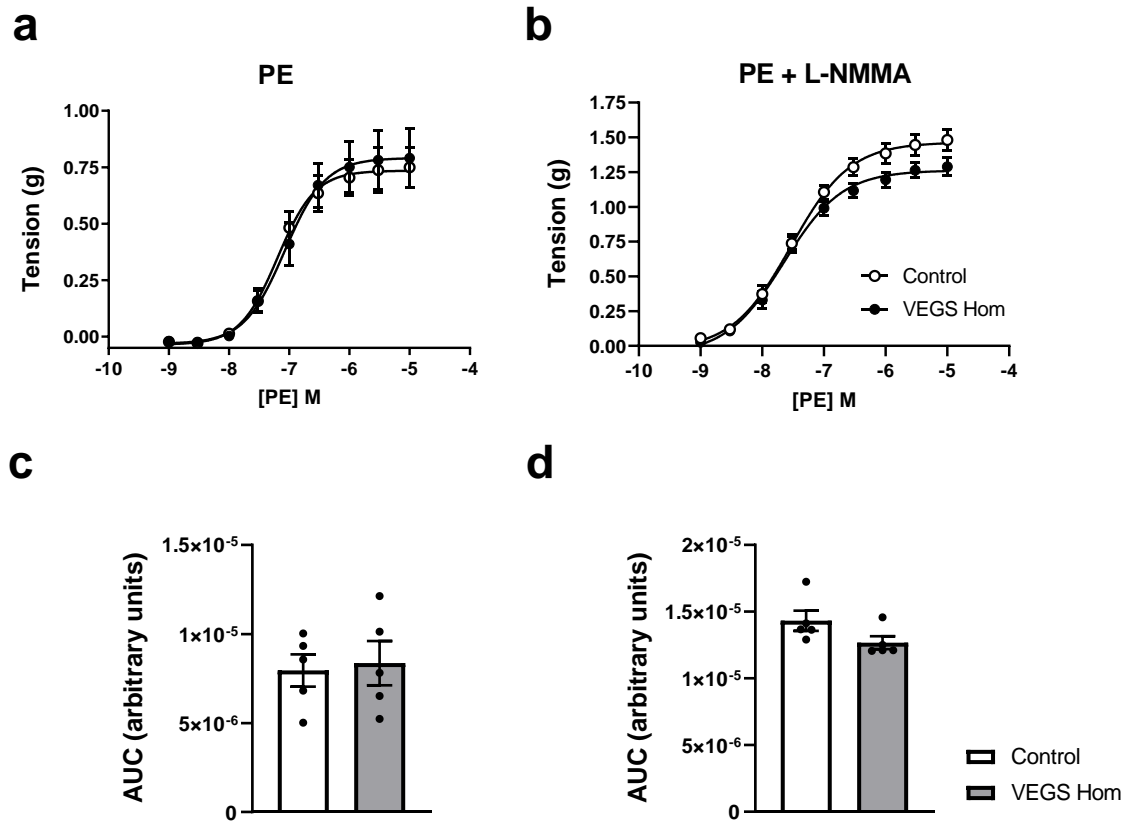


**Figure 3.13 Vasomotor function of aortic rings from STZ-treated VEGS Hom and control mice following exposure to PE with and without L-NMMA**

Aortic rings were treated with incremental doses of PE to induce vasoconstriction (a). PE application was repeated following incubation with NOS inhibitor L-NMMA (b). Constriction response data was analysed using a repeated measures ANOVA and the Sidak post-hoc test. AUC was also determined for PE (c) and PE with L-NMMA (d) and analysed using unpaired t-tests. Black circles in c and d represent data from individual mice. (Control  $n=5$ ; VEGS Hom  $n=5$ ).

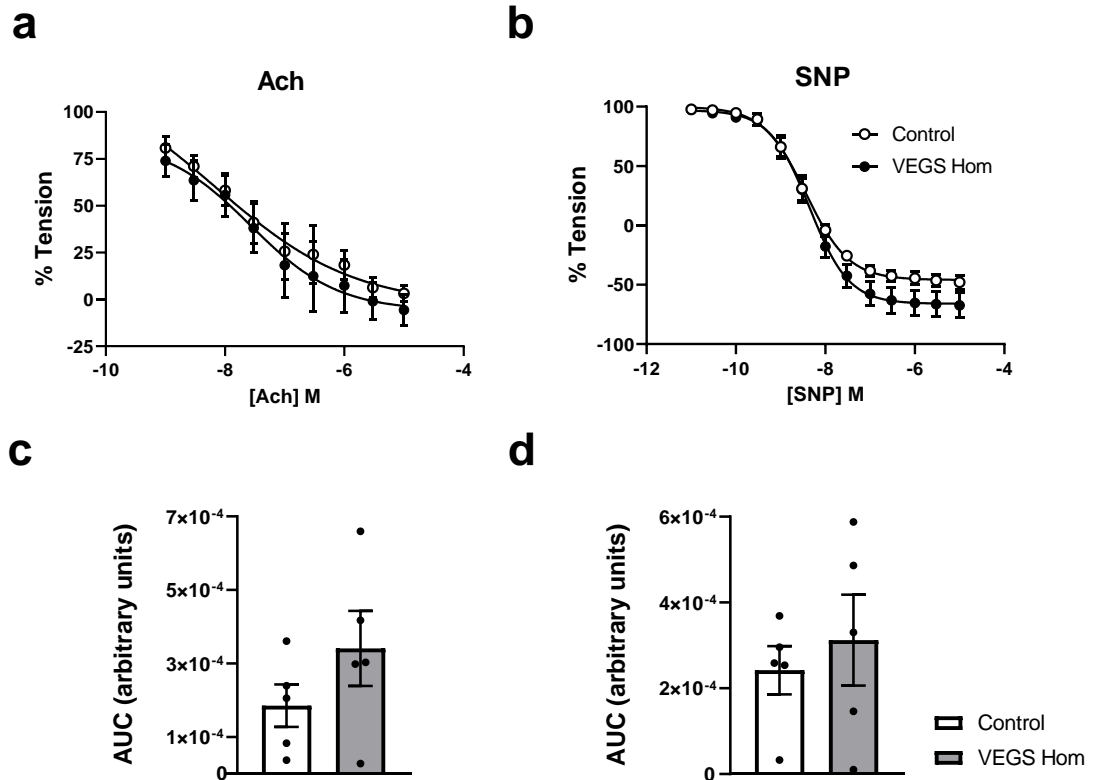


**Figure 3.14 Ach and SNP-induced vasorelaxation of aortic rings from STZ-treated VEGS Hom and control mice**

Aortic rings were treated with incremental concentrations of Ach (a) or SNP (b) after PE pre-constriction and relaxation responses were assessed. Dose-response data was analysed using a repeated measures ANOVA and the Sidak post-hoc test. AUC was calculated for Ach (c) and SNP (d) and tested using an unpaired t-test. Black circles shown in c and d represent data from individual mice. (Control  $n=5$ ; VEGS Hom  $n=5$ ).

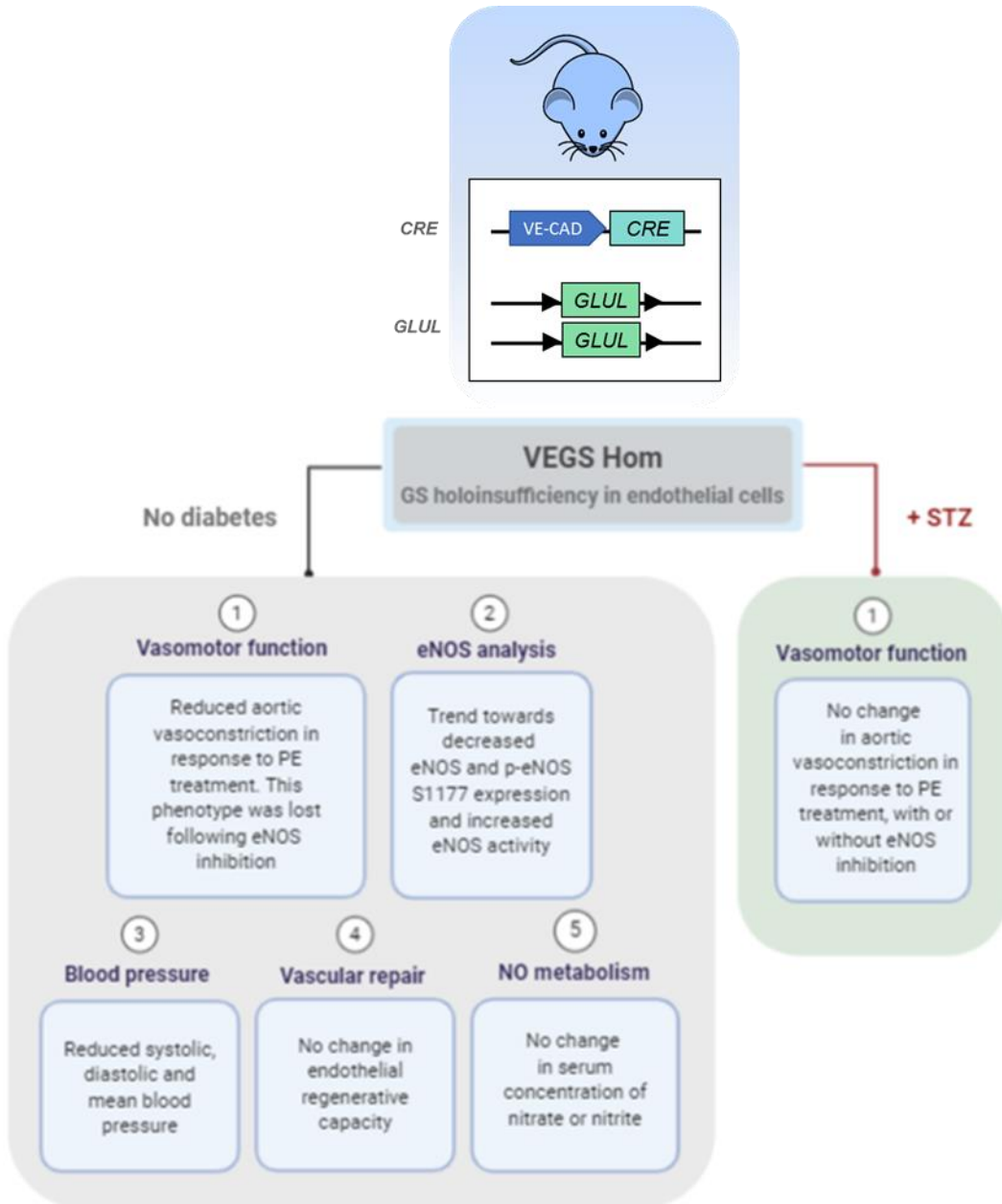


Figure 3.15 Summary of key findings from VEGS Hom experiments

### 3.3 The effect of endothelial GS haploinsufficiency on vascular function *in vivo*

The previous chapters present data which hints at amplified basal NO availability in mice with GS holoinsufficiency in the endothelium. It was important to evaluate whether these findings were also present in mice with endothelial GS haploinsufficiency, verifying whether there is a gene-dose effect. Additionally, the levels of GS expression in GS haploinsufficient mouse endothelial cells would be a closer representation of that observed in rs10911021 homozygous risk variant carriers, as described by Qi et al. (2013). Consequently, VEGS Het was created and vascular reactivity and endothelial repair were examined.

'VEGS Het' mice were derived as outlined in section 2.2.2.3. Their Cre-negative *GLUL*<sup>flox/+</sup> littermates were employed as controls.

Body weight of VEGS Het was recorded to assess if endothelial GS haploinsufficiency resulted in systemic metabolic perturbation. Weight data were collected at the beginning and end of the tamoxifen injection course (Figure 3.16a) and then weekly until the time of experimentation (Figure 3.16b) and were similar for VEGS Het and control littermates. Statistical analysis revealed no significant difference in the weight gain displayed between groups from the cessation of tamoxifen induction to the time of tissue harvest (repeated measures ANOVA  $p=0.791$ ; AUC  $p=0.9208$ ).

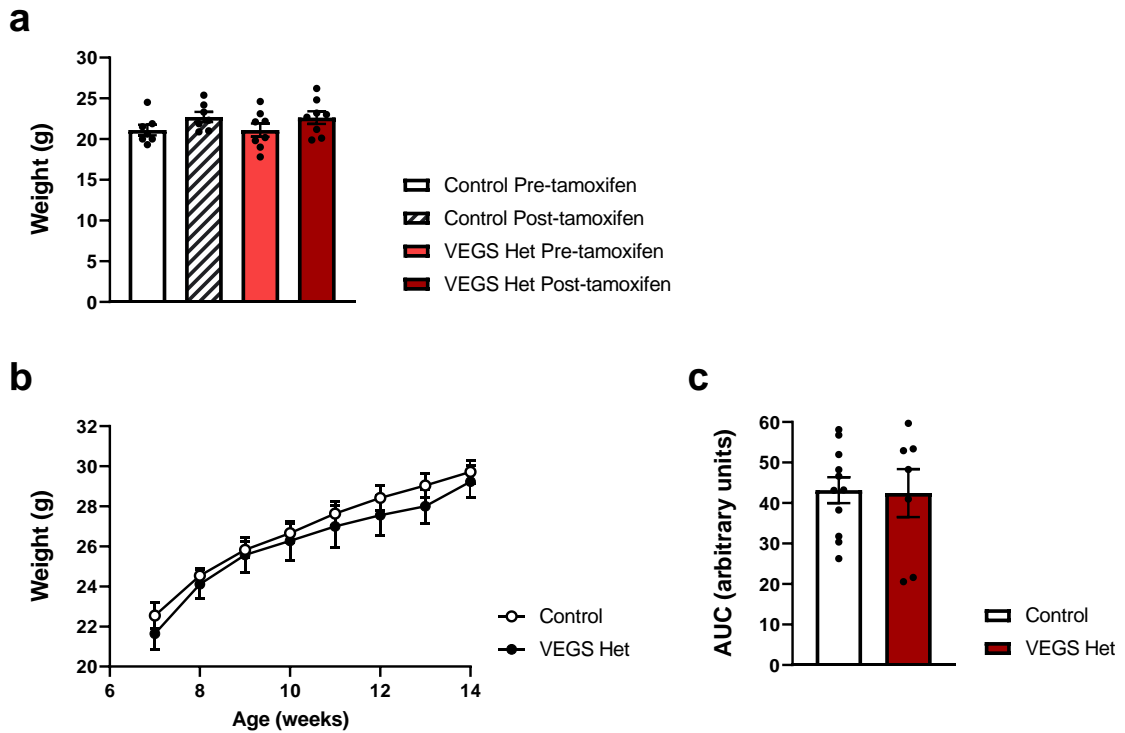


**Figure 3.16 Metabolic profile of VEGS Het mice and control mice**

Mean body weight of control and VEGS Het mice at 6 weeks of age at the start and end of the 5-day tamoxifen treatment schedule (control  $n=7$ , VEGS Het  $n=8$ ) (a). Mean weekly weights of control and VEGS Het mice were then observed from 7 to 14 weeks of age and assessed with a repeated measures ANOVA and the Sidak post-hoc test (b). AUC was determined alongside and analysed using an unpaired t-test (c). In graphs a and c, black circles represent individual data. (Control  $n=11$ , VEGS Hom  $n=7$ ).

In order to confirm knockdown of endothelial GS in the VEGS Het model, LECs were obtained and GS mRNA expression levels were analysed using RT-qPCR. HPRT was analysed as the housekeeper gene. A significant reduction in GS mRNA expression of 45.1% was noted in endothelial cells collected from VEGS Het, compared with those isolated from control mice ( $p=0.013$ ) (Figure 3.17).

The effect of GS haploinsufficiency on vasomotor function was established using aortic rings from VEGS Het mice and the organ bath protocol, as outlined in section 2.2.11. Rings were exposed to the vasoconstrictor PE and dose-response data were recorded (Figure 3.18a). VEGS Het demonstrated a similar maximal tension to PE ( $0.696 \pm 0.04$  g) versus control littermates ( $0.753 \pm 0.11$  g) and overall response was not significantly different (repeated measures ANOVA  $p=0.977$ ; AUC  $p=0.5671$ ). VEGS Het and control mice displayed comparable maximal vasoconstriction and overall tension response to PE following L-NMMA incubation ( $1.337 \pm 0.05$  g and  $1.498 \pm 0.04$  g, respectively) (repeated measures ANOVA  $p=0.493$ ; AUC  $p=0.1138$ ). Upon application of Ach as an endothelial-dependent vasodilator (Figure 3.19a), there was no difference in response between VEGS Het and controls (repeated measures ANOVA  $p=0.902$ ; AUC  $p=0.6803$ ). Aortic rings were also treated with the endothelial-independent vasodilator, SNP (Figure 3.19b), and no difference was noted between genotypes (repeated measures ANOVA  $p=0.217$ ; AUC  $p=0.2072$ ).

Since systolic, diastolic and mean blood pressure were markedly reduced in the VEGS Hom model, this was examined in the VEGS Het colony. Unlike VEGS Hom, SBP of VEGS Het mice was almost identical to that of the control group ( $103.4 \pm 2.87$  mm/Hg and  $104.6 \pm 5.05$  mm/Hg,  $p=0.84$ ). This was also the case for both DBP (VEGS Het:  $77.2 \pm 2.16$  mm/Hg; control:  $76.6 \pm 3.06$  mm/Hg;  $p=0.88$ ) and MBP (VEGS Het:  $85.6 \pm 2.38$  mm/Hg; control:  $85.5 \pm 3.64$  mm/Hg;  $p=0.99$ ) (Figure 3.20).

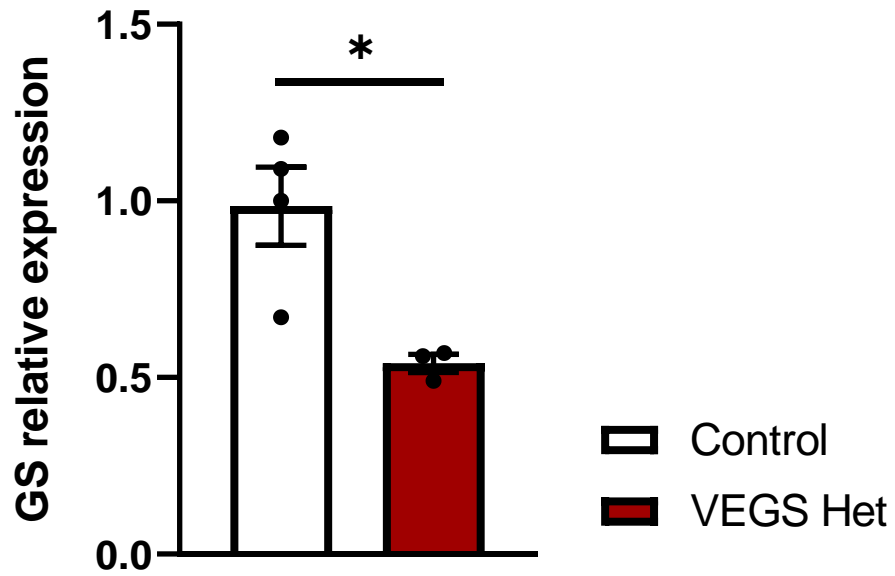


**Figure 3.17 Validation of GS knockdown in VEGS Het endothelial cells**

RT-qPCR analysis of relative GS mRNA expression in LECs isolated from VEGS Het mice and control littermates was conducted. HPRT was employed as the housekeeping gene. Individual data points are displayed as black circles. Data was analysed using an unpaired t-test ( $*p < 0.05$ ). (Control  $n=4$ ; VEGS Het  $n=3$ ).

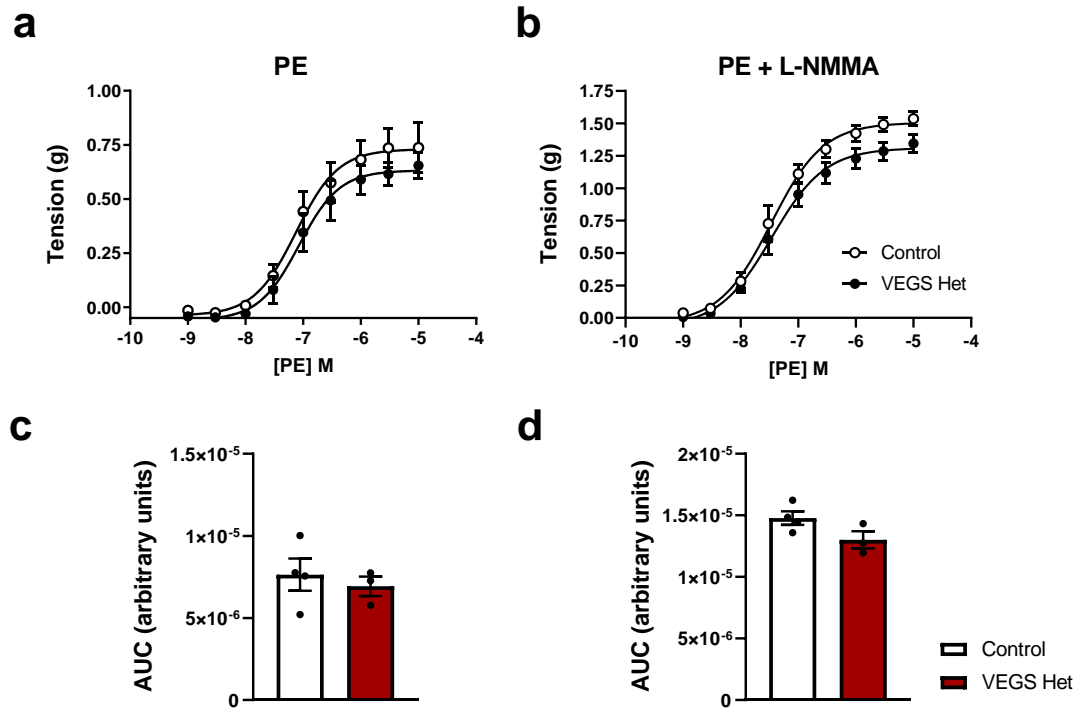


**Figure 3.18 Vasoconstriction of aortic rings from VEGS Het and control mice following PE treatment with and without L-NMMA**

Vessel tension was measured in response to incremental doses of PE (a). PE application was assessed again following incubation with NOS inhibitor L-NMMA (b). Constriction was evaluated with a repeated measures ANOVA and the Sidak post-hoc test. AUC for PE (c) and PE with L-NMMA (d) response data was also calculated and analysed using an unpaired t-test. Individual data in c and d are shown as black circles. (Control  $n=4$ ; VEGS Het  $n=3$ ).

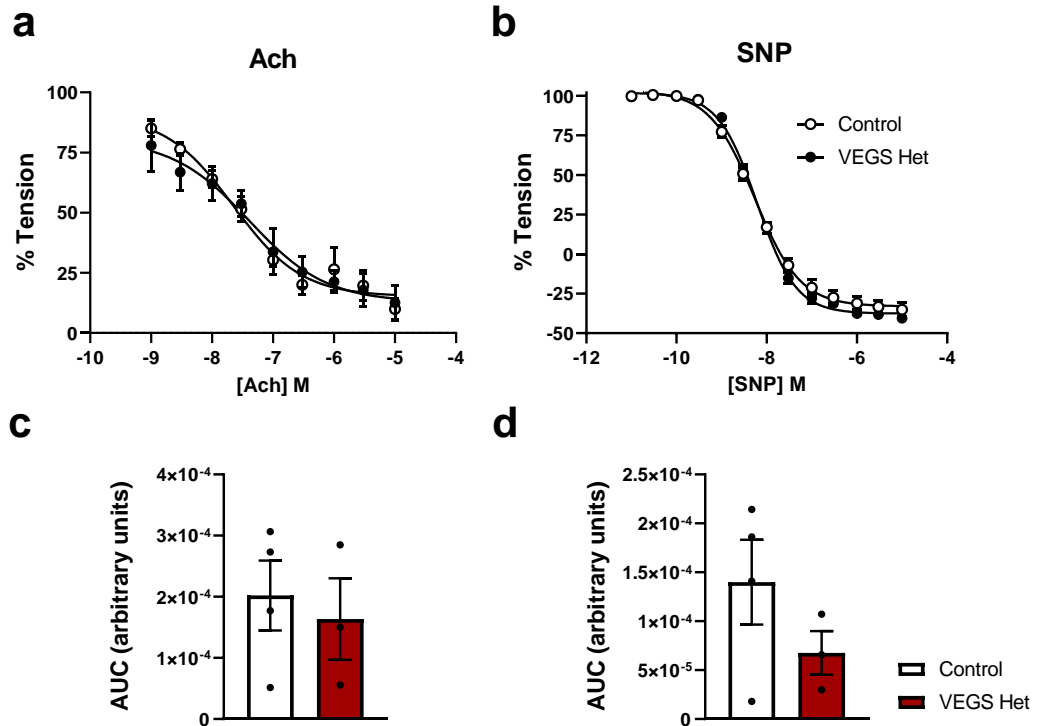


**Figure 3.19 Vasorelaxation of aortic rings from VEGS Het and control mice in response to vasodilators Ach and SNP**

Incremental doses of Ach (a) or SNP (b) were applied after PE pre-constriction and vasodilator response was investigated. Data were assessed by a repeated measures ANOVA, followed by the Sidak post-hoc test. AUC for Ach (c) and SNP (d) vasorelaxation was also determined and compared using an unpaired t-test. Individual data points are shown as black circles in c and d. (Control  $n=4$ ; VEGS Het  $n=3$ ).

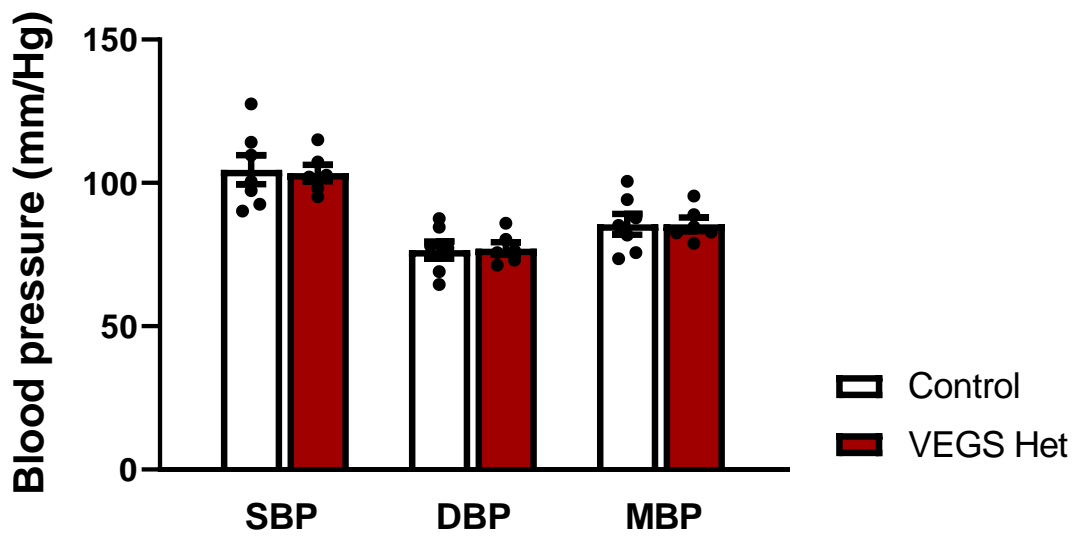


**Figure 3.20 Blood pressure of VEGS Het mice and control littermates**

Systolic (SBP), diastolic (DBP) and mean (MBP) blood pressure readings were taken between 10 and 14 weeks of age and genotypes compared using unpaired t-tests. Black circles indicate values from individual mice. (Control  $n=4$ ; VEGS Het  $n=3$ ).

The impact of endothelial GS haploinsufficiency on endothelial repair was next assessed using denuding wire-injury of the femoral artery, followed by perfusion of Evans Blue dye 4 days post-procedure. Regions of residual damage stained blue. These areas were quantified within a 5 mm segment of interest, as explained in section 2.2.17.3.2. There was no significant difference in the extent of endothelial regeneration between VEGS Het mice and controls. Representative images of VEGS Het and control arteries and their analysis are presented in Figure 3.21, with quantification shown in Figure 3.21c ( $p=0.7794$ ).

Aorta lysates were prepared from VEGS Het and control littermates and protein expression of eNOS, p-eNOS S1177 and GS were assessed by western blotting, with  $\beta$ -actin used as the loading control (Figure 3.22a). Whilst the sample size is too small for statistical analysis, these suggested that VEGS Het had slightly lower eNOS expression than control mice (Figure 3.22b). Similarly, p-eNOS S1177 expression relative to eNOS appeared attenuated in VEGS Het versus control littermates (Figure 3.22c), although no clear difference in GS expression was noted (Figure 3.22d). This was probably due to the non-endothelial cells also present in the aorta lysates ( $p=0.3420$ ).

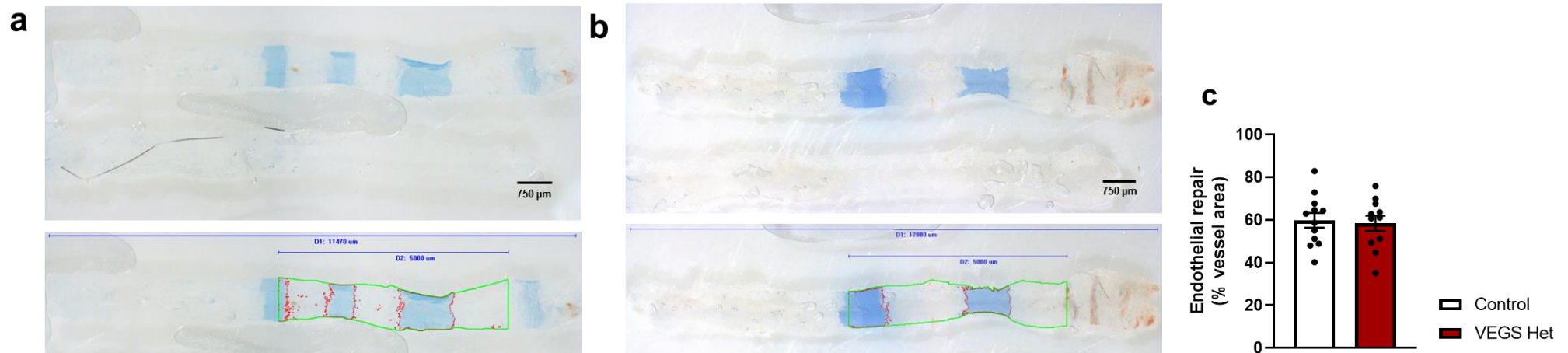


**Figure 3.21 Endothelial repair in VEGS Het and control femoral arteries 4 days following wire-injury**

Representative images of control (a) and VEGS Het (b) explanted femoral arteries after perfusion with Evans Blue dye are shown, with scales bars representing 750 µm. Corresponding areas of analysis are displayed in the lower panels. The upper blue line is the defined length of the specimen. The lower blue line denotes the 5 mm region of interest within which endothelial regeneration was assessed. This segment is outlined in green. Locations where Evans Blue dye were detected are bordered by red lines. These were quantified and endothelial repair was calculated as a percentage of the 5 mm analysis area unstained by Evans Blue dye (c). These data were analysed with an unpaired t-test. Black circles indicate data from individual mice. (Control  $n=12$ ; VEGS Het  $n=11$ ).

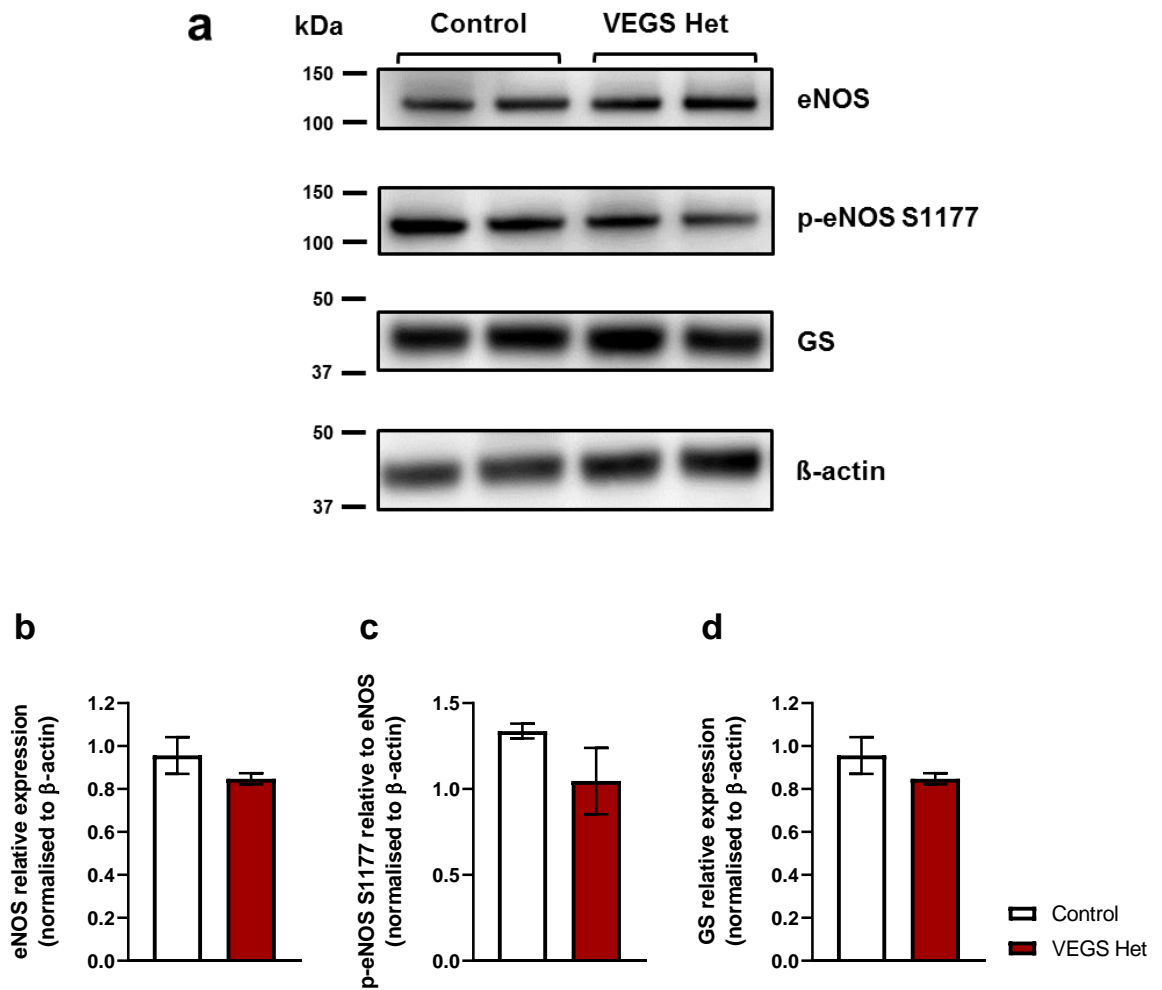


**Figure 3.22 Protein expression of eNOS, p-eNOS S1177 and GS in control and VEGS Het aortic lysates**

Representative western blot of eNOS, p-eNOS S1177, and GS in control mice and VEGS Het (a). Mean data showing relative expression of eNOS (b), expression of p-eNOS S1177 relative to eNOS (c) and GS relative expression (d). Data in b, c and d are all normalised to  $\beta$ -actin. (Control  $n=2$ ; VEGS Hom  $n=2$ ).

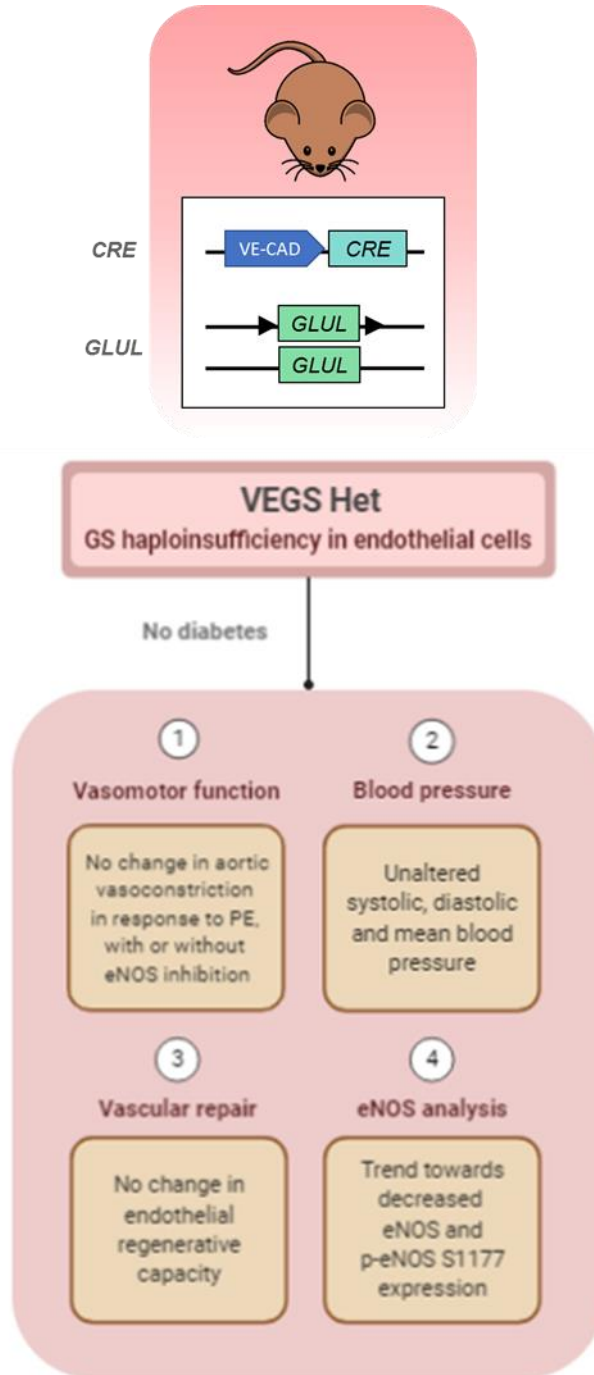
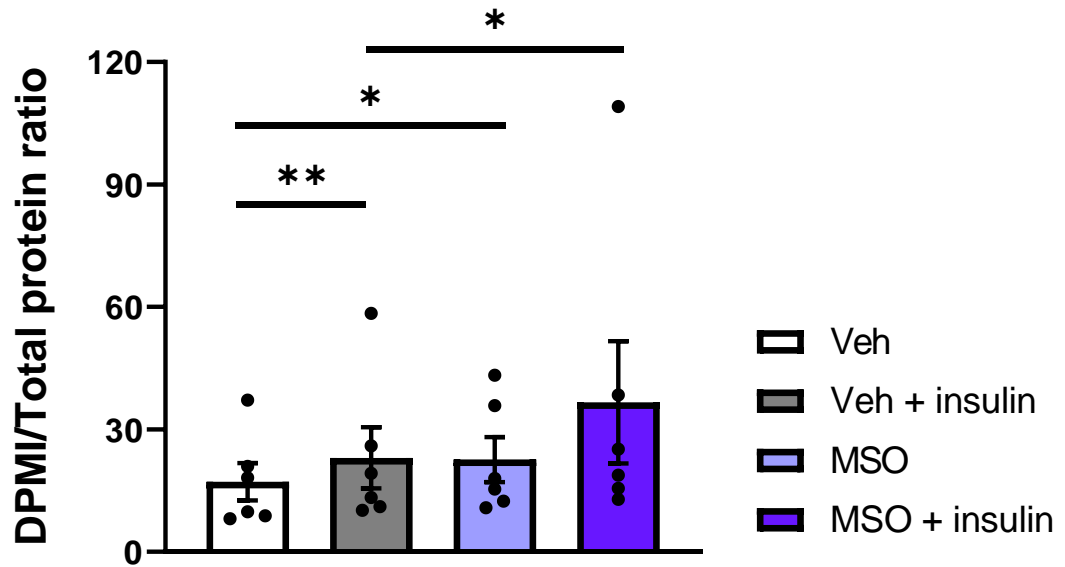


Figure 3.23 Summary of key findings from VEGS Het experiments

### 3.4 Pharmacological inhibition of endothelial GS *in vitro*

Previously published data show that shRNA silencing of *GLUL* in HUVECs impairs sprouting angiogenesis in a glutamine-independent manner (Eelen et al., 2018). However, the influence of decreased endothelial GS activity on NO metabolism in the human endothelium remains unexplored. Treatment of HUVECs with the irreversible pharmacological GS inhibitor, MSO, was employed to validate and extend the observations outlined in previous chapters.

The effect of GS inhibition on NO metabolism was examined by applying MSO to HUVECs for 24 hrs, prior to assessing their eNOS activity. Following incubation with <sup>14</sup>C-arginine, HUVECs treated with MSO exhibited significantly higher DMPI/Total protein ratio values compared with vehicle control HUVECs ( $p=0.033$ ). In response to co-treatment with <sup>14</sup>C-arginine and insulin, HUVECs exposed to MSO also displayed an increase in DMPI/Total protein ratio by comparison to control cells ( $p=0.014$ ). Such increases in DMPI/Total protein ratio suggest augmented eNOS activity in response to GS inhibition (Figure 3.24), corroborating the findings in murine aortic rings.



**Figure 3.24 eNOS activity in HUVECs following pharmacological inhibition of GS with MSO**

HUVECs were exposed to 1 mM MSO or a vehicle (Veh) for 24 hrs before treatment with  $^{14}\text{C}$ -arginine alone or  $^{14}\text{C}$ -arginine with insulin. The resulting abundance of  $^{14}\text{C}$ -citrulline was assessed and quantified as DPMI, which was normalised to the total protein concentration of the sample lysate. Black circles indicate individual data. Data was analysed with paired t-tests ( $*p < 0.05$ ;  $**p < 0.01$ ) ( $n=6/N=1$ ).

As eNOS activity is influenced by both its cellular location and protein partner interaction, it was important to consider the possibility that these factors could be altered by attenuated GS activity. shRNA-induced *GLUL* knockdown in endothelial cells augments actin stress fibre formation due to suppression of RhoJ (Eelen et al., 2018). Since eNOS activity is increased on  $\beta$ -actin binding (Kondrikov et al., 2010), the spatial relationship between eNOS and F-actin was examined in HUVECs after GS inhibition with MSO using immunocytochemistry. HUVECs were immuno-stained for eNOS, and phalloidin was applied to distinguish filamentous actin (F-actin). DAPI was also employed to identify nuclei. The mean fluorescence intensity was determined for each stain, and for eNOS and F-actin co-fluorescence, as explained earlier (section 2.2.20.2).

Representative images of vehicle control and MSO-treated HUVECs immuno-stained for eNOS, F-actin and DAPI, are displayed in Figure 3.25a. DAPI staining confirmed a comparable number of HUVECs in each image, regardless of treatment condition, verifying that any difference in mean fluorescence intensity was not due to disparities in cell density ( $p=0.881$ ) (Figure 3.25b). There was no significant difference in the mean fluorescence intensity values for either eNOS (Figure 3.25c) or F-actin (Figure 3.25d) in MSO-treated HUVECs compared with control cells ( $p=0.065$  and  $p=0.184$  respectively). However, MSO cells exhibited a significantly higher mean fluorescence intensity for areas of eNOS and F-actin co-fluorescence, suggesting an increase in their colocalization ( $p=0.028$ ) (Figure 3.25e).

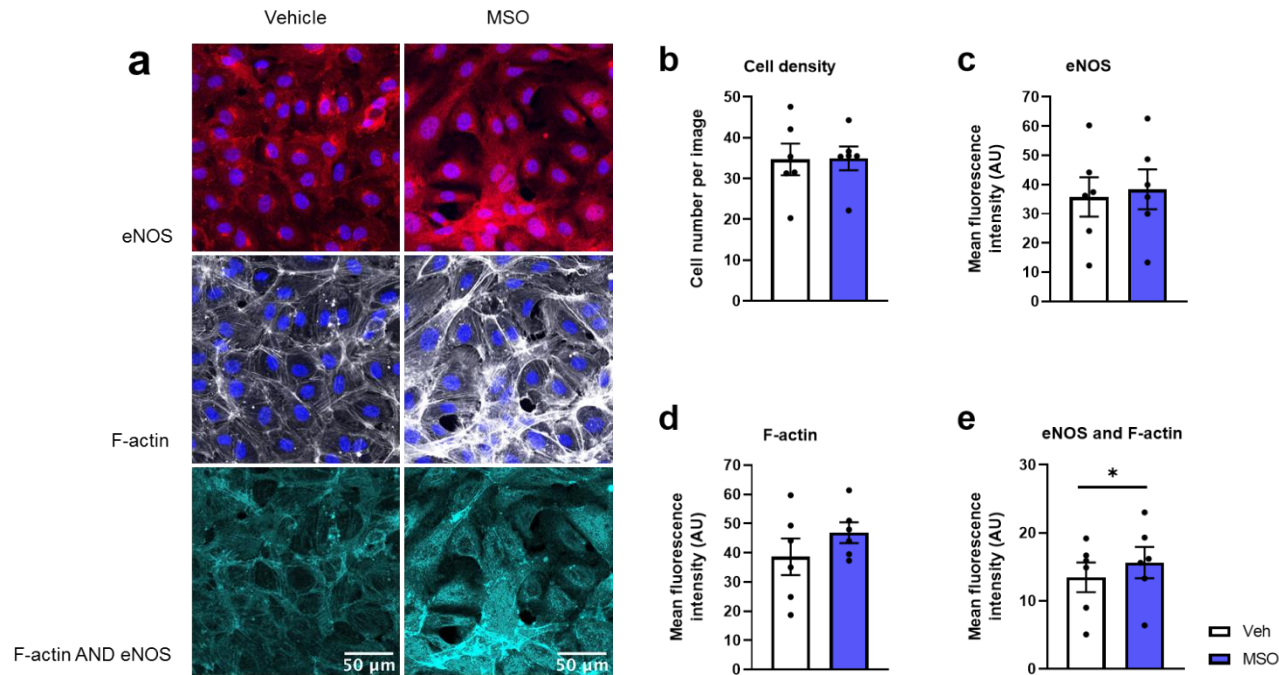


### Figure 3.25 Co-immunofluorescence of eNOS and F-actin in HUVECs with and without GS inhibition

HUVECs were treated with a vehicle control (Veh) or 1 mM MSO for 24 hrs before immunofluorescent staining (a). Scale bars represent a distance of 50  $\mu\text{m}$ . Mean fluorescence intensities of eNOS (red), F-actin (white) and DAPI (blue) were evaluated, in addition to co-immunofluorescence of F-actin and eNOS (cyan) (c, d and e respectively). DAPI signal was used to determine cell number per image (b). Black circles represent data from individual staining experiments (b, c, d, e). Data was analysed using paired t-tests ( $*p < 0.05$ ) ( $n=6$ ). Blinded assessment of immunofluorescence was performed by Dr. Richard Cubbon.

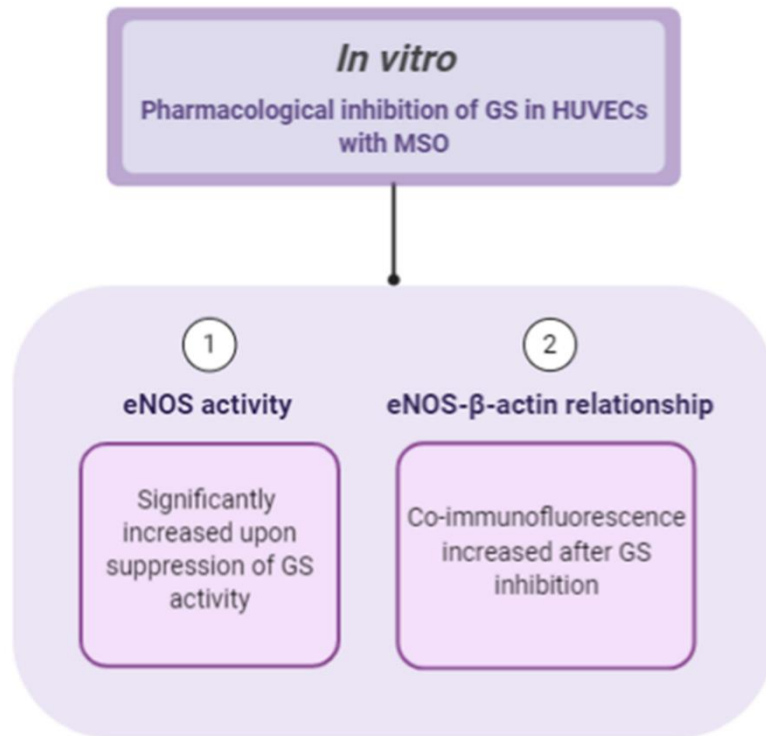


Figure 3.26 Summary of key findings from *in vitro* experiments

### 3.5 The consequences of endothelial GS deficiency on the development of atherosclerosis

It is evident from earlier chapters that altering GS has important implications for vascular phenotype, possibly mediated through increased production of NO. This may be especially significant in the context of atherosclerosis; it is well-established that NO has potent anti-atherogenic actions. Since the interaction between endothelial GS and atherosclerosis development has not previously been modelled *in vivo*, VEGA Hom and VEGA Het were generated.

As explained in section 2.2.2.4.1, a VE-Cadherin<sup>CreERT2</sup>/*ApoE*<sup>-/-</sup> male was crossed with a *GLUL*<sup>flox/+</sup>/*ApoE*<sup>-/-</sup> female to create a model with both endothelial GS haploinsufficiency and *ApoE* deletion. This line was 'VEGA Het'. From here, a model with homozygous GS knockdown in the endothelium and *ApoE* deficiency was generated, as outlined in section 2.2.2.4.2 and was called 'VEGA Hom'. For both VEGA Het and Hom, Cre negative littermates (*GLUL*<sup>flox/+</sup>/*ApoE*<sup>-/-</sup> and *GLUL*<sup>flox/flox</sup>/*ApoE*<sup>-/-</sup> respectively) were used as control animals.

At 8 weeks of age, these colonies received 12 weeks of western diet feeding to induce atherosclerotic plaque formation. This was then assessed using various histological methods.

First, the weight gain of VEGA Hom over the course of western diet feeding was assessed to define if this was influenced by endothelial GS expression. VEGA Hom and control mice displayed comparable pre and post tamoxifen weights (Figure 3.27a). Weight gain over 12 weeks of western diet was also similar between the genotypes, with no significant differences observed at any point (Figure 3.27b) (repeated measures ANOVA  $p=0.927$ ; AUC  $p=0.5381$ ).

To confirm successful knockdown of GS in endothelial cells, LECs were isolated and GS mRNA expression was analysed using RT-qPCR. LECs from VEGA Hom mice exhibited a significant reduction in GS mRNA of 62.5% compared with those collected from control counterparts ( $p=0.0072$ ) (Figure 3.28).

Glucose and insulin metabolism of VEGA Hom was investigated at the start of western diet feeding. GTT revealed almost identical responses to a glucose bolus between VEGA Hom and control mice (Figure 3.29a) and was confirmed by statistical analysis (repeated measures ANOVA  $p=0.294$ ; AUC  $p=0.2527$ ). Insulin sensitivity was also comparable between VEGA Hom and control littermates (Figure 3.29b), with no significant differences exhibited post-insulin bolus at any timepoint (repeated measures ANOVA  $p=0.834$ ; AUC  $p=0.5562$ ).

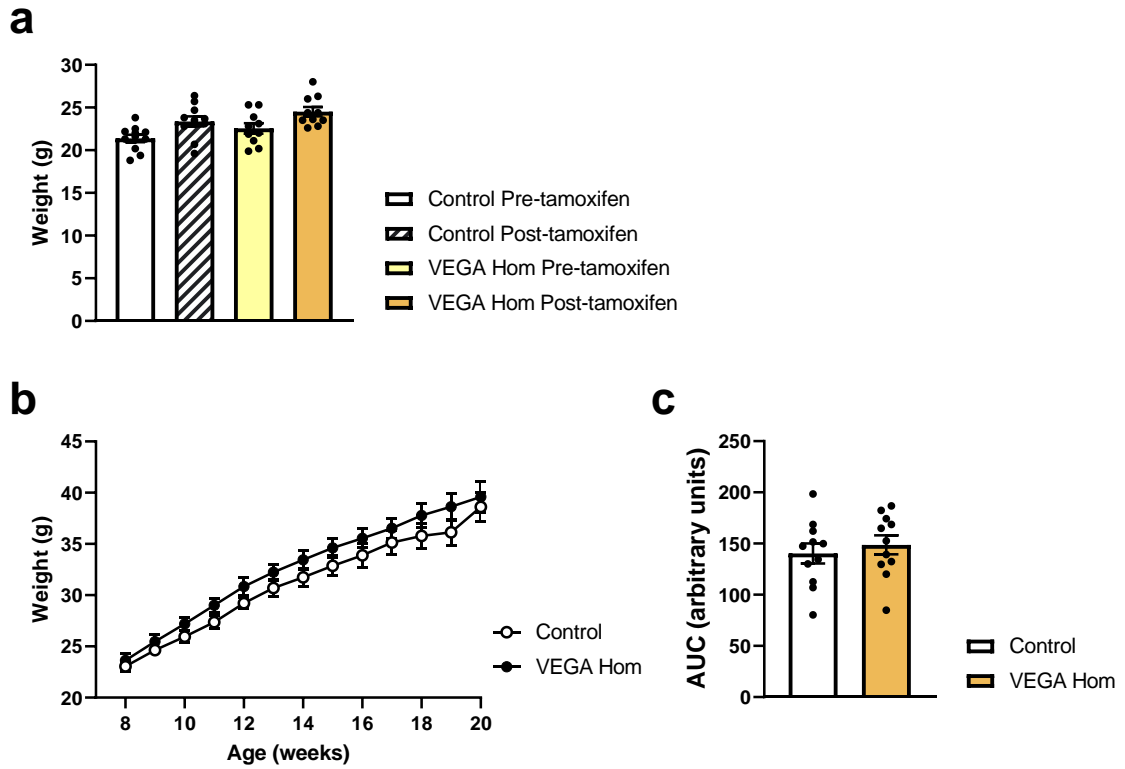


**Figure 3.27 Weight profile of VEGA Hom and control mice**

Mean body weights of control and VEGA Hom mice were recorded at 6 weeks of age on the first and last day of the 5-day tamoxifen course (a). Weights were recorded weekly for both genotypes over the 12 week western diet course (b) and data was analysed using a repeated measured ANOVA and the Sidak post-hoc test. AUC was also determined for weight data and examined using an unpaired t-test (c). In graphs a and c, black circles represent values from individual mice. (Control  $n=11$ , VEGA Hom  $n=11$ ).

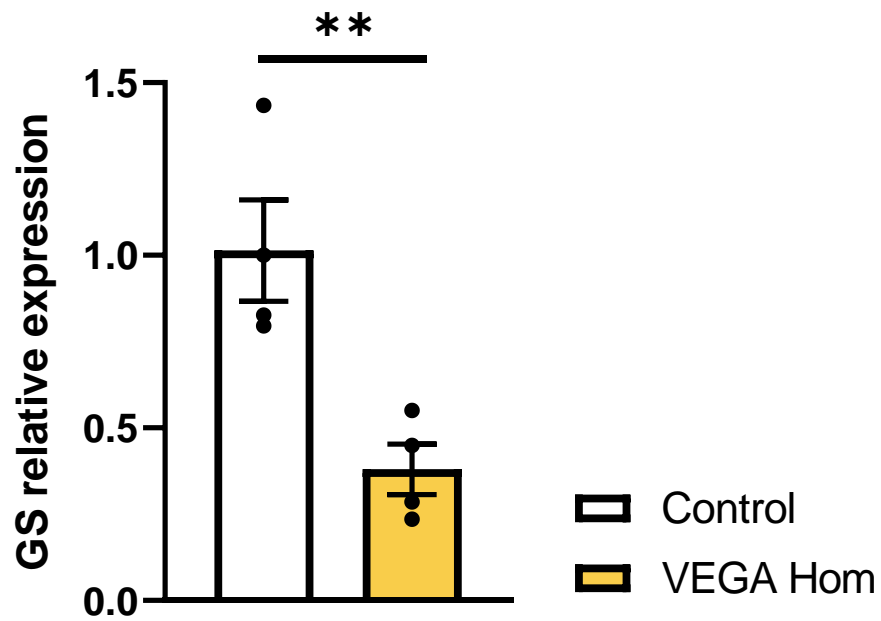


**Figure 3.28 Validation of GS knockdown in VEGA Hom endothelial cells**

LECs were collected from VEGA Hom and control littermates. Relative GS mRNA expression was analysed using RT-qPCR, with HPRT as the housekeeping gene. Black circles indicate individual data points. Data was analysed using an unpaired t-test (\*\*  $p < 0.01$ ) (control  $n=4$ ; VEGA Hom  $n=4$ ).

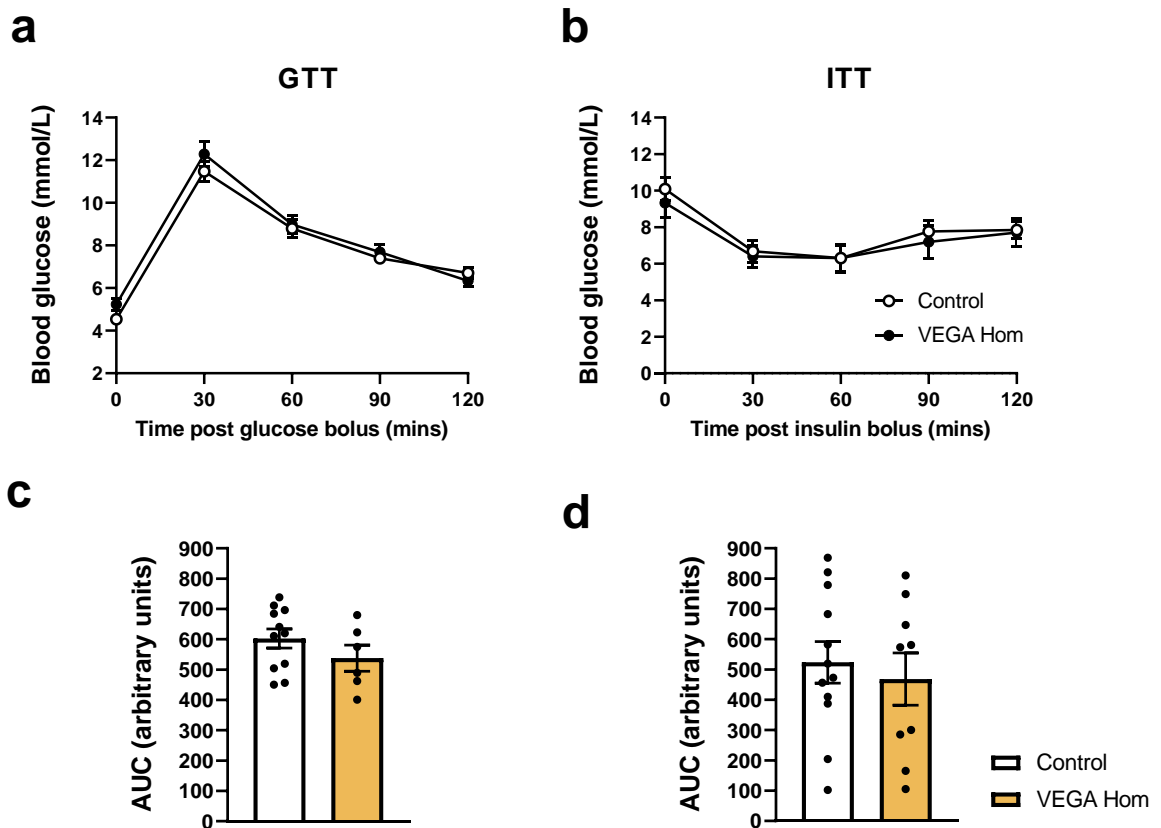


**Figure 3.29** Glucose and insulin tolerance of control and VEGA Hom mice at the start of western diet feeding

Blood glucose concentration was examined prior to and following a glucose bolus over a 2 hr period (a). Insulin tolerance was also investigated before and after insulin challenge (b). Response data from a and b were analysed using a repeated measures ANOVA, followed by the Sidak post-hoc test. Glucose and insulin tolerance were also assessed using AUC (c and d, respectively). AUC underwent statistical testing using an unpaired t-test. Black circles shown in c and d indicate individual data. (Control  $n=12$ , VEGA Hom  $n=9$ ).

Atherosclerosis development in VEGA Hom was studied using oil red O staining of dissected aortae. Fat soluble oil red O dye stains neutral triglycerides and lipids, and is a common histological method for identifying atherosclerotic lesions (Zhao et al., 2017; Chang et al., 2012).

After western diet feeding, aortae from control mice and VEGA Hom were collected and stained (Figure 3.30a and Figure 3.30b, respectively). Atherosclerotic lesions were quantified and their coverage of the aorta was calculated as a percentage of the total area of the vessel. Plaque burden in VEGA Hom was markedly decreased, displaying  $3.5 \pm 0.3\%$  coverage, compared with  $5.6 \pm 0.9\%$  in controls, which equates to a relative reduction of 37.6% ( $p=0.04$ ) (Figure 3.30c). VEGA Hom and controls exhibited no significant differences in aortic length, with mean measurements of  $3.663 \pm 0.07$  cm and  $3.662 \pm 0.04$  cm recorded, respectively ( $p=0.6708$ ) (Figure 3.30d).

The formation of atherosclerotic lesions was also examined at the level of the aortic sinus. Hearts were collected from VEGA Hom and control mice and embedded in paraffin, before sectioning and Miller van Gieson staining. Using Image-Pro Plus 7.0, the area of the aortic sinus with plaque coverage was determined. Comparison of VEGA Hom and controls revealed a significant relative reduction of 31.6% in sinus plaque coverage in VEGA Hom ( $17.7 \pm 3.0\%$  versus  $25.9 \pm 1.5\%$  respectively;  $p=0.048$ ) (Figure 3.31).

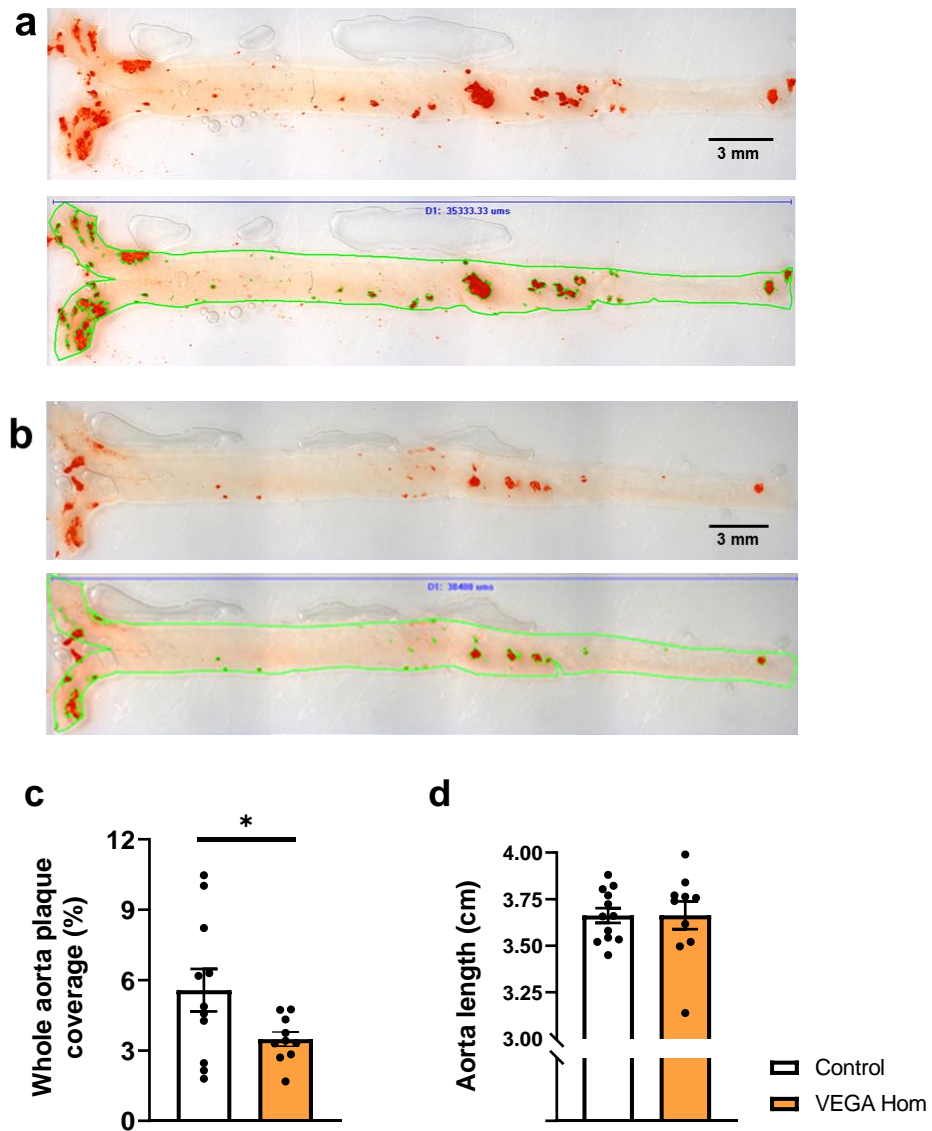


**Figure 3.30 Aortic atherosclerotic plaque burden in control and VEGA Hom mice following 12 weeks of western diet**

The extent of atherosclerosis development was determined using oil red O staining. Representative images for control mice (a) and VEGA Hom (b) are presented, as are corresponding areas of analysis. Scale bars represent a distance of 3 mm. Blue lines show the length of the specimen. Green lines outline both the field analysed and the areas detected as plaques. Plaque burden quantification is displayed in c. Aortic length was also recorded (d). The data of c and d were analysed using unpaired t-tests. Individual data values are shown by black circles. (\* $p < 0.05$ ) (control  $n = 11$ ; VEGA Hom  $n = 10$ ).

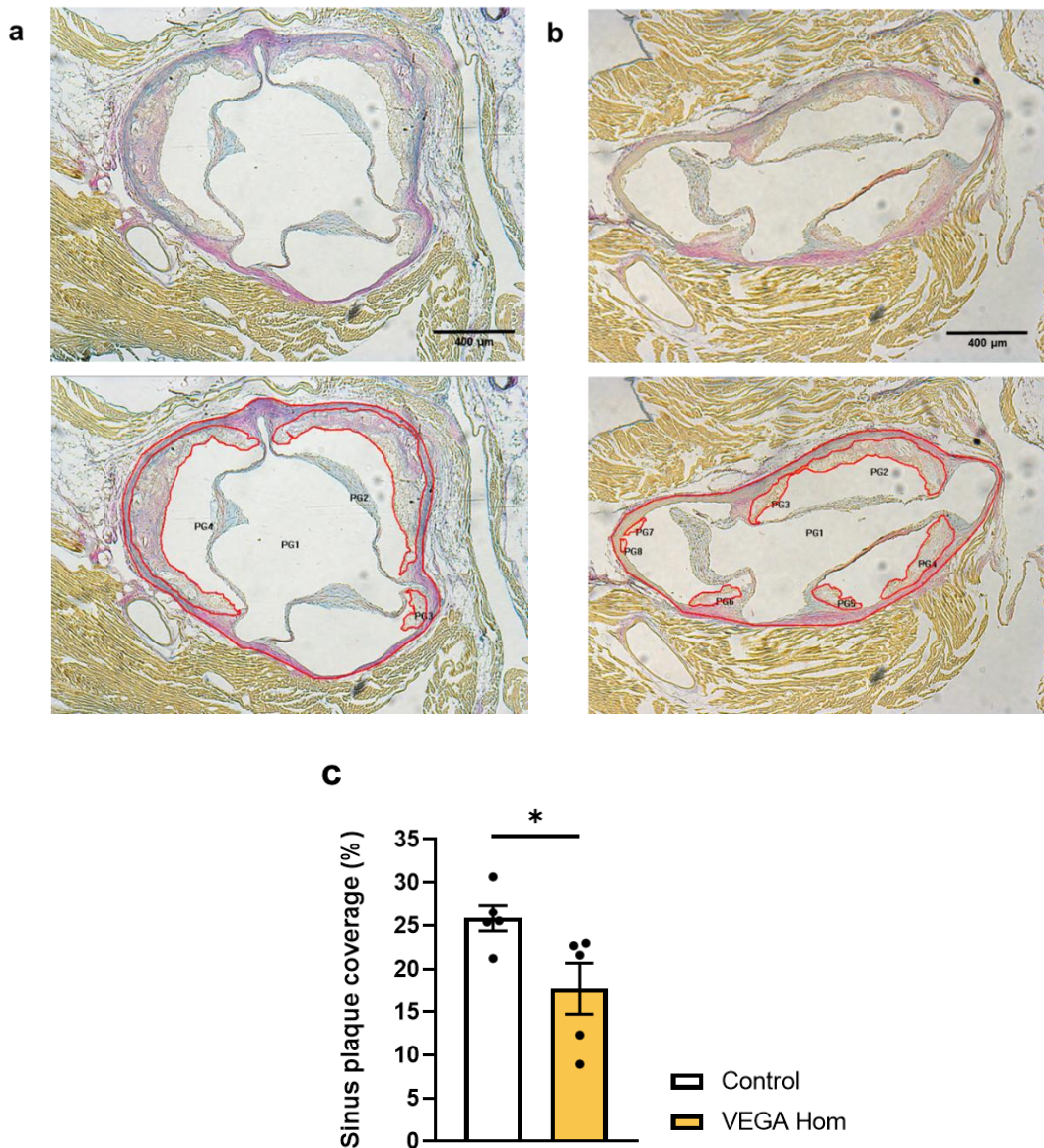


**Figure 3.31 Atherosclerotic lesion development within the aortic sinus of VEGA Hom and control mice**

Sections of aortic sinus were stained with Miller van Gieson. Representative brightfield microscopic images are shown for control and VEGA Hom ((a) and (b) respectively), along with their areas of analyses. In analysis images, 'PG' stands for 'polygon'. Scale bars represent 400  $\mu\text{m}$ . Elastic fibres and cell nuclei stain blue to black, collagen stains pink to red and other tissues appear yellow. The quantification of sinus plaque coverage is displayed in (c) and was analysed using an unpaired t-test ( $*p < 0.05$ ). Data from individual aorta is shown by black circles. (Control  $n=5$ ; VEGA Hom  $n=5$ ).

As with VEGA Hom, the weight gain of VEGA Het mice during western diet feeding was monitored to ensure this was comparable to controls. VEGA Het weight before and after tamoxifen did not differ significantly from controls. Weight gain over 12 weeks of feeding also revealed no significant difference between genotypes (Figure 3.32) (repeated measures ANOVA  $p=0.673$ ; AUC  $p=0.6114$ ).

At the beginning of the western diet course, VEGA Het and control mice exhibited similar blood glucose profiles during GTT (Figure 3.33a), with no significant difference in measurements (repeated measures ANOVA  $p=0.538$ ; AUC  $p=0.0662$ ). Regarding insulin tolerance, VEGA Het appeared to be slightly more sensitive to insulin (Figure 3.33b), but statistical testing of response to the insulin bolus revealed no significant difference between genotypes (repeated measures ANOVA  $p=0.246$ ; AUC  $p=0.5562$ ).

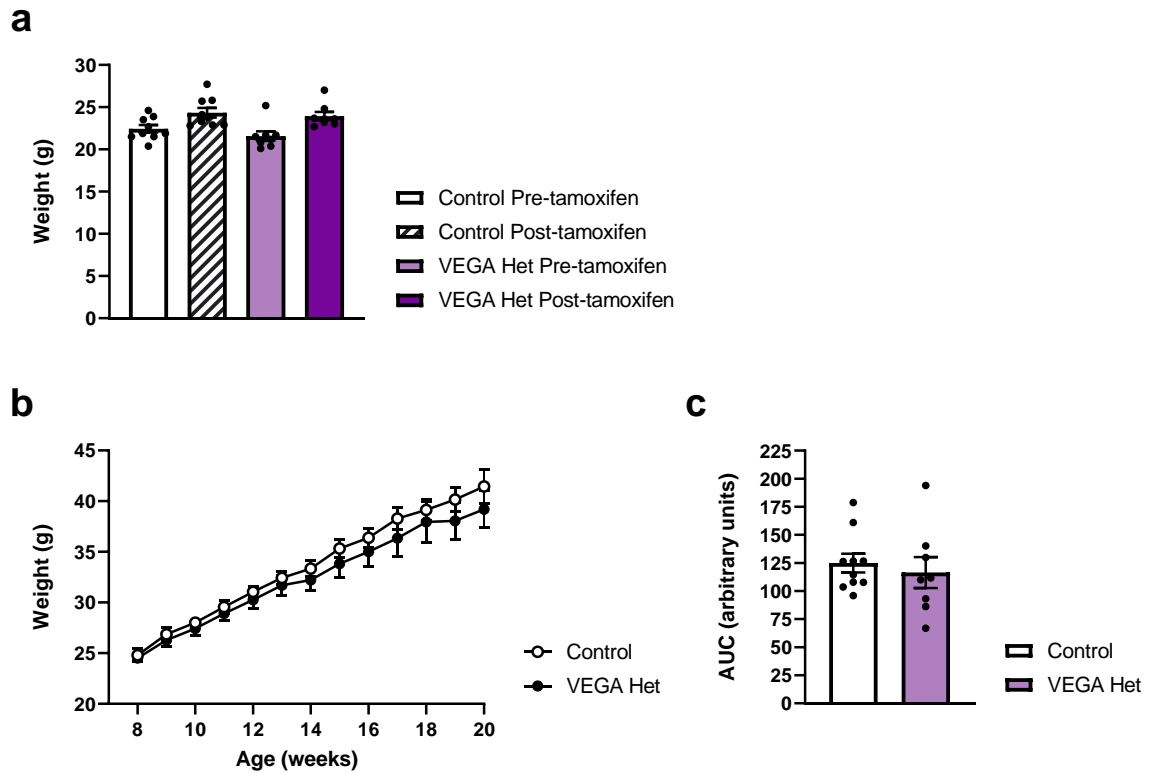


**Figure 3.32 Weight profile of VEGA Het and control mice**

Body weights of control mice and VEGA Het were recorded at 6 weeks of age on the first and last day of the 5 day tamoxifen course (a). Weights of controls and VEGA Het were documented on a weekly basis over the 12 weeks of western diet feeding (b). Weight data was tested using a repeated measures ANOVA and the Sidak post-hoc test. AUC for weight gain data was also calculated and analysed using an unpaired t-test (c). In a and c, values from individual mice are depicted by black circles. (Control  $n=9$ , VEGA Het  $n=8$ ).

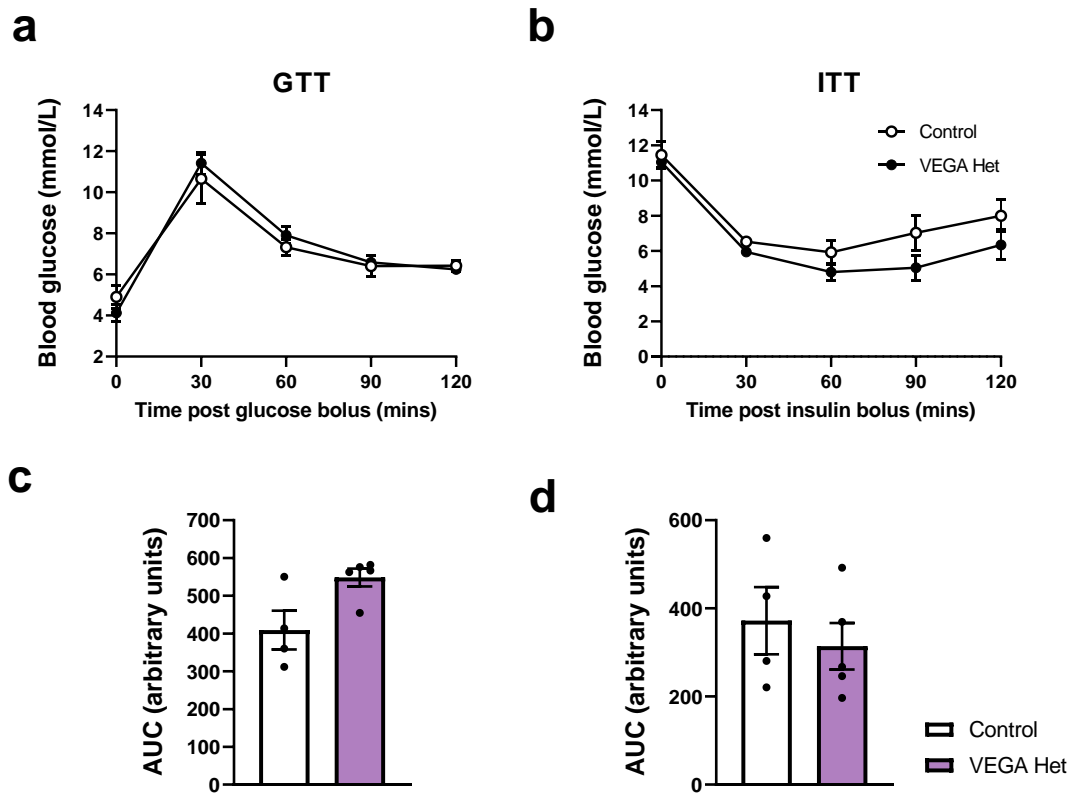


**Figure 3.33** Glucose and insulin tolerance of control and VEGA Het mice at the start of western diet feeding

Measurement of blood glucose concentration was undertaken prior to and post glucose challenge over a 2 hr period (a). This was also done following insulin injection to define insulin tolerance (b). A repeated measures ANOVA and the Sidak post-hoc test was used to analyse the data presented in a and b. AUC data was also determined for both glucose (c) and insulin tolerance (d) data and compared with unpaired t-tests. In c and d, black circles indicate individual data. (Control  $n=4$ , VEGA Het  $n=5$ ).

Following 12 weeks of western diet feeding, aortae were harvested and stained with oil red O (Figure 3.34). Plaque burden was quantified as outlined in section 2.2.16.2. The percentage area of the aorta containing atherosclerotic plaque was significantly decreased in VEGA Het mice ( $4.3 \pm 0.5\%$ ) versus controls ( $6.5 \pm 0.6\%$ ) ( $p=0.0102$ ) (Figure 3.34c). No difference in aortic length was seen between genotypes (VEGA Het:  $3.58 \pm 0.07$  cm; control:  $3.66 \pm 0.03$  cm;  $p=0.3441$ ) (Figure 3.34d).

Atherosclerosis was examined at the aortic sinus using Miller van Gieson staining. Despite detection of an obvious difference in plaque occurrence across the whole aorta defined with oil red O, no significant alteration was seen at the sinus, with VEGA Het exhibiting  $16.55 \pm 1.69\%$  sinus plaque coverage, compared with  $19.6 \pm 2.46\%$  in control mice ( $p=0.34$ ) (Figure 3.35).

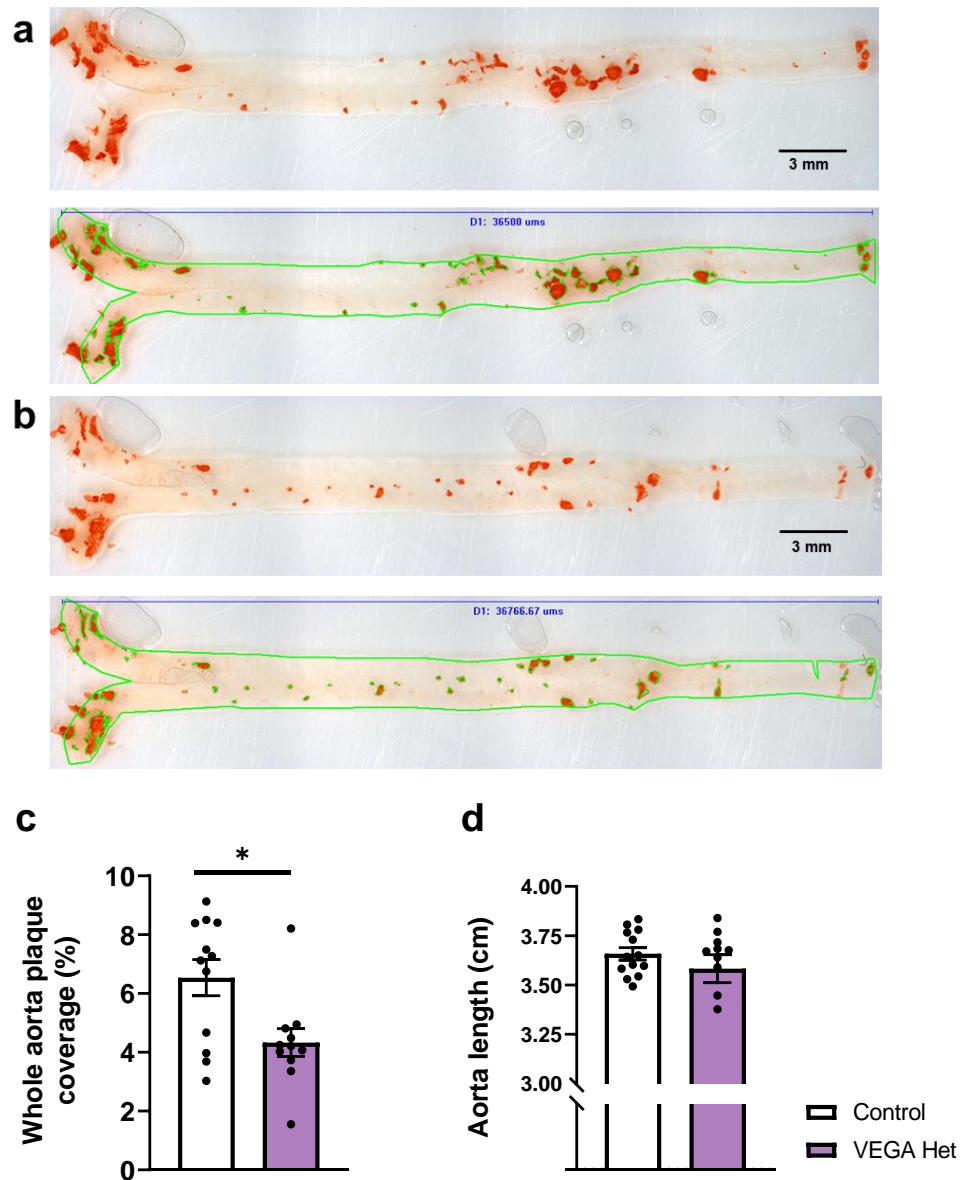


**Figure 3.34 Aortic atherosclerosis development in control and VEGA Het mice following 12 weeks of western diet feeding**

Plaque burden was assessed using oil red O staining. Representative images for controls (a) and VEGA Het (b) are shown, along with their corresponding areas of analysis. Scale bars represent a distance of 3 mm. The blue line shows aortic length. The region of the aorta considered the field of analysis, and the areas detected as plaques within this field, are bordered by green lines. Quantification of aortic plaque coverage was calculated (c). The length of aorta specimens were also recorded (d). Statistical testing of c and d was conducted with unpaired t-tests. Black circles indicate values from individual aorta. (\* $p < 0.05$ ) (control  $n = 13$ ; VEGA Het  $n = 11$ )

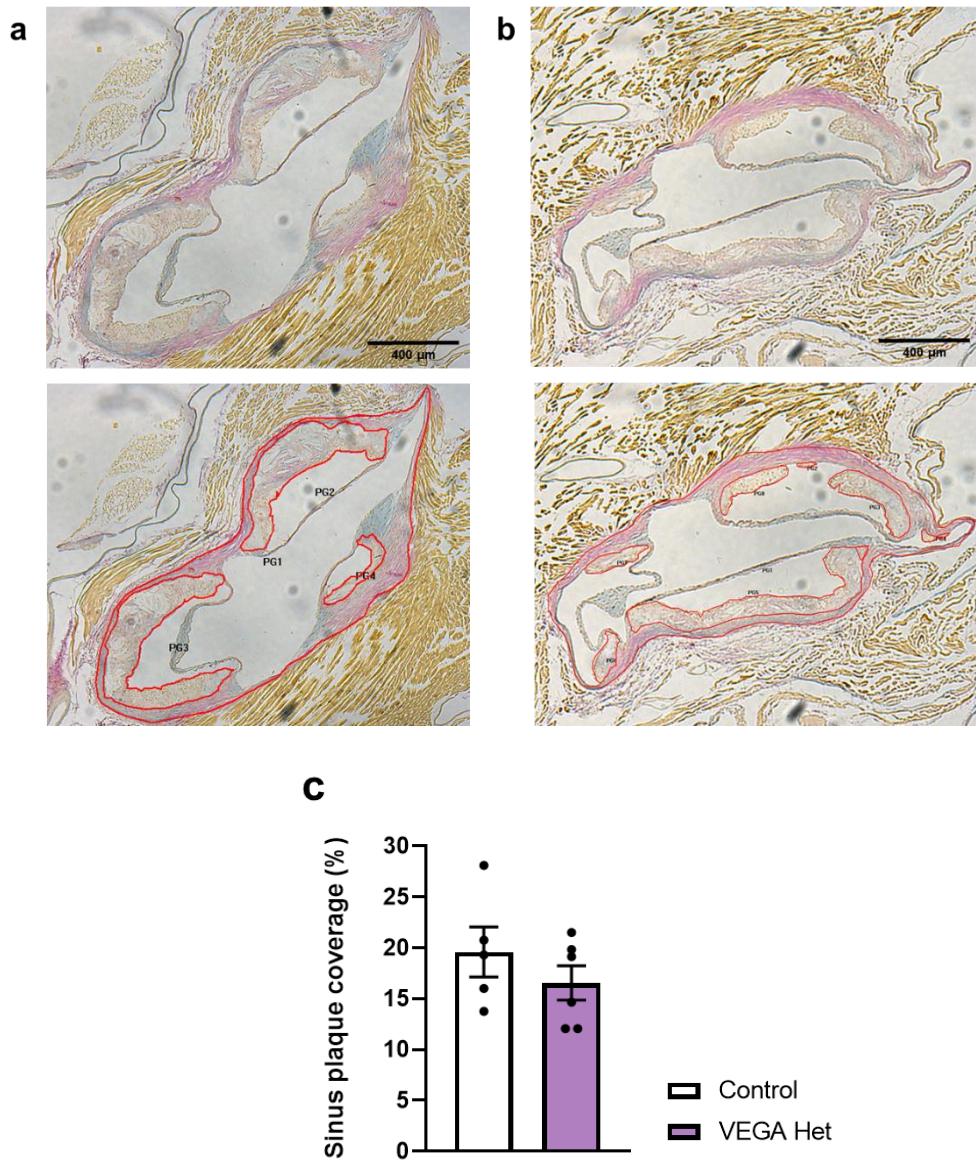


**Figure 3.35 Atherosclerotic lesion development at the level of the aortic sinus in VEGA Het and control littermates**

Representative brightfield microscopy images and their corresponding areas of analysis are presented for control (a) and VEGA Het (b) aortic sinus sections following Miller van Gieson staining. In analysis images, 'PG' stands for 'polygon'. Scale bars represent 400 µm. Elastic fibres and cell nuclei appear blue to black, collagen stains pink to red and yellow staining indicates other tissue types. Quantification of plaque coverage is shown in c, which was analysed using an unpaired t-test. Black circles represent individual data. (Control  $n=5$ , VEGA Het  $n=6$ )

### **3.6 Examining the influence of endothelial GS holoinsufficiency on diabetic vascular disease *in vivo***

To capture diabetic vascular disease and assess the effect that diminished endothelial GS has on its progression, STZ was administered to VEGA Hom and control mice at the start of western diet feeding.

Daily, single dose injections of STZ were conducted over 5 consecutive days. Weights and NFBG measurements were measured on day 1 and day 5 of STZ administration and then recorded weekly for the succeeding 4 weeks. Mice were deemed diabetic when NFBG exceeded 11.1 mmol/L.

Both VEGA Hom and control mice exhibited a small degree of weight loss over the 5 day STZ treatment, as expected, but this was not significant for either group (Figure 3.36a). No difference in NFBG prior to STZ was seen between genotypes (Figure 3.36b). In the 4 weeks following the STZ course, while VEGA Hom were consistently lower in weight compared with controls (Figure 3.36c), this was not statistically significant (repeated measures ANOVA  $p=0.587$ ; AUC  $p=0.158$ ). With respect to NFBG, a large elevation was displayed in both VEGA Hom and controls 4 weeks after STZ administration, which surpassed the threshold indicating the presence of diabetes (Figure 3.36d). The degree of increase between VEGA Hom and control littermates was similar, implying comparable sensitivity to STZ.

Following STZ and 12 weeks of western diet feeding, aortae were harvested from VEGA Hom and control mice and stained with oil red O. Plaque coverage of the whole aorta was calculated. This preliminary data suggests there is a trend towards reduced atherosclerotic plaque formation in VEGA Hom given STZ and western diet, compared to control mice receiving the same treatment ( $3.5 \pm 1.2\%$  versus  $5.2 \pm 1.2\%$  respectively;  $p=0.366$ ). The data does not show statistical significance, but this experiment is currently underpowered. Aortic length was similar between genotypes (Figure 3.37).

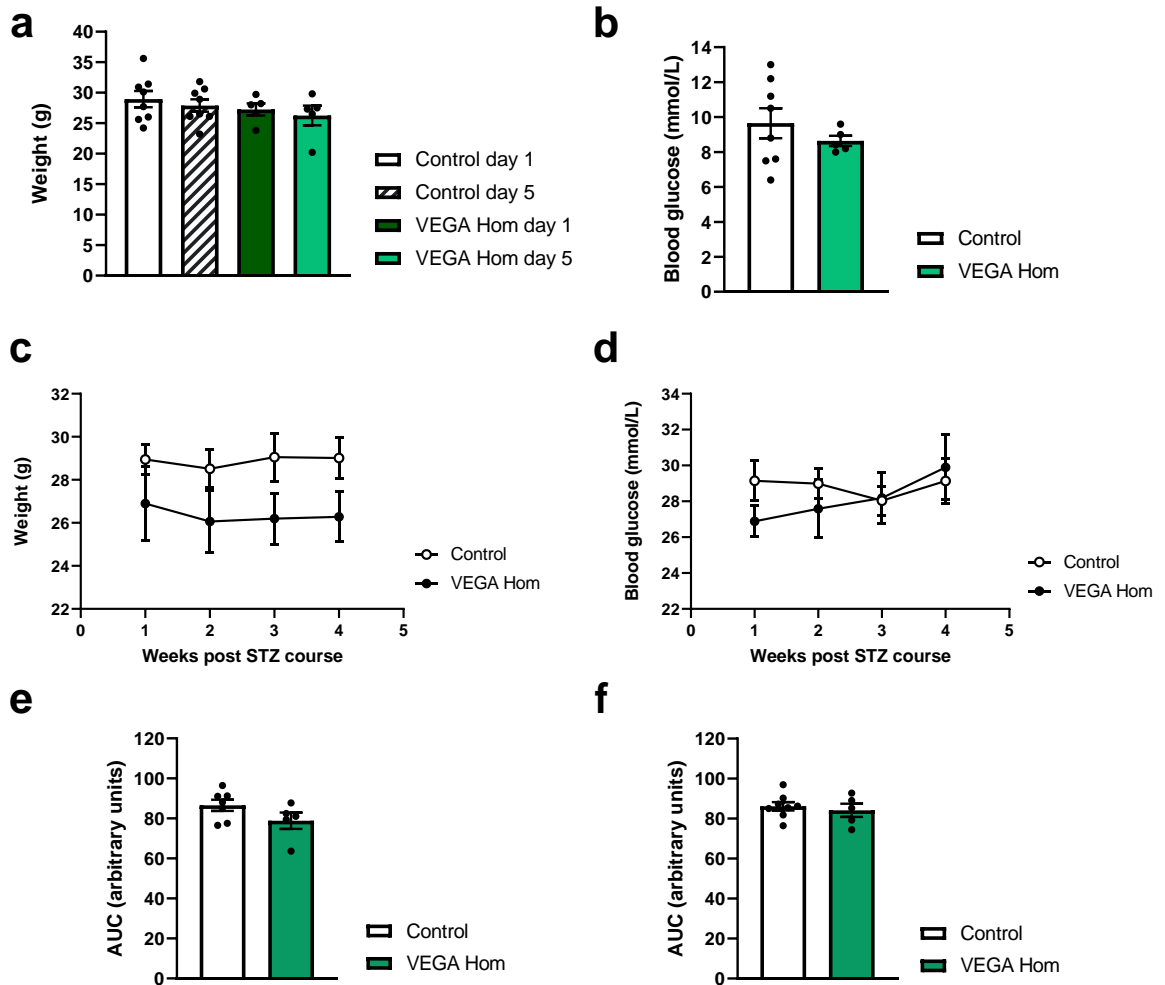


**Figure 3.36 Metabolic profile of VEGA Hom and control mice treated with STZ and receiving western diet**

STZ was administered in single daily injections over 5 consecutive days. Weight was recorded on day 1 and day 5 of the STZ course (a). NFBG was also measured on day 1 prior to injections (b). VEGA Hom and control weights were then monitored over 4 weeks following STZ administration (c). The same was done for NFBG (d). The data of c and d was tested using a repeated measures ANOVA and the Sidak post-hoc test. AUC was calculated for c and d (shown in e and f, respectively) and analysed with unpaired t-tests. Black circles indicate individual data (a, b, e, f). (Control  $n=8$ ; VEGS Hom  $n=5$ )

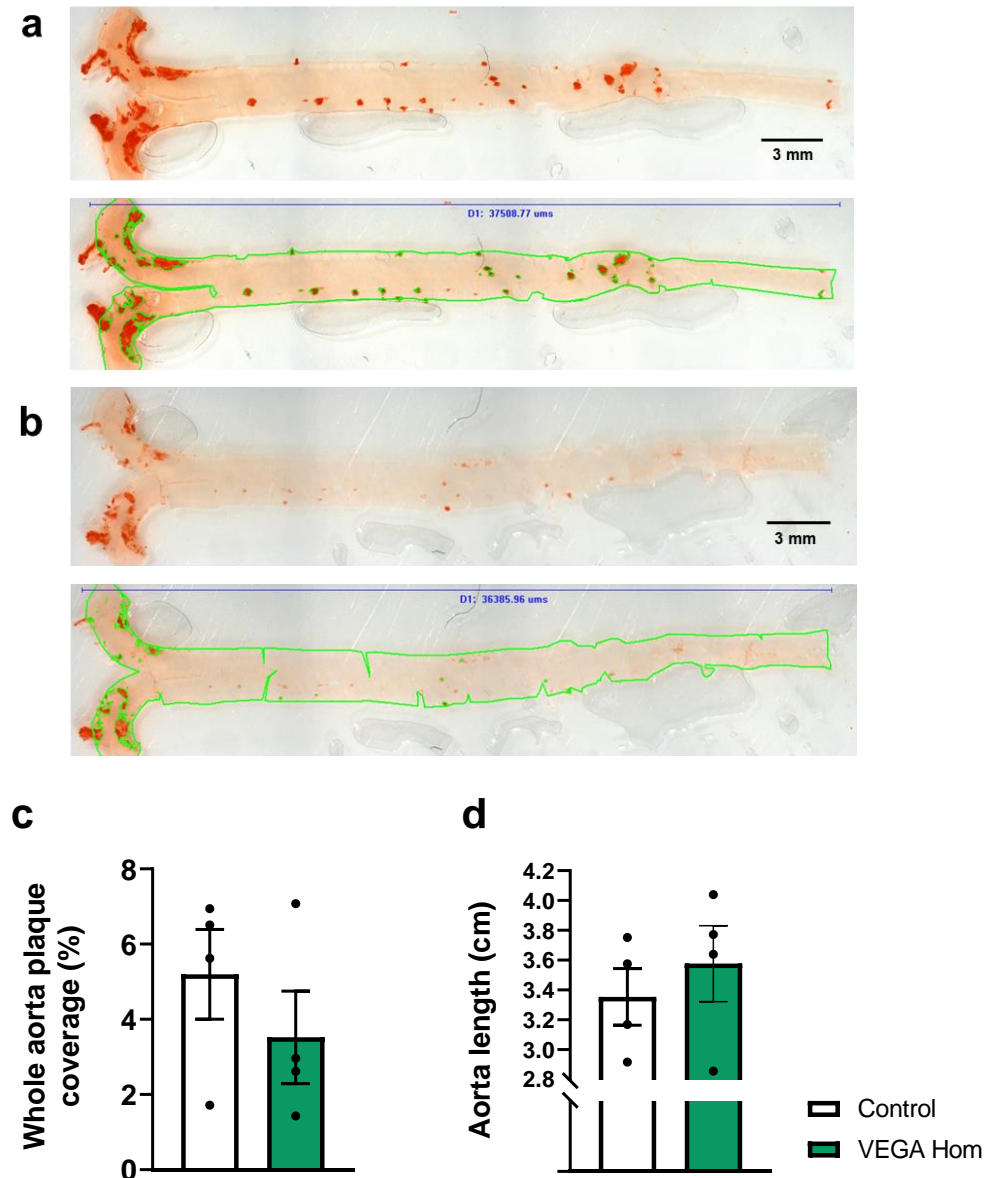


**Figure 3.37 Whole aortic atherosclerosis development in VEGA Hom and control mice treated with STZ and receiving 12 weeks of western diet**

Plaque burden was assessed using oil red O, with representative images for control and VEGA Hom displayed in (a) and (b) respectively, along with corresponding areas of analysis. Scale bars represent a distance of 3 mm. Blue lines indicate aorta length. Green lines border both the region of interest, and the areas within it that were detected as red-stained plaques. Mean atherosclerotic plaque area was quantified (c). Aortic length was also recorded (d). In c and d, individual data is shown with black circles and results were analysed with an unpaired t-test. (Control  $n=4$ ; VEGA Hom  $n=4$ ).

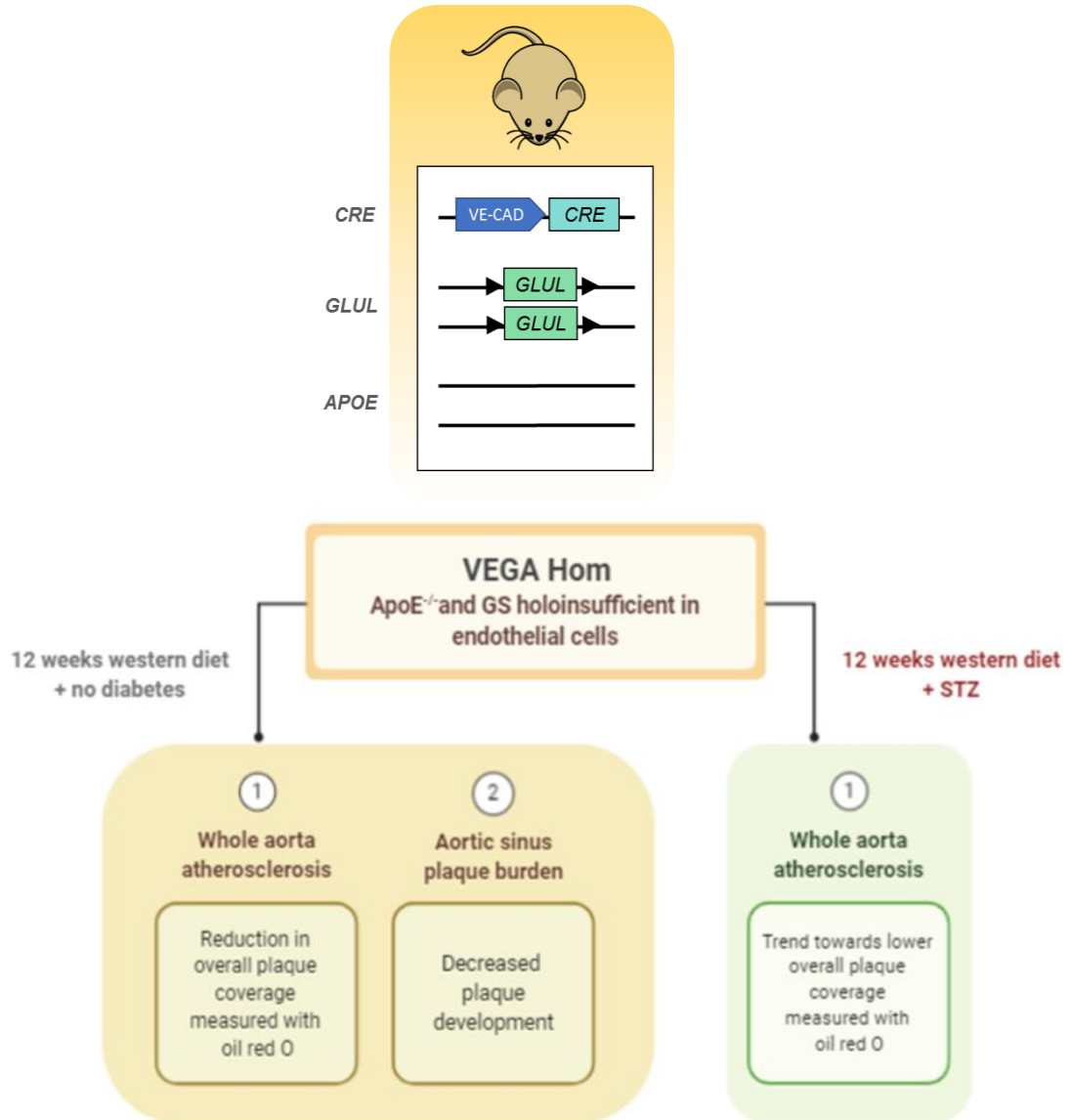


Figure 3.38 Summary of key findings from VEGA Hom experiments

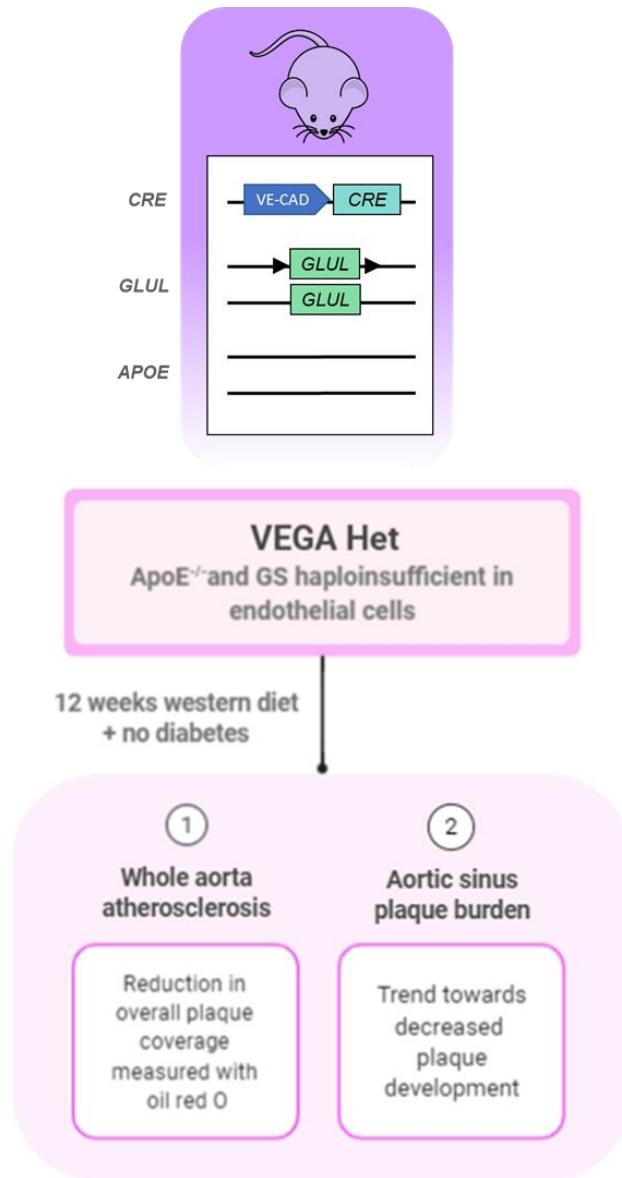


Figure 3.39 Summary of key findings from VEGA Het experiments

## Chapter 4 Discussion

### 4.1 Key findings

This project was undertaken with the intention of elucidating the role of endothelial GS in the vascular system, both in a healthy physiological context and that of atherosclerosis and diabetes. Since altered GS expression has been observed in vascular disease, unearthing its role in the endothelium may aid in guiding the advent of more efficacious and personalised treatments targeting cardiovascular disease and diabetes.

Initial investigations were conducted using VEGS Hom mice, which are a model of GS holoinsufficiency exclusively in endothelial cells. These mice had previously been validated by Eelen et al. (2018), who discovered that endothelial GS deficiency resulted in impaired endothelial motility and disrupted angiogenic sprouting.

For the first time, this work has linked reduced endothelial GS expression with amplified NO bioavailability. VEGS Hom display an attenuated aortic vasoconstriction response to PE, which is lost in the presence of the NOS inhibitor, L-NMMA. The argument for increased NO production *in vivo* was also supported by decreased systolic, diastolic and mean blood pressures. Interestingly, however, endothelial regenerative capacity remained unchanged following denuding wire-injury of the femoral artery.

Upon induction of diabetes with STZ, VEGS Hom exhibited comparable vasoconstriction responses to PE compared to control mice. This was also the case following NOS inhibition, pointing to a loss of their increased NO bioavailability in the presence of diabetes.

Development of VEGS Het, an endothelial GS haploinsufficient mouse, allowed further evaluation of the influence of GS on vascular function. With the exception of neutral findings after vascular injury, the aforementioned observations in VEGS Hom were not recapitulated in VEGS Het. This suggests that a threshold of endothelial GS knockdown must be achieved to alter NO bioavailability.

Examination of the role of endothelial GS has not previously been carried out in the context of atherosclerosis *in vivo*, either in the absence or presence of

diabetes. This was motivation for crossing both VEGS Hom and VEGS Het with mice of an ApoE knockout background, to create VEGA Hom and VEGA Het, respectively. After western diet feeding, a clear reduction in atherosclerosis development was noted in VEGA Hom and VEGA Het. Preliminary data from VEGA Hom with STZ-induced diabetes also hints at decreased plaque burden.

In addition to the *in vivo* studies, pharmacological GS inhibition with MSO in HUVECs was utilised to define the underlying cellular mechanisms responsible for the observations mentioned earlier. *In vitro* data supported a role for endothelial GS in regulating NO availability; MSO-treated HUVECs exhibited higher basal eNOS activity and an increase in eNOS- $\beta$ -actin colocalisation.

Altogether, the whole animal and cellular models of reduced GS within the endothelium point to an important role for the enzyme in regulating endothelial function.

## 4.2 The effect of endothelial-specific GS holoinsufficiency on vascular function

### 4.2.1 Vasomotor function

Eelen et al. (2018) have shown, using VEGS Hom, that decreased endothelial GS expression inhibits sprouting angiogenesis by suppressing plasma membrane localisation of RhoJ, which requires GS-catalysed RhoJ palmitoylation. However, the model has not previously been employed to study the effect of endothelial GS deficiency on vasomotor function, either *ex vivo* or at whole animal level. This was accomplished in this project.

Firstly, organ bath apparatus was utilised. Such equipment is an established and reliable method for investigating tissue contractility. Here, it allowed the vasomotor profile of the aorta to be investigated, a parameter which could not have been replicated *in vitro*. The short time between harvesting tissue and placement in the organ bath allowed for a relevant physiological response to be retained.

Examination of aortic rings revealed that VEGS Hom exhibit a significantly reduced contractile response to PE. When repeated in the presence of L-NMMA, a NOS inhibitor, VEGS Hom vasoconstriction was comparable to that of control mice, suggesting that amplified basal NO availability underpins the reduced basal tone of VEGS Hom. Additionally, systolic, diastolic and mean blood pressure readings from VEGS Hom were all significantly lower than those taken from control mice, further supporting the possibility of increased basal NO availability *in vivo*.

Upon investigation of aortic ring response to Ach, the degree of vasorelaxation was no different between VEGS Hom and control littermates. Ach induces eNOS activity through calmodulin activation. These results demonstrate that stimulated NO production via calmodulin is unchanged between genotypes. Vascular smooth muscle responsiveness to exogenous NO was also unaltered in VEGS Hom, as shown by similar relaxation responses to the NO donor, SNP.

Other research findings indirectly support the notion that disruption of GS expression could impact NO availability in the vasculature. Glutamine is thought

to downregulate the activity of ASS, a urea cycle enzyme responsible for re-synthesising arginine (Okada et al., 2000). Attenuation of GS action, and the subsequent drop in the levels of glutamine, may lead to an increase in ASS activity. This in turn would cause a rise in arginine available for eNOS-directed NO production. However, whilst plausible, this seems unlikely; Eelen et al. (2018) found that endothelial GS silencing did not alter cytoplasmic glutamine content, and furthermore, that endothelial GS synthesised very little glutamine in basal conditions.

The use of catalase in further organ bath experiments with VEGS Hom aortic tissue did not reveal any additional mechanism of reduced vessel tone, beyond the previously described higher basal NO. The decreased maximal contractile response of VEGS Hom to PE was still detected following exposure to PE in the presence of catalase, implying that increased H<sub>2</sub>O<sub>2</sub> concentrations are unlikely to be responsible for the more relaxed vascular phenotype of VEGS Hom.

#### **4.2.2 Endothelial regeneration**

NO is documented to encourage endothelial cell migration and proliferation, processes vital for angiogenesis and vessel repair. Inhibition of NO with N<sup>ω</sup>-nitro-L-arginine methyl ester (L-NAME) prevents endothelial cell migration *in vitro*, as well as impairing expression of integrin αvβ3, which contributes to cell-to-cell interactions required for movement of endothelial cells (Murohara et al., 1999). Application of NO donors to cultured endothelial cells has also been observed to enhance their proliferative capacity (Guo et al., 1995). Given the possible elevation in basal NO availability, it may be expected that VEGS Hom would exhibit improved endothelial repair following denudation. However, endothelial-specific GS holoinsufficiency did not translate into enhanced endothelial regeneration, with no significant difference in levels of repair displayed after wire-injury surgery when compared to the control group. RhoJ-dependent disruption of the cytoskeleton and cell motility, seen with deletion of GS in the endothelium (Eelen et al., 2018), may underlie these findings, with repair mechanisms encouraged by NO offset by impaired endothelial cell migration. Furthermore, alterations in GS expression are thought to impact on autophagy. This process,

by which cells degrade defective organelles and proteins, is an important survival mechanism and its disruption has been reported in several pathologies (Glick et al., 2010). Upregulation of GS results in inhibition of mTOR signalling and increased autophagy (van der Vos & Coffey, 2012). It is feasible, therefore, that endothelial GS knockdown may lead to autophagy suppression. Impairment of autophagy has been linked to defective endothelial cell alignment, along with exacerbated apoptosis (Vion et al., 2017). This may have occurred in the endothelium of VEGS Hom following denuding injury and counteracted theoretical benefits of increased basal NO.

#### **4.2.3 Expression of eNOS and phosphorylated eNOS S1177**

While meaningful statistical analysis could not be conducted due to small sample size, immunoblotting suggests that eNOS expression is not upregulated in VEGS Hom aortic tissue. This supports the possibility that enhanced eNOS activity causes the increased NO bioavailability, rather than elevated absolute eNOS protein concentrations. p-eNOS S1177 also appears to be suppressed in VEGS Hom, which would indicate that changes in eNOS activity are associated with the basal activity of the enzyme, and not its capacity to be stimulated. This reinforces the results of VEGS Hom vasomotor studies, where no significant difference between relaxation response to Ach were noted between transgenic and control mice. Such findings are potentially complemented by previous investigations. Eelen et al. (2018) detected enhanced ROCK signalling upon endothelial GS knockdown and Hassona et al. (2010) demonstrated a reduction in both eNOS expression and phosphorylation in murine mesenteric arteries following ROCK activation.

#### **4.2.4 NO metabolism**

Given the observations from organ bath experiments, it may also be predicted that an increase in basal NO production would be reflected in higher serum NO<sub>x</sub> concentrations from VEGS Hom mice. Indeed, studies which have generated transgenic mice models with upregulated eNOS-mediated NO production

document higher NO<sub>x</sub> levels in blood plasma (Cantalupo et al., 2015). This was not the case for this project, with no significant difference recorded between VEGS Hom and control littermates.

NO has an extremely short half-life in blood, at less than 1 second (Bryan & Grisham, 2007). Consequently, determining NO levels often relies on measuring its metabolites. The main pathway for NO metabolism is oxidation to nitrite and nitrate and the concentration of these molecules in blood is often used as an indicator of eNOS activity (Bryan & Grisham, 2007). However, it is important to consider that NO metabolism does not exclusively involve conversion to nitrate and nitrite, and that these substances themselves are subject to degradation. NO, nitrate and nitrite readily interact with protein thiols and secondary amines, creating *S*-nitrosothiols and *N*-nitrosamines, respectively (Bryan & Grisham, 2007). Nitrate and nitrite concentrations are also influenced by renal clearance and animal dietary nitrate intake, so care must be taken when comparing to other transgenic models with altered NO manufacture (Luiking et al., 2005; Bryan & Grisham, 2007; Luiking et al., 2010).

#### **4.2.5 eNOS activity**

With regard to eNOS activity measured in LECs with <sup>14</sup>C-radiolabelled arginine, or with <sup>14</sup>C-radiolabelled arginine in the presence of insulin, there was a trend towards increased activity in VEGS Hom LECs in comparison to those from control mice, but this did not reach statistical significance. It should be noted, however, that this data set was hampered by low sample size. It is also conceivable that LECs experienced some loss of their original phenotype through culturing. Additionally, for adequate growth of LECs to be achieved, MV2 media was used which contains concentrations of glutamine that are higher than those seen physiologically in the blood. Increases in glutamine availability cause downregulation of GS expression (Eelen et al., 2018), so it is possible that GS protein levels in control mice LECs were reduced closer to that of VEGS Hom, thereby confounding results. Another limitation of this experimental set-up is the use of LECs. There is considerable phenotypic heterogeneity amongst endothelial cells from different vascular beds and this extends to the distribution

of both eNOS and GS. For example, eNOS is primarily localised to the Golgi body in endothelial cells of the endocardium. In myocardial endothelial cells, by contrast, eNOS is found to be more evenly spread through the cytoplasm (Andries et al., 1998). The subcellular location of eNOS heavily influences its activity (Boo et al., 2006; Wang et al., 2009; Radulović et al., 2020). There may be distinct differences between the areas of eNOS localisation seen in the endothelium of the aorta and the liver, which could have impacted on the activity levels seen here. Recent single cell RNA sequencing studies have shown that GS expression is highly enriched in the arterial endothelium (Kalucka et al., 2020). Beyond suggesting an important role of endothelial GS in arterial function, these data suggest arterial endothelial cells may be a better *in vitro* model. Those from the aorta, for example, represent a more appropriate physiological system and would complement the use of aortic rings in organ bath experiments. However, the endothelial cell yield from murine aorta would be low, making them highly challenging to culture.

#### **4.2.6 Vascular reactivity following STZ treatment**

Preliminary work looking at the interaction between diabetes and endothelial GS holoinsufficiency was performed using the STZ model. STZ is a potent diabetogenic agent, with its effects exerted mainly through alkylation of pancreatic  $\beta$ -cell DNA (Szkudelski 2001). VEGS Hom and control littermates were injected with STZ and aorta contractility was assessed in the organ bath one month after mice were verified to have diabetes. Diabetic VEGS Hom exhibited near identical PE constriction responses to diabetic control mice. VEGS Hom displayed a slightly reduced degree of vasoconstriction when PE was administered after L-NMMA incubation, but this was not significant. This was also the case for vasorelaxation following Ach and SNP.

Given the preliminary nature of these findings, it is difficult to make definite judgements about the role that GS may play in vascular function in a diabetic setting. However, a comparable contractile response to PE between VEGS Hom and controls, in contrast to the lower constriction of VEGS Hom mice without diabetes, may not be surprising when one considers that heightened oxidative

stress is a classic characteristic of diabetes (Fernandes et al., 2016). As outlined earlier, such conditions cause the oxidation of NO to create peroxynitrite, possibly masking differences in eNOS activity between genotypes. Impairment of eNOS dimer formation, or 'eNOS uncoupling', in the diabetic context could lead to decreased NO generation, alongside increased eNOS-mediated  $O_2^{\cdot-}$  production. Higher concentrations of  $O_2^{\cdot-}$  may explain the detrimental association between reduced vascular GS and diabetes. The development of significant eNOS uncoupling may require a prolonged period of diabetes and so for further development of this work, it could be valuable to use a STZ model of longer duration. Inhibition of NOS activity with L-NMMA in such a model would determine whether diabetes results in normalisation of tension response or if it perhaps exacerbates vasoconstriction through eNOS uncoupling. It is also feasible that large increases in  $O_2^{\cdot-}$  formation through uncoupled eNOS monomers could evoke a paradoxical vasodilation upon L-NMMA administration.

Once the effect of diabetes here is verified, additional work could be conducted to examine the degree of uncoupling and the concentrations of  $O_2^{\cdot-}$ . Initially, a crude measurement of monomer to dimer ratio could be carried out with western blotting using aortic tissue lysates. Incubation of aortic rings with DHE, a fluorescent probe used for ROS detection, would complement protein analysis. A high-performance liquid chromatography fluorescence-based detector assay could then be utilised, as demonstrated by Yang et al. (2009). This enables quantification of 2-EOH, an oxidative product derived from  $O_2^{\cdot-}$  specifically.

### **4.3 Endothelial GS haploinsufficiency and vascular phenotype**

The impact of lowering GS expression in the endothelium was investigated further with VEGS Het mice, which were generated as a model of endothelial-specific GS haploinsufficiency. This avenue of research was deemed particularly relevant since the findings of Qi et al. (2013) highlighted that those people with both rs10911021 risk alleles exhibited a 32% decrease in endothelial *GLUL* expression. A homozygous knockout carries the limitation of presenting an extreme phenotype. Many human diseases have a complex and multifaceted aetiology, rather than resulting from the complete absence of a gene. A reduction

in endothelial GS expression of 32% is more likely to be captured by a haploinsufficient mouse line.

With RT-qPCR, a satisfactory level of 45.1% GS knockdown in VEGS Het endothelial cells was achieved. Organ bath experiments were conducted to look at vasomotor function, as had been done with VEGS Hom. Exposure of VEGS Het aortic rings to PE resulted in a maximal tension response similar to that of control littermates. This was also the case when aortic tissue was treated with PE following NOS inhibition with L-NMMA. Vasorelaxation to Ach also appeared to be unchanged by endothelial GS haploinsufficiency, with statistically similar responses recorded for VEGS Het and controls. Comparable levels of vasodilation were noted after application of SNP.

The dissimilarity to the results of VEGS Hom also extended to blood pressure measurements, where systolic, diastolic and mean blood pressure data for VEGS Het was almost identical to that gathered from control littermates. In the same manner, the capacity of VEGS Het endothelial cells to regenerate following denuding wire-injury was not significantly different from control counterparts.

It could be concluded from these data sets that GS haploinsufficiency in the endothelium does not have an impact on basal NO bioavailability. The sample sizes for organ bath and blood pressure experiments, however, were small. Since heterozygous animal models often present with more subtle phenotypes, it is possible that an increase in basal NO would not be detected with the sample sizes used here. It is also conceivable that compensatory mechanisms have masked elevations in NO caused by haploinsufficiency, although this seems unlikely given the level of GS knockdown shown with RT-qPCR. Further testing of VEGS Het is required if clear conclusions are to be made about the effect of GS haploinsufficiency on endothelial cell biology.

## **4.4 The impact of pharmacological inhibition of GS in endothelial cells**

### **4.4.1 eNOS activity**

To further study the effect of endothelial GS impairment on endothelial cell biology, HUVECs were exposed to the irreversible GS inhibitor MSO. After cells underwent 24-hr treatment with MSO, or a vehicle control, eNOS activity was examined using radiolabelled  $^{14}\text{C}$ -arginine. HUVECs exposed to MSO displayed significantly elevated DPPII/protein ratios, implying increased eNOS activity, both in the presence and absence of insulin. This complements the decreased blood pressure seen in the VEGS Hom murine model and the reduced contractile responses from VEGS Hom aortic rings to PE stimulation. Insulin application to control HUVECs evoked a significant increase in eNOS activity, confirming that the assay was successful. The impact of insulin appeared to be mirrored in MSO-treated HUVECs, but high variability meant it did not reach significance. Cells were subject to identical culturing conditions and reagent stocks. Consequently, it is unlikely that the variability has arisen from these aspects of HUVEC treatment. Given the pharmacological nature of MSO as the means of GS inhibition, it is feasible that it has off-target effects which may alter the insulin signalling pathway. Tardito et al. (2012) noted that MSO enhances mTOR activity via phosphorylation of mTOR complex 1 substrate, S6K1. Activated S6K1 has been seen to phosphorylate serine residues on IRS-1 in both human and murine systems, thereby downregulating insulin signalling (Shah & Hunter, 2006). It should be considered that these studies were performed in non-endothelial cell lines and may exhibit very different metabolic profiles to HUVEC culture. Nonetheless, the variability seen in the data for this project justifies reconsidering insulin as the assay positive control when using MSO for GS inhibition in HUVECs.

### **4.4.2 Colocalisation of eNOS and $\beta$ -actin**

Previous findings that attenuation of GS activity in endothelial cells resulted in increased formation of stress fibres (Eelen et al., 2018) prompted investigation

into whether this may in turn affect eNOS activity, which is known to functionally interact with actin (Kondrikov et al., 2014). The spatial relationship of F-actin and eNOS was examined with immunocytochemistry of MSO-treated HUVECs and confocal microscopy. These techniques are popular for assessing protein colocalization, since they are experimentally straightforward and allow for the preservation of cellular morphology (Jensen 2014). With immunofluorescence, colocalisation is identified when two or more probes with different excitation wavelengths are observed in the same area. Each probe has a different colour and molecules of interest are classed as colocalised in regions stained with the combined colours upon merging of images of the individual probes (Dunn et al 2011; Jensen 2014).

The co-immunofluorescence data presented earlier suggests that, in HUVECs subject to MSO-mediated GS inhibition, there is a significant rise in colocalization of F-actin and eNOS. It is well-established that association between actin and eNOS induces eNOS activation and amplifies NO synthesis. Indeed, if this increased colocalisation is present in the endothelium of VEGS Hom, it may account for the decreased blood pressure and reduced tension response of aortic rings. No significant increase in stress fibre formation was recorded in these immunofluorescent staining experiments. However, the original findings by Eelen et al. (2018) were made following use of genetic lentiviral knockdown of GS, whereas MSO only inhibits GS activity rather than expression. Eelen et al. (2018) also conducted knockdown over 3 to 4 days, which contrasts with the 24-hr period of GS inhibition used for the work of this project.

Colocalisation in the context of immunofluorescence does not necessarily confirm direct communication between F-actin and eNOS. Direct protein interactions occur at distances between 1–10 nm, which is too close to be identified with the resolution of confocal microscopy and immuno-staining (Dunn et al., 2011; Lagache et al., 2015). To confidently conclude the close proximity of molecules, a higher resolution system would need to be employed. Förster resonance energy transfer (FRET) is a robust method for evaluating molecular interactions at this level and involves the transfer of energy from one fluorophore, referred to as the donor, to a second fluorophore, which is the acceptor. The FRET process can only occur when the 2 fluorophores are less than 10 nm apart

(Broussard & Green, 2017). For the study of protein interactions, one molecule of interest is tagged with a fluorescent protein as the FRET donor and is expressed in a cell line. The second molecule is also fused to a fluorescent protein, which acts as the acceptor species and is microinjected into cells. If the proteins are in proximity of under 10 nm, FRET signal is generated (Rowland et al., 2015). As well as providing a more sensitive approach for identifying direct protein interaction, FRET-based detection does not suffer from background emission caused by excess fluorophores, something which often hampers colour staining techniques (Rowland et al., 2015).

In spite of the obvious benefits for colocalisation studies, FRET is expensive and technically challenging. Another option for investigating eNOS and F-actin association in endothelial cells with GS inhibition would be use of the cell permeable P326TAT peptide. It is composed of an amino acid sequence matching that of the actin binding pocket of eNOS (residues 326–333) and its introduction into cells is mediated by fusion to the 10-amino acid transduction domain of HIV-tat (Kondrikov et al., 2014). P326TAT is known to inhibit  $\beta$ -actin induced eNOS activation and its use with MSO-treated HUVECs would allow assessment of the functional importance eNOS-actin colocalization in the observed increase of NO bioavailability.

## **4.5 The influence of endothelial GS deficiency on diabetic vascular disease**

### **4.5.1 Atherosclerotic plaque development**

To fully appreciate the impact of endothelial GS insufficiency in vascular disease, a model was required which adequately captured pathological elements. VEGS Hom and VEGS Het were crossed with ApoE<sup>-/-</sup> mice to create VEGA Hom and VEGA Het, respectively. Under normal conditions, mice exposed to a high cholesterol diet are largely resistant to developing atherosclerosis. Upon deletion of the ApoE gene, obvious and relatively quick atherosclerosis formation occurs, allowing insight into plaque development mechanisms. Through creation of VEGA Hom and VEGA Het, this is the first time that endothelial GS deficiency

and its impact with atherosclerosis has been investigated in a murine *in vivo* model.

After tamoxifen induction and 12 weeks of western diet feeding, whole aorta plaque development in both VEGA Hom and VEGA Het were assessed with oil red O staining, a method commonly employed for quantification of atherosclerosis. VEGA Hom exhibited significantly decreased plaque burden across the whole aorta. This was also observed in VEGA Het mice. For VEGA Hom, suppressed atherosclerosis development extended to the aortic sinus, where Miller van Gieson staining revealed a significant drop of more than 30% in plaque coverage. This was not mirrored in VEGS Het, where a trend for reduced plaque abundance was not statistically significant. Since VEGA Het experiences GS haploinsufficiency in endothelial cells, rather than full knockout of the enzyme, it may be that this results in a smaller effect and changes at the aortic sinus may therefore only be detected with larger sample sizes. This could explain the unaffected plaque coverage at the sinus despite an obvious decrease in lesion occurrence throughout the remaining aorta, since more mice were available for the latter dataset.

While eNOS activity was not measured in the VEGA colonies, the reduced atherosclerosis development supports the possibility of increased NO production following endothelial GS inhibition, given the anti-atherogenic nature of NO. It is also reasonable to propose that in addition to its direct vascular effects, increased NO bioavailability could prevent atherosclerosis in the VEGA models through indirect mechanisms. One example is its metabolism to NO<sub>2</sub>-FAs. In the context of vascular disease, NO<sub>2</sub>-FAs not only act as a NO reservoir, but also exert an anti-inflammatory effect. They augment Nrf2 signalling, a critical pathway for regulating inflammatory processes. Nrf2 activation leads to down regulation of the cell adhesion molecules, such as VCAM-1, associated with lesion formation. Nrf2 knockout mice also present with increased expression of COX-2 and other pro-inflammatory markers; these substances are heavily implicated in plaque initiation and progression (Ahmed et al., 2017). Levonen et al. (2007) noted that NO<sub>2</sub>-FAs further promote an anti-atherogenic environment through heightened expression of several antioxidant enzymes and reduced VSMC proliferation. For developing the work of this project, it would be

interesting to investigate whether levels of NO<sub>2</sub>-FAs are altered in VEGA mice versus control littermates. Measurement of S-nitrosylation represents another potential area of examination. This NO-mediated modification of proteins has been documented to attenuate various pro-atherosclerotic processes, such as O<sub>2</sub><sup>•-</sup> generation (Selemidis et al., 2007). S-nitrosylation has also been shown to hamper apoptotic mechanisms through inhibiting caspase activity and promoting internalisation of TNF-α receptor (Iwakiri 2011).

It is important to note, that at least in the area of endothelial GS haploinsufficiency, certain datasets do not support amplified NO bioavailability, even though atherosclerosis development is suppressed. This suggests the anti-atherogenic effect of GS deficiency in the endothelium may be facilitated by an alternative mechanism. Whether increased NO is essential to the phenotype could be addressed experimentally through administration of a NOS inhibitor, versus vehicle control, in the drinking water of VEGA Hom mice during western diet feeding.

Increased glutathione concentrations are a possible downstream effect of diminished GS activity. Decreased GS expression could cause a build-up of glutamate, which may be re-directed for production of the antioxidant peptide glutathione. Glutathione is manufactured from glutamate, cysteine and glycine and perturbations of its concentration and oxidation state occur regularly in vascular disease (Bajic et al., 2019). Several human studies have uncovered a link between lower serum glutathione levels and increased susceptibility to atherosclerosis (Morrison et al., 1999; Ashfaq et al., 2006). Similar alterations to glutathione concentrations have been recorded in animal experiments, with Biswas and colleagues (2005) noting a significant depletion in glutathione preceding and during plaque formation in ApoE<sup>-/-</sup> mice. However, the relevance of these observations is complicated by data highlighting the detrimental impact of S-glutathionylation of proteins in atherosclerosis. This post-translational modification involves the formation of a disulphide bond between glutathione and the cysteine residues of a protein. eNOS uncoupling in response to angiotensin II is facilitated by glutathionylation in both human and animal endothelial cells (Galougahi et al., 2014). Additionally, S-glutathionylation of the GTPase, p21ras, has been recorded in bovine aortic cells following exposure to oxLDL. This leads

to p21ras activation and in turn, stimulation of ERK signalling, which plays a role in promoting atherosclerosis (Clavreul et al., 2006; Hu et al., 2012). Importantly, glutathione has been shown to be unaffected by GS silencing in HUVECs (Eelen et al., 2018), but this remains to be assessed in the context of atherosclerosis or diabetes.

To study the interaction between reduced endothelial GS expression and vascular disease, specifically in a diabetic context, VEGA Hom mice were injected with STZ at the start of western diet feeding. Atherosclerosis was analysed again using whole aorta specimens and oil red O staining. Small sample sizes prevent definitive conclusions from being made, but these preliminary oil red O data suggest a trend towards decreased atherosclerosis in VEGA Hom mice receiving both western diet and STZ.

#### **4.5.2 Plaque stability and rupture**

The datasets from VEGA mice raise some interesting points of discussion. It should be considered, that while it appears to prevent atherosclerosis development in both normal and diabetic conditions in the VEGA colonies, human endothelial GS deficiency (i.e. rs10911021 risk allele carriers), but only in the presence of diabetes, is associated with increases in both cardiovascular events and mortality (Qi et al., 2013; Prudente et al., 2015). The discrepancy between these observations may highlight the importance of plaque stability. It is feasible that GS insufficiency in the endothelium results in fewer lesions, but that they are more vulnerable to rupture, particularly in the setting of diabetes.

Stable plaques are often comprised of a small lipid centre with mild inflammatory and oxidative conditions, overlaid with a thick fibrous cap strengthened by numerous VSMCs. This is in stark contrast to unstable lesions, which exhibit an intensely inflammatory and oxidative environment with high macrophage content, accompanied by a large lipid core with a thin fibrous covering (Halvorsen et al., 2008). As outlined earlier, multiple factors are thought to influence plaque propensity to rupture. Compared to its general impact on atherosclerosis progression, the influence of NO on the stability of plaques specifically is less well understood. The current body of evidence suggests that increased NO

concentrations may contribute to more stabilised lesions. Using ApoE<sup>-/-</sup> mice expressing mutant fibrillin-1 (ApoE<sup>-/-</sup>Fbn1<sup>C1039G+/-</sup>) to mimic atherosclerosis and vascular ageing, Roth et al. (2019) investigated the effect of NO on plaque stability through administration of western diet and the NO donor, molsidomine. The group did not detect changes in total content of macrophages, collagen or VSMCs within lesions, but did notice improvements in other parameters of plaque stability following molsidomine treatment. Plaque cap thickness was significantly increased, as was the frequency of macrocalcifications. In contrast to microcalcifications, macrocalcifications are believed to strengthen plaques and represent areas of vascular repair (Roth et al., 2019).

The means by which endothelial GS may be involved in plaque stability is unclear. At least in the setting of atherosclerosis alone, the data presented here suggests that GS deficiency in the endothelium may enhance plaque stability. The impairment of endothelial cell motility and sprouting angiogenesis following GS deletion (Eelen et al., 2018) could impede development of microvessels in advanced lesions. Plaque neovascularisation is heavily implicated in plaque stability. The delivery of nutrients, immune cells, erythrocytes and inflammatory mediators drives atheroma growth, and plaques which are susceptible to rupture display more extensive neovessel development (Finn & Jain, 2010; Purushothaman et al., 2011). Indeed, in models of breast and lung carcinoma, inactivity of RhoJ, which is known to result from endothelial GS deficiency, correlated with reduced neovessel formation and suppressed tumour growth (Kim et al., 2014). It is worth considering, however, that these findings were made in the context of angiogenesis. It is possible that reduced GS expression has a different effect in quiescent endothelial cells. Importantly, unstable plaques are described to have increased GS content (Saksi et al., 2011; Perisic et al., 2013), although the endothelial contribution to this is unexplored, and it is unclear whether this is a protective or maladaptive response.

The effect of reduced endothelial cell GS on plaque vulnerability in the setting of diabetes alongside atherosclerosis is also uncertain. The dramatic increases in ROS seen in diabetic vascular disease originate primarily from uncoupled eNOS (Sharma et al., 2015) and create a highly oxidative environment ideal for plaque destabilisation (Halvorsen et al., 2008). It is possible that these conditions in

combination with increased NOS activity following endothelial GS attenuation could further promote plaque oxidative stress, driving plaques towards an unstable phenotype.

There are several areas within the VEGA datasets that would require attention upon further development of the project. It would be necessary to record glucose and insulin tolerance at the end of the western diet course. Western diet has been shown not to induce diabetes, but this should be verified following induction of endothelial GS deficiency (Gage et al., 2013). Additionally, measurement of blood cholesterol levels and blood pressure would need to be conducted, both at the commencement and end of the western diet schedule. It would also be interesting to induce GS knockdown after atherosclerotic plaques have developed. This may allow separation of the potentially opposing effects of endothelial GS knockdown on atherogenesis versus plaque stability.

Oil red O and Miller van Gieson enabled simple and clear assessment of atherosclerosis development and so provided useful insights into plaque formation in the VEGA colonies. Both methods, however, suffer from being 2-dimensional in nature, thus limiting the information which can be gathered about plaque structure and stability. Furthermore, the murine heart rate is more than 400 bpm, resulting in turbulent blood flow at the mouse aortic sinus and promotion of atheroma growth. Humans, by contrast, exhibit heart rates between 60–100 bpm. Subsequently, the aortic sinus is not a typical location for human atherosclerosis development (Heinonen et al., 2015). It is also acknowledged that studying atherosclerotic plaque rupture is challenging in mice; this generally relies on assumptions about plaque stability rather than directly observing rupture events (Schwartz et al., 2007). Nevertheless, murine models still offer interesting data and form a good foundation for further experiments in human tissue.

Molecular imaging may allow more understanding of the influence of endothelial GS and plaque stability, with various 3-dimensional imaging techniques having already been used in atherosclerosis animal studies, such as magnetic resonance imaging and contrast-enhanced ultrasound, amongst others. These methods can be coupled with imaging agents which are associated with targeting ligands, allowing detection of vulnerable lesions (Gargiulo et al., 2016). For

example, iron oxide nanoparticles detecting LOX-1, a lipoprotein present on atheroma endothelial, inflammatory and smooth muscle cells and implicated in plaque weakening, have been used successfully in ApoE<sup>-/-</sup> mice (Wen et al., 2014). Molecular imaging is non-invasive and represents a group of modalities which are more translatable to a human clinical setting (Gargiulo et al., 2016).

## **4.6 Endothelial GS insufficiency and increased NO bioavailability**

### **4.6.1 Arginine**

Arginine is a vital substrate for eNOS-mediated NO production. Since endothelial GS deficiency results in increased basal NO, it is important to establish whether intracellular arginine availability is affected, and if any elevation in arginine concentration is a cause, or a consequence, of enhanced eNOS activity.

Intracellular arginine can be acquired through protein catabolism, *de novo* synthesis and membrane transport (Morris 2016). The latter is facilitated by the cationic amino acid transporter protein family, with CAT-1 representing the predominant system of arginine uptake in endothelial cells (Mann et al., 2003).

Despite a breadth of research, much about endothelial arginine transport and metabolism remains unclear. It is feasible that elevated intracellular arginine concentrations may be detected in endothelial GS insufficient models, resulting from increased arginine demands of eNOS. Heightened arginine flux through the enzyme, and a subsequently increased arginine concentration gradient across the endothelial membrane, could enhance CAT-1 transporter activity or evoke its upregulation. It is also possible that CAT-1 expression may be upregulated as a consequence of decreased glutamine availability following attenuation of endothelial GS. Reduced glutamine availability has been shown to activate the protein kinase GCN2 (Ye et al., 2015) and such stimulation of GCN2 augments translation of CAT-1 mRNA (Hatzoglou et al., 2004). However, since Eelen et al. (2018) demonstrated that cytoplasmic glutamine concentrations in the endothelium are unchanged following endothelial GS deletion, this theory seems unlikely.

Amplified NO generation through eNOS may also be secondary to changes in arginine transportation induced by endothelial GS insufficiency. Post-translation modifications to CAT-1 may have been altered, impacting on membrane trafficking of the transporters or making them more receptive to arginine uptake. Since the GS palmitoylome has not yet been defined, it is also conceivable that CAT-1 is an additional target of GS palmitoylation.

Endothelial cells possess different arginine pools for NO formation and it is important to note that the specific pool utilised is often dictated by the NOS isoform. For example, arginine derived from endogenous sources is the favoured substrate for eNOS, whereas iNOS expressed in endothelial cells preferentially takes up arginine delivered by transporters (Shen et al., 2005).

#### **4.6.2 iNOS**

iNOS supplies NO primarily for regulation of inflammation and immune responses to pathogens. This generation of NO is at concentrations much greater than those produced by endothelial and neuronal NOS isoforms (Aktan 2004). The classical view is that endothelial iNOS expression occurs following induction by inflammatory mediators. However, expression has been detected in the healthy endothelium (Zadeh et al., 2000; Reventun et al., 2017; Kalucka et al., 2020).

Similar to the other NOS enzymes, iNOS exists in association with calmodulin, but differences in iNOS molecular structure result in tighter binding (Venema et al., 1996). This stronger interaction allows iNOS to be activated at much lower concentrations of  $\text{Ca}^{2+}$ , roughly 40 nM, compared with the 400 nM needed by nNOS and eNOS (Hemmens & Mayer, 1998). With normal  $\text{Ca}^{2+}$  levels in the cytoplasm reaching around 100 nM, iNOS can synthesise a constant low level of NO (Clapham 2007; Cinelli et al., 2020). Upon stimulation with substances such as lipopolysaccharide and inflammatory cytokines, the amount of NO produced by iNOS increases significantly. There is, however, a fine balance between beneficial and detrimental iNOS activity. While high concentrations of iNOS-derived NO are vital for immune defences, they have been implicated in a multitude of diseases, including those of the cardiovascular system (Cinelli et al.,

2020). The contribution of iNOS to these pathologies, is in part, due to its susceptibility to become uncoupled, much like eNOS and nNOS (Soskić et al., 2011). Indeed, mice with overexpression of iNOS in cardiomyocytes develop cardiac fibrosis and hypertrophy, and display increased generation of peroxynitrite (Mungrue et al., 2002).

Observations revealing deleterious consequences of heightened iNOS also extend to studies of atherosclerosis. ApoE and iNOS double knockout mice display both markedly reduced levels of oxidative stress and atherosclerotic lesions following western diet (Kuhlencordt et al., 2001), highlighting the pro-atherogenic potential of iNOS. In humans, Sigala et al. (2017) noted upregulated iNOS to be associated with unstable plaques. Several studies have also reported improvements to insulin resistance in mice upon iNOS deletion (Noronha et al., 2005; Zanotto et al., 2016;).

There are investigations proposing a beneficial role for increased iNOS in the vascular system, with elevated iNOS expression linked to protection against murine aortic aneurysm development (Lee et al., 2001) and myocardial ischemia-reperfusion injury in insulin resistant rats (Prakash et al., 2011). With respect to atherosclerosis and diabetes, however, most evidence suggests that iNOS amplification is unfavourable. Nonetheless, the presence of iNOS in the healthy endothelium implies that it contributes to normal vascular physiology, and the point at which its activity becomes damaging is probably highly context specific.

Since iNOS expression is detected in unstimulated endothelial cells and iNOS-derived NO is involved in vascular disease development, it is important that iNOS is examined in the setting of endothelial GS insufficiency. If the increased eNOS activity observed in the data of this project is secondary to elevated arginine availability, it is reasonable to assume that this may also amplify iNOS-mediated NO production. This additive rise in available NO may exert a protective effect within the endothelium, thus accounting for the reduced plaque burden seen in the VEGA colonies. It is also possible that reduced endothelial GS expression alters iNOS through  $\beta$ -actin. Witteck et al. (2003) found that disassembly of F-actin fibres, induced by both toxins and specific inhibition of ROCK signalling, caused a significant rise in cytokine-stimulated iNOS expression. The increased

formation of F-actin stress fibres and ROCK activation seen upon endothelial GS deletion may inhibit excessive iNOS activity in the inflammatory environment of atherosclerosis, providing an alternative explanation for the reduced atheroma burden exhibited by VEGA mice. In conditions of diabetes, the additional oxidative stress could cause increased peroxynitrite synthesis from the high NO concentration, promoting uncoupling of both eNOS and iNOS and ultimately lesion development.

#### **4.7 Measurement of NO**

While the use of radiolabelled  $^{14}\text{C}$ -arginine and  $\text{NO}_x$  assays offered practical and established methods for evaluating eNOS activity, both possess shortcomings. Measurement of  $^{14}\text{C}$ -citrulline does not account for possible conversion of  $^{14}\text{C}$ -arginine to  $^{14}\text{C}$ -ornithine and urea through the action of arginase (Shin et al., 2015). As mentioned earlier,  $\text{NO}_x$  do not constitute the only products of NO breakdown. They also undergo fast degradation, meaning that  $\text{NO}_x$  concentration may not accurately correlate with true NO availability. Further development of this project would therefore warrant the employment of other techniques.

Fluorescent dyes, such as DAF-2, are popular for assessing NO levels. Such probes generate fluorescence upon reaction with NO and are considered relatively cheap and technically straightforward. However, they can lack in specificity, creating fluorescent products from other metabolites, such as ascorbic acid and certain divalent cations (Möller et al., 2019). To overcome some of the issues associated with fluorogenic assays, genetically encoded NO probes (geNOp) have been developed, like those by Eroglu et al. (2016). The group conjugated the NO binding domain of a bacteria-derived transcription factor to a fluorescent protein and expressed this geNOp in HeLa cells. Through interaction with NO, the domain undergoes a conformational change, which quenches the emission of the fluorescent protein. geNOp systems are particularly useful for live imaging of NO in single cells, allowing more detailed interpretations of NO production, diffusion and degradation (Eroglu et al., 2016).

Despite this, they are sensitive to cellular pH changes. geNOp generation and cell line expression would also be experimentally challenging.

It would also be possible to investigate eNOS activity through mass spectrometry. The system involves ionising samples and separating ions based on their mass-to-charge ratio. The electrical signal of the separated ions is measured and used to determine the quantify of ions present in the sample. Mass spectrometry can detect analytes at attomolar concentrations, thus providing high specificity and sensitivity (Mellon 2003). Application of a stable-isotope labelled arginine,  $^{15}\text{N}_4$ -arginine has been used successfully by other groups. eNOS metabolises  $^{15}\text{N}_4$ -arginine as a substrate for NO production and forms  $^{15}\text{N}_3$ -citrulline. This is recycled to  $^{15}\text{N}_3$ -arginine by ASS and ASL enzymes, and is acquired by eNOS, creating unlabelled NO and more  $^{15}\text{N}_3$ -citrulline. The measurement of  $^{15}\text{N}_3$ -citrulline with a mass spectrometer can be used as an index for eNOS activity (Shin et al., 2015).

Electron paramagnetic resonance or 'EPR', a technique which identifies molecules carrying one or more unpaired electrons, is another avenue for assessing NO production. EPR operates on the basis that unpaired electrons produce a magnetic field and consequently possess 'poles'. When placed in an external magnetic field, they become aligned in an energetically favourable position i.e. the pole of a particular charge will be directed towards the oppositely charged region of the magnetic field. A certain amount of energy is needed to flip an unpaired electron to its energetically unfavourable position. If this energy is applied, it is absorbed by the unpaired electron as it rotates, and the absorption is detected by the EPR system (Hogg 2010). Since EPR is measuring paramagnetism, it can be used with cell or tissue preparations, which are often dense and opaque in nature. The method can also be coupled with stable-isotope labelled compounds, like the aforementioned  $^{15}\text{N}_3$ -arginine, enabling more information to be gathered on the origin of NO within a biological sample (Hogg 2010). However, this is a specialist and technically difficult assay.

#### **4.8 The interaction between endothelial GS deficiency and diabetes in atherosclerosis**

Disturbances in metabolic homeostasis in endothelial cells have been noted in atherosclerosis. Aside from perturbations in NO level, increased  $O_2^{\cdot-}$  production through NADPH oxidases and disruption to the cholesterol-generating mevalonate pathway contribute to a dysfunctional metabolic state (Eelen et al., 2015). Diabetes both exacerbates these changes, but also induces additional alterations to endothelial cell metabolism. Redirection of glucose through the polyol pathway results in the creation of AGEs. Furthermore, excess glucose is prevented from entering the pentose phosphate pathway, reducing available NADPH, leading to heightened oxidative stress (Eelen et al., 2015). Amino acids may also contribute to metabolic abnormalities in diabetes. Insulin resistance can correlate with excess glutamate, causing a rise in transamination of pyruvate to alanine, a particularly gluconeogenic molecule (Newgard et al., 2009). As outlined earlier, there is conflicting evidence surrounding the influence of glutamine levels on diabetes. While the canonical glutamine-synthesising function of GS appears minimal in the healthy endothelium, it is feasible that in the environment of atherosclerosis and diabetes, endothelial cells experience different glutamine requirements, similar to other pathological conditions (Rohlenova et al., 2018).

Eelen et al. (2018) demonstrated that GS undergoes autopalmitylation, alongside palmitylating RhoJ and stimulating its activity. Palmitylation is an important post-translational modification, whereby palmitic acid is attached to cysteine side chains of a protein. This process regulates a number of endothelial proteins (Marin et al., 2012). Various hallmarks of diabetes, such as defective insulin signalling and increased oxidative stress, disturb normal palmitylation (Parat et al 2002; Wei et al., 2014). It is unknown whether GS has other palmitylation targets, besides RhoJ. The presence of diabetes may impede the palmitylating capacity of GS, thus affecting other areas of endothelial biology.

Additionally, it is possible that decreased GS expression in endothelial cells and diabetes act synergistically to promote vascular disease through their relationships with the ROCK signalling cascade and eNOS. In diabetic

retinopathy, hyperglycaemia activates the ROCK pathway, resulting in disrupted tight junction expression in the endothelium (Lu et al., 2014). Similarly, endothelial GS deletion causes ROCK activation and actin stress fibre accumulation (Eelen et al., 2018). This is particularly important when one considers the increase in eNOS activity upon eNOS-actin association. The high oxidative stress that characterises diabetes results in eNOS uncoupling and  $O_2^{\cdot-}$  generation. This combined with the amplified NOS activity which accompanies reduced endothelial GS could further enhance  $O_2^{\cdot-}$  formation, intensifying the oxidative conditions.

## **4.9 Project limitations**

### **4.9.1 Murine models**

*In vivo* models can provide detailed insights into disease mechanism. *In vitro* alternatives were used for this project where possible, thus implementing the principle of the 3Rs: replacement, reduction and refinement. However, there were aspects which could not have performed without either *in vivo* or *ex vivo* systems. For example, analysis of aortic vasomotor function requires an intact vessel. The interplay between the endothelium and VSMCs, and resulting vessel dynamics, cannot be replicated *in vitro*. By the same means, the conditions for atheroma formation can only be captured at whole animal level. While murine models were employed here, it has been argued that atherosclerosis in mice does not truly mimic that of humans. Pigs or non-human primates display lesions which exhibit a closer morphological profile to human plaques (Ni et al., 2009). However, use of such species would not be feasible. Aside from ethical concerns, genetic manipulation for these animals is challenging and maintenance is expensive. Mice share 80% genetic homology with humans, have a low maintenance cost and develop atherosclerosis in much shorter time frames (Gargiulo et al., 2016), making them the most suitable *in vivo* system for this project.

#### **4.9.2 STZ as a model of diabetes**

The STZ model of diabetes is widely used in diabetes research and was adopted for this project. Mice received STZ injections over 5 consecutive days, which elicits  $\beta$ -cell dysfunction via DNA fragmentation and heightened ROS generation (Szkudelski 2001). There are several issues with using the STZ model. Firstly, destruction of  $\beta$ -cells resembles the pathogenesis of T1DM, as opposed to T2DM. Furthermore, STZ toxicity is not isolated to pancreatic tissue, with some groups observing alterations to cytochrome P450 isoenzyme expression in kidneys, liver and lungs amongst other organs (Gvazava et al., 2018). Disparities across different mouse strains with respect to responsiveness to STZ have also been reported (Hayashi et al., 2006). For this project, it would be challenging to initiate diabetes with alternate diet or additional genetic manipulation in the context of atherosclerosis induction with western diet and ApoE knockout. With this in mind, the STZ model provided the most effective and practical method for inducing diabetes.

#### **4.9.3 ApoE<sup>-/-</sup> mice for studying atherosclerosis**

The ApoE<sup>-/-</sup> mouse, is employed frequently for the study of atherosclerosis, both in our laboratory and in the wider research community. Mice are highly resistant to developing atherosclerosis under normal circumstances, due in part to their natural deficiency in cholesteryl ester transfer protein (CETP) (Heinonen et al., 2015). Consequently, murine genetic alterations are required if atherosclerosis is to occur. Knockout of the ApoE gene is one such example. The model effectively allows development of lesions, with around a 4-fold increase in cholesterol concentration seen even with chow diet (Nakashima et al., 1994). The resulting lipoprotein profile, however, does not bear resemblance to that of a human, with ApoE<sup>-/-</sup> mice exhibiting high levels of chylomicrons and VLDLs (Curtiss & Boisvert, 2000). More recently generated models, such as that used by Westerterp et al. (2006), which express a mutated form of ApoE (ApoE\*3-Leiden) along with human CETP, arguably give a better representation of the human lipoprotein environment.

Another common alternative is the LDL receptor knockout (LDLR<sup>-/-</sup>) mouse. The LDL receptor mediates uptake of LDL, as well as ApoB and ApoE lipoproteins (Zadelaar et al., 2007). Only slight increases in plasma cholesterol are exhibited by LDLR<sup>-/-</sup> mice, and atherosclerosis development is negligible when they receive a chow diet (Ishibashi et al., 1994). However, when given a western diet, the LDLR<sup>-/-</sup> model displays plaques with a similar morphology to those seen in ApoE<sup>-/-</sup> mice. Whilst the models are alike in several areas, the LDLR<sup>-/-</sup> mouse does carry certain advantages. Since cholesterol is transported mainly by LDL particles, LDLR<sup>-/-</sup> mice present a lipid profile closer to that of humans. Additionally, the ApoE protein influences more physiological processes than the LDL receptor, including inflammatory response and leukocyte activity. Inducing ApoE deficiency risks not only making mice more prone to bacterial infection, but also complicating interpretation of ApoE<sup>-/-</sup> data, since the immune system can influence atherosclerosis independently of lipid metabolism (Getz & Reardon, 2009; Getz & Reardon, 2012).

STZ treatment of ApoE<sup>-/-</sup> mice receiving western diet is a common protocol when attempting to recreate diabetic macrovascular disease (Heinonen et al., 2015). While this model still possesses the aforementioned shortcomings associated with STZ and an ApoE<sup>-/-</sup> background, more representative alternatives were not available. Additionally, despite their drawbacks, the use of STZ and ApoE<sup>-/-</sup> with western diet feeding robustly initiated diabetes and atherosclerosis respectively and were adequate for pursuing the hypothesis of this thesis.

However, continued use of ApoE<sup>-/-</sup>, with or without STZ, would be not ideal for specific examination of plaque vulnerability. Differences in the biochemical environment of the vasculature between humans and mice mean that spontaneous lesion destabilisation is rarely seen in murine atherosclerosis models. Consequently, rupture has to be induced. Traditionally, it has been evoked by surgical procedures, including compression of abdominal aortic lesions using forceps, and implantation of a cuff around the common carotid arteries. These are, however, invasive procedures and do not recapitulate spontaneous plaque rupture as would occur in humans (Gargiulo et al., 2016). Models utilising retroviral gene therapy have been used successfully, whereby specific macrophage overexpression of MMP-9, which has been implicated in

initiating lesion destabilisation, was induced by transfection of murine haemopoietic stem cells (Gough et al., 2006). The ApoE<sup>-/-</sup>Fbn1<sup>C1039G<sup>+/-</sup></sup> mouse mentioned in section 4.5.2 is another potential *in vivo* system for examining plaque rupture. Mice are deficient for ApoE and carry a heterozygous mutation in the *FBN1* gene, which encodes the glycoprotein, fibrillin-1. ApoE<sup>-/-</sup>Fbn1<sup>C1039G<sup>+/-</sup></sup> display elastic fibre fragmentation and similar alterations to human *FBN1* have been associated with increased cardiovascular disease severity (Medley et al., 2002). The vascular disease that develops in ApoE<sup>-/-</sup>Fbn1<sup>C1039G<sup>+/-</sup></sup> receiving western diet has been deemed a closer representation of human atherosclerosis. For example, plaques arise frequently in human brachiocephalic and common carotid arteries, and exhibit extensive neovessel networks and intra-plaque haemorrhaging. These features are rare in most murine atherosclerosis models, but are regularly captured in ApoE<sup>-/-</sup>Fbn1<sup>C1039G<sup>+/-</sup></sup> (Virmani et al., 2005; Emini Veseli et al., 2017). Importantly, unlike other models, ApoE<sup>-/-</sup>Fbn1<sup>C1039G<sup>+/-</sup></sup> are susceptible to spontaneous plaque rupture leading to myocardial infarction, stroke and sudden death (Van der Donckt et al., 2015). These closely mimic human disease end-points and seldom occur spontaneously in ApoE<sup>-/-</sup> mice receiving western diet (Emini Veseli et al., 2017). For developing this project, there are also other options which would be easier to implement. Plaque rupture can be provoked by administration of lipopolysaccharide and PE, followed by exposure to cold, as demonstrated by Ma et al. (2013).

#### **4.9.4 Origin of endothelial cells**

Endothelial cells from macrovascular, microvascular and venous vessels were analysed. Since there is great heterogeneity between vascular beds, it is reasonable to highlight that differences in endothelial cell origin may impact experimental outcome (Kalucka et al., 2020). This is particularly relevant with regard to both the localisation and activity of eNOS, and GS expression. However, the data was collected using complementary experimental approaches and are largely in agreement, suggesting this limitation was not detrimental to the project.

#### 4.10 Future work

Whilst this project has revealed new and exciting information, there are still many areas to be developed if the role of GS deficiency in the endothelium is to be properly understood.

Firstly, both GS and eNOS activity would need to be examined in all the models outlined with mass spectrometry. By using the  $^{15}\text{NH}_4\text{Cl}$  probe, GS activity could be assessed through quantifying  $^{15}\text{N}$  present in glutamine. Likewise,  $^{15}\text{N}_4$ -arginine would be suitable for investigating eNOS activity. Concentrations of  $^{15}\text{N}_3$ -citrulline produced by the enzyme could be measured and would be a proxy of NO formation. Given the significance of palmitoylation on the action and downstream effects of GS, its palmitoylating capacity is another avenue worth investigation, and could be carried out with the 17-ODYA palmitoylation probe. This fatty acid analogue is incorporated at protein palmitoylation sites. It is assessed by click chemistry, a tool by which a fluorescently labelled molecule (in this case, TAMRA-azide) detects the probe and is then quantified by immunoprecipitation (Martin 2013). These evaluations of enzyme action would be conducted under both normal conditions, but also in mouse endothelial cells following STZ administration and MSO-treated HUVECs cultured in high-glucose media.

The next important step is to clarify the interaction between eNOS and  $\beta$ -actin in the conditions of reduced endothelial GS expression. Inhibition of the association can be achieved with the P326TAT protein. Performing this in both murine endothelial cells from all models and in MSO-treated HUVECs would verify if GS depletion in the endothelium does indeed promote direct interaction between the proteins, leading to increased basal NO synthesis. Again, such experiments would be repeated in all models under conditions mimicking diabetes.

The potential contribution of increased arginine availability would also need to be considered in future work. Initially, eNOS activity would need to be blocked in mouse endothelial cells *in vitro*, with a NOS inhibitor such as L-NAME, followed by measurement of intracellular arginine concentration. This would allow evaluation of whether an increase in arginine transportation is driving eNOS activity, or if perhaps amplified arginine influx is secondary to heightened eNOS

demand for the substrate. By the same means, a possible contribution of iNOS to the vascular phenotype seen after reduced endothelial GS expression should be assessed. Verification of iNOS mRNA and protein expression would be required in each murine models. For the VEGA colonies, useful insight may be gained from measuring iNOS expression both upon initiation of western diet and at the end of the regimen, since the influence of iNOS in atheroma progression may differ over the course of vascular disease (Miyoshi et al., 2006).

With regard to uncovering the effect of decreased GS expression on eNOS in the context of atherosclerosis, it would be interesting to measure NO<sub>2</sub>-FA concentrations and protein S-nitrosylation in the VEGA models, alongside levels of glutathione, S-glutathionylation and nitro-tyrosine adducts. Further to these experiments, it is critical that the influence of GS on plaque morphology is fully defined in the VEGA colonies, with and without STZ treatment. Immunostaining would allow the specific cellular components of VEGA lesions to be determined. However, there is limited information which can be gained from such methods alone when examining plaque vulnerability. It may be necessary to consider inducing plaque rupture with a model similar to that reported by Ma et al. (2013), utilising lipopolysaccharide and PE administration alongside cold exposure. Additionally, a 3D imaging method would complement the aforementioned tools and strengthen judgements about plaque stability following endothelial-specific GS attenuation. These data could be used to guide studies of human atherosclerotic plaque, correlating plaque GS abundance with histological and clinical features of stability.

For exploring the interaction between altered endothelial GS expression and diabetic vascular disease, the initial point of investigation would be whether a synergistic relationship exists. ROCK signalling, reported to increase in VEGS Hom by Eelen et al. (2018), would need to be evaluated in mouse endothelial cells, in addition to HUVECs incubated with MSO and high glucose media. Assessment of eNOS uncoupling can be conducted through measuring oxidative stress markers, such as nitrotyrosine. This would also need to be replicated in STZ-treated mice and MSO-HUVECs exposed to high-glucose media.

## 4.11 Conclusion

Despite advances in current treatment strategies, patients with diabetes are still twice as likely to suffer from a cardiovascular event, highlighting a complex underlying pathophysiology that is not addressed by existing therapies (Kahn et al., 2012; IDF Diabetes Atlas 2019). Diabetes and related complications have traditionally been believed to result from poor diet and a lack of physical activity. While this undoubtedly plays a role in disease development, there is an increasing body of evidence emphasising the significance of genetic predisposition.

The discovery that SNP rs10911021 is associated with cardiovascular disease and mortality in people with diabetes has supported the notion that genetic factors can influence disease progression and outcome. This variant is found in a non-coding region adjacent to *GLUL*, which encodes the enzyme, GS. In risk allele homozygotes, the SNP confers a 32% reduction in GS in endothelial cells and is associated with increased cardiovascular risk and cardiovascular-related mortality. It was recently established that GS possesses additional roles within the vasculature, besides glutamine synthesis. Notably, it regulates sprouting angiogenesis through palmitoylation of the small GTPase, RhoJ. This project aimed to expand on these observations and uncover more regarding the impact of GS deficiency on vascular biology.

This was done primarily with newly established murine models. VEGS Hom, which is holoinsufficient for GS specifically in endothelial cells, exhibited reduced aortic constriction in response to PE, which was lost upon inhibition of eNOS. Vasodilation following Ach and SNP was no different to control mice, overall indicating increased basal NO production. There were no changes in the level of endothelial repair after wire-injury or serum NO<sub>x</sub> concentration. Additionally, no significant difference was shown in eNOS activity in VEGS Hom LECs. However, VEGS Hom did display a marked decrease in blood pressure, further supporting amplified basal NO generation. VEGS Hom were also administered with STZ to induce diabetes. This treatment caused a normalisation of aortic contractile response to PE, indicating that diabetes prevented their higher basal NO bioavailability.

A model of endothelial GS haploinsufficiency, VEGS Het, was also generated. The reduced vessel tone of VEGS Hom was not reflected in VEGS Het and more work is needed to fully elucidate the effect of reduced GS in the endothelium of these mice. In addition, GS was manipulated in HUVECs using pharmacological inhibition with MSO. eNOS activity was significantly enhanced by MSO treatment. The inhibitor also induced an increase in eNOS and  $\beta$ -actin colocalisation, highlighting a possible mechanism linking endothelial GS insufficiency with a rise in basal NO availability; future studies will test this hypothesis.

To explore reduced endothelial GS in the context of atherosclerosis, VEGS Hom and VEGS Het were crossed with ApoE<sup>-/-</sup> mice, creating VEGA Hom and VEGA Het, respectively. Both lines displayed a significant decrease in plaque abundance following western diet, compared to controls. While it did not reach significance, plaque development seemed to be suppressed in VEGA Hom mice receiving STZ. Here, attenuation of GS expression in the endothelium appears to prevent atheroma formation. Yet, the rs10911021 variant results in heightened cardiovascular risk. This highlights the possibility that endothelial GS influences plaque stability and this will be a key focus of future experiments.

There are still many unanswered questions regarding the role of endothelial GS in vascular biology. This project has, however, identified a novel relationship between the enzyme and regulation of eNOS activity, as well as atherogenesis. Further elucidation of the function of endothelial GS may assist in developing not only new methods for predicting cardiovascular risk in patients with diabetes, but also more effective, personalised therapies.

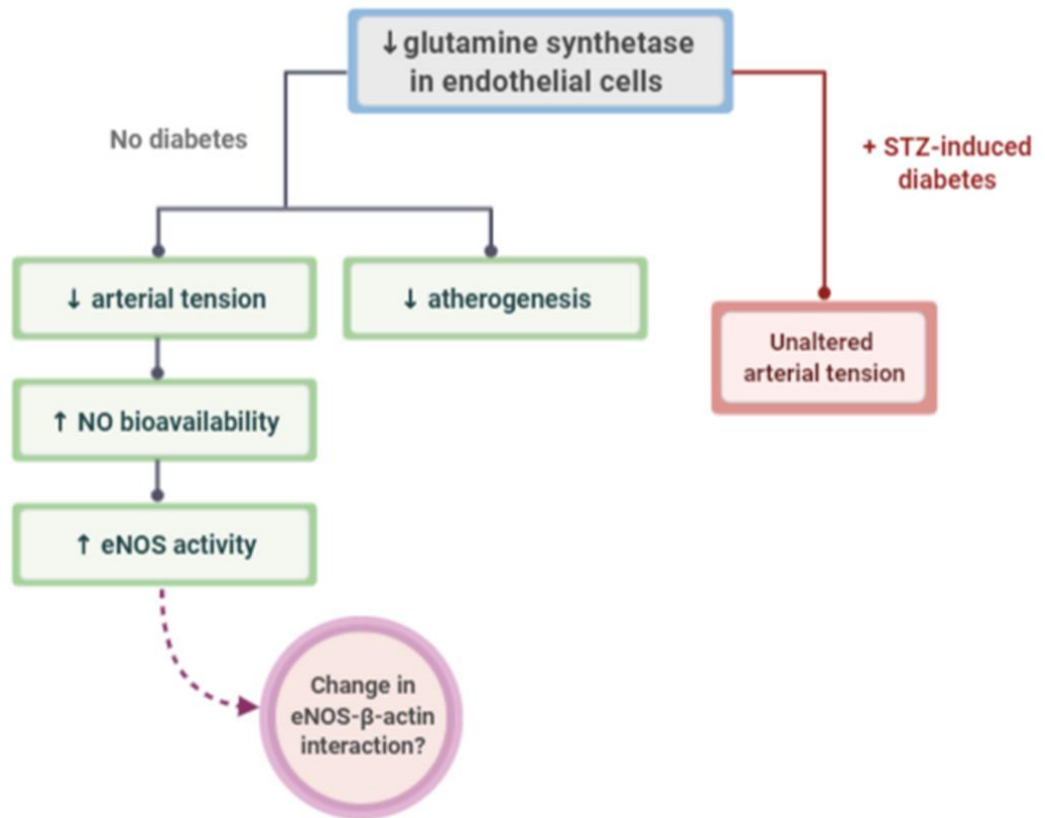


Figure 4.1 Key project findings

## References

- Adams L, Franco MC, Estevez AG. 2015. Reactive nitrogen species in cellular signaling. *Exp Biol Med (Maywood)*. **240**(6):711-7
- Ahlqvist E, Storm P, Käräjämäki A, Martinell M, Dorkhan M, Carlsson A, Vikman P, Prasad RB, Aly DM, Almgren P, Wessman Y, Shaat N, Spégel P, Mulder H, Lindholm E, Melander O, Hansson O, Malmqvist U, Lernmark Å, Lahti K, Forsén T, Tuomi T, Rosengren AH, Groop L. 2018. Novel subgroups of adult-onset diabetes and their association with outcomes: a data-driven cluster analysis of six variables. *Lancet Diabetes Endocrinol*. **6**(5):361-369
- Ahmed SM, Luo L, Namani A, Wang XJ, Tang X. 2017. Nrf2 signaling pathway: Pivotal roles in inflammation. *Biochim Biophys Acta Mol Basis Dis*. **1863**(2):585-597
- Aktan F. 2004. iNOS-mediated nitric oxide production and its regulation. *Life Sci*. **75**(6):639-53.
- Alfonso-Prieto M, Biarnés X, Vidossich P, Rovira C. 2009. The molecular mechanism of the catalase reaction. *J Am Chem Soc*. **131**(33):11751-61
- Alkayali S, Lyssenko V. 2014. Genetics of diabetes complications. *Mamm Genome*. **25**(9-10):384-400
- Allen RG, Lafuse WP, Powell ND, Webster Marketon JI, Stiner-Jones LM, Sheridan JF, Bailey MT. 2012. Stressor-induced increase in microbicidal activity of splenic macrophages is dependent upon peroxynitrite production. *Infect Immun*. **80**(10):3429-37
- Anand P, Stamler JS. 2012. Enzymatic mechanisms regulating protein S-nitrosylation: implications in health and disease. *Journal of Molecular Medicine (Berlin, Germany)*. **90**(3):233-244.
- Andries LJ, Brutsaert DL, Sys SU. 1998. Nonuniformity of endothelial constitutive nitric oxide synthase distribution in cardiac endothelium. *Circ Res*. **82**(2):195-203.
- Aoyagi M, Arvai AS, Tainer JA, Getzoff ED. 2003. Structural basis for endothelial nitric oxide synthase binding to calmodulin. *EMBO J*. **22**(4):766-75
- Aref Z, de Vries MR, Quax P. 2019. Variations in surgical procedures for inducing hind limb ischemia in mice and the impact of these variations on neovascularization assessment. *International journal of molecular sciences*. **20**(15):3704
- Arnal JF, Münzel T, Venema RC, James NL, Bai CL, Mitch WE, Harrison DG. 1995. Interactions between L-arginine and L-glutamine change endothelial NO production.

- An effect independent of NO synthase substrate availability. *J Clin Invest.* **95**(6):2565-72.
- Ashfaq S, Abramson JL, Jones DP, Rhodes SD, Weintraub WS, Hooper WC, Vaccarino V, Harrison DG, Quyyumi AA. 2006. The relationship between plasma levels of oxidized and reduced thiols and early atherosclerosis in healthy adults. *J Am Coll Cardiol.* **47**(5):1005-11.
- Atkinson MA, Eisenbarth GS, Michels AW. 2014. Type 1 diabetes. *Lancet.* **383**(9911):69-82
- Bajic VP, Van Neste C, Obradovic M, Zafirovic S, Radak D, Bajic VB, Essack M, Isenovic ER. 2019. Glutathione "Redox Homeostasis" and Its Relation to Cardiovascular Disease. *Oxid Med Cell Longev.* **2019**:5028181.
- Basatemur GL, Jørgensen HF, Clarke MCH, Bennett MR, Mallat Z. 2019. Vascular smooth muscle cells in atherosclerosis. *Nat Rev Cardiol.* **16**(12):727-744
- Bazzoni G, Dejana E. 2004. Endothelial Cell-to-Cell Junctions: Molecular Organization and Role in Vascular Homeostasis. *Physiol Rev.* **84**(3):869-901
- Benedito R, Roca C, Sørensen I, Adams S, Gossler A, Fruttiger M, Adams RH. 2009. The notch ligands Dll4 and Jagged1 have opposing effects on angiogenesis. *Cell.* **137**(6):1124-35.
- Bio-Rad Laboratories. 2019. *SYBR® Green for qPCR*. [Online]. [Accessed 6<sup>th</sup> November 2019]. Available from <https://www.bio-rad.com/featured/en/sybr-green-for-qpcr.html>
- Biswas SK, Newby DE, Rahman I, Megson IL. 2005. Depressed glutathione synthesis precedes oxidative stress and atherogenesis in Apo-E(-/-) mice. *Biochem Biophys Res Commun.* **338**(3):1368-73
- Boo YC, Kim HJ, Song H, Fulton D, Sessa W, Jo H. 2006. Coordinated regulation of endothelial nitric oxide synthase activity by phosphorylation and subcellular localization. *Free Radic Biol Med.* **41**(1):144-53
- Broussard JA, Green KJ. 2017. Research Techniques Made Simple: Methodology and Applications of Förster Resonance Energy Transfer (FRET) Microscopy. *J Invest Dermatol.* **137**(11):e185-e191
- Bryan NS, Grisham MB. 2007. Methods to detect nitric oxide and its metabolites in biological samples. *Free Radic Biol Med.* **43**(5):645-657
- Cahill PA, Redmond EM. 2016. Vascular endothelium - Gatekeeper of vessel health. *Atherosclerosis.* **248**:97-109

- Cantalupo A, Zhang Y, Kothiya M, Galvani S, Obinata H, Bucci M, Giordano FJ, Jiang XC, Hla T, Di Lorenzo A. 2015. Nogo-B regulates endothelial sphingolipid homeostasis to control vascular function and blood pressure. *Nat Med.* **21**(9):1028-1037
- Cardillo C, Nambi SS, Kilcoyne CM, Choucair WK, Katz A, Quon MJ, Panza JA. 1999. Insulin stimulates both endothelin and nitric oxide activity in the human forearm. *Circulation.* **100**(8):820-5
- Castegna A, Menga A. 2018. Glutamine Synthetase: Localization Dictates Outcome. *Genes (Basel).* **9**(2):108
- Cayman Chemical. 2019. *Nitrite/Nitrate Colorimetric Assay Kit*. [Online]. [Accessed 13<sup>th</sup> November 2019]. Available from: <https://www.caymanchem.com/pdfs/780001.pdf>
- Chalut KJ, Paluch EK. 2016. The Actin Cortex: A Bridge between Cell Shape and Function. *Dev Cell.* **38**(6):571-3
- Chang L, Villacorta L, Li R, Hamblin M, Xu W, Dou C, Zhang J, Wu J, Zeng R, Chen YE. 2012. Loss of perivascular adipose tissue on peroxisome proliferator-activated receptor- $\gamma$  deletion in smooth muscle cells impairs intravascular thermoregulation and enhances atherosclerosis. *Circulation.* **126**(9):1067-78
- Cheng S, Rhee EP, Larson MG, Lewis GD, McCabe EL, Shen D, Palma MJ, Roberts LD, Dejam A, Souza AL, Deik AA, Magnusson M, Fox CS, O'Donnell CJ, Vasan RS, Melander O, Clish CB, Gerszten RE, Wang TJ. 2012. Metabolite profiling identifies pathways associated with metabolic risk in humans. *Circulation.* **125**(18):2222-31
- Chepkova AN, Sergeeva OA, Görg B, Haas HL, Klöcker N, Häussinger D. 2017. Impaired novelty acquisition and synaptic plasticity in congenital hyperammonemia caused by hepatic glutamine synthetase deficiency. *Sci Rep.* **7**:40190
- Cinelli MA, Do HT, Miley GP, Silverman RB. 2020. Inducible nitric oxide synthase: Regulation, structure, and inhibition. *Med Res Rev.* **40**(1):158-189
- Clapham DE. 2007. Calcium signaling. *Cell.* **131**:1047-1058.
- Clavreul N, Adachi T, Pimental DR, Ido Y, Schöneich C, Cohen RA. 2006. S-glutathiolation by peroxynitrite of p21ras at cysteine-118 mediates its direct activation and downstream signaling in endothelial cells. *FASEB J.* **20**(3):518-20
- Cooper AJL. 1988. Glutamine synthetase in Glutamine and Glutamate Mammals. In: Kvamme, E. ed. *Glutamine and Glutamate Mammals Volume I*. Boca Raton: CRC press, pp.7-31

- Cooper GM. 2000. *The Cell: A Molecular Approach*. [Online]. 2nd ed. Sunderland (MA): Sinauer Associates. [Accessed 24<sup>th</sup> April 2019]. Available from: <https://www.ncbi.nlm.nih.gov/books/NBK9908/>
- Curtiss LK, Boisvert WA. 2000. Apolipoprotein E and atherosclerosis. *Curr Opin Lipidol*. **11**(3):243-51.
- Dahlström E, Sandholm N. 2017. Progress in Defining the Genetic Basis of Diabetic Complications. *Curr Diab Rep*. **17**(9):80
- Davis ME, Grumbach IM, Fukai T, Cutchins A, Harrison DG. 2004. Shear stress regulates endothelial nitric-oxide synthase promoter activity through nuclear factor kappaB binding. *J Biol Chem*. **279**(1):163-8
- De la Vega-Monroy MLL, Fernandez-Mejia C. 2011. Beta-Cell Function and Failure in Type 1 Diabetes. In: Wagner, D. ed. *Type 1 Diabetes - Pathogenesis, Genetics and Immunotherapy*. [Online]. IntechOpen. [Accessed 26<sup>th</sup> March 2019]. Available from: <https://www.intechopen.com/books/type-1-diabetes-pathogenesis-genetics-and-immunotherapy/beta-cell-function-and-failure-in-type-1-diabetes>
- Degendorfer G, Chuang CY, Kawasaki H, Hammer A, Malle E, Yamakura F, Davies MJ. 2016. Peroxynitrite-mediated oxidation of plasma fibronectin. *Free Radic Biol Med*. **97**:602-615
- Deignan JL, Cederbaum SD, Grody WW. 2008. Contrasting features of urea cycle disorders in human patients and knockout mouse models. *Mol Genet Metab*. **93**(1):7-14.
- do Carmo A, Lopes C, Santos M, Proença R, Cunha-Vaz J, Carvalho AP. 1998. Nitric oxide synthase activity and L-arginine metabolism in the retinas from streptozotocin-induced diabetic rats. *Gen Pharmacol*. **30**(3):319-24.
- Dominguez R, Holmes KC. 2011. Actin structure and function. *Annu Rev Biophys*. **40**:169-86
- Doran AC, Meller N, McNamara CA. 2008. Role of smooth muscle cells in the initiation and early progression of atherosclerosis. *Arterioscler Thromb Vasc Biol*. **28**(5):812-9
- Drab M, Verkade P, Elger M, Kasper M, Lohn M, Lauterbach B, Menne J, Lindschau C, Mende F, Luft FC, Schedl A, Haller H, Kurzchalia TV. 2001. Loss of caveolae, vascular dysfunction, and pulmonary defects in caveolin-1 gene-disrupted mice. *Science*. **293**(5539):2449-52
- Du XL, Edelstein D, Rossetti L, Fantus IG, Goldberg H, Ziyadeh F, Wu J, Brownlee M. 2000. Hyperglycemia-induced mitochondrial superoxide overproduction activates

- the hexosamine pathway and induces plasminogen activator inhibitor-1 expression by increasing Sp1 glycosylation. *Proc Natl Acad Sci U S A*. **97**(22):12222-6.
- Duarte AI, Proença T, Oliveira CR, Santos MS, Rego AC. 2006. Insulin restores metabolic function in cultured cortical neurons subjected to oxidative stress. *Diabetes*. **55**(10):2863-70.
- Duarte AI, Santos MS, Seïça R, de Oliveira CR. 2003. Insulin affects synaptosomal GABA and glutamate transport under oxidative stress conditions. *Brain Res*. **977**(1):23-30.
- Dudzinski DM, Michel T. 2007. Life history of eNOS: partners and pathways. *Cardiovasc Res*. **75**(2):247-60
- Dunn KW, Kamocka MM, McDonald JH. 2011. A practical guide to evaluating colocalization in biological microscopy. *Am J Physiol Cell Physiol*. **300**(4):C723-42
- Eagle H, Washington CL, Levy M, Cohen L. 1966. The population-dependent requirement by cultured mammalian cells for metabolites which they can synthesize. II. Glutamic acid and glutamine; aspartic acid and asparagine. *J Biol Chem*. **241**(21):4994-9.
- Eelen G, de Zeeuw P, Simons M, Carmeliet P. 2015. Endothelial cell metabolism in normal and diseased vasculature. *Circ Res*. **116**(7):1231-44
- Eelen G, Dubois C, Cantelmo AR, Goveia J, Brüning U, DeRan M, Jarugumilli G, van Rijssel J, Saladino G, Comitani F, Zecchin A, Rocha S, Chen R, Huang H, Vandekeere S, Kalucka J, Lange C, Morales-Rodriguez F, Cruys B, Treps L, Ramer L, Vinckier S, Brepoels K, Wyns S, Souffreau J, Schoonjans L, Lamers WH, Wu Y, Hastraete J, Hofkens J, Liekens S, Cubbon R, Ghesquière B, Dewerchin M, Gervasio FL, Li X, van Buul JD, Wu X, Carmeliet P. 2018. Role of glutamine synthetase in angiogenesis beyond glutamine synthesis. *Nature*. **561**(7721):63-69
- Ehrensvarð G, Fischer A, Stjernholm R. 1949. Protein metabolism of tissue cells in vitro. The chemical nature of some obligate factors of tissue cell nutrition. *Acta Physiologica Scandinavica*. **18**(2-3):218-30.
- Eid T, Behar K, Dhaher R, Bumanglag AV, Lee TS. 2012. Roles of glutamine synthetase inhibition in epilepsy. *Neurochem Res*. **37**(11):2339-50
- El-Assaad W, Buteau J, Peyot ML, Nolan C, Roduit R, Hardy S, Joly E, Dbaïbo G, Rosenberg L, Prentki M. 2003. Saturated fatty acids synergize with elevated glucose to cause pancreatic beta-cell death. *Endocrinology*. **144**(9):4154-63

- Ellinsworth DC, Shukla N, Fleming I, Jeremy JY. 2014. Interactions between thromboxane A<sub>2</sub>, thromboxane/prostaglandin (TP) receptors, and endothelium-derived hyperpolarization. *Cardiovasc Res.* **102**(1):9-16
- Emanuelli B, Peraldi P, Filloux C, Chavey C, Freidinger K, Hilton DJ, Hotamisligil GS, Van Obberghen E. 2001. SOCS-3 inhibits insulin signaling and is up-regulated in response to tumor necrosis factor-alpha in the adipose tissue of obese mice. *J Biol Chem.* **276**(51):47944-9
- Emini Veseli B, Perrotta P, De Meyer GRA, Roth L, Van der Donckt C, Martinet W, De Meyer GRY. 2017. Animal models of atherosclerosis. *Eur J Pharmacol.* **816**:3-13
- Eroglu E, Gottschalk B, Charoensin S, Blass S, Bischof H, Rost R, Madreiter-Sokolowski CT, Pelzmann B, Bernhart E, Sattler W, Hallström S, Malinski T, Waldeck-Weiermair M, Graier WF, Malli R. 2016. Development of novel FP-based probes for live-cell imaging of nitric oxide dynamics. *Nat Commun.* **7**:10623
- Erwin PA, Lin AJ, Golan DE, Michel T. 2005. Receptor-regulated dynamic S-nitrosylation of endothelial nitric-oxide synthase in vascular endothelial cells. *J Biol Chem.* **280**(20):19888-94
- Erwin PA, Mitchell DA, Sartoretto J, Marletta MA, Michel T. 2006. Subcellular targeting and differential S-nitrosylation of endothelial nitric-oxide synthase. *J Biol Chem.* **281**(1):151-7
- Esper RJ, Nordaby RA, Vilariño JO, Paragano A, Cacharrón JL, Machado RA. 2006. Endothelial dysfunction: a comprehensive appraisal. *Cardiovasc Diabetol.* **5**:4.
- Farah C, Michel LYM, Balligand JL. 2018. Nitric oxide signalling in cardiovascular health and disease. *Nat Rev Cardiol.* **15**(5):292-316
- Feil S, Valtcheva N, Feil R. 2009. Inducible Cre Mice. In: Wurst W., Kühn R. eds. *Gene Knockout Protocols. Methods in Molecular Biology (Methods and Protocols) Volume 530*. [Online]. Humana Press, pp.343–363. [Accessed 13<sup>th</sup> June 2018]. Available from: <https://link.springer.com/content/pdf/10.1007%2F978-1-59745-471-1.pdf>
- Fernandes SM, Cordeiro PM, Watanabe M, Fonseca CD, Vattimo MF. 2016. The role of oxidative stress in streptozotocin-induced diabetic nephropathy in rats. *Arch Endocrinol Metab.* **60**(5):443-449.
- Fernández-Hernando C, Fukata M, Bernatchez PN, Fukata Y, Lin MI, Bredt DS, Sessa WC. 2006. Identification of Golgi-localized acyl transferases that palmitoylate and regulate endothelial nitric oxide synthase. *J Cell Biol.* **174**(3):369-77.

- Feron O, Michel JB, Sase K, Michel T. 1998. Dynamic regulation of endothelial nitric oxide synthase: complementary roles of dual acylation and caveolin interactions. *Biochemistry*. **37**(1):193-200
- Finn AV, Jain RK. 2010. Coronary plaque neovascularization and hemorrhage: a potential target for plaque stabilization? *JACC Cardiovasc Imaging*. **3**(1):41-4
- Fleming I. 2010. Molecular mechanisms underlying the activation of eNOS. *Pflugers Arch*. **459**(6):793-806
- Förstermann U, Münzel T. 2006. Endothelial nitric oxide synthase in vascular disease: from marvel to menace. *Circulation*. **113**(13):1708-14.
- Förstermann U, Sessa WC. 2012. Nitric oxide synthases: regulation and function. *Eur Heart J*. **33**(7):829-37
- Foster MW, McMahon TJ, Stamler JS. 2003. S-nitrosylation in health and disease. *Trends Mol Med*. **9**(4):160-8.
- Fu Z, Gilbert ER, Liu D. 2013. Regulation of insulin synthesis and secretion and pancreatic Beta-cell dysfunction in diabetes. *Curr Diabetes Rev*. **9**(1):25-53.
- Furchgott RF, Zawadzki JV. 1980. The obligatory role of endothelial cells in the relaxation of arterial smooth muscle by acetylcholine. *Nature*. **288**(5789):373-6.
- Gage MC, Yuldasheva NY, Viswambharan H, Sukumar P, Cubbon RM, Galloway S, Imrie H, Skromna A, Smith J, Jackson CL, Kearney MT, Wheatcroft SB. 2013. Endothelium-specific insulin resistance leads to accelerated atherosclerosis in areas with disturbed flow patterns: a role for reactive oxygen species. *Atherosclerosis*. **230**(1):131-9
- Galley HF, Webster NR. 2004. Physiology of the endothelium. *Br J Anaesth*. **93**(1):105-13.
- Galoughi KK, Liu CC, Gentile C, Kok C, Nunez A, Garcia A, Fry NA, Davies MJ, Hawkins CL, Rasmussen HH, Figtree GA. 2014. Glutathionylation mediates angiotensin II-induced eNOS uncoupling, amplifying NADPH oxidase-dependent endothelial dysfunction. *J Am Heart Assoc*. **3**(2):e000731
- Gammelsaeter R, Coppola T, Marcaggi P, Storm-Mathisen J, Chaudhry FA, Attwell D, Regazzi R, Gundersen V. 2011. A role for glutamate transporters in the regulation of insulin secretion. *PLoS One*. **6**(8):e22960
- Gao Z, Zuberi A, Quon MJ, Dong Z, Ye J. 2003. Aspirin inhibits serine phosphorylation of insulin receptor substrate 1 in tumor necrosis factor treated cells through targeting multiple serine kinases. *J Biol Chem*. **278**(27):24944-50

- Gargiulo S, Gramanzini M, Mancini M. 2016. Molecular Imaging of Vulnerable Atherosclerotic Plaques in Animal Models. *Int J Mol Sci.* **17**(9):1511
- Getz GS, Reardon CA. 2012. Animal models of atherosclerosis. *Arterioscler Thromb Vasc Biol.* **32**(5):1104-15
- Getz GS, Reardon CA. 2016. ApoE knockout and knockin mice: the history of their contribution to the understanding of atherogenesis. *J Lipid Res.* **57**(5):758-66
- Getz GS, Reardon CA. 2009. Apoprotein E as a lipid transport and signaling protein in the blood, liver, and artery wall. *J Lipid Res.* **50** Supp:S156-61.
- Gielis JF, Lin JY, Wingler K, Van Schil PE, Schmidt HH, Moens AL. 2011. Pathogenetic role of eNOS uncoupling in cardiopulmonary disorders. *Free Radic Biol Med.* **50**(7):765-76
- Gisterå A, Hansson GK. 2017. The immunology of atherosclerosis. *Nat Rev Nephrol.* **13**(6):368-380
- Glick D, Barth S, Macleod KF. 2010. Autophagy: cellular and molecular mechanisms. *J Pathol.* **221**(1):3-12
- Góth MI, Hubina E, Raptis S, Nagy GM, Tóth BE. 2003. Physiological and pathological angiogenesis in the endocrine system. *Microsc Res Tech.* **60**(1):98-106.
- Gough PJ, Gomez IG, Wille PT, Raines EW. 2006. Macrophage expression of active MMP-9 induces acute plaque disruption in apoE-deficient mice. *J Clin Invest.* **116**(1):59-69.
- Greif DM, Sacks DB, Michel T. 2004. Calmodulin phosphorylation and modulation of endothelial nitric oxide synthase catalysis. *Proc Natl Acad Sci U S A.* **101**(5):1165-70
- Guo JP, Panday MM, Consigny PM, Lefer AM. 1995. Mechanisms of vascular preservation by a novel NO donor following rat carotid artery intimal injury. *Am J Physiol.* **269**(3 Pt 2):H1122-31.
- Gvazava IG, Rogovaya OS, Borisov MA, Vorotelyak EA, Vasiliev AV. 2018. Pathogenesis of Type 1 Diabetes Mellitus and Rodent Experimental Models. *Acta Naturae.* **10**(1):24–33.
- Halvorsen B, Otterdal K, Dahl TB, Skjelland M, Gullestad L, Øie E, Aukrust P. 2008. Atherosclerotic plaque stability—what determines the fate of a plaque? *Prog Cardiovasc Dis.* **51**(3):183-94
- Hansson GK, Hermansson A. 2011. The immune system in atherosclerosis. *Nat Immunol.* **12**(3):204-12

- Harcourt BE, Penfold SA, Forbes JM. 2013. Coming full circle in diabetes mellitus: from complications to initiation. *Nat Rev Endocrinol.* **9**(2):113-23
- Hartell NA, Archer HE, Bailey CJ. 2005. Insulin-stimulated endothelial nitric oxide release is calcium independent and mediated via protein kinase B. *Biochem Pharmacol.* **69**(5):781-90
- Hassona MD, Abouelnaga ZA, Elnakish MT, Awad MM, Alhaj M, Goldschmidt-Clermont PJ, Hassanain H. 2010. Vascular hypertrophy-associated hypertension of proflin1 transgenic mouse model leads to functional remodeling of peripheral arteries. *Am J Physiol Heart Circ Physiol.* **298**(6):H2112-20
- Hatzoglou M, Fernandez J, Yaman I, Closs E. 2004. Regulation of cationic amino acid transport: the story of the CAT-1 transporter. *Annu Rev Nutr.* **24**:377-99.
- Hayashi K, Kojima R, Ito M. 2006. Strain differences in the diabetogenic activity of streptozotocin in mice. *Biol Pharm Bull.* **29**(6):1110-9.
- He Y, Hakvoort TB, Vermeulen JL, Labruyère WT, De Waart DR, Van Der Hel WS, Ruijter JM, Uylings HB, Lamers WH. 2010. Glutamine synthetase deficiency in murine astrocytes results in neonatal death. *Glia.* **58**(6):741-54
- Heinonen SE, Genové G, Bengtsson E, Hübschle T, Åkesson L, Hiss K, Benardeau A, Ylä-Herttuala S, Jönsson-Rylander AC, Gomez MF. 2015. Animal models of diabetic macrovascular complications: key players in the development of new therapeutic approaches. *J Diabetes Res.* **2015**:404085.
- Heiss EH, Dirsch VM. 2014. Regulation of eNOS enzyme activity by posttranslational modification. *Curr Pharm Des.* **20**(22):3503-13.
- Hemmens B, Mayer B. 1998. Enzymology of nitric oxide synthases. In: Titheradge MA, ed. *Nitric oxide protocols. Methods in Molecular Biology™, vol 100.* Totowa, NJ: Humana Press, pp.1-32.
- Hill BG, Dranka BP, Bailey SM, Lancaster JR Jr, Darley-Usmar VM. 2010. What part of NO don't you understand? Some answers to the cardinal questions in nitric oxide biology. *J Biol Chem.* **285**(26):19699-704
- Hirase T, Node K. 2012. Endothelial dysfunction as a cellular mechanism for vascular failure. *Am J Physiol Heart Circ Physiol.* **302**(3):H499-505
- Hogg N. 2010. Detection of nitric oxide by electron paramagnetic resonance spectroscopy. *Free Radic Biol Med.* **49**(2):122–129

- Hottinger DG, Beebe DS, Kozhimannil T, Prielipp RC, Belani KG. 2014. Sodium nitroprusside in 2014: A clinical concepts review. *J Anaesthesiol Clin Pharmacol.* **30**(4):462-71
- Hrometz SL, Edelmann SE, McCune DF, Olges JR, Hadley RW, Perez DM, Piascik MT. 1999. Expression of multiple alpha1-adrenoceptors on vascular smooth muscle: correlation with the regulation of contraction. *J Pharmacol Exp Ther.* **290**(1):452-63.
- Hu P, Lai D, Lu P, Gao J, He H. 2012. ERK and Akt signaling pathways are involved in advanced glycation end product-induced autophagy in rat vascular smooth muscle cells. *Int J Mol Med.* **29**(4):613-8
- Hutcheson IR, Griffith TM. 1996. Mechanotransduction through the endothelial cytoskeleton: mediation of flow- but not agonist-induced EDRF release. *Br J Pharmacol.* **118**(3):720-6.
- International Diabetes Federation. 2019. *IDF Diabetes Atlas, 9th edn.* Brussels, Belgium: International Diabetes Federation.
- Ishibashi S, Goldstein JL, Brown MS, Herz J, Burns DK. 1994. Massive xanthomatosis and atherosclerosis in cholesterol-fed low density lipoprotein receptor-negative mice. *J Clin Invest.* **93**(5):1885-93
- Ishikawa S, Nakazawa M, Ishikawa A, Ishiguro S, Tamai M. 1995. Alteration of glutamine concentration in the vitreous humor in patients with proliferative vitreoretinopathy. *Curr Eye Res.* **14**(3):191-7.
- Iwakiri Y. 2011. S-nitrosylation of proteins: a new insight into endothelial cell function regulated by eNOS-derived NO. *Nitric Oxide.* **25**(2):95–101
- Jeitner TM, Battaile K, Cooper AJ. 2015. Critical Evaluation of the Changes in Glutamine Synthetase Activity in Models of Cerebral Stroke. *Neurochem Res.* **40**(12):2544-56
- Jensen E. 2014. Technical review: colocalization of antibodies using confocal microscopy. *Anat Rec (Hoboken).* **297**(2):183-7
- Jia G, Durante W, Sowers JR. 2016. Endothelium-Derived Hyperpolarizing Factors: A Potential Therapeutic Target for Vascular Dysfunction in Obesity and Insulin Resistance. *Diabetes.* **65**(8):2118-20
- Kahn MB, Cubbon RM, Mercer B, Wheatcroft AC, Gherardi G, Aziz A, Baliga V, Blaxill JM, McLenachan JM, Blackman DJ, Greenwood JP, Wheatcroft SB. 2012. Association of diabetes with increased all-cause mortality following primary percutaneous coronary intervention for ST-segment elevation myocardial infarction in the contemporary era. *Diab Vasc Dis Res.* **9**(1):3-9

- Kalucka J, de Rooij LPMH, Goveia J, Rohlenova K, Dumas SJ, Meta E, Conchinha NV, Taverna F, Teuwen LA, Veys K, García-Caballero M, Khan S, Geldhof V, Sokol L, Chen R, Treps L, Borri M, de Zeeuw P, Dubois C, Karakach TK, Falkenberg KD, Parys M, Yin X, Vinckier S, Du Y, Fenton RA, Schoonjans L, Dewerchin M, Eelen G, Thienpont B, Lin L, Bolund L, Li X, Luo Y, Carmeliet P. 2020. Single-Cell Transcriptome Atlas of Murine Endothelial Cells. *Cell*. **180**(4):764-779.e20
- Kang DH, Choi M, Chang S, Lee MY, Lee DJ, Choi K, Park J, Han EC, Hwang D, Kwon K, Jo H, Choi C, Kang SW. 2015. Vascular Proteomics Reveal Novel Proteins Involved in SMC Phenotypic Change: OLR1 as a SMC Receptor Regulating Proliferation and Inflammatory Response. *PLoS One*. **10**(8):e0133845
- Kang-Decker N, Cao S, Chatterjee S, Yao J, Egan LJ, Semela D, Mukhopadhyay D, Shah V. 2007. Nitric oxide promotes endothelial cell survival signaling through S-nitrosylation and activation of dynamin-2. *J Cell Sci*. **120**(Pt 3):492-501.
- Kashiwagi S, Atochin DN, Li Q, Schleicher M, Pong T, Sessa WC, Huang PL. 2013. eNOS phosphorylation on serine 1176 affects insulin sensitivity and adiposity. *Biochem Biophys Res Commun*. **431**(2):284-90
- Kim C, Yang H, Fukushima Y, Saw PE, Lee J, Park JS, Park I, Jung J, Kataoka H, Lee D, Heo WD, Kim I, Jon S, Adams RH, Nishikawa S, Uemura A, Koh GY. 2014. Vascular RhoJ is an effective and selective target for tumor angiogenesis and vascular disruption. *Cancer Cell*. **25**(1):102–117
- Kim H, Kim M, Im SK, Fang S. 2018. Mouse Cre-LoxP system: general principles to determine tissue-specific roles of target genes. *Lab Anim Res*. **34**(4):147-159
- Kim JA, Montagnani M, Koh KK, Quon MJ. 2006. Reciprocal relationships between insulin resistance and endothelial dysfunction: molecular and pathophysiological mechanisms. *Circulation*. **113**(15):1888-904.
- Kim JH, Bugaj LJ, Oh YJ, Bivalacqua TJ, Ryoo S, Soucy KG, Santhanam L, Webb A, Camara A, Sikka G, Nyhan D, Shoukas AA, Ilies M, Christianson DW, Champion HC, Berkowitz DE. 2009. Arginase inhibition restores NOS coupling and reverses endothelial dysfunction and vascular stiffness in old rats. *J Appl Physiol (1985)*. **107**(4):1249-57
- Kondrashova A, Hyöty H. 2014. Role of viruses and other microbes in the pathogenesis of type 1 diabetes. *Int Rev Immunol*. **33**(4):284-95
- Kondrikov D, Fonseca FV, Elms S, Fulton D, Black SM, Block ER, Su Y. 2010. Beta-actin association with endothelial nitric-oxide synthase modulates nitric oxide and superoxide generation from the enzyme. *J Biol Chem*. **285**(7):4319-27

- Kondrikov D, Gross C, Black SM, Su Y. 2014. Novel peptide for attenuation of hyperoxia-induced disruption of lung endothelial barrier and pulmonary edema via modulating peroxynitrite formation. *J Biol Chem.* **289**(48):33355–33363
- Kuhlencordt PJ, Chen J, Han F, Astern J, Huang PL. 2001. Genetic deficiency of inducible nitric oxide synthase reduces atherosclerosis and lowers plasma lipid peroxides in apolipoprotein E-knockout mice. *Circulation.* **103**(25):3099-104
- Kulijewicz-Nawrot M, Syková E, Chvátal A, Verkhatsky A, Rodríguez JJ. 2013. Astrocytes and glutamate homeostasis in Alzheimer's disease: a decrease in glutamine synthetase, but not in glutamate transporter-1, in the prefrontal cortex. *ASN Neuro.* **5**(4):273-82
- Kumar A, Bachhawat AK. 2012. Pyroglutamic acid: throwing light on a lightly studied metabolite. *Current Science.* **102**, 288–297
- Kunieda T, Minamino T, Miura K, Katsuno T, Tateno K, Miyauchi H, Kaneko S, Bradfield CA, FitzGerald GA, Komuro I. 2008. Reduced nitric oxide causes age-associated impairment of circadian rhythmicity. *Circ Res.* **102**(5):607-14
- Kwon GP, Schroeder JL, Amar MJ, Remaley AT, Balaban RS. 2008. Contribution of macromolecular structure to the retention of low-density lipoprotein at arterial branch points. *Circulation.* **117**(22):2919-27
- Lagache T, Sauvonnnet N, Danglot L, Olivo-Marin JC. 2015. Statistical analysis of molecule colocalization in bioimaging. *Cytometry A.* **87**(6):568-79
- Lee HW, Osis G, Handlogten ME, Lamers WH, Chaudhry FA, Verlander JW, Weiner ID. 2016. Proximal tubule-specific glutamine synthetase deletion alters basal and acidosis-stimulated ammonia metabolism. *Am J Physiol Renal Physiol.* **310**(11):F1229-42
- Lee JK, Borhani M, Ennis TL, Upchurch GR Jr, Thompson RW. 2001. Experimental abdominal aortic aneurysms in mice lacking expression of inducible nitric oxide synthase. *Arterioscler Thromb Vasc Biol.* **21**(9):1393-401
- Lee SG, Yim YS, Lee YH, Lee BW, Kim HS, Kim KS, Lee YW, Kim JH. 2018. Fasting serum amino acids concentration is associated with insulin resistance and pro-inflammatory cytokines. *Diabetes Res Clin Pract.* **140**:107-117
- Levonen AL, Inkala M, Heikura T, Jauhiainen S, Jyrkkänen HK, Kansanen E, Määttä K, Romppanen E, Turunen P, Rutanen J, Ylä-Herttuala S. 2007. Nrf2 gene transfer induces antioxidant enzymes and suppresses smooth muscle cell growth in vitro and reduces oxidative stress in rabbit aorta in vivo. *Arterioscler Thromb Vasc Biol.* **27**(4):741-7

- Li H, Horke S, Förstermann U. 2014. Vascular oxidative stress, nitric oxide and atherosclerosis. *Atherosclerosis*. **237**(1):208-19
- Liaudet L, Vassalli G, Pacher P. 2009. Role of peroxynitrite in the redox regulation of cell signal transduction pathways. *Front Biosci (Landmark Ed)*. **14**:4809-14.
- Libby P, Ridker PM, Hansson GK. 2011. Progress and challenges in translating the biology of atherosclerosis. *Nature*. **473**(7347):317-25
- Lima B, Forrester MT, Hess DT, Stamler JS. 2010. S-nitrosylation in cardiovascular signaling. *Circ Res*. **106**(4):633-46
- Lo Sasso G, Schlage WK, Boué S, Veljkovic E, Peitsch MC, Hoeng J. 2016. The Apoe(-/-) mouse model: a suitable model to study cardiovascular and respiratory diseases in the context of cigarette smoke exposure and harm reduction. *J Transl Med*. **14**(1):146
- Look AHEAD Research Group. 2016. Prospective Association of GLUL rs10911021 With Cardiovascular Morbidity and Mortality Among Individuals With Type 2 Diabetes: The Look AHEAD Study. *Diabetes*. **65**(1):297–302
- Lu QY, Chen W, Lu L, Zheng Z, Xu X. 2014. Involvement of RhoA/ROCK1 signaling pathway in hyperglycemia-induced microvascular endothelial dysfunction in diabetic retinopathy. *Int J Clin Exp Pathol*. **7**(10):7268-77
- Luiking YC, Engelen MP, Deutz NE. 2010. Regulation of nitric oxide production in health and disease. *Curr Opin Clin Nutr Metab Care*. **13**(1):97–104
- Luiking YC, Hallemeesch MM, Lamers WH, Deutz NE. 2005. The role of NOS2 and NOS3 in renal protein and arginine metabolism during early endotoxemia in mice. *Am J Physiol Renal Physiol*. **288**(4):F816-22
- Lundberg JO, Gladwin MT, Weitzberg E. 2015. Strategies to increase nitric oxide signalling in cardiovascular disease. *Nat Rev Drug Discov*. **14**(9):623-41
- Ma T, Gao Q, Zhu F, Guo C, Wang Q, Gao F, Zhang L. 2013. Th17 cells and IL-17 are involved in the disruption of vulnerable plaques triggered by short-term combination stimulation in apolipoprotein E-knockout mice. *Cell Mol Immunol*. **10**(4):338-48
- Madonna R, De Caterina R. 2011a. Cellular and molecular mechanisms of vascular injury in diabetes--part I: pathways of vascular disease in diabetes. *Vascul Pharmacol*. **54**(3-6):68-74
- Madonna R, De Caterina R. 2011b. Cellular and molecular mechanisms of vascular injury in diabetes--part II: cellular mechanisms and therapeutic targets. *Vascul Pharmacol*. **54**(3-6):75-9

- Mann GE, Yudilevich DL, Sobrevia L. 2003. Regulation of amino acid and glucose transporters in endothelial and smooth muscle cells. *Physiol Rev.* **83**(1):183-252.
- Marin EP, Derakhshan B, Lam TT, Davalos A, Sessa WC. 2012. Endothelial cell palmitoylproteomic identifies novel lipid-modified targets and potential substrates for protein acyl transferases. *Circ Res.* **110**(10):1336-44
- Martin BR. 2013. Nonradioactive analysis of dynamic protein palmitoylation. *Curr Protoc Protein Sci.* **73**:14.15.1-14.15.9
- Medley TL, Cole TJ, Gatzka CD, Wang WY, Dart AM, Kingwell BA. 2002. Fibrillin-1 genotype is associated with aortic stiffness and disease severity in patients with coronary artery disease. *Circulation.* **105**(7):810-5.
- Meininger CJ, Wu G. 1997. L-glutamine inhibits nitric oxide synthesis in bovine venular endothelial cells. *J Pharmacol Exp Ther.* **281**(1):448-53.
- Mellon FA. 2003. Mass Spectrometry Principles and Instrumentation. In: Caballero, B. ed. *Encyclopedia of Food Sciences and Nutrition (Second Edition)*. Academic Press, pp.3739-3749
- Mitchell BJ, Chen Zp, Tiganis T, Stapleton D, Katsis F, Power DA, Sim AT, Kemp BE. 2001. Coordinated control of endothelial nitric-oxide synthase phosphorylation by protein kinase C and the cAMP-dependent protein kinase. *J Biol Chem.* **276**(21):17625-8
- Michiels C. 2003. Endothelial cell functions. *Journal of Cellular Physiology.* **196**(3):430-43
- Miltenyi Biotec. 2019. *Magnetic cell separation*. [Online]. [Accessed 13<sup>th</sup> November 2019]. Available from: <https://www.miltenyibiotec.com/GB-en/resources/macshandbook/macstechnologies/cellseparation/magneticcellseparation.html>
- Mitchell JA, Ali F, Bailey L, Moreno L, Harrington LS. 2008. Role of nitric oxide and prostacyclin as vasoactive hormones released by the endothelium. *Exp Physiol.* **93**(1):141-7
- Mitri J, Pittas AG. 2014. Vitamin D and diabetes. *Endocrinol Metab Clin North Am.* **43**(1):205-32
- Miyoshi T, Li Y, Shih DM, Wang X, Laubach VE, Matsumoto AH, Helm GA, Lusis AJ, Shi W. 2006. Deficiency of inducible NO synthase reduces advanced but not early atherosclerosis in apolipoprotein E-deficient mice. *Life Sci.* **79**(6):525-31

- Möller MN, Rios N, Trujillo M, Radi R, Denicola A, Alvarez B. 2019. Detection and quantification of nitric oxide-derived oxidants in biological systems. *J Biol Chem.* **294**(40):14776–14802.
- Montagnani M, Chen H, Barr VA, Quon MJ. 2001. Insulin-stimulated activation of eNOS is independent of Ca<sup>2+</sup> but requires phosphorylation by Akt at Ser(1179). *J Biol Chem.* **276**(32):30392-8
- Moore KJ, Sheedy FJ, Fisher EA. 2013. Macrophages in atherosclerosis: a dynamic balance. *Nat Rev Immunol.* **13**(10):709-21
- Morris SM Jr. 2016. Arginine Metabolism Revisited. *J Nutr.* **146**(12):2579S-2586S
- Morrison JA, Jacobsen DW, Sprecher DL, Robinson K, Khoury P, Daniels SR. 1999. Serum glutathione in adolescent males predicts parental coronary heart disease. *Circulation.* **100**(22):2244-7.
- Moura R, Tjwa M, Vandervoort P, Van Kerckhoven S, Holvoet P, Hoylaerts MF. 2008. Thrombospondin-1 deficiency accelerates atherosclerotic plaque maturation in ApoE<sup>-/-</sup> mice. *Circ Res.* **103**:1181–1189.
- Mungrue IN, Gros R, You X, Pirani A, Azad A, Csont T, Schulz R, Butany J, Stewart DJ, Husain M. 2002. Cardiomyocyte overexpression of iNOS in mice results in peroxynitrite generation, heart block, and sudden death. *J Clin Invest.* **109**(6):735-43
- Muniyappa R, Montagnani M, Koh KK, Quon MJ. 2007. Cardiovascular actions of insulin. *Endocr Rev.* **28**(5):463-91
- Murohara T, Witzenbichler B, Spyridopoulos I, Asahara T, Ding B, Sullivan A, Losordo DW, Isner JM. 1999. Role of endothelial nitric oxide synthase in endothelial cell migration. *Arterioscler Thromb Vasc Biol.* **19**(5):1156-61
- Nakashima Y, Plump AS, Raines EW, Breslow JL, Ross R. 1994. ApoE-deficient mice develop lesions of all phases of atherosclerosis throughout the arterial tree. *Arterioscler Thromb.* **14**(1):133-40.
- Napoli C, de Nigris F, Williams-Ignarro S, Pignalosa O, Sica V, Ignarro LJ. 2006. Nitric oxide and atherosclerosis: an update. *Nitric Oxide.* **15**(4):265-79
- Needell JC, Zipris D. 2017. Targeting Innate Immunity for Type 1 Diabetes Prevention. *Curr Diab Rep.* **17**(11):113
- Newgard CB, An J, Bain JR, Muehlbauer MJ, Stevens RD, Lien LF, Haqq AM, Shah SH, Arlotto M, Slentz CA, Rochon J, Gallup D, Ilkayeva O, Wenner BR, Yancy WS Jr, Eisenson H, Musante G, Surwit RS, Millington DS, Butler MD, Svetkey LP. 2009.

- A branched-chain amino acid-related metabolic signature that differentiates obese and lean humans and contributes to insulin resistance. *Cell Metab.* **9**(4):311-26
- Newsholme P, Bender K, Kiely A, Brennan L. 2007. Amino acid metabolism, insulin secretion and diabetes. *Biochem Soc Trans.* **35**(Pt 5):1180-6.
- Newsholme P, Krause M. 2012. Nutritional regulation of insulin secretion: implications for diabetes. *Clin Biochem Rev.* **33**(2):35-47.
- Newsholme P, Lima MM, Procopio J, Pithon-Curi TC, Doi SQ, Bazotte RB, Curi R. 2003. Glutamine and glutamate as vital metabolites. *Braz J Med Biol Res.* **36**(2):153-63
- Ni M, Chen WQ, Zhang Y. 2009. Animal models and potential mechanisms of plaque destabilisation and disruption. *Heart.* **95**(17):1393-8
- Nolan CJ, Damm P, Prentki M. 2011. Type 2 diabetes across generations: from pathophysiology to prevention and management. *Lancet.* **378**(9786):169-81
- Nolan CJ, Madiraju MS, Delghingaro-Augusto V, Peyot ML, Prentki M. 2006. Fatty acid signaling in the beta-cell and insulin secretion. *Diabetes.* **55** Suppl 2:S16-23
- Noronha BT, Li JM, Wheatcroft SB, Shah AM, Kearney MT. 2005. Inducible nitric oxide synthase has divergent effects on vascular and metabolic function in obesity. *Diabetes.* **54**(4):1082-9.
- Oess S, Icking A, Fulton D, Govers R, Müller-Ester W. 2006. Subcellular targeting and trafficking of nitric oxide synthases. *Biochem J.* **396**(3):401-9.
- Okada T, Watanabe Y, Brusilow SW, Traystman RJ, Koehler RC. 2000. Interaction of glutamine and arginine on cerebrovascular reactivity to hypercapnia. *Am J Physiol Heart Circ Physiol.* **278**(5):H1577-84.
- Ormazabal V, Nair S, Elfeky O, Aguayo C, Salomon C, Zuñiga FA. 2018. Association between insulin resistance and the development of cardiovascular disease. *Cardiovasc Diabetol.* **17**(1):122
- Ozkor MA, Quyyumi AA. 2011. Endothelium-derived hyperpolarizing factor and vascular function. *Cardiol Res Pract.* **2011**:156146
- Palmieri EM, Menga A, Lebrun A, Hooper DC, Butterfield DA, Mazzone M, Castegna A. 2017a. Blockade of Glutamine Synthetase Enhances Inflammatory Response in Microglial Cells. *Antioxid Redox Signal.* **26**(8):351-363
- Palmieri EM, Menga A, Martín-Pérez R, Quinto A, Riera-Domingo C, De Tullio G, Hooper DC, Lamers WH, Ghesquière B, McVicar DW, Guarini A, Mazzone M, Castegna A. 2017b. Pharmacologic or Genetic Targeting of Glutamine Synthetase

- Skews Macrophages toward an M1-like Phenotype and Inhibits Tumor Metastasis. *Cell Rep.* **20**(7):1654-1666
- Paneni F, Beckman JA, Creager MA, Cosentino F. 2013. Diabetes and vascular disease: pathophysiology, clinical consequences, and medical therapy: part I. *Eur Heart J.* **34**(31):2436-43
- Papetti M, Herman IM. 2002. Mechanisms of normal and tumor-derived angiogenesis. *Am J Physiol Cell Physiol.* **282**(5):C947-70.
- Parat MO, Stachowicz RZ, Fox PL. 2002. Oxidative stress inhibits caveolin-1 palmitoylation and trafficking in endothelial cells. *Biochem J.* **361**(Pt 3):681-8
- Payne S, De Val S, Neal A. 2018. Endothelial-Specific Cre Mouse Models. *Arterioscler Thromb Vasc Biol.* **38**(11):2550-2561
- Pearson JD. 2000. Normal endothelial cell function. *Lupus.* **9**(3):183-8.
- Percival KR, Radi ZA. 2016. A modified Verhoeff's elastin histochemical stain to enable pulmonary arterial hypertension model characterization. *Eur J Histochem.* **60**(1):2588
- Perisic L, Hedin E, Razuvaev A, Lengquist M, Osterholm C, Folkersen L, Gillgren P, Paulsson-Berne G, Ponten F, Odeberg J, Hedin U. 2013. Profiling of atherosclerotic lesions by gene and tissue microarrays reveals PCSK6 as a novel protease in unstable carotid atherosclerosis. *Arterioscler Thromb Vasc Biol.* **33**(10):2432-43
- Pi X, Wu Y, Ferguson JE 3rd, Portbury AL, Patterson C. 2009. SDF-1alpha stimulates JNK3 activity via eNOS-dependent nitrosylation of MKP7 to enhance endothelial migration. *Proc Natl Acad Sci U S A.* **106**(14):5675-80.
- Poitout V, Hagman D, Stein R, Artner I, Robertson RP, Harmon JS. 2006. Regulation of the insulin gene by glucose and fatty acids. *J Nutr.* **136**(4):873-6
- Prakash P, Khanna V, Singh V, Jyoti A, Jain M, Keshari RS, Barthwal MK, Dikshit M. 2011. Atorvastatin protects against ischemia-reperfusion injury in fructose-induced insulin resistant rats. *Cardiovasc Drugs Ther.* **25**(4):285-97
- Prudente S, Shah H, Bailetti D, Pezzolesi M, Buranasupkajorn P, Mercuri L, Mendonca C, De Cosmo S, Niewczas M, Trischitta V, Doria A. 2015. Genetic Variant at the GLUL Locus Predicts All-Cause Mortality in Patients With Type 2 Diabetes. *Diabetes.* **64**(7):2658-63
- Purushothaman KR, Purushothaman M, Muntner P, Lento PA, O'Connor WN, Sharma SK, Fuster V, Moreno PR. 2011. Inflammation, neovascularization and intra-plaque

- hemorrhage are associated with increased reparative collagen content: implication for plaque progression in diabetic atherosclerosis. *Vasc Med.* **16**(2):103-8
- Qi L, Qi Q, Prudente S, Mendonca C, Andreozzi F, di Pietro N, Sturma M, Novelli V, Mannino GC, Formoso G, Gervino EV, Hauser TH, Muehlschlegel JD, Niewczas MA, Krolewski AS, Biolo G, Pandolfi A, Rimm E, Sesti G, Trischitta V, Hu F, Doria A. 2013. Association between a genetic variant related to glutamic acid metabolism and coronary heart disease in individuals with type 2 diabetes. *JAMA.* **310**(8):821-8
- Qiu AW, Liu QH, Wang JL. 2017. Blocking IL-17A Alleviates Diabetic Retinopathy in Rodents. *Cell Physiol Biochem.* **41**(3):960-972
- Qvartskhava N, Lang PA, Görg B, Pozdeev VI, Ortiz MP, Lang KS, Bidmon HJ, Lang E, Leibrock CB, Herebian D, Bode JG, Lang F, Häussinger D. 2015. Hyperammonemia in gene-targeted mice lacking functional hepatic glutamine synthetase. *Proc Natl Acad Sci U S A.* **112**(17):5521-6.
- Radu M, Chernoff J. 2013. An in vivo assay to test blood vessel permeability. *J Vis Exp.* (73):e50062
- Radulović S, Gottschalk B, Hörl G, Zardoya-Laguardia P, Schilcher I, Hallström S, Vujić N, Schmidt K, Trieb M, Graier WF, Malli R, Kratky D, Marsche G, Frank S. 2020. Endothelial lipase increases eNOS activating capacity of high-density lipoprotein. *Biochim Biophys Acta Mol Cell Biol Lipids.* **1865**(4):158612
- Ravi K, Brennan LA, Levic S, Ross PA, Black SM. 2004. S-nitrosylation of endothelial nitric oxide synthase is associated with monomerization and decreased enzyme activity. *Proc Natl Acad Sci U S A.* **101**(8):2619-24.
- Resh MD. 1999. Fatty acylation of proteins: new insights into membrane targeting of myristoylated and palmitoylated proteins. *Biochim Biophys Acta.* **1451**(1):1-16
- Reventun P, Alique M, Cuadrado I, Márquez S, Toro R, Zaragoza C, Saura M. 2017. iNOS-Derived Nitric Oxide Induces Integrin-Linked Kinase Endocytic Lysosome-Mediated Degradation in the Vascular Endothelium. *Arterioscler Thromb Vasc Biol.* **37**(7):1272-1281
- Rhee SY, Jung ES, Park HM, Jeong SJ, Kim K, Chon S, Yu SY, Woo JT, Lee CH. 2018. Plasma glutamine and glutamic acid are potential biomarkers for predicting diabetic retinopathy. *Metabolomics.* **14**(7):89
- Roduit R, Nolan C, Alarcon C, Moore P, Barbeau A, Delghingaro-Augusto V, Przybykowski E, Morin J, Masse F, Massie B, Ruderman N, Rhodes C, Poitout V, Prentki M. 2004. A role for the malonyl-CoA/long-chain acyl-CoA pathway of lipid

- signaling in the regulation of insulin secretion in response to both fuel and nonfuel stimuli. *Diabetes*. **53**(4):1007-19
- Rohlenova K, Veys K, Miranda-Santos I, De Bock K, Carmeliet P. 2018. Endothelial Cell Metabolism in Health and Disease. *Trends Cell Biol*. **28**(3):224-236
- Ronzio RA, Meister A. 1968. Phosphorylation of methionine sulfoximine by glutamine synthetase. *Proc Natl Acad Sci U S A*. **59**(1):164-70
- Ross R, Glomset J, Harker L. 1977. Response to injury and atherogenesis. *Am J Pathol*. **86**(3): 675-84.
- Roth L, Van der Donckt C, Emini Veseli B, Van Dam D, De Deyn PP, Martinet W, Herman AG, De Meyer GRY. 2019. Nitric oxide donor molsidomine favors features of atherosclerotic plaque stability and reduces myocardial infarction in mice. *Vascul Pharmacol*. **118-119**:106561
- Rowland CE, Brown CW, Medintz IL, Delehanty JB. 2015. Intracellular FRET-based probes: a review. *Methods Appl Fluoresc*. **3**(4):042006
- Rudijanto A. 2007. The role of vascular smooth muscle cells on the pathogenesis of atherosclerosis. *Acta Med Indones*. **39**(2):86-93
- Rudolph TK, Rudolph V, Edreira MM, Cole MP, Bonacci G, Schopfer FJ, Woodcock SR, Franek A, Pekarova M, Khoo NK, Hasty AH, Baldus S, Freeman BA. 2010. Nitro-fatty acids reduce atherosclerosis in apolipoprotein E-deficient mice. *Arterioscler Thromb Vasc Biol*. **30**(5):938-45
- Sakakura K, Nakano M, Otsuka F, Ladich E, Kolodgie FD, Virmani R. 2013. Pathophysiology of atherosclerosis plaque progression. *Heart Lung Circ*. **22**(6):399-411
- Saksi J, Ijäs P, Nuotio K, Sonninen R, Soinne L, Salonen O, Saimanen E, Tuimala J, Lehtonen-Smeds EM, Kaste M, Kovanen PT, Lindsberg PJ. 2011. Gene expression differences between stroke-associated and asymptomatic carotid plaques. *J Mol Med (Berl)*. **89**(10):1015-26
- Sandoo A, van Zanten JJ, Metsios GS, Carroll D, Kitis GD. 2010. The endothelium and its role in regulating vascular tone. *Open Cardiovasc Med J*. **4**:302-12
- Sappington DR, Siegel ER, Hiatt G, Desai A, Penney RB, Jamshidi-Parsian A, Griffin RJ, Boysen G. 2016. Glutamine drives glutathione synthesis and contributes to radiation sensitivity of A549 and H460 lung cancer cell lines. *Biochim Biophys Acta*. **1860**(4):836-43

- Schmitt CA, Heiss EH, Aristei Y, Severin T, Dirsch VM. 2009. Norfuranol dephosphorylates eNOS at threonine 495 and enhances eNOS activity in human endothelial cells. *Cardiovasc Res.* **81**(4):750-7
- Schousboe A, Scafidi S, Bak LK, Waagepetersen HS, McKenna MC. 2014. Glutamate metabolism in the brain focusing on astrocytes. *Adv Neurobiol.* **11**:13-30
- Schwartz SM, Galis ZS, Rosenfeld ME, Falk E. 2007. Plaque rupture in humans and mice. *Arterioscler Thromb Vasc Biol.* **27**(4):705-13
- Selemidis S, Dusting GJ, Peshavariya H, Kemp-Harper BK, Drummond GR. 2007. Nitric oxide suppresses NADPH oxidase-dependent superoxide production by S-nitrosylation in human endothelial cells. *Cardiovasc Res.* **75**(2):349-58
- Sena CM, Pereira AM, Seiça R. 2013. Endothelial dysfunction - a major mediator of diabetic vascular disease. *Biochim Biophys Acta.* **1832**(12):2216-31
- Shah OJ, Hunter T. 2006. Turnover of the active fraction of IRS1 involves raptor-mTOR- and S6K1-dependent serine phosphorylation in cell culture models of tuberous sclerosis. *Mol Cell Biol.* **26**(17):6425-34.
- Sharma A, Sellers S, Stefanovic N, Leung C, Tan SM, Huet O, Granville DJ, Cooper ME, de Haan JB, Bernatchez P. 2015. Direct Endothelial Nitric Oxide Synthase Activation Provides Atheroprotection in Diabetes-Accelerated Atherosclerosis. *Diabetes.* **64**(11):3937-50
- Shen LJ, Beloussow K, Shen WC. 2005. Accessibility of endothelial and inducible nitric oxide synthase to the intracellular citrulline-arginine regeneration pathway. *Biochem Pharmacol.* **69**(1):97-104.
- Shin BS, Fung HL, Upadhyay M, Shin S. 2015. Estimation of nitric oxide synthase activity via liquid chromatography/tandem mass spectrometric assay determination of 15N3-citrulline in biological samples. *Rapid Commun Mass Spectrom.* **29**(5):447-455.
- Sigala F, Efentakis P, Karageorgiadi D, Filis K, Zampas P, Iliodromitis EK, Zografos G, Papapetropoulos A, Andreadou I. 2017. Reciprocal regulation of eNOS, H2S and CO-synthesizing enzymes in human atheroma: Correlation with plaque stability and effects of simvastatin. *Redox Biol.* **12**:70-81
- Sigma-Aldrich. 2020. *Aldrich Polymer Products Application & Reference Information. Ion Exchange Resins: Classification and Properties.* [Online]. [Accessed 26<sup>th</sup> February 2020]. Available from:  
[https://www.sigmaaldrich.com/content/dam/sigma-aldrich/docs/Aldrich/Brochure/al\\_pp\\_ionx.pdf](https://www.sigmaaldrich.com/content/dam/sigma-aldrich/docs/Aldrich/Brochure/al_pp_ionx.pdf)

- Silvestre-Roig C, de Winther MP, Weber C, Daemen MJ, Lutgens E, Soehnlein O. 2014. Atherosclerotic plaque destabilization: mechanisms, models, and therapeutic strategies. *Circ Res.* **114**(1):214-26
- Simionescu M, Sima AV. 2012. Morphology of atherosclerotic lesions. In: Wick G, Grundtman C, ed. *Inflammation and Atherosclerosis*. Vienna: Springer, pp.19–37
- Singh R, Barden A, Mori T, Beilin L. 2001. Advanced glycation end-products: a review. *Diabetologia.* **44**(2):129-46.
- Siragusa M, Fleming I. 2016. The eNOS signalosome and its link to endothelial dysfunction. *Pflugers Arch.* **468**(7):1125-37
- Sitia S, Tomasoni L, Atzeni F, Ambrosio G, Cordiano C, Catapano A, Tramontana S, Perticone F, Naccarato P, Camici P, Picano E, Cortigiani L, Bevilacqua M, Milazzo L, Cusi D, Barlassina C, Sarzi-Puttini P, Turiel M. 2010. From endothelial dysfunction to atherosclerosis. *Autoimmun Rev.* **9**(12):830-4
- Smyth EM, Grosser T, Wang M, Yu Y, FitzGerald GA. 2009. Prostanoids in health and disease. *J Lipid Res.* **50** Suppl:S423-8
- Sobczak M, Dargatz J, Chrzanowska-Wodnicka M. 2010. Isolation and culture of pulmonary endothelial cells from neonatal mice. *J Vis Exp.* (46):2316
- Sobrevia L, Nadal A, Yudilevich DL, Mann GE. 1996. Activation of L-arginine transport (system y+) and nitric oxide synthase by elevated glucose and insulin in human endothelial cells. *J Physiol.* **490** (Pt 3):775-81.
- Song F, Xue Y, Dong D, Liu J, Fu T, Xiao C, Wang H, Lin C, Liu P, Zhong J, Yang Y, Wang Z, Pan H, Chen J, Li Y, Cai D, Li Z. 2016. Insulin Restores an Altered Corneal Epithelium Circadian Rhythm in Mice with Streptozotocin-induced Type 1 Diabetes. *Sci Rep.* **6**:32871
- Soskić SS, Dobutović BD, Sudar EM, Obradović MM, Nikolić DM, Djordjevic JD, Radak DJ, Mikhailidis DP, Isenović ER. 2011. Regulation of Inducible Nitric Oxide Synthase (iNOS) and its Potential Role in Insulin Resistance, Diabetes and Heart Failure. *Open Cardiovasc Med J.* **5**:153-63
- Stefanadis C, Antoniou CK, Tsiachris D, Pietri P. 2017. Coronary Atherosclerotic Vulnerable Plaque: Current Perspectives. *J Am Heart Assoc.* **6**(3):e005543
- Steffek AE, McCullumsmith RE, Haroutunian V, Meador-Woodruff JH. 2008. Cortical expression of glial fibrillary acidic protein and glutamine synthetase is decreased in schizophrenia. *Schizophr Res.* **103**(1-3):71-82

- Stein DT, Esser V, Stevenson BE, Lane KE, Whiteside JH, Daniels MB, Chen S, McGarry JD. 1996. Essentiality of circulating fatty acids for glucose-stimulated insulin secretion in the fasted rat. *J Clin Invest.* **97**(12):2728-35
- Strawbridge RJ, van Zuydam NR. 2018. Shared Genetic Contribution of Type 2 Diabetes and Cardiovascular Disease: Implications for Prognosis and Treatment. *Curr Diab Rep.* **18**(8):59
- Su Y, Edwards-Bennett S, Bubb MR, Block ER. 2003. Regulation of endothelial nitric oxide synthase by the actin cytoskeleton. *Am J Physiol Cell Physiol.* **284**(6):C1542-9
- Su Y, Kondrikov D, Block ER. 2007. Beta-actin: a regulator of NOS-3. *Sci STKE.* **2007**(404):pe52.
- Sukriti S, Tauseef M, Yazbeck P, Mehta D. 2014. Mechanisms regulating endothelial permeability. *Pulm Circ.* **4**(4):535-51
- Szkudelski T. 2001. The mechanism of alloxan and streptozotocin action in B cells of the rat pancreas. *Physiol Res.* **50**(6):537-46.
- Tai N, Wong FS, Wen L. 2015. The role of gut microbiota in the development of type 1, type 2 diabetes mellitus and obesity. *Rev Endocr Metab Disord.* Mar;**16**(1):55-65
- Talbot K, Wang HY, Kazi H, Han LY, Bakshi KP, Stucky A, Fuino RL, Kawaguchi KR, Samoyedny AJ, Wilson RS, Arvanitakis Z, Schneider JA, Wolf BA, Bennett DA, Trojanowski JQ, Arnold SE. 2012. Demonstrated brain insulin resistance in Alzheimer's disease patients is associated with IGF-1 resistance, IRS-1 dysregulation, and cognitive decline. *J Clin Invest.* **122**(4):1316-38
- Tao Z, Shi A, Zhao J. 2015. Epidemiological Perspectives of Diabetes. *Cell Biochem Biophys.* **73**(1):181-5
- Tardito S, Chiu M, Franchi-Gazzola R, Dall'Asta V, Comi P, Bussolati O. 2012. The non-proteinogenic amino acids L-methionine sulfoximine and DL-phosphinothricin activate mTOR. *Amino Acids.* **42**(6):2507-12.
- Tesch GH, Allen TJ. 2007. Rodent models of streptozotocin-induced diabetic nephropathy. *Nephrology (Carlton).* **12**(3):261-6.
- Thermo Scientific. 2019. *Pierce™ BCA Protein Assay Kit*. [Online]. [Accessed 13<sup>th</sup> November 2019]. Available from:  
[http://tools.thermofisher.com/content/sfs/manuals/MAN0011430\\_Pierce\\_BCA\\_Protein\\_Asy\\_UG.pdf](http://tools.thermofisher.com/content/sfs/manuals/MAN0011430_Pierce_BCA_Protein_Asy_UG.pdf)
- Thorin E, Webb DJ. 2010. Endothelium-derived endothelin-1. *Pflugers Arch.* **459**(6):951-8

- Tokarz VL, MacDonald PE, Klip A. 2018. The cell biology of systemic insulin function. *J Cell Biol.* **217**(7):2273-2289
- Treuer AV, Gonzalez DR. 2015. Nitric oxide synthases, S-nitrosylation and cardiovascular health: from molecular mechanisms to therapeutic opportunities (review). *Mol Med Rep.* **11**(3):1555-65
- Van der Donckt C, Van Herck JL, Schrijvers DM, Vanhoutte G, Verhoye M, Blockx I, Van Der Linden A, Bauters D, Lijnen HR, Sluimer JC, Roth L, Van Hove CE, Fransen P, Knaapen MW, Hervent AS, De Keulenaer GW, Bult H, Martinet W, Herman AG, De Meyer GR. 2015. Elastin fragmentation in atherosclerotic mice leads to intraplaque neovascularization, plaque rupture, myocardial infarction, stroke, and sudden death. *Eur Heart J.* **36**(17):1049-58.
- Van der Vos KE, Coffey PJ. 2012. Glutamine metabolism links growth factor signaling to the regulation of autophagy. *Autophagy.* **8**(12):1862–1864
- Van der Weyden L, Shaw-Smith C, Bradley A. 2009. Chromosome Engineering in ES Cells. In: Wurst W., Kühn R. eds. *Gene Knockout Protocols. Methods in Molecular Biology (Methods and Protocols) Volume 530*. [Online]. Humana Press, pp.49-77. [Accessed 13th June 2018]. Available from: <https://link.springer.com/content/pdf/10.1007%2F978-1-59745-471-1.pdf>
- Vandekeere S, Dewerchin M, Carmeliet P. 2015. Angiogenesis Revisited: An Overlooked Role of Endothelial Cell Metabolism in Vessel Sprouting. *Microcirculation.* **22**(7):509-17
- Vanhoutte PM, Zhao Y, Xu A, Leung SW. 2016. Thirty Years of Saying NO: Sources, Fate, Actions, and Misfortunes of the Endothelium-Derived Vasodilator Mediator. *Circ Res.* **119**(2):375-96
- Venema RC, Sayegh HS, Kent JD, Harrison DG. 1996. Identification, characterization, and comparison of the calmodulin-binding domains of the endothelial and inducible nitric oxide synthases. *J Biol Chem.* **271**(11):6435-40.
- Venugopal SK, Devaraj S, Yuhanna I, Shaul P, Jialal I. 2002. Demonstration that C-reactive protein decreases eNOS expression and bioactivity in human aortic endothelial cells. *Circulation.* **106**(12):1439-41
- Vicent D, Ilany J, Kondo T, Naruse K, Fisher SJ, Kisanuki YY, Bursell S, Yanagisawa M, King GL, Kahn CR. 2003. The role of endothelial insulin signaling in the regulation of vascular tone and insulin resistance. *J Clin Invest.* **111**(9):1373-80

- Vikramadithyan RK, Hu Y, Noh HL, Liang CP, Hallam K, Tall AR, Ramasamy R, Goldberg IJ. 2005. Human aldose reductase expression accelerates diabetic atherosclerosis in transgenic mice. *J Clin Invest.* **115**(9):2434-43
- Villacorta L, Chang L, Salvatore SR, Ichikawa T, Zhang J, Petrovic-Djergovic D, Jia L, Carlsen H, Schopfer FJ, Freeman BA, Chen YE. 2013. Electrophilic nitro-fatty acids inhibit vascular inflammation by disrupting LPS-dependent TLR4 signalling in lipid rafts. *Cardiovasc Res.* **98**(1):116-24
- Villacorta L, Gao Z, Schopfer FJ, Freeman BA, Chen YE. 2016. Nitro-fatty acids in cardiovascular regulation and diseases: characteristics and molecular mechanisms. *Front Biosci (Landmark Ed).* **21**:873-89
- Vion AC, Kheloufi M, Hammoutene A, Poisson J, Lasselin J, Devue C, Pic I, Dupont N, Busse J, Stark K, Lafaurie-Janvore J, Barakat AI, Loyer X, Souyri M, Viollet B, Julia P, Tedgui A, Codogno P, Boulanger CM, Rautou PE. 2017. Autophagy is required for endothelial cell alignment and atheroprotection under physiological blood flow. *Proc Natl Acad Sci U S A.* **114**(41):E8675-E8684
- Virmani R, Kolodgie FD, Burke AP, Finn AV, Gold HK, Tulenko TN, Wrenn SP, Narula J. 2005. Atherosclerotic plaque progression and vulnerability to rupture: angiogenesis as a source of intraplaque hemorrhage. *Arterioscler Thromb Vasc Biol.* **25**(10):2054-61
- Visscher PM, Wray NR, Zhang Q, Sklar P, McCarthy MI, Brown MA, Yang J. 2017. 10 Years of GWAS Discovery: Biology, Function, and Translation. *Am J Hum Genet.* **101**(1):5-22
- Viswambharan H, Yuldasheva NY, Sengupta A, Imrie H, Gage MC, Haywood N, Walker AM, Skromna A, Makova N, Galloway S, Shah P, Sukumar P, Porter KE, Grant PJ, Shah AM, Santos CX, Li J, Beech DJ, Wheatcroft SB, Cubbon RM, Kearney MT. 2017. Selective Enhancement of Insulin Sensitivity in the Endothelium In Vivo Reveals a Novel Proatherosclerotic Signaling Loop. *Circ Res.* **120**(5):784-798
- Víteček J, Lojek A, Valacchi G, Kubala L. 2012. Arginine-based inhibitors of nitric oxide synthase: therapeutic potential and challenges. *Mediators Inflamm.* **2012**:318087
- Wang H, Wang AX, Liu Z, Chai W, Barrett EJ. 2009. The trafficking/interaction of eNOS and caveolin-1 induced by insulin modulates endothelial nitric oxide production. *Mol Endocrinol.* **23**(10):1613-23

- Wang M, Hao H, Leeper NJ, Zhu L; Early Career Committee. 2018. Thrombotic Regulation From the Endothelial Cell Perspectives. *Arterioscler Thromb Vasc Biol.* **38**(6):e90-e95
- Wang Z, Yan X. 2013. CD146, a multi-functional molecule beyond adhesion. *Cancer Lett.* **330**(2):150-62
- Weber C, Noels H. 2011. Atherosclerosis: current pathogenesis and therapeutic options. *Nat Med.* **17**(11):1410-22
- Wei X, Song H, Semenkovich CF. 2014. Insulin-regulated protein palmitoylation impacts endothelial cell function. *Arterioscler Thromb Vasc Biol.* **34**(2):346-54
- Weiner ID, Verlander JW. 2017. Ammonia Transporters and Their Role in Acid-Base Balance. *Physiol Rev.* **97**(2):465-494
- Wen S, Liu DF, Cui Y, Harris SS, Chen YC, Li KC, Ju SH, Teng GJ. 2014. In vivo MRI detection of carotid atherosclerotic lesions and kidney inflammation in ApoE-deficient mice by using LOX-1 targeted iron nanoparticles. *Nanomedicine.* **10**(3):639-49
- Westerterp M, van der Hoogt CC, de Haan W, Offerman EH, Dallinga-Thie GM, Jukema JW, Havekes LM, Rensen PC. 2006. Cholesteryl ester transfer protein decreases high-density lipoprotein and severely aggravates atherosclerosis in APOE\*3-Leiden mice. *Arterioscler Thromb Vasc Biol.* **26**(11):2552-9
- Wheatcroft SB, Shah AM, Li JM, Duncan E, Noronha BT, Crossey PA, Kearney MT. 2004. Preserved glucohomeostasis but attenuation of the vascular actions of insulin in mice heterozygous for knockout of the insulin receptor. *Diabetes.* **53**(10):2645-52.
- Wilcox G. 2005. Insulin and insulin resistance. *Clin Biochem Rev.* **26**(2):19-39
- Witteck A, Yao Y, Fechir M, Förstermann U, Kleinert H. 2003. Rho protein-mediated changes in the structure of the actin cytoskeleton regulate human inducible NO synthase gene expression. *Exp Cell Res.* **287**(1):106-15
- World Health Organisation. 2016. *Global report on diabetes*. [Online]. Geneva: World Health Organisation. [Accessed 17 October 2018]. Available from: [https://apps.who.int/iris/bitstream/handle/10665/204871/9789241565257\\_eng.pdf;jsessionid=C6423357C050D42DC3922D82A5E2079E?sequence=1](https://apps.who.int/iris/bitstream/handle/10665/204871/9789241565257_eng.pdf;jsessionid=C6423357C050D42DC3922D82A5E2079E?sequence=1)
- World Health Organization. 2018. *The top 10 causes of death*. [Online]. [Accessed 10<sup>th</sup> August 2019]. Available from: <https://www.who.int/news-room/fact-sheets/detail/the-top-10-causes-of-death>

- Wu G, Haynes TE, Li H, Yan W, Meininger CJ. 2001. Glutamine metabolism to glucosamine is necessary for glutamine inhibition of endothelial nitric oxide synthesis. *Biochem J.* **353**(Pt 2):245-52.
- Xiao D, Zeng L, Yao K, Kong X, Wu G, Yin Y. 2016. The glutamine-alpha-ketoglutarate (AKG) metabolism and its nutritional implications. *Amino Acids.* **48**(9):2067-80
- Yang YM, Huang A, Kaley G, Sun D. 2009. eNOS uncoupling and endothelial dysfunction in aged vessels. *Am J Physiol Heart Circ Physiol.* **297**(5):H1829-36
- Yaribeygi H, Farrokhi FR, Butler AE, Sahebkar A. 2019. Insulin resistance: Review of the underlying molecular mechanisms. *J Cell Physiol.* **234**(6):8152-8161
- Ye J, Palm W, Peng M, King B, Lindsten T, Li MO, Koumenis C, Thompson CB. 2015. GCN2 sustains mTORC1 suppression upon amino acid deprivation by inducing Sestrin2. *Genes Dev.* **29**(22):2331-6.
- Zadeh MS, Kolb JP, Geromin D, D'Anna R, Boulmerka A, Marconi A, Dugas B, Marsac C, D'Alessio P. 2000. Regulation of ICAM-1/CD54 expression on human endothelial cells by hydrogen peroxide involves inducible NO synthase. *J Leukoc Biol.* **67**(3):327-34.
- Zadelaar S, Kleemann R, Verschuren L, de Vries-Van der Weij J, van der Hoorn J, Princen HM, Kooistra T. 2007. Mouse models for atherosclerosis and pharmaceutical modifiers. *Arterioscler Thromb Vasc Biol.* **27**(8):1706-21
- Zanotto TM, Quaresma PGF, Guadagnini D, Weissmann L, Santos AC, Vecina JF, Calisto K, Santos A, Prada PO, Saad MJA. 2016. Blocking iNOS and endoplasmic reticulum stress synergistically improves insulin resistance in mice. *Mol Metab.* **6**(2):206-218.
- Zhao J, Ou SL, Wang WY, Yan C, Chi LX. 2017. MicroRNA-1907 enhances atherosclerosis-associated endothelial cell apoptosis by suppressing Bcl-2. *Am J Transl Res.* **9**(7):3433-3442
- Zhao Y, Vanhoutte PM, Leung SW. 2015. Vascular nitric oxide: Beyond eNOS. *J Pharmacol Sci.* **129**(2):83-94
- Zhao YY, Malik AB. 2009. A novel insight into the mechanism of pulmonary hypertension involving caveolin-1 deficiency and endothelial nitric oxide synthase activation. *Trends Cardiovasc Med.* **19**(7):238-42
- Zharikov SI, Sigova AA, Chen S, Bubb MR, Block ER. 2001. Cytoskeletal regulation of the L-arginine/NO pathway in pulmonary artery endothelial cells. *Am J Physiol Lung Cell Mol Physiol.* **280**(3):L465-73.

Zhou Y, Qiu L, Xiao Q, Wang Y, Meng X, Xu R, Wang S, Na R. 2013. Obesity and diabetes related plasma amino acid alterations. *Clin Biochem.* **46**(15):1447-52